THE DYNAMICS OF TWO-DIMENSIONAL CANTILEVERED FLEXIBLE PLATES IN AXIAL FLOW AND A NEW ENERGY-HARVESTING CONCEPT

LIAOSHA TANG

Department of Mechanical Engineering
McGill University, Montréal

November, 2007

A Thesis submitted to the Faculty of Graduate Studies and Research
in partial fulfilment of the requirements for the degree of
Doctorate of Philosophy

Your file Votre référence
ISBN: 978-0-494-51004-9
Our file Notre référence
ISBN: 978-0-494-51004-9

Dedicated to
my wife, Xiaofeng Ma,
and our son, Martin Tang.

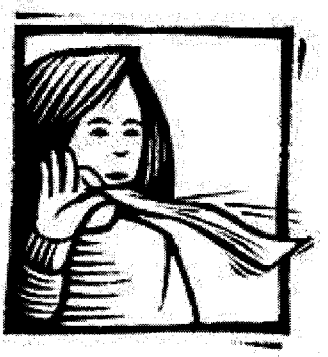

非风动，非幡动，仁者心动

六祖慧能

于公元六七六年

Neither the wind nor the flag, but your mind,
is the truth of the motions of a flag in wind.

by **Master Hui Neng**,
the Sixth Patriarch
of Chinese Chan Buddhism
January 8, A.D. 676

Many "simple" things are fraught with mystery.

Consider a flag: Why does it flap,

instead of streaming straight in a steady breeze?

Five centuries after the Scientific Revolution swept the Western world,

scientists surely can explain the flapping of flags, right?

No, they can't – not yet. But they're working on it.

by **Keay Davidson**,

Chronicle Science Writer

San Francisco Chronicle

January 21, 2002

Abstract

This thesis studies the dynamics of two-dimensional cantilevered flexible plates subjected to axial flow and proposes a new energy-harvesting concept, the flutter-mill, utilizing the flutter motions to generate electrical power.

The nonlinear model of the cantilevered flexible plate is developed using the inextensibility assumption. The panel method, in particular the unsteady lumped vortex model associated with a dynamic vortical wake, is used for calculating the aero/hydro-dynamic loads acting on the plate. The investigation of the dynamics of this system is conducted systematically in the multiparameter space involved, in order to give a comprehensive picture of the global dynamics of the system. The influence of various factors on the dynamics of the system are discussed, including the length of the upstream rigid segment, the material damping and the viscous drag. Moreover, the dynamics of the system in a variety of modified configurations, i.e., with the gravitational force taken into account, with parallel solid walls, an additional spring support, an additional concentrated mass, an oscillating angle of incidence in the undisturbed flow, and two identical parallel plates, is also studied.

The energy transfer between the cantilevered flexible plate and the surrounding fluid flow is examined. Based on the analysis of energy transfer, the concept of a flutter-mill, which utilizes the self-induced vibrations of a cantilevered flexible plate in axial flow to generate electrical power is proposed. The performance of this device is preliminarily evaluated and compared to other wind-energy converters. Design considerations of the flutter-mill are summarized in the light of the dynamics of the system, in both the basic configuration and various modified configurations.

Finally, experiments with cantilevered flexible plates in axial flow are conducted in a vertical-type water tunnel. The experimental observations are compared with the simulation results based on the present theory.

Sommaire

Cette thèse traite de la dynamique des plaques bidimensionnelles flexibles en porte-à-faux dans un écoulement axial et propose un nouveau concept, le moulin flottant, qui utilise le flottement de le plaque pour la production du courant électrique.

Le modèle non-linéaire de la plaque en porte-à-faux est développé en utilisant la condition d'inextensibilité. Pour ce qui est du fluide, le modèle de tourbillous ponctuels associés à un sillage vortical dynamique est employé pour calculer les charges aéro/hydro-dynamiques sur la plaque. La recherche est systématiquement conduite dans un espace comprenant de multiples paramètres afin de donner une image complète de la dynamique du système. Les influences de divers facteurs sur la dynamique du système sont discutées, y compris la longueur du segment rigide amont, la dissipation du matériau de la plaque et de la trainée visquense. En plus, la dynamique du système dans une variété de différentes configurations a été étudiée, i.e., considérant la force de la gravité, la friction, l'ajout d'un ressort, on d'une masse concentrée additionnelle, un angle d'incidence oscillatoire, et deux plaques parallèles identiques.

Le transfert d'énergie entre la plaque flexible en porte-à-faux et le flux de fluide environnant est examiné. Basé sur l'analyse du transfert d'énergie, on propose le concept d'un moulin flottant, qui utilise les vibrations auto-entretenues d'une plaque flexible en porte-à-faux dans un écoulement axial pour la génération d'électricité. Le design de ce dispositif est évalué d'une façon préliminaire.

En conclusion, des expériences avec de plaques flexibles en porte-à-faux dans un écoulement axial dans un tunnel hydrodynamique ont été réalisées. Les observations expérimentales sont comparées aux résultats de simulation basés sur la théorie actuelle.

Statement of Contributions to Original Knowledge

This thesis studies the dynamics of two-dimensional cantilevered flexible plates in axial flow, of which the main contributions to original knowledge can be summarized as follows.

- This is the most comprehensive investigation to date on the dynamics of cantilevered flexible plates in axial flow. The dynamics is systematically studied in the multiparameter space; various factors influencing the dynamics are examined in detail. The simulation results based on the present theory have been compared with previous theoretical predictions and experimental observations; the present theory captures the principal attributes of the global dynamics of the system and achieves a better agreement with experimental observations than previous theories.
- The discrepancy between theoretical predictions and experimental observations are discussed in detail, in particular the type of the instability (subcritical or supercritical) of the system. When a von-Kármán-type wake street is taken into account in association with the dynamic wake behind the plate, it was shown for the first time that the dynamics of the system is dependent on initial conditions, and that a hysteresis phenomenon can be predicted with the present theory in the vicinity of the critical point, similar to that observed in previous experiments.
- The dynamics of the system in a variety of modified configurations, i.e., with the gravitational force taken into account, with parallel solid walls, an additional spring support, an additional concentrated mass, an oscillating angle of incidence in the undisturbed flow, and the case of two identical parallel plates, has been studied for the first time. Rich dynamics is observed and various new phenomena are found. For example, a stronger constraint is found to

lead to a less stable system, when an additional linear spring support is added to somewhere along the plate.

- The energy transfer between the cantilevered flexible plate and the surrounding fluid flow, along the length of the plate and in terms of various vibration modes, has been studied; it was found that the fluid always does negative work on the plate at the most leeward segment of the plate.
- Based on the studies of the dynamics of the system, a new energy-harvesting concept, the flutter-mill, is proposed, utilizing the flutter motions of cantilevered flexible plates in axial flow to generate electrical power.
- For the first time, experiments of cantilevered flexible plates in axial flow have been conducted in a vertical-type water tunnel, and the experimental observations were compared with the predictions obtained using the present theory.

Acknowledgements

The first person I would like to thank is my supervisor, professor Michael P. Païdoussis (ΜΙΧΑΗΛ Π. ΠΑΪΔΟΥΣΗΣ). I have been working with him since 2002 when I was still in my master's program. During these years I have known Professor Païdoussis as a sympathetic and principled person. His enthusiasm and integrity concerning research has made a deep impression on me. His extensive knowledge, profound insight and almost forty-years experience in the field of the fluid-structure interactions helped me progress smoothly on my own road and, at the same time, enjoy the splendid scenes revealed along the way.

Special thanks to Professor Bogdan I. Epureanu for his encouragement and support, Dr. Eugeni Grinevich and Mr. Bill Mark for their technical assistance, Mrs. Mary Fiorilly St. Germain for her administrative work. Thanks extend also to my colleagues in the fluid-structure interactions group at McGill University, Konstantinos N. Karagiozis, Yahya Modarres-Sadeghi, James Wang and Stephanie Rinaldi, for their friendship and constructive discussions. Many thanks to the computers "freedom", "independence" and "liberty"; they are real supercomputers that have generated more than 200G data for two theses and six journal papers.

I am grateful to the Natural Sciences and Engineering Research Council of Canada (NSERC) and Le Fonds Québécois de la Recherche sur la Nature et les Technologies (FQRNT) of Québec for providing me the scholarships and honouring me with this support.

Deepest thanks to my wife Xiaofeng Ma, for her love and patience during the Ph.D. period. One of the best experiences that we lived through in this period was the birth of our son Martin, who provided an additional and joyful dimension to our life's mission. I am also very grateful to my parents for their support.

Nomenclature

Alphabetic

a	material damping coefficient
$(a, b)_{1,2,3,4}$	coefficient of the fourth-order scheme of the Houbolt method
A, $A_{1,2}$	wind receiving area
A_i, $\widehat{A}_{im}$	numerical constants
$\mathbb{A}^{m,n}$	matrix of influence coefficient of plate n on plate m
$\mathcal{AR}$	aspect ratio
B	spanwise dimension (i.e., the width) of the plate
B_{imnl}, $\widehat{B}_{imn}$	numerical constants
C_{B}	Betz limit
C_{imnl}, $\widehat{C}_{imn}$	numerical constants
C_{D}	viscous drag coefficient
C_Y	Cauchy number
D	bending stiffness of the (two-dimensional) plate
D_i, $\widehat{D}_{imn}$	numerical constants
d_{P}, D_{P}	non-/dimensional distance between two parallel plates
d_{V}, D_{V}	non-/dimensional distance between the two rows of von Kármán vortices
E	Young's modulus
E_{imnl}, $\widehat{E}_{imnl}$	numerical constants
$f^\star$, f	non-/dimensional frequency of the plate vibration

$f^{\star}_{\alpha_U}$, f_{α_U}	non-/dimensional frequency of the oscillating incidence angle
$\mathcal{F}$	a function
$\mathbf{F}$	force vector
$\mathbb{F}$	state matrix
f_{D}, F_{D}	non-/dimensional longitudinal force acting on the plate
$F_{\mathrm{D}}{}^{\star}$	viscous drag modelled using Blasius-type solution
f_{eff}	effective nondimensional force
f_i	generalized force used in the Galerkin method
$\widehat{F}_i$	numerical constant
F_{imnl}	numerical constant
f_{L}, F_{L}	non-/dimensional transverse fluid load acting on the plate
g	gravitational acceleration
$\widehat{G}_{imn}$	numerical constant
h	plate thickness
$h_{1,2}$, $H_{1,2}$	non-/dimensional distance between a solid wall parallel to the plate and the neutral plane of the plate
H_{Hg}	height of Hg-column
H_{imnl}, $\widehat{H}_{imnl}$	numerical constants
H_{W}	translation distance of the plunging motion
I	second moment of area
I_{imnl}	numerical constant
$\mathbb{J}$	the Jacobian
J_{imnl}	numerical constant
k_{C}, K_{C}	non-/dimensional stiffness of cubic spring
k_{L}, K_{L}	non-/dimensional stiffness of linear-type spring
L	length of the flexible plate

$\mathcal{L}$	the Lagrangian
l_0, L_0	non-/dimensional length of the upstream rigid segment
L_P	total length of the plate, including the upstream rigid segment
M	number of Galerkin modes
m_A	additional concentrated mass
$\overline{M}_\mathrm{A}$	magnitude of the added-mass compensation
N	number of panels
N_M	number of the levels of mirroring process
O	origin of the coordinate system
Δp, ΔP	non-/dimensional pressure difference across the plate
P/P', Q/Q'	material points on the plate before/after a deformation
$\widehat{P}^\star_\mathrm{F}$, $\widehat{P}_\mathrm{F}$	non-/dimensional summation of the fluid power over the whole length of the plate
$\overline{P}^\star_\mathrm{F}$, $\overline{P}_\mathrm{F}$	non-/dimensional time-averaged total power of the fluid load
$P^\star_{\mathrm{F}i}$, $P_{\mathrm{F}i}$	non-/dimensional power of the fluid load working on the ith panel
p_i, q_i	generalized coordinates used in the Galerkin method
P_I	theoretical/idealized power that can be extracted from fluid flow
$\mathbf{R}$	vector of the right-hand-side
R_D	radius of a wind turbine disk
r_i	state variable
Re, Re_X	Reynolds number
s, S	non-/dimensional curvilinear coordinate
s_i	state variable or the location of the ith panel in terms of the nondimensional curvilinear coordinate
Δs, ΔS	non-/dimensional length of each individual panel

s_{K}, S_{K}	non-/dimensional location of spring support
s_{M}, S_{M}	non-/dimensional location of concentrated mass
s_{V}, S_{V}	non-/dimensional longitudinal separation between two von Kármán vortices
t, Δt	time/time step
$T^{\star}$, T	non-/dimensional tension inside the plate
$\mathcal{T}$	kinetic energy
T_{F}, T_{S}	fluid/solid time scale of a fluid-structure interaction system
U	undisturbed flow velocity
U_{R}, U_{Rc}	reduced flow velocity, critical reduced flow velocity (i.e., the critical point)
$\mathbf{V}$	vector of bound vortices and the latest wake vortex
$\mathcal{V}$	potential energy
(v, w), (V, W)	non-/dimensional longitudinal/transverse displacements of the plate
$(v, w)_{\mathrm{W}}$	nondimensional wake-induced flow velocity
$(V, W)_{\mathrm{W}}$	dimensional wake-induced flow velocity
$(v, w)_{\Gamma}$	nondimensional flow velocity induced by bound vortices
$\mathcal{W}$	virtual work
$\widehat{W}_{\mathrm{F}}^{\star}$, $\widehat{W}_{\mathrm{F}}$	non-/dimensional total work done by the fluid load over the whole length of the plate
$W_{\mathrm{F}i}^{\star}$, $W_{\mathrm{F}i}$	non-/dimensional work done by the fluid load at the ith panel
$\mathbf{Y}$	state vector
(x, y, z)	coordinate
(X, Y, Z)	coordinate

Greek symbols

α	nondimensional material damping coefficient
α_i	angle between a panel and the X axis
$\alpha_{i,j}$	influence coefficient of the jth panel on the ith panel
α_U	the magnitude of the oscillating incidence angle
$\overline{\beta}_{\mathrm{A}}$	coefficient of added-mass compensation
β_i	eigenvalue of the ith mode of a cantilevered beam
$\gamma^\star$	summation of all bound vortices at the last previous time step
γ_{G}	gravity parameter
γ_i, Γ_i	non-/dimensional strength of bound vortex
$\gamma_{\mathrm{W}j}$, $\Gamma_{\mathrm{W}j}$	non-/dimensional strength of wake vortex
γ_{V}, Γ_{V}	non-/dimensional strength of von Kármán wake vortex
δ	Dirac delta function, or a small increasement, or a variational operator, as the case may be
δ_{D}	logarithmic decrement
δ_{F}	Feigenbaum number
$\delta_{i,j}$	Dirac delta
ϵ	the bookmark for a small quantity
ε	axial strain along the centreline of the plate
ζ	length-to-thickness ratio
ζ_{P}	power coefficient
ζ_{W}	work coefficient
θ	angle between the tangent of the plate centreline and the X axis
κ	curvature
λ	wavelength
λ_{W}	wavelength of the wake

$\lambda_{1,2,3_i}$	time-dependent coefficients used in the Houbolt method
μ	mass ratio
ν	Poisson ratio
υ_{F}	kinematic viscosity of the fluid
ρ_{F}, ρ_{P}	mass density of fluid/plate material
ρ_{Hg}, ρ_{Water}	mass density of mercury/water
σ_{M}	concentrated mass parameter
ς_i	constant coefficient in associated with the ith linear mode of a cantilevered beam
τ, $\Delta\tau$	nondimensional time/time step
τ_{E}	stop-time
$\Delta\tau_{\mathrm{R}}$	nondimensional time step for recording simulation data
ϕ_i	ith eigenmode of the transverse displacement of the plate
χ	length parameter
ψ_i	ith eigenmode of the longitudinal displacement of the plate
$\Psi^{\star}_{\mathrm{F}m}$	nondimensional work done by the fluid load in terms of the mth
Ω	circular frequency of oscillation

Superscripts, subscripts, overdot and prime

$(\cdot)^k$	quantity at discrete time instant k
$(\cdot)^m$	quantity of the mth plate
$(\cdot)^{\mathrm{T}}$	transpose operation
$(\cdot)_{\mathrm{C}i}$	quantity for the ith collocation point
$(\cdot)_{\mathrm{V}i}$	quantity for the ith bound vortex
$(\cdot)_{\mathrm{W}i}$	quantity for the ith wake vortex

$(\cdot)_i(\cdot)_i$	repeating indices denoting summation
$\dot{(\,)}$	overdot denoting temporal derivative
$(\,)'$	prime denoting spatial derivative

Table of Contents

List of Figures

List of Tables

Chapter 1

Introduction

1.1. The problem and motivation

Why and how does a flag flutter?

What can one expect from the flutter motions of a flag?

Although the flapping motions of a flag in wind is such a trivial everyday phenomenon, it has been challenging the wisdom of human beings from ancient times. In A.D. 676, just before his inauguration as the the Sixth Patriarch of Chinese Chan Buddhism, Master Hui Neng run into two young monks at the gate of Faxing Temple who were arguing about the flapping motions of a flag: one ascribed the flag motions to the wind; while, the other one insisted that the wind was caused by the flag. To settle the argument, Master Hui Neng spoke out one of his most famous Chan statements: *neither the wind nor the flag, but your mind, is the truth of the motions of a flag in wind.*

This thesis aims to give some answers to the *why-how-what* questions through a systematic investigation on the dynamics of cantilevered flexible plates subjected to axial flow. Although it has a very simple configuration, the flag flutter problem is indeed a difficult topic in the study of fluid-structure interactions, in which a deformable structure with certain mass and stiffness (for example, the flexible plate studied in

this thesis), the fluid flow surrounding the structure and the wake behind the structure have to be considered as inseparable parts of an integrated system. When the flow velocity is low, the plate remains in its original flat state; any disturbance to the system is attenuated. However, when the flow velocity grows and exceeds a critical value, the plate loses its stability; flutter takes place.

The earliest study of the flapping motion of flag can be found in the work by Lord Rayleigh (1879), dating back to the nineteenth century. Although its theoretical worthiness has attracted scientists to work on this fundamental problem for over one hundred years, pure curiosity is definitely not the only source of the effort devoted thereto. The momentum of the studies also originates from interests in, see Fig. 1.1, the human snoring problem caused by the vibrations of the soft palate (Huang, 1995; Aurégan and Depollier, 1995; Balint and Lucey, 2005; Tetlow et al., 2006), the sheet flutter observed in the operation of printing presses and other manufacturing processes involving travelling webs (Yamaguchi et al., 2000a,b; Watanabe et al., 2002a,b; Wu and Kaneko, 2005), the design of the flexible control surface attached to an airplane wing (De Breuker et al., 2006), the design of energy-harvesting devices (Allen and Smits, 2001; Taylor et al., 2001), the swimming pattern and propulsion efficiency of aquatic animals (Lighthill, 1969; Katz and Weihs, 1978; Wolfgang et al., 1999; Pedley and Hill, 1999; Triantafyllou et al., 2000; Müller, 2003; Alban and Michel, 2004), and many others, including the strip stabilizer/decelartor of cluster bomblet/rocket-dispersed grenades (Auman and Dahlke, 2001) and the advertising streamers towed by aircraft (Hoerner, 1958), as shown in Fig. 1.2.

As stated by Païdoussis (2004, Chapter 10), indeed, the dynamics of plates in fluid flow is a huge topic. In this thesis, the flag flutter problem is studied through an idealized model as a cantilevered flexible plate in axial flow. That is, the structure is considered to be a flexible homogenous rectangular plate of finite length. The plate is clamped at its upstream edge; all the other edges are free. The fluid passes over both surfaces of the plate in the direction from the clamped leading edge to the free trailing edge; no cross-flow is considered. Finally, the plate is very thin and very pliable; hence flutter is expected at low flow velocities. Even working with such a

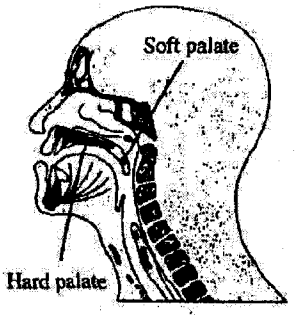

(a) The human snoring problem studied by Huang (1995)

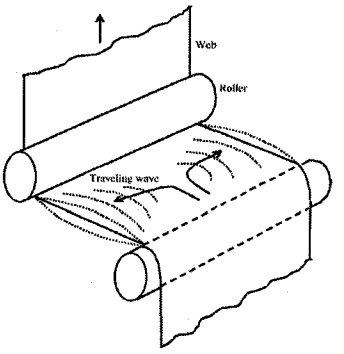

(b) The paper flutter problem studied by Watanabe et al. (2002a,b)

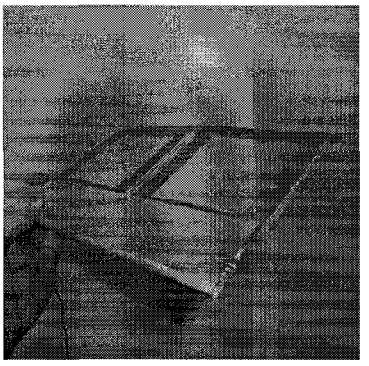

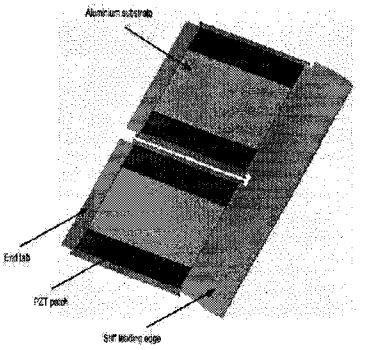

(c) The flexible control surface studied by De Breuker et al. (2006)

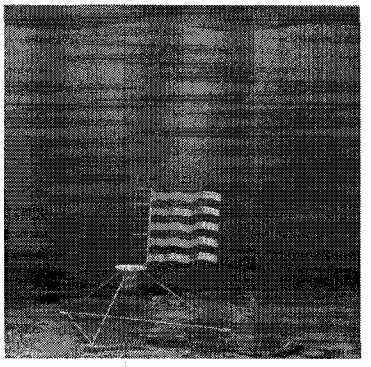

(d) The energy-harvesting eels studied by Taylor et al. (2001)

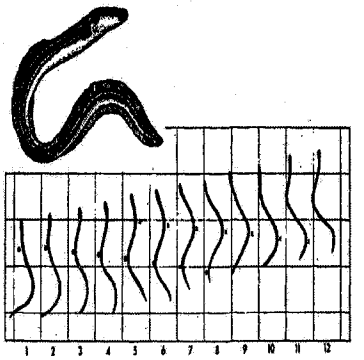

(e) The eel motion studied by Lighthill (1969)

FIGURE 1.1. The study of cantilevered flexible plates in axial flow originated from various practical applications.

considerably simplified system, the flag flutter problem demonstrates its difficulties and distinguishing characteristics from other problems of plates in fluid flow in two aspects: the large amplitude of the motion, which may be of the order of a fraction of the length of the plate, and the dynamic wake behind the structure.

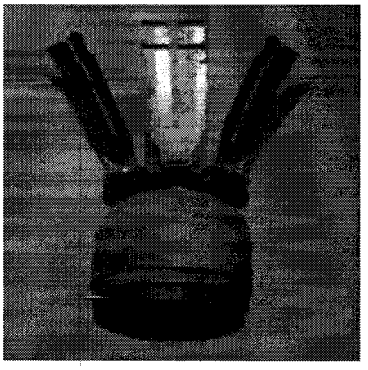

(a) BLU-3 cluster bomblet
(WIKIPEDIA, 2007)

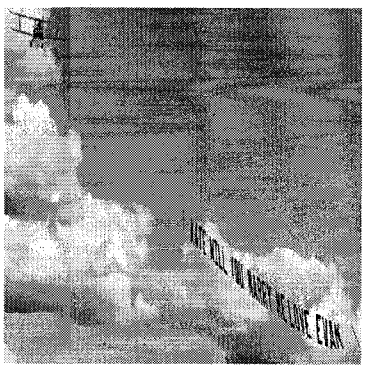

(b) Banner towed by an aircraft
(Hempels Aviation, 2007)

FIGURE 1.2. Other applications of cantilevered flexible plates in axial flow.

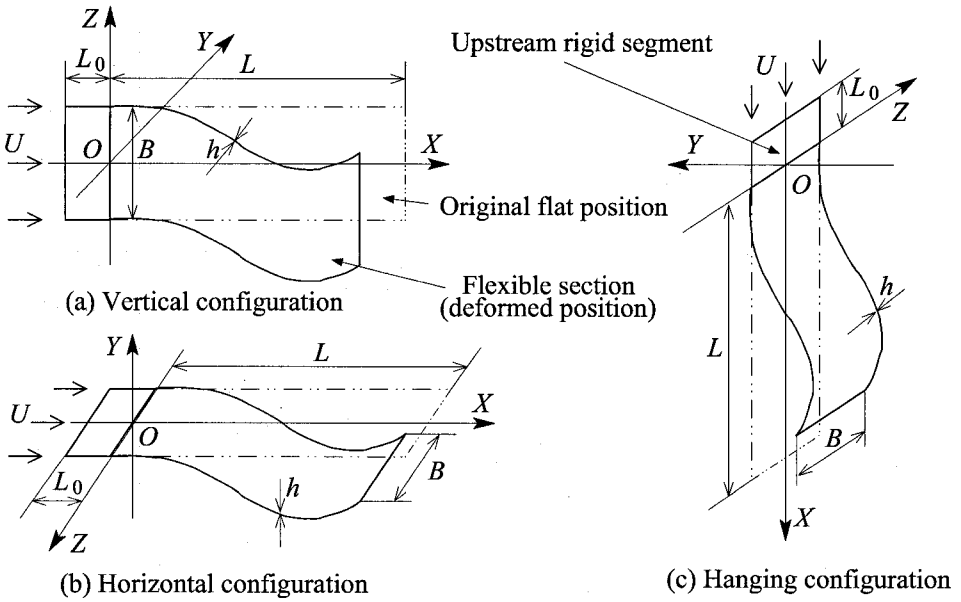

FIGURE 1.3. Three arrangements of cantilevered flexible plates in axial flow: (a) vertical configuration, (b) horizontal configuration and (c) hanging configuration, with the gravitational force, respectively, in the negative Z, negative Y, positive X direction.

As shown in Fig. 1.3, cantilevered flexible plates in axial flow may have vertical, horizontal or hanging configurations. How the gravitational force acts on the plate is the only difference among them. The geometrical characteristics of the plate are the length of flexible section L, width B and thickness h ($h \ll L$ for a thin plate). Normally, there is a rigid segment of length L_0 as part of the clamping arrangement at the upstream edge. The other physical parameters of the system are: the plate material density ρ_P and bending stiffness $D = Eh^3B/[12(1-\nu^2)]$ (in the case of a two-dimensional plate $D = Eh^3/[12(1-\nu^2)]$), where E and ν are, respectively,

Young's modulus and the Poisson ratio of the plate material, the fluid density ρ_F, and the mean undisturbed flow velocity U. The plate may be called a flag, a sheet, or specifically a two-dimensional plate, when the aspect ratio $\mathcal{AR} = B/L$ is large. Conversely, it may be called a strip when $\mathcal{AR}$ is small. Historically, the terms *flag* and *strip* were frequently used to refer to a plate-like structure with perfect flexibility (i.e., $D \to 0$). However, these terminologies are interchangeable with *plate* when the bending stiffness, no matter how small, is taken into account.

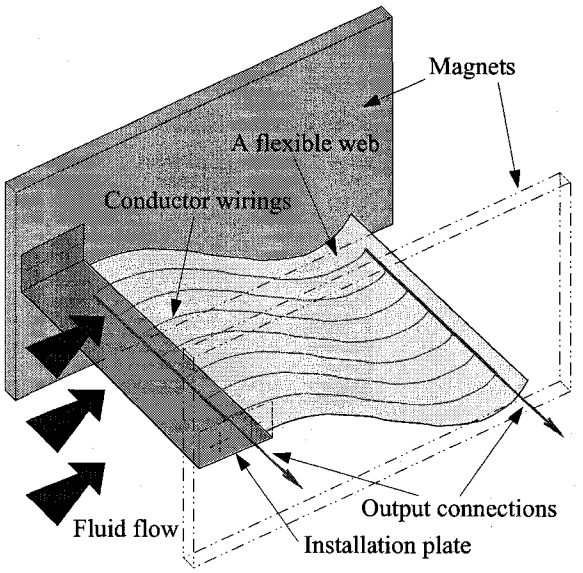

FIGURE 1.4. A schematic diagram of flutter-mill: a new energy-harvesting concept utilizing the flutter motions of cantilevered flexible plates in axial flow to generate electrical power.

The motivation of this thesis is two-fold. First, keeping in mind the *why* and *how* questions stated at the beginning of this thesis, the behaviour of cantilevered flexible plates in axial flow, both the onset of instability and the post-critical vibrations, is systematically investigated in various parameter spaces of the fluid-structure interaction system; the purpose is to obtain a comprehensive, though by no means complete, picture of the dynamics of the system and a further insight into the flutter mechanism. A variety of factors affecting the dynamics of the system are taken into account, including the length of the upstream rigid segment, the material damping, the viscous drag and the gravitational forces in the case of the system being in the horizontal or hanging configuration. Moreover, the dynamics of the system with additional features, i.e., the system with parallel solid walls, with an additional spring

support, with an additional concentrated mass, with a small oscillating component in the upstream mean flow, and multiple parallel plates, are examined. Second, the energy transfer between the cantilevered flexible plate and the surrounding fluid flow is studied; based on the theoretical work, a new energy-harvesting concept utilizing the flutter motions of plates subjected to axial flow, as illustrated in Fig. 1.4, i.e., "the flutter-mill" (borrowing the terminology from *wingmill* coined by Adamko and DeLaurier (1978)), is proposed. The performance of the flutter-mill is preliminarily evaluated, at this stage, without extensive optimization in the multiparameter space of the system. However, design considerations in the light of the dynamics of cantilevered flexible plates in axial flow, which may be in the basic plain configuration or in modified versions (for example, with an additional spring support and/or concentrated mass), are summarized.

The rapid advances in numerical techniques and computational facilities definitely contribute a lot to the current vigorous studies in fluid-structure interaction problems, more particularly, the recent resurgence of interest in the flapping flag problem. During the preparation of this thesis, some commercial software products, such as ANSYS (2006, Version 10.0) and ADINA (2006), have made available functional modules for coupled fluid-structure interaction problems. However, the theme of this thesis is the global dynamics of the system in question in the multiparameter space, instead of the case study of a specific system with a fixed set of parameters or the development of a state-of-the-art solver for the fluid-structure interactions. Therefore, regarding the solution technique aspect, a relatively simple model and the resulting effective numerical/computational approaches are developed in this thesis to produce physically meaningful simulation results using ordinary personal computers.

1.2. Literature review

1.2.1. What causes the flutter motions of a flag in wind? Flag flutter was explained by Lord Rayleigh (1879) as the growth of the instability developed

at the interface between two heterogeneous continua moving in parallel with sufficient shear velocity, i.e., the Kelvin-Helmholtz instability (Chandrasekhar, 1961). Argentina and Mahadevan (2005) argued that the lack of a differential velocity profile across the flag and the finite flexibility and length of the flag result in the failure of the application of Kelvin-Helmholtz instability. However, a velocity difference of the fluid flow across the flag does exist when the system is somewhat perturbed; also, the finite flexibility and length of the flag may make the problem more complicated but this does not preclude the possibility of the Kelvin-Helmholtz instability.

The waving motions of a flag may be induced by the vortices shedding from an upstream bluff body, say the flagpole, as in the cases studied by Allen and Smits (2001) and Müller (2003). That is, the instability of the system is studied as a vortex-induced vibration problem (Allen and Smits, 2001). One may postulate that the instability of a flag in wind is due to the wake of the structure itself. Because the flag has a finite length, a von Kármán wake street forms beyond the trailing edge of the flag when the flow velocity is below the critical flow velocity and the flag is still in its static flat state (Taneda, 1958; Zhang et al., 2000). With increasing flow velocity, the strength of the wake vortices grows, and instability of the system is thus caused. However, no evidence has been found yet that the instability of the flag is *caused* by the unsteady aero/hydro-dynamics in the wake. On the contrary, in the experiments conducted by Kornecki et al. (1976), in which a rigid splitter plate was placed behind a flexible plate in axial flow with different clearances to the trailing edge of the plate, no significant change in the critical flow velocity was observed.

Pressure fluctuations in the turbulent boundary layer may be another possible explanation to the flag flutter problem (Dowell, 1975). In the review papers by Carpenter and Garrad (1985, 1986) on the hydrodynamic stability of flow over Kramer-type compliant surfaces, it is concluded that both a Tollmien-Schlichting instability and the so-called flow-induced surface instability, and the interaction of these two categories of instabilities, may be the underlying mechanism.

The flag flutter has also been regarded and hence extensively studied as an aero/hydro-elastic phenomenon, i.e., the interaction of the outer flow and a solid

body, with a certain number of degrees of freedom. That is, the nature of the flag flutter problem is akin to the classical aero/hydro-elastic topics of airfoil flutter (Dowell et al., 1989; Fung, 1993) and plate/panel flutter (Dowell, 1975; Païdoussis, 2004). The underlying instability (flutter) mechanism is, as Dowell (1975) stated: *the motion of the solid itself creates significant fluctuations in the fluid loads which in turn modify the motion of the solid.* In this thesis, the study of the dynamics of cantilevered flexible plates in axial flow is conducted in the vein of aero/hydro-elasticity theories; a review of previous work relevant to the current research will be presented later.

Strictly speaking, the exact mechanism of a waving flag in wind is still an open question. Maybe the best statement summarizing the extensive efforts contributed to this deceptively simple everyday phenomenon is that made by Davidson (2002): *Five centuries after the Scientific Revolution swept the Western world, scientists surely can explain the flapping of flags, right? No, they can't – not yet. But they're working on it.*

1.2.2. Cantilevered flexible plates in axial flow. Plate flutter in fluid flow has been studied for a long time. An early monograph on this topic was published by Dowell (1975). A recent review is also available in one of the books by Païdoussis (2004, Chapter 10). In the literature review that follows, it is very interesting to find that the past 10 years have witnessed a resurgence in the study of cantilevered flexible plates in axial flow.

Taneda (1968) investigated flag flutter in a series of carefully conducted experiments; his work may be the earliest one on flags and strips in the hanging configuration. Datta and Gottenberg (1975) conducted similar experiments on strip flutter and tried to give theoretical predictions of the critical flow velocity U_c in terms of strip thickness and length; the strip was modelled as a cantilevered beam, and slender wing theory (Katz and Plotkin, 2001) was used in the evaluation of the aerodynamic loads. Interesting experiments on hanging filaments, a single one or two identical ones in parallel, in a flowing soap film were conducted by Zhang et al. (2000); important observations were made on the evolution of the wake vortices and its correlation to

the stability of the system. Hanging strips were recently restudied by Yadykin et al. (2001) using a nonlinear beam model based on the inextensibility condition (Semler et al., 1994) and slender wing theory for the aerodynamics; the gravitational force was considered in the theoretical model, but its influence on the system dynamics was omitted. The latest work on strip flutter in the hanging configuration was undertaken by Lemaitre et al. (2005), who concentrated on the possible independence of the critical flow velocity U_c of strip length if the latter is sufficiently large, as observed in their experiments; a linear beam model and slender wing theory were used in their theoretical analysis, and the aforementioned phenomenon was attributed to the effect of the gravitational force.

In the hanging configuration, a major source of axial tension is due to gravity. In the vertical and horizontal configurations, however, the effects of gravity are normally neglected, and so the two arrangements in Figs. 1.3(a) and (b) may be considered to be identical.

Kornecki et al. (1976) may have been the first to study cantilevered flexible plates in axial flow having a vertical/horizontal configuration. They used a linear beam model for the structure and Theodorsen's theory (Theodorsen, 1935; Bisplinghoff et al., 1955) for the aerodynamics. The influence on the critical flow velocity U_c and frequency f_c of the circulatory and non-circulatory parts of the aerodynamic forces was discussed and correlated to their own experimental results. An extension of the theoretical work of Kornecki et al. (1976) was made by Shayo (1980) who considered plates of finite width and also three-dimensional fluid flow surrounding the plate.

Cantilevered flexible plates in axial flow were investigated by Huang (1995), Aurégan and Depollier (1995), Balint and Lucey (2005) and Tetlow et al. (2006) for the purpose of describing, and suggesting treatments for, human snoring caused by flutter of the soft palate. Huang (1995) developed an analytical model using Theodorsen's theory combined with a linear beam model to predict the critical flow velocity U_c and frequency f_c; with a special treatment for the time history of the wake vortices, a time-domain analysis was made possible. Experiments were also conducted by Huang (1995) and compared with their own theoretical predictions.

Aurégan and Depollier (1995) worked with a linear beam model and developed the expression for fluid loads using the assumption that the fluid mass is conserved along the whole length of the passageway between the plate undergoing deformations and the channel walls. It should be noted that, although the system studied by Aurégan and Depollier (1995) represented a very narrow channel flow, the fluid was still considered to be inviscid. Both Balint and Lucey (2005) and Tetlow et al. (2006) coupled a linear beam model with a two-dimensional Navier-Stokes solver; the former work used a prescribed inlet flow velocity, and the latter one defined the pressure difference between inset and outlet. Parallel solid walls were naturally taken into account in the work of Balint and Lucey (2005) and Tetlow et al. (2006) with the usage of the Navier-Stokes solver. A similar work involving the parallel solid walls was conducted by Howell et al. (2006), in which a linear beam model and the panel method (Katz and Plotkin, 2001) were used for the plate and the channel flow, respectively; although fluid flow was assumed to be inviscid and incompressible (potential flow) in this work, it was found that reducing the channel size would result in a higher critical flow velocity U_c.

Guo and Païdoussis (2000) examined the problem in question in their work on plates in axial flow with different upstream/downstream structural boundary conditions. They used a linear beam model and obtained the fluid loads through a direct solution of the potential flow surrounding the plate, in which the channel walls were considered as boundaries of the fluid domain. The work of Guo and Païdoussis (2000) was recently extended by Eloy et al. (2007); in their studies of rectangular plates with various aspect ratios $\mathcal{R}$ in open flow (without the parallel solid walls), a linear beam model was still adopted for the plate with a finite spanwise dimension. Eloy et al. (2007) concluded that the plate with a smaller aspect ratio $\mathcal{R}$ (i.e., a narrow and long plate) would have a higher critical flow velocity, which correlated with the experimental observations made by Souilliez et al. (2006).

Cantilevered plates in axial flow were studied by Yamaguchi et al. (2000a,b) and Watanabe et al. (2002a,b) in order to obtain a better understanding of sheet flutter phenomena, widely observed in the operation of printing presses and paper machines.

Both groups of researchers separately conducted a large number of experiments to reveal the relation between the critical flow velocity U_c and certain system parameters. In their theoretical work, both Yamaguchi et al. (2000a) and Watanabe et al. (2002b) adopted a linear beam model for the structure. However, Yamaguchi et al. (2000a) used a linearly varying vortex model together with a shedding wake to solve the lifting surface problem; Watanabe et al. (2002b) used Theodorsen's theory. Moreover, Watanabe et al. (2002b) also coupled their structural model with a two-dimensional compressible Navier-Stokes solver to obtain several reference results for their analysis. The sheet flutter problem was recently studied by Wu and Kaneko (2005) using a linear beam model and leakage flow theory (Païdoussis, 2004, Chapter 11) for the fluid loads. Moreover, aiming to reduce or eliminate the undesirable sheet flutter, feedback control schemes working on the plate and/or the fluid flow were, respectively, investigated by Doaré et al. (2006) and Watanabe and Koyama (2006).

Tang et al. (2003) conducted experiments and used a nonlinear structural model, making use of the inextensibility condition, to study cantilevered plates in axial flow. They used a vortex lattice model (Anderson, 2001) to calculate the aerodynamic lift over the plate. It should be noted that in the theoretical work by Tang et al. (2003), a compact system was developed using model reduction techniques, and it was directly used to study the system dynamics. Moreover, in the calculation of the pressure difference across the plate, the vibration velocity of the plate was omitted. The work by Tang et al. (2003) was theoretically extended by Attar et al. (2003) to take into account nonlinearities in the vortex lattice model by considering the interaction between individual bound/wake vortices.

More investigations on the instability of cantilevered flexible plates in axial flow can be found in the work of Argentina and Mahadevan (2005), Shelley et al. (2005) and De Breuker et al. (2006). Argentina and Mahadevan (2005) investigated the flutter mechanism of cantilevered plates in axial flow using a linear beam model and a simplified analytical model based on Theodorsen's theory for the fluid flow. Shelley et al. (2005) conducted experiments in water flow and predicted the flutter boundary by means of a linear beam model and the localized excitation theory (Crighton and

Oswell, 1991) for the fluid loads. Finally, De Breuker et al. (2006) proposed the concept of an adaptive wing for micro-aerial vehicle applications, consisting of a flexible control surface attached to the rigid wing; the stability of the rigid-flexible wing was studied using a linear beam model and Theodorsen's theory for calculating the fluid loads.

1.2.3. Other relevant work. The investigations on cantilevered flexible plates in axial flow cannot be isolated form the other plate flutter problems with different configurations; they share, to a large extent, the same theoretical concerns and study methodologies. Some of the early work of plate/panel flutter was concerned with the dynamics of space vehicle and missile skins (Dowell, 1975), particularly in supersonic flow; this work was recently reviewed by Epureanu et al. (2004a,b). To confine our interests to *subsonic* axial flow, on the one hand, the plate may be rigid; this leads to a bulk of researches on airfoil/wing flutter (Bisplinghoff et al., 1955; Bisplinghoff and Ashley, 1962; Dowell et al., 1989; Fung, 1993), which has been, and still is, under extensive investigation; the coupling between the pitching and plunging motions of an airfoil/wing may cause dynamic instability of the system and thus lead to flutter motions. On the other hand, the flexible plate may have various geometrical configurations and/or edge constraints; for example, Miles (1956) and Kornecki (1978) examined the instability of plates of infinite length in axial flow; the flag flutter problem was studied as a half-infinite membrane in axial flow by Sparenberg (1962); the trailing-edge flutter problem was investigated by Chang and Moretti (2002) for plates clamped/tensioned at the side-edges and clamped at the leading edge; the flutter of sails, the so-called luffing problem, was studied by Greenhalgh et al. (1984), Newman (1987) and Newman and Low (1991); if the plate does not have any constraint at all its edges, the free falling paper problem has been studied by Bejan (1982) and Anderson et al. (2005); and, the flutter of cantilevered plates in spanwise flow has been investigated by Ye and Dowell (1991) and Tang et al. (1999a,b). Moreover, although not covered in this thesis, it should be pointed out that the dynamics of cantilevered flexible plates in axial flow has a close relation to the swimming pattern and propulsion efficiency of aquatic animals as one can find from the work by Lighthill (1969),

Katz and Weihs (1978), Wolfgang et al. (1999), Pedley and Hill (1999), Triantafyllou et al. (2000), Müller (2003) and Alban and Michel (2004).

It should be mentioned that the problem of cantilevered flexile plates in axial flow can be otherwise placed in the broad category of slender structures in axial flow (Païdoussis, 1998, 2004), which also covers pipes conveying fluid, and cylinders and shells subjected to axial flow. In particular, one may find that quite a few aspects of the work conducted in this thesis can find counterparts in the work by Semler (1991, 1996), Semler et al. (1994), Païdoussis and Semler (1994), Wadham-Gagnon et al. (2007), Païdoussis et al. (2007) and Modarres-Sadeghi et al. (2007) for cantilevered pipes conveying fluid and Païdoussis et al. (2002), Lopes et al. (2002), Semler et al. (2002) and Modarres-Sadeghi et al. (2005) for cantilevered cylinders subjected to axial flow.

1.2.4. Energy-harvesting. Flutter is not always an unfavourable phenomenon; it can be utilized to do useful work, for example, electricity generation. The oil crisis in the mid-1970s encouraged the pursuit of alternative sources of energy; many designs of energy-harvesting devices utilizing the flutter motions of airfoils/wings came into being at that time; some of the designs are presented in Fig. 1.5.

The idea of an oscillating-wing windmill (the so-called wingmill), as shown in Fig. 1.5(a), was proposed by Adamko and DeLaurier (1978) and McKinney and DeLaurier (1981); a prototype of this wind energy converter was developed and tested. When this kind of device is properly designed so as to achieve a $-\pi/2$ phase difference between the plunging and pitching motions, Ly and Chasteau (1981) have demonstrated that the efficiency is equivalent to that of the vertical axis wind turbine (Darrieus-type) (Manwell et al., 2002). The studies on the wingmill continued, and a patent (Lee, 2004) was granted in 2004. In particular, as shown in Fig. 1.5(b), Jones and Platzer (1997, 1999) conducted theoretical studies as well as experiments with a wingmill design similar to that of McKinney and DeLaurier (1981). In the design of McKinney and DeLaurier (1981), an entirely mechanical mechanism is used to couple the plunging and pitching motions of the wing; while, as shown in Fig. 1.5(d),

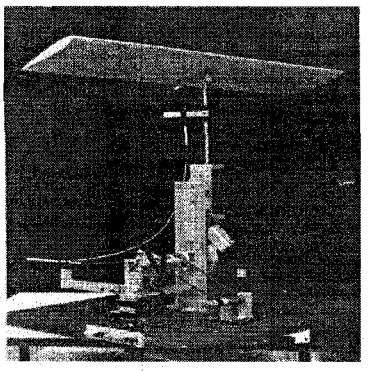

(a) The wingmill proposed by McKinney and DeLaurier (1981)

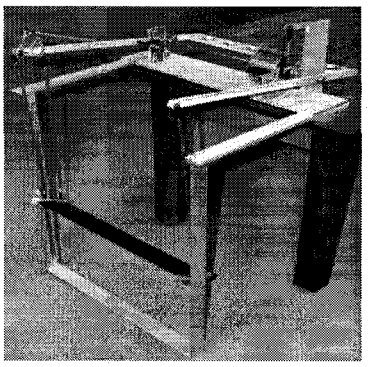

(b) The flapping-wing power extraction device proposed by Jones and Platzer (1999)

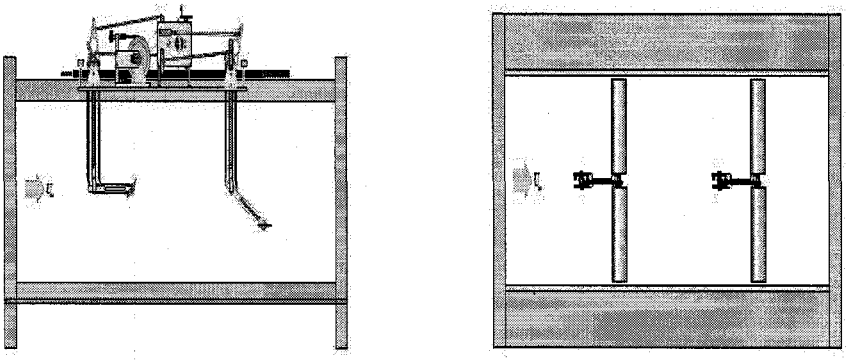

(c) The oscillating-wing micro-hydropower generator proposed by Jones et al. (2003)

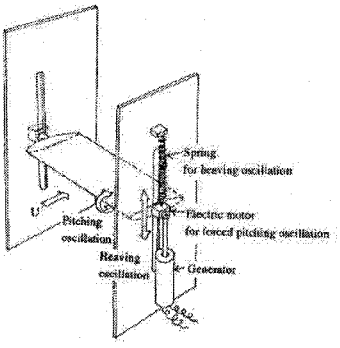

(d) The flapping-wing power generator proposed by Isogai et al. (2003)

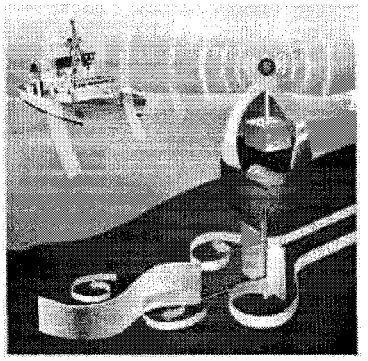

(e) The energy-harvesting eel proposed by Allen and Smits (2001)

FIGURE 1.5. Various concepts of energy-harvesting utilizing the flutter motions of structures in fluid flow.

Isogai et al. (2003) proposed a design with the wing elastically supported for the plunging motion and driven by a electric motor with prescribed frequency and amplitude for the pitching motion. In the design of Isogai et al. (2003) power is supplied

to the active pitching motion, and the plunging branch of the combined motion is used to extract energy from the airstream; it was claimed that the power gained was as high as one-hundred times of the power supplied. The fundamental investigations on the performance of the design proposed by Isogai et al. (2003) was recently conducted by Matsumoto et al. (2006). Finally, as shown in Fig. 1.5(c), Jones et al. (2003) considered two wings in the tandem arrangement, and demonstrated through water tunnel tests the feasibility of power extraction from water flows at speeds as low as 0.4 m/s.

Unlike the wingmill, which aims to compete with conventional wind turbines, energy-harvesting eels, as shown in Fig. 1.5(e), were proposed by Allen and Smits (2001) and Taylor et al. (2001) as an electricity source to power small, remotely located, wireless sensors. In the design of energy-harvesting eels, a film made of piezoelectric polymer (i.e. the eel) is put in the wake generated from an upstream bluff body; this device converts the mechanical energy of the wake-induced vibrations to electrical power. A patent has been filed by Carroll (2002) for the concept of energy-harvesting eels; and the project is still under way with the goal of building a prototype capable of generating 1 watt electrical power in a 1 m/s water current.

1.3. Organization of the thesis

The work conducted for this thesis is incorporated into six chapters, as illustrated by the organizational diagram shown in Fig. 1.6, as well as the present chapter (Introduction) and the last chapter (Conclusion and Future Work).

In Chapter 2, we focus on the model of two-dimensional cantilevered flexible plates in axial flow. The nonlinear equation of motion of the plate is developed using the inextensibility assumption, and the panel method is used for calculating the fluid loads acting the plate. Some specific topics regarding the model of the fluid-structure interaction system are discussed. The detailed derivation of the plate model based on the inextensibility assumption can be found in Appendix A. Moreover, the model of the system developed without using the inextensibility assumption is

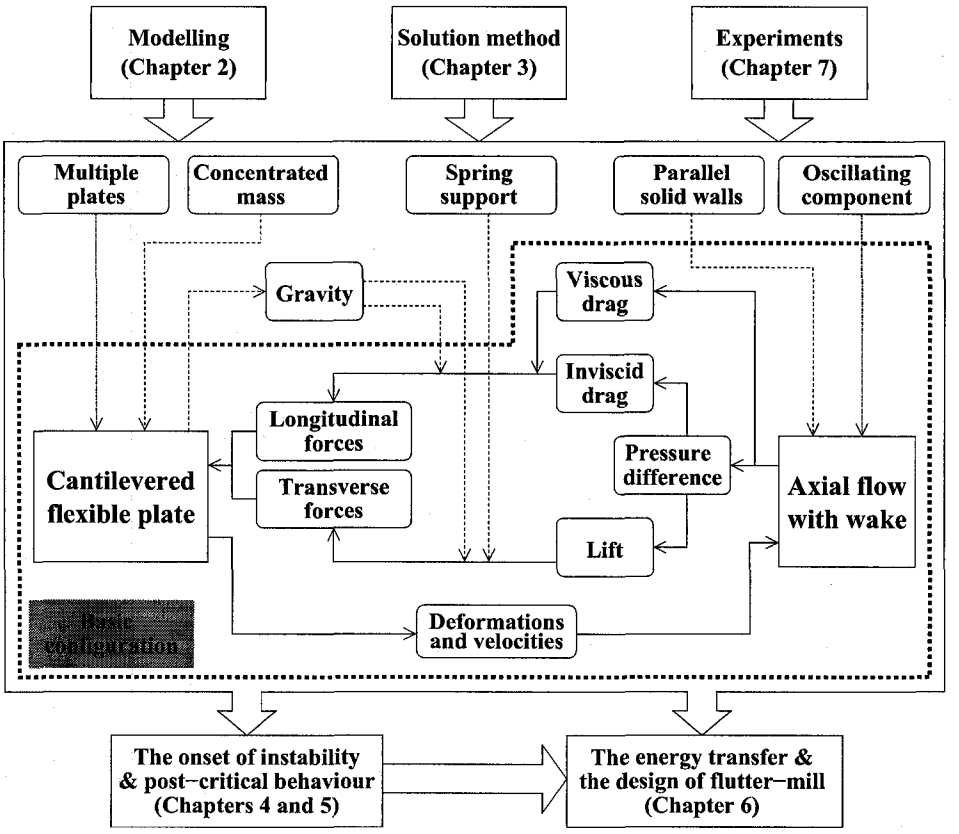

FIGURE 1.6. The organizational diagram.

discussed in Appendix B. The model of the system is nondimensionalized and various nondimensional parameters of the fluid-structure interaction system are identified; in Appendix C, the values of these nondimensional parameters are calculated for a real system for reference.

In Chapter 3, we summarize the solution methods utilized in this thesis. The analytical model of the system is discretized, and convergence tests with respect to various numerical parameters of the numerical model of the system are presented. Moreover, in this chapter, preliminary simulation results are compared with published experimental observations for the purpose of validating the model developed.

In Chapter 4, we study the dynamics, both the onset of instability and the post-critical behaviour, of cantilevered flexible plates in axial flow set up in the basic configuration. The dynamics of the system are examined in a multi-parameter space; the influence of each individual nondimensional parameter of the system is discussed in detail. The simulation results obtained using the present theory are compared

with previous theoretical predictions and experimental observations; some findings obtained through this comparison are summarized; in particular, the influence of the wake on the instability of the system is further discussed in Appendix D.

In Chapter 5, modified versions of the basic configuration of the system are studied; as shown in Fig. 1.6, these new features include the cases of the system with gravity, with parallel solid walls, with an additional spring support, with an additional concentrated mass, with a small oscillating component in the fluid flow, and with two identical plates in parallel. As new features are introduced to the system in the basic configuration, the model of the system is accordingly updated, and new parameters of the system are identified. The influences of these new parameters on the dynamics, both the onset of instability and the post-critical behaviour of the system, are examined.

In Chapter 6, we return to the system in the basic configuration and investigate the energy transfer between the cantilevered flexible plate and the surrounding fluid flow. The dynamics of the system is reviewed from the point of view of energy transfer. Moreover, based on the analysis of energy transfer, we propose a new energy-harvesting concept, which utilizes the flutter motions of cantilevered flexible plates in axial flow to generate electrical power. The performance of the proposed energy-harvesting device is preliminarily evaluated and the design considerations are summarized in the light of the dynamics of the system in either the basic configuration or various modified configurations discussed in Chapters 4 and 5, respectively.

In Chapter 7, we discuss the experiments conducted with the closed-type vertical water tunnel in the Fluid-Structure Interactions Laboratory at McGill University; simulation results pertinent to the experiments are also presented and compared with experimental observations/measurements. The preparation of the experiment, including the refurbishment work carried on the water tunnel, is summarized in Appendix E as a documentation for future use.

Finally, in Chapter 8, we summarize the work conducted in this thesis and outline possible future work.

Chapter 2

Modelling

2.1. Introduction

In this chapter, the model of two-dimensional cantilevered flexible plates in axial flow is developed. The system is assumed to be set up in its basic configuration, i.e., the vertical configuration as shown in Fig. 1.3(a). The effect of the gravitational force is neglected. Moreover, the plate is assumed to be placed in an unconfined fluid flow. Modified versions of this basic configuration, including the systems in either horizontal or hanging configuration (see Figs. 1.3(b) and (c)), with parallel solid walls, with an additional spring support, with an additional concentrated mass, with a small oscillating component in the undisturbed flow and with two identical parallel plates, one at a time, will be discussed in Chapter 5.

As mentioned in Chapter 1, the two principal distinguishing characteristics of cantilevered flexible plates in axial flow are: (i) the large amplitude of the post-critical flutter and (ii) the dynamic vortical wake beyond the trailing edge of the plate. Therefore, the model developed herein should account for these two features in the ensuing investigation of the stability and the post-critical behaviour of the system. Moreover, for the purpose of an extensive study of the system dynamics in various parameter spaces, the model has to be very efficient for results of reasonable accuracy to be obtained.

In this chapter, the nonlinear equations of motion of the two-dimensional cantilevered flexible plate are developed using the inextensibility assumption, and an unsteady lumped-vortex model associated with a dynamic vortical wake is utilized for evaluating the fluid loads acting on the plate. Moreover, some specific questions regarding the model of the fluid-structure system are discussed.

It should be mentioned that the equations of motion of the cantilevered flexible plate can also be developed without using the inextensibility assumption; that is, the plate is supposed to be extensible, as it should be. The derivation of the equations of motion of extensible plates is summarized in Appendix B. However, as one can ascertain in Appendix B, considerable difficulties are encountered in the solution of the extensible equations of motion; no stable limit cycle oscillations (flutter) can be obtained using the conventional solution methods that we have found to be fruitful for the inextensible plates, as discussed in Chapter 3. Under these circumstances, in this thesis (and as is almost universally done by others), the investigations on the dynamics of cantilevered flexible plates in axial flow are largely based on the inextensible model of the flexible plate.

2.2. Equation of motion of the plate

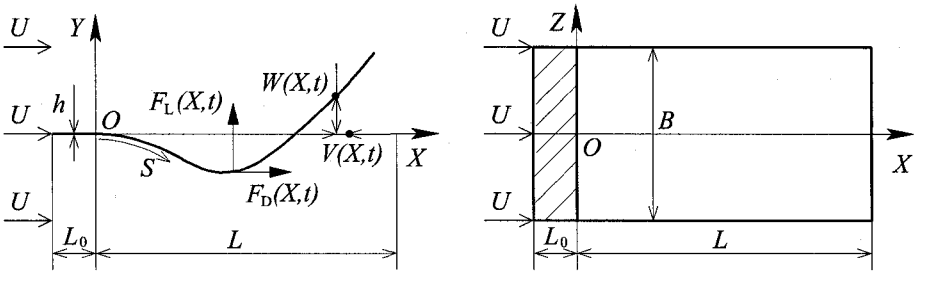

FIGURE 2.1. A cantilevered flexible plate in axial flow.

As shown in Fig. 2.1, a two-dimensional thin plate ($B \to \infty$ and $h \ll L$) can be considered as a classical Euler-Bernoulli beam with deflections only in the X-Y plane; any effect of rotatory inertia or shear deformation is assumed negligible and hence neglected. Specifically regarding the clamped-free configuration, the level of

strains inside the beam is assumed to be very low; however, the deflections may be quite large.

Large amplitude static-deflections/vibrations of cantilevered flexible beams and plates, as well as other slender structures in axial flow, such as cylinders and pipes modelled as cantilevered flexible beams, have been for a long time and are still a topic attracting extensive attention; recent reviews in this aspect can be found in two successive doctoral theses, by Arafat (1999) and Malatkar (2003). In previous work, cantilevered beams undergoing large deformations were assumed to be either inextensible or extensible in regard of the total length of the beam centreline. However, it is interesting to find that the inextensibility assumption was used in almost all dynamic analyses, excepting the work by Cveticanin et al. (1995) who studied the parametric excitation/instability of Beck's problem (Elishakoff, 2005); see the theses by Arafat (1999) and Malatkar (2003) and the relevant references reviewed therein, the work by Pai and Lee (2003) on various nonlinear dynamics of cantilevered beams, the work on cantilevered flexible plates in axial flow by Yadykin et al. (2001) and Tang et al. (2003), the work on cantilevered pipes conveying fluid by Semler (1991), Semler et al. (1994) and Wadham-Gagnon et al. (2007), and the work on cantilevered cylinders in axial flow by Lopes et al. (2002). In other words, extensibility has only been considered in static problems; see, for example, the work using the finite-element method with either an updated-Lagrangian or total-Lagrangian formulation by Bathe and Bolourchi (1979), Saje (1990), Libai (1992), Pai et al. (2000) and Nanakorn and Vu (2006), to name just a few.

Using the inextensibility assumption, the equation of motion of the plate is obtained as (see Appendix A for details):

$$\begin{aligned} & \rho_{\mathrm{P}} h \ddot{W} + D\left(1 + a\frac{\partial}{\partial t}\right)\left[W''''\left(1 + W'^2\right) + 4W'W''W''' + W''^3\right] \\ + \; & \rho_{\mathrm{P}} h W' \int_0^S \left(\dot{W}'^2 + W'\ddot{W}'\right) dS - \rho_{\mathrm{P}} h W'' \int_S^L \left[\int_0^S \left(\dot{W}'^2 + W'\ddot{W}'\right) dS\right] dS \\ = \; & F_{\mathrm{L}} - W' F_{\mathrm{D}} + W'' \int_S^L F_{\mathrm{D}}\, dS, \end{aligned} \tag{2.1}$$

$$V = -\frac{1}{2}\int_0^S W'^2\, dS, \tag{2.2}$$

where, as shown in Fig. 2.1, W and V are, respectively, the transverse and longitudinal displacements of the plate; S is the distance of a material point on the plate from the origin, measured along the plate centreline in a coordinate system embedded in the plate; F_{L} and F_{D} are, respectively, the transverse and longitudinal fluid loads acting on the plate; a is the material damping coefficient, assuming a Kelvin-Voigt model (Snowdon, 1968). The overdot and the prime, respectively, represent temporal and spatial derivatives, i.e., $\partial(\,)/\partial t$ and $\partial(\,)/\partial S$. Note that both Eq. (2.1) and Eq. (2.2) are accurate to $\mathcal{O}(\epsilon^3)$, where ϵ is the label for small quantities and it is assumed that W and $W' \sim \mathcal{O}(\epsilon)$. The associated boundary conditions are (see Eqs. (A.25), (A.27), (A.32) and (A.37))

$$W(S=0,t) = W'(S=0,t) = W''(S=L,t) = W'''(S=L,t) \equiv 0. \tag{2.3}$$

It should be mentioned that an one-dimensional equation of motion of the plate, i.e., Eq. (2.1), is obtained using the inextensibility assumption; Eq. (2.2) is used to recover the two-dimensional deformed shape of the plate in the fixed X-Y coordinate system, which is essential in the aero/hydro-dynamics model of the system. One can see in Eq. (2.2) that the longitudinal displacement $V(S)$ is consistently negative along the length the plate whenever $W(S) \neq 0$. Moreover, when flutter takes place, the frequency of the longitudinal displacement is always twice that of the transverse displacement. It should be noted that, whenever the frequency of the system is mentioned in this thesis, we refer to the frequency of the transverse displacement.

Moreover, utilizing the relationship $\ddot{V} = -\int_0^S \left(\dot{W}'^2 + W'\ddot{W}'\right) dS$ (i.e., Eq. (A.18)), Eq. (2.1) may be rewritten as

$$\rho_{\mathrm{P}} h\ddot{W} + D(1 + a\frac{\partial}{\partial t})\left[W''''\left(1+W'^2\right) + 4W'W''W''' + W''^3\right] - (TW')' = F_{\mathrm{L}}, \tag{2.4}$$

where T is the tension in the plate, defined by

$$T = \int_S^L (F_{\mathrm{D}} - \rho_{\mathrm{P}} h\ddot{V})\, dS. \tag{2.5}$$

That is, although the plate is assumed to be inextensible, tension still exists in it, originating from the fluid load as well as the inertia force of the plate in the longitudinal direction.

Using nondimensional variables defined as

$$x = \frac{X}{L}, \quad y = \frac{Y}{L}, \quad v = \frac{V}{L}, \quad w = \frac{W}{L}, \quad s = \frac{S}{L}, \quad \tau = \frac{t}{\sqrt{\rho_{\mathrm{P}} h L^4/D}},$$
$$f^\star = f\sqrt{\frac{\rho_{\mathrm{P}} h L^4}{D}}, \quad \alpha = \frac{a}{\sqrt{\rho_{\mathrm{P}} h L^4/D}}, \quad f_{\mathrm{L}} = \frac{F_{\mathrm{L}}}{\rho_{\mathrm{F}} U^2}, \quad f_{\mathrm{D}} = \frac{F_{\mathrm{D}}}{\rho_{\mathrm{F}} U^2}, \tag{2.6}$$

where $f^\star$ and f are, respectively, the nondimensional and dimensional vibration frequencies of the system, Eqs. (2.1) through (2.3) become

$$\ddot{w} + \left(1 + \alpha\frac{\partial}{\partial\tau}\right)\left[w''''\left(1 + w'^2\right) + 4w'w''w''' + w''^3\right]$$
$$+ \; w'\int_0^s \left(\dot{w}'^2 + w'\ddot{w}'\right) ds - w''\int_s^1 \left[\int_0^s \left(\dot{w}'^2 + w'\ddot{w}'\right) ds\right] ds = f_{\mathrm{eff}}, \tag{2.7}$$

$$v = -\frac{1}{2}\int_0^s w'^2\, ds, \tag{2.8}$$

$$w(s=0,\tau) = w'(s=0,\tau) = w''(s=1,\tau) = w'''(s=1,\tau) \equiv 0, \tag{2.9}$$

where the overdot and the prime, whenever they are present in a nondimensional equation, represent $\partial(\;)/\partial\tau$ and $\partial(\;)/\partial s$, respectively; the effective force f_{eff} acting on the plate is defined by

$$f_{\mathrm{eff}} = \mu {U_{\mathrm{R}}}^2 \left(f_{\mathrm{L}} - w' f_{\mathrm{D}} + w''\int_s^1 f_{\mathrm{D}}\, ds\right). \tag{2.10}$$

In the nondimensionalization, the length of the flexible section of the plate has been used as the length scale and the characteristic time of free vibration of the plate as the time scale, i.e., the *solid time scale*

$$T_{\mathrm{S}} = \sqrt{\frac{\rho_{\mathrm{P}} h L^4}{D}}. \tag{2.11}$$

Note that there is another time scale, the *fluid time scale*, defined as

$$T_{\mathrm{F}} = \frac{L}{U}. \tag{2.12}$$

The ratio of these two time scales is the reduced flow velocity (de Langre, 2002)

$$U_{\mathrm{R}} = \frac{T_{\mathrm{S}}}{T_{\mathrm{F}}} = UL\sqrt{\frac{\rho_{\mathrm{P}} h}{D}}. \tag{2.13}$$

Normally, when $U_{\mathrm{R}} \gg 1$, i.e., $1/T_{\mathrm{S}} \ll 1/T_{\mathrm{F}}$, it can be assumed that the response of the fluid flow due to the deformation of the plate is much faster than the plate motion itself; therefore, it is not necessary to take into account time-lag effects (McCroskey, 1982). Moreover, of major importance is the mass ratio μ defined by

$$\mu = \frac{\rho_{\mathrm{F}} L}{\rho_{\mathrm{P}} h}. \tag{2.14}$$

Both the reduced flow velocity U_{R} and the mass ratio μ characterize the interaction between the fluid and the structure, and the Cauchy number C_Y representing the ratio of the *fluid force* to the *solid force* (de Langre, 2002) is defined by

$$C_Y = \mu {U_{\mathrm{R}}}^2 = \frac{\rho_{\mathrm{F}} U^2}{D/L^3}. \tag{2.15}$$

Moreover, another frequently used parameter in the study of unsteady aero/hydrodynamics is the reduced frequency, which can be defined by

$$f_{\mathrm{R}} = \frac{2\pi f^\star}{U_{\mathrm{R}}} = \frac{2\pi f L}{U}. \tag{2.16}$$

Eq. (2.7) has both geometrical and inertial nonlinearities, respectively coming from the nonlinear curvature (see Eq. (A.21)) and the longitudinal deformation of the plate. Through theoretical analysis as well as experiments of parametric excitations longitudinally applied to the fixed end of a cantilevered beam, Anderson et al. (1996) found that: for the fist mode, the geometrical nonlinearity, which is of the hardening type, is dominant; while, for the second and higher modes, the inertial nonlinearity, which is of the softening type, becomes dominant. Tang et al. (2003) also theoretically examined the effects of individual nonlinearities involved in Eq. (2.7) using harmonic excitation transversally applied at the trailing edge of the plate. Their tests were conducted in the vicinity of the second *natural* frequency, and it was observed that the geometrical and the inertial nonlinearities are, respectively, of the hardening and

the softening type; moreover, when both types of nonlinearities were considered, the overall effect is of the softening type.

2.3. The aero/hydro-dynamics model

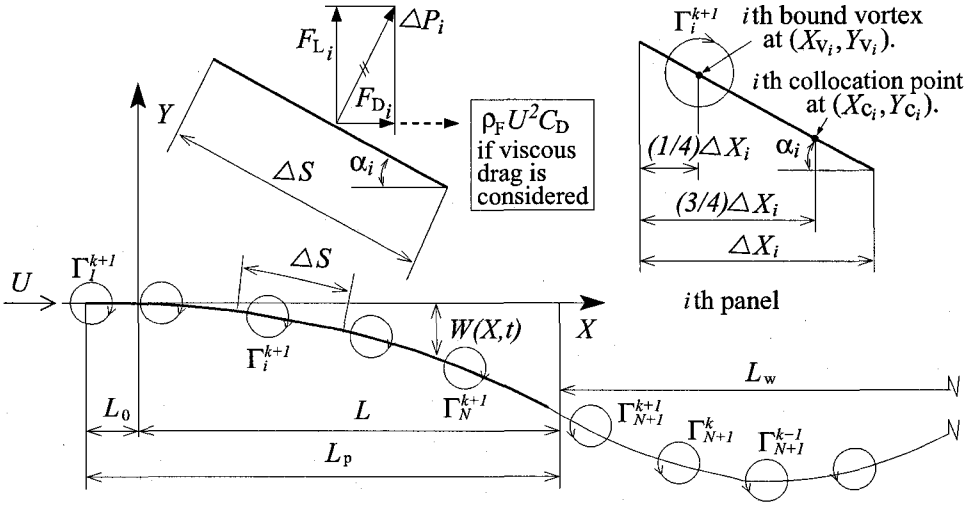

FIGURE 2.2. The panel method applied to a cantilevered flexible plate in axial flow.

As for the aero/hydro-dynamics part of the model for a two-dimensional cantilevered flexible plate in axial flow, because the plate is very thin and flexible, the flow velocity U is supposed to be low enough when flutter takes place for the fluid to be assumed to be incompressible. Also, for simplicity, the flow can initially be considered to be inviscid; however the effect of viscosity will be incorporated in the longitudinal fluid load F_D empirically as a surface viscous force. Under these conditions, the panel method, in particular the unsteady lumped-vortex model (Katz and Plotkin, 2001), is used to predict the aero/hydro-dynamics, as illustrated in Fig. 2.2.

The flexible section of the plate is evenly divided into N panels, each of length $\Delta s = 1/N$. Individual panels are put on the deformed contour of the plate centreline. The bound vortices, γ_1 through γ_N, together with the instantaneously formed wake vortex γ_{N+1} at a given instant, say time step $k+1$, are obtained from the following

equations:

$$\begin{bmatrix} \alpha_{11} & \alpha_{12} & \cdots & \alpha_{1N} & \alpha_{1,N+1} \\ \alpha_{21} & \alpha_{22} & \cdots & \alpha_{2N} & \alpha_{2,N+1} \\ \vdots & \vdots & \ddots & \vdots & \vdots \\ \alpha_{N1} & \alpha_{N2} & \cdots & \alpha_{NN} & \alpha_{N,N+1} \\ 1 & 1 & \cdots & 1 & 1 \end{bmatrix} \begin{Bmatrix} \gamma_1 \\ \gamma_2 \\ \cdots \\ \gamma_N \\ \gamma_{N+1} \end{Bmatrix} = \begin{Bmatrix} \mathrm{rhs}_1 \\ \mathrm{rhs}_2 \\ \cdots \\ \mathrm{rhs}_N \\ \gamma^\star \end{Bmatrix}, \tag{2.17}$$

where the influence coefficients α_{ij} and the right-hand-side $[\mathrm{rhs}_i, \gamma^\star]^{\mathrm{T}}$ are given by

$$\alpha_{ij} = \frac{(y_{\mathrm{C}i} - y_{\mathrm{V}j})\sin\alpha_i + (-x_{\mathrm{C}i} + x_{\mathrm{V}j})\cos\alpha_i}{2\pi\left[(y_{\mathrm{C}i} - y_{\mathrm{V}j})^2 + (x_{\mathrm{C}i} - x_{\mathrm{V}j})^2\right]}, \tag{2.18}$$

$$\mathrm{rhs}_i = (\frac{\dot{v}_i}{U_{\mathrm{R}}} - 1 - v_{\mathrm{W}i})\sin\alpha_i + \left(\frac{\dot{w}_i}{U_{\mathrm{R}}} - w_{\mathrm{W}i}\right)\cos\alpha_i, \tag{2.19}$$

$$\gamma^{\star k+1} = \sum_{i=1}^{N} \gamma_i^k. \tag{2.20}$$

In Eq. (2.17), $\gamma_{i,i=1,2,\cdots,N}$ and γ_{N+1} are, respectively, the strengths of the bound vortices $\Gamma_{i,i=1,2,\cdots,N}$ and the latest wake vortex $\Gamma_{\mathrm{W}1}$ normalized by UL. In Eqs. (2.18) and (2.19), $(x,y)_{\mathrm{C}i}$ and $(x,y)_{\mathrm{V}i}$ are, respectively, the coordinates of the bound vortex and the collocation point on the ith panel $(X,Y)_{\mathrm{C}i}$ and $(X,Y)_{\mathrm{V}i}$ normalized by L; $(v,w)_{\mathrm{W}i}$ is the wake-induced flow velocity at the ith collocation point $(V,W)_{\mathrm{W}i}$ normalized by the undisturbed flow velocity U. In Eq. (2.20), the superscript $k+1$ represents the current time step; it has been dropped for clarity in Eqs. (2.17) through (2.19).

The plate is supposed to be initially held in place with a slightly deformed shape. It is then released, and fresh wake vortices are formed and shed off the trailing edge of the plate. The latest wake vortex is assumed to be born on the prolongation of the last panel (note that the plate is assumed to be of zero thickness in the aero/hydrodynamics model) and to have a longitudinal clearance of $0.25U_{\mathrm{R}}\Delta\tau$ from the trailing edge of the plate, where $\Delta\tau$ is the nondimensional time step. For simplicity, it is assumed that the movement of each individual wake vortex is not affected by the

bound vortices or the other wake vortices. Therefore, they travel downstream with the same velocity as the undisturbed flow; the longitudinal distance between two neighbouring wake vortices is always $U_{\mathrm{R}}\Delta\tau$ (i.e., $U\Delta t$ normalized by L, where Δt is the dimensional time step).

The shape of the wake street is shown in Fig. 2.2, and it has a wavy form. In previous studies, slender wing theory (a localized excitation theory) was often utilized, and the wake was explicitly neglected when considering low aspect ratio plates (i.e., $\mathcal{R} \ll 1$), e.g., by Datta and Gottenberg (1975), Yadykin et al. (2001) and Lemaitre et al. (2005). Wake effects were not considered, either in the direct solution of the potential flow problem by neither Guo and Païdoussis (2000) or Eloy et al. (2007), nor in the studies of Shelley et al. (2005) based on localized excitation theory (Crighton and Oswell, 1991). On the other hand, Theodorsen's theory was adopted by Kornecki et al. (1976), Shayo (1980), Huang (1995), Watanabe et al. (2002a), Argentina and Mahadevan (2005), and De Breuker et al. (2006), and a flat wake on the extension of the plate neutral plane was considered to satisfy the Kutta-Joukowski condition at the trailing edge of the plate. A vortex sheet model and a vortex lattice model were respectively used by Yamaguchi et al. (2000b) and Tang et al. (2003); in their implementation, the wake was constrained to be along the plate neutral plane. An improvement was made by Attar et al. (2003); a vortex lattice model was again used and the wake vortices were considered to be free to move in the local flow field.

As shown in Fig. 2.2, the truncated wake street is assumed to have a normalized longitudinal length l_{W} ($l_{\mathrm{W}} = L_{\mathrm{W}}/L$), and the total number of wake vortices N_{W} can be determined by $N_{\mathrm{W}} = L_{\mathrm{W}}/(U\Delta t) = l_{\mathrm{W}}/(U_{\mathrm{R}}\Delta\tau)$ (taking the closest integer). Thus, the wake-induced flow velocity at the ith collocation point is calculated by

$$v_{\mathrm{W}i} = \sum_{j=1}^{N_{\mathrm{W}}} \frac{\gamma_{\mathrm{W}j}}{2\pi} \frac{y_{\mathrm{C}i} - y_{\mathrm{W}j}}{(y_{\mathrm{C}i} - y_{\mathrm{W}j})^2 + (x_{\mathrm{C}i} - x_{\mathrm{W}j})^2}, \tag{2.21a}$$

$$w_{\mathrm{W}i} = \sum_{j=1}^{N_{\mathrm{W}}} \frac{\gamma_{\mathrm{W}j}}{2\pi} \frac{-x_{\mathrm{C}i} + x_{\mathrm{W}j}}{(y_{\mathrm{C}i} - y_{\mathrm{W}j})^2 + (x_{\mathrm{C}i} - x_{\mathrm{W}j})^2}, \tag{2.21b}$$

where $\gamma_{\mathrm{W}j}$ and $(x,y)_{\mathrm{W}_j}$ are, respectively, the strength and coordinates of the jth wake vortex $\Gamma_{\mathrm{W}j}$ normalized by UL and $(X,Y)_{\mathrm{W}_j}$ normalized by L.

When discrete vortices γ_1 through γ_{N+1} are available at the current time step, the pressure difference Δp_i (i.e., ΔP_i normalized by $\rho_{\mathrm{F}}U^2$) at the ith panel, can be calculated by the following expression (Katz and Plotkin, 2001):

$$\Delta p_i = \left[\left(-\frac{\dot{v}_i}{U_{\mathrm{R}}} + 1 + v_{\mathrm{W}i}\right)\cos\alpha_i + \left(\frac{\dot{w}_i}{U_{\mathrm{R}}} - w_{\mathrm{W}i}\right)\sin\alpha_i\right]\frac{\gamma_i}{\Delta s} + \frac{1}{U_{\mathrm{R}}}\frac{\partial}{\partial\tau}\left(\sum_{j=1}^{i}\gamma_j\right). \tag{2.22}$$

Consequently, the distributions of the *lift* $f_{\mathrm{L}i}$ and the inviscid drag $f_{\mathrm{D}i}$ over the ith panel are obtained by

$$(f_{\mathrm{L}i}, f_{\mathrm{D}i}) = \Delta p_i(\cos\alpha_i, \sin\alpha_i). \tag{2.23}$$

Note that, in Eq. (2.22), the pressure difference Δp across the plate is dependent on not only the time rate change of the total strength of all bound vortices, but also the undisturbed flow velocity, the wake-induced flow velocity and the vibration velocity (in both transverse and longitudinal directions) of the plate.

Eq. (2.23) gives the drag resulting only from the pressure difference across the plate; it is an inviscid drag. In this thesis, a nondimensional drag coefficient C_{D} is used for the drag acting on the plate due to the viscous effects of the fluid flow, i.e., the effective drag caused by viscous stresses acting on the plate surfaces (both the upper and lower surfaces) and/or flow separation. An additional uniform distribution of longitudinal force given by $\rho_{\mathrm{F}}U^2C_{\mathrm{D}}$ is thus assumed to act on the plate for simplicity, and the term $f_{\mathrm{D}i}$ in Eq. (2.23) becomes

$$f_{\mathrm{D}i} = \Delta p_i \sin\alpha_i + C_{\mathrm{D}}. \tag{2.24}$$

2.4. Dimensional analysis

It is necessary to carry out a dimensional analysis (de Langre, 2002) to identify the nondimensional parameters in various aero/hydro-elastic models developed in this thesis. To this end, the problem of a two-dimensional cantilevered flexible plate in

axial flow in its basic configuration is stated as

$$\mathcal{F}(D/h^3, \rho_{\mathrm{P}}, L, h; \rho_{\mathrm{F}}, U; t, W, V) \equiv 0, \tag{2.25}$$

where, in the fluid-structure interaction system, physical variables D, ρ_{P}, L and h belong to the structure; ρ_{F} and U are fluid flow parameters; and t, W and V are shared by both the structure and the fluid flow. Some explanations are necessary for the statement made in Eq. (2.25). First, the fluid flow is assumed to be incompressible and inviscid so that only the mass density of the fluid ρ_{F} and the (undisturbed) flow velocity U are taken into account. Second, the bending stiffness of the plate is $D = Eh^3/[12(1-\nu^2)]$, where Young's modulus E and the Poisson ratio ν (a nondimensional quantity regarded as a fixed constant in the current analysis) belong to the properties of the plate material; therefore, the term D/h^3 is used in the statement to eliminate the involvement of the plate thickness (a geometrical parameter) in D. Third, the current problem is a dynamic one, and the time variable t is included in the statement. Fourth, both the transverse and longitudinal displacements W and V are considered, although V is solely dependent on W when the plate is assumed to be inextensible. Fifth, the other features of the system in the basic configuration, i.e., the upstream leading segment L_0, material damping coefficient a and the viscous drag $\rho_{\mathrm{F}}U^2C_{\mathrm{D}}$, are not considered in the statement because the corresponding nondimensional parameters (l_0, α and C_{D}) can be otherwise introduced to account for them. Finally, in the various modified configurations of the system (see Chapter 5), additional nondimensional parameters can accordingly be determined as the case may be.

TABLE 2.1. The dimensions of the physical variables of the system

	D/h^3	ρ_{P}	L	h	ρ_{F}	U	t	W	V
[kg]	1	1	0	0	1	0	0	0	0
[m]	-1	-3	1	1	-3	1	0	1	1
[s]	-2	0	0	0	0	-1	1	0	0

It can be found in Eq. (2.25) that there are *nine* physical variables, and the rank of the dimensional analysis matrix, as shown in Table 2.1, is calculated as *three*. According to the Buckingham Π-theorem (White, 2003), there should be *six*

nondimensional parameters to describe the system. However, through the scheme defined in Eq. (2.6), only *five* are available, i.e., τ, w, v (defined in Eq. (2.6)), U_{R} (defined in Eq. (2.13)) and μ (defined in Eq. (2.14)); there is a deficit in the number of required nondimensional parameters. This deficit problem can be resolved by either adding a new nondimensional parameter or eliminating one independent physical variable from Eq. (2.25).

A supplementary nondimensional parameter accounting for the ratio of the length of the flexible plate L to the plate thickness h, i.e., the length-to-thickness ratio ζ, may defined as

$$\zeta = \frac{L}{h}. \tag{2.26}$$

It follows that the mass ratio μ and the reduced flow velocity U_{R} can be otherwise rewritten as

$$\mu = \frac{\rho_{\mathrm{F}}}{\rho_{\mathrm{P}}}\frac{L}{h} = \zeta\frac{\rho_{\mathrm{F}}}{\rho_{\mathrm{P}}}, \tag{2.27}$$

and

$$U_{\mathrm{R}} = UL\sqrt{\frac{\rho_{\mathrm{P}}h}{D}} = U\frac{L}{h}\sqrt{\frac{12(1-\nu^2)\rho_{\mathrm{P}}}{E}} = \zeta\sqrt{12(1-\nu^2)}\sqrt{\frac{\rho_{\mathrm{P}}}{E}}U, \tag{2.28}$$

where $D = Eh^3/[12(1-\nu^2)]$ has been utilized, and ν is regarded as a fixed constant. Therefore, the system is prototyped as

$$\mathcal{F}(\tau, w, v, \mu, U_{\mathrm{R}}, \zeta) \equiv 0. \tag{2.29}$$

Another way to resolve the deficit in the number of nondimensional parameters is to reduce the independent physical variables. It is noticed that the physical parameter h does not appear in the aero/hydro-dynamics model of the system, where the thin plate is assumed to be of zero thickness. Therefore, it is normally regarded that the plate thickness h is not an independent variable when the plate is assumed to be inextensible; and, the variables D/h^3 and ρ_{P} are, respectively, replaced by the combined ones D (the bending stiffness of the plate) and $\rho_{\mathrm{P}}h$ (the mass per unit area

of the plate). That is, the system is prototyped as

$$\mathcal{F}(D, \rho_{\mathrm{P}} h, L; \rho_{\mathrm{F}}, U; t, W, V) \equiv 0, \tag{2.30}$$

or in terms of nondimensional parameters as

$$\mathcal{F}(\tau, w, v, \mu, U_{\mathrm{R}}) \equiv 0. \tag{2.31}$$

Finally, it should be mentioned that when the plate is supposed to be extensible, as is the case in Appendix B, the motion of the plate is governed by two equations: one for the longitudinal displacement V and the other for the transverse displacement W, respectively; an additional nondimensional parameter, i.e., the length parameter $\chi = EhL^2/D$ (see Eq. (B.51)), is naturally recognized in the nondimensionalization process applied to the equations of motion.

2.5. Discussion concerning modelling

2.5.1. Two-dimensional or three-dimensional. In this thesis, we study the dynamics of two-dimensional cantilevered flexible plates in axial flow. It is supposed that the plate width B is infinite, i.e., the aspect ratio $\mathcal{R} \to \infty$; both the plate and the fluid flow surrounding the plate are thus two-dimensional. Although three-dimensional flutter was reported by Taneda (1968), its existence *de facto* became significant only when the plate flapped wildly at relatively high flow velocities. On the other hand, it was observed in the experiments by Datta and Gottenberg (1975), Kornecki et al. (1976), Huang (1995), Aurégan and Depollier (1995), Yamaguchi et al. (2000a), Yadykin et al. (2001), Watanabe et al. (2002b), Tang et al. (2003), Shelley et al. (2005), Lemaitre et al. (2005) and Souilliez et al. (2006) for the systems in either the vertical or the hanging configuration that the spanwise deformation of the plate was very small, at least at the critical point where flutter takes place and for a considerable range of flow velocity beyond the critical point; the experimental observations thus show that the two-dimensional assumption for the plate is reasonable. On the other hand, the fluid flow should be considered as three-dimensional to take

into account the side-edge effects (Katz and Plotkin, 2001) and the spanwise variation in the fluid loads when the plate width is finite, especially when the value of $\mathcal{R}$ is moderate or less than 1, which is true in all previous experiments; therefore, the two-dimensional axial flow surrounding a two-dimensional plate is indeed an idealized model of the real physical system.

In previous theoretical work on cantilevered flexible plates in axial flow, the plate was considered as a two-dimensional structure by all researchers excepting Shayo (1980), who took into account the spanwise deformation of the plate and also solved the three-dimensional aero/hydro-dynamics of the system using small perturbation theory (Dowell and Hall, 2001). Moreover, the case of two-dimensional plates in three-dimensional flow was considered by Tang et al. (2003) and Eloy et al. (2007) using the vortex lattice model and the direct solution of the potential flow, respectively; the pressure difference at a fixed chordwise location was thus obtained by averaging its spanwise distribution according to a certain prescribed profile.

2.5.2. Linear theory versus nonlinear theory. In this thesis nonlinear equations of motion are developed for the cantilevered flexible plate to account for the post-critical flutter with large amplitudes. On the other hand, the lumped-vortex model itself for the aero/hydro-dynamics is linear; however, nonlinearity is introduced when the wavy form of the dynamic vortical wake, which is correlated to the motion of the plate, is taken into account in the model.

In previous work, nonlinear structural models were considered by Yadykin et al. (2001) and Tang et al. (2003); all the other researchers used linear models for the cantilevered flexible plate. As for the aero/hydro-dynamics, the models based on Theodorsen's theory (Kornecki et al., 1976; Huang, 1995; Watanabe et al., 2002a; Argentina and Mahadevan, 2005; De Breuker et al., 2006), the slender wing theory (Datta and Gottenberg, 1975; Yadykin et al., 2001; Lemaitre et al., 2005), the vortex sheet theory (Yamaguchi et al., 2000b) as well as the vortex lattice theory (Tang et al., 2003) with the wake confined on the neutral plane of the plate, the boundary element theory (Howell et al., 2006), the localized excitation theory (Shelley et al.,

2005), the mass conservation theory (Aurégan and Depollier, 1995), and the direct solution of the potential flow problem (Guo and Païdoussis, 2000; Eloy et al., 2007) are linear ones. Nonlinear models for the aero/hydro-dynamics were considered in the work by Attar et al. (2003) using the vortex lattice theory, Wu and Kaneko (2005) using leakage flow theory (which was based on simplified Navier-Stokes equation with specific assumptions for leakage flow), and Watanabe et al. (2002a), Balint and Lucey (2005) and Tetlow et al. (2006) based on Navier-Stokes solvers.

Using linear models, the problem in question was usually transformed into an eigenvalue problem, and a frequency-domain analysis ensued in the investigation of system stability (Datta and Gottenberg, 1975; Kornecki et al., 1976; Aurégan and Depollier, 1995; Guo and Païdoussis, 2000; Watanabe et al., 2002a; Shelley et al., 2005; Argentina and Mahadevan, 2005; Lemaitre et al., 2005; Eloy et al., 2007; De Breuker et al., 2006). Linear models were also solved in the time-domain by Huang (1995), Yamaguchi et al. (2000b), Wu and Kaneko (2005) and Howell et al. (2006) in the study of the system stability. Note that no information about the post-critical behaviour of the system can be obtained when using linear models.

In the work by Watanabe et al. (2002a), Balint and Lucey (2005) and Tetlow et al. (2006), in which the linear structural model was coupled with a nonlinear Navier-Stokes solver, corresponding analyses were conducted in the time-domain for the system stability; these studies were not extended to the post-critical domain, possibly due to the heavy computational load. Finally, both stability and the post-critical behaviour of the system were studied, through a time-domain analysis, in the work by Wu and Kaneko (2005) with a linear structural model and a nonlinear aero/dyhro-dynamics model, by Yadykin et al. (2001) and Tang et al. (2003) with a nonlinear structural model coupled with a linear aero/hydro-dynamics model, and by Attar et al. (2003) with both nonlinear structural and nonlinear aero/hydro-dynamics models. Unfortunately, in the work by Attar et al. (2003), the effect of using a nonlinear aero/hydro-dynamics model is not discussed in detail.

2.5.3. Material damping. Material damping is considered in the models of cantilevered flexible plates in axial flow for two purposes: first, this is an inherent property of all materials, which provides a way for dissipating energy pumped into the plate from the fluid flow; and second, this gives a chance to examine the effect of dissipation on the system stability, which may be rather complicated in a continuous non-conservative system such as a cantilevered flexible plate in axial flow (Ziegler, 1977; Païdoussis, 1998; Sugiyama and Langthjem, 2007). It should be mentioned that in previous work by Tang et al. (2003), Balint and Lucey (2005), Howell et al. (2006) and Tetlow et al. (2006), viscous damping proportional to the velocity of the plate (i.e., $\dot{w}$) was considered; however, this treatment is fallacious in that such a damping mechanism should have already been included in the aero/hydro-dynamics part of the model if one considers the plate and the fluid flow as an integrated system.

2.5.4. Fluid flow surrounding the oscillating plate and the vortical wake. The fluid is assumed to be incompressible and inviscid in this thesis; the boundary layer and the flow separation phenomenon are not considered in the aero/hydro-dynamics model of the system. It has been noticed in previous experiments (for example, see the flow visualization snapshots in Fig. 2.3) that the boundary layer is rather thin and the flow separation is not significant even when the plate flutters. In fact, the occurrence of flow separation may be delayed by the oscillations of the flexible plate (Carpenter and Garrad, 1985, 1986).

It can be seen in Fig. 2.3(a) that a von Kármán vortical wake street is formed when the plate remains stretched straight (Zhang et al., 2000), where the wake vortices are organized in two parallel rows: each row consists of vortices of the same sign; but the vortices belonging to different rows are of opposite signs. It should be emphasized that the existence of the von Kármán vortical wake street will not destroy the stable static state of the plate when the flow velocity is below the critical point. On the other hand, when the flow velocity exceeds the critical point *and/or* the initial disturbance made to the plate is sufficiently large, flutter takes place, and the von Kármán vortical wake street is replaced by another vortical wake street with a wavy form; just as Zhang

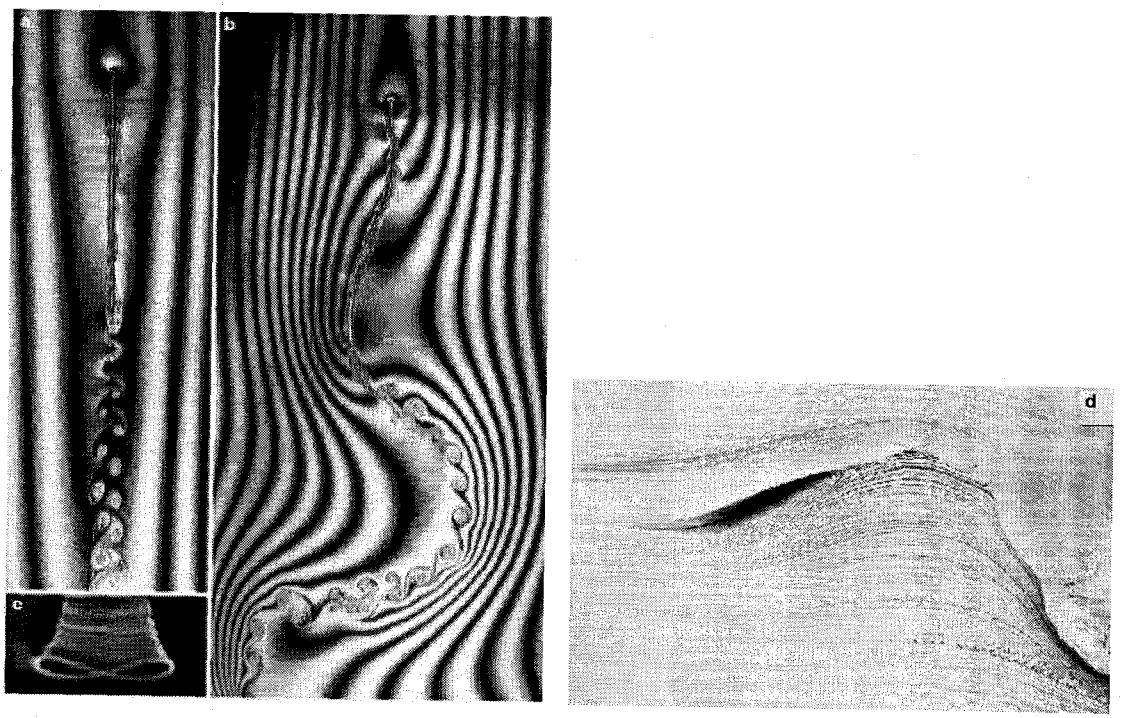

FIGURE 2.3. The dynamics of cantilevered flexible plates in axial flow, the fluid flow surrounding the plate and the dynamic vortical wake. The pictures taken by Zhang et al. (2000, Fig. 2): (a) the filament stretched straight in the flow, (b) the flutter state, and (c) the trajectory of the free end. (d) The picture taken by Watanabe et al. (2002b, Fig. 13): the fluid flow surrounding a fluttering plate.

et al. (2000) observed in their experiments, the successive small eddies produced by a single stroke of the plate are of the same sign, as shown in Fig. 2.3(b).

When flutter takes place, the wavy form of the vortical wake street can be captured by the unsteady lumped-vortex model and the associated time-stepping scheme for the generation of wake vortices, as illustrated in Fig. 2.2; similar models have been used extensively for studying the airfoil/wing flutter problem, for example, the work by Katz and Weihs (1978), Jones and Center (1996), Jones et al. (1996) and Katz and Plotkin (2001). However, it should be noted that the von Kármán vortical wake street and the transition from such a wake pattern to the wavy form cannot be studied using the current aero/hydro-dynamics model. The evolution of the vortical wake from one pattern to another, in conjunction with the dynamics of the cantilevered plate, is very interesting but still a mystery; no theoretical work has been done on this aspect before, although it is believed that this phenomenon has a close relation to the onset of flutter.

2.5.5. Unsteady Kutta-Joukowski condition. The Kutta-Joukowski condition is well established for steady cases, although it is something of a mixture of physical interpretation and mathematical manipulation; this condition claims the continuity of fluid load and flow velocity at the tailing edge of a streamlined structure. Based on the Kutta-Joukowski condition (as well as the thin airfoil approximation), Theodorsen's theory and various other theories using singularity representations for the *lifting surface* are developed. However, as indicated in the work by McCroskey (1982), Crighton (1985) and Frederiks et al. (1986), the applicability of the Kutta-Joukowski condition to unsteady cases is still a controversial fundamental topic in the study of unsteady aero/hydro-dynamics, and the situation becomes more complicated in aero/hydro-elastic problems.

In this thesis, because the panel method, i.e., the lumped-vortex model, has been used for the aero/hydro-dynamics part of the problem, the Kutta-Joukowski condition at the trailing edge of the plate is automatically satisfied; using the present model, the pressure difference across the plate diminishes at the trailing edge of the plate. Nevertheless, the justification of the Kutta-Joukowski condition lies in that it has been and still is commonly used in unsteady problems, at least for the cases where the trailing edge separation is not significant and the reduced frequency is moderate (Jones and Platzer, 1997; Katz and Plotkin, 2001).

2.5.6. Drag and the tension in the plate. Regarding its importance, the drag acting on the plate may be the weakest part of the model developed in this thesis for cantilevered flexible plates in axial flow.

The literature on hydro/aero-dynamic drag acting on oscillating flexible plates is surprisingly scant, although as early as 1930 Fairthrone (1930) tested the drag data for advertising streamers towed by aircraft. Hoerner (1958, Section 3-25) discussed the drag acting on flapping flags and attributed it to flow separation; however, insufficient data were made available to give a solid support to the conclusion that the drag is dependent on the length-to-width ratio and the weight per unit area of the flag. Taneda (1958) also believed that the major part of the drag acting on the plate was

caused by flow separation as he observed a significant jump in drag accompanying the onset of flutter. Levin et al. (1997) carefully conducted a large number of experiments to measure the drag acting on flapping ribbons in the vertical configuration (see, Fig. 1.3(a)); it was concluded that the drag coefficient decreases as the length-to-width ratio and the weight per unit area of the ribbon increases, and that it decreases with increasing flow velocity in the higher velocity range; note that the conclusion by Levin et al. (1997) about the trend with respect to the length-to-width ratio is contrary to Hoerner's (1958). Recently, Auman and Dahlke (2001) studied the drag of various ribbons attached to rocket-dispersed grenades and extended the observations of drag acting on oscillating cantilevered flexible plates to the high subsonic and supersonic ranges. More experimental data were recently made available by Carruthers and Filippone (2005), who confirmed the conclusions of Levin et al. (1997). Moreover, Carruthers and Filippone (2005) also reported the dependence of the drag on the planform area, the surface roughness and the bending stiffness of the flag.

It should be mentioned that the source of the drag acting on oscillating plates is not limited to the fluid flow. Moretti (2003, 2004) studied the chordwise tension in flapping flags and correlated it to the dynamics of the flag, i.e, the mode, the amplitude and the frequency of the flapping motion; it was proposed that the tension dynamically induced by the centrifugal force may be more important than that caused by viscous effects. Note that the theory of dynamically induced drag can be used to explain some of the phenomena observed by Levin et al. (1997) and Carruthers and Filippone (2005); for example, the dependence of the drag on the length-to-width ratio and the weight per unit area of the flag.

Regardless of the other factors, what we are specially concerned with is the drag caused by viscous effects of the fluid flow, including flow separation phenomena and the boundary layer. As discussed earlier in this chapter, even when flutter takes place, flow separation should not be sufficiently significant so as to affect greatly the level of drag; in this aspect, the longitudinal contribution of the pressure difference across the plate, i.e., the inviscid drag in the model developed in this thesis, quite possibly accounts for the increase. As for the boundary layer effect, one approach

for taking into account viscous drag in the model is to use a Blasius-type solution (White, 1991), for either the laminar or the turbulent case, as a first approximation (see the work by Datta and Gottenberg (1975) and Yadykin et al. (2000)). However, it has been found through extensive tests in this thesis and confirmed by the work of Lemaitre et al. (2005) that the viscous drag calculated using a Blasius-type solution has a negligible effect on the system dynamics, as will be seen in Chapter 4.

It is very difficult to include the drag, no matter whether it is a viscous drag or a dynamically induced drag, in the analysis of the dynamics of cantilevered flexible plates in axial flow. Empirical models are impossible either, because experimental data available up to date are for the *time-averaged total* drag measured at the upstream clamped edge; no information about time-dependent drag along the plate length is available. Under these circumstances, in this thesis (see also the work by Watanabe et al. (2002a)), it is assumed that the drag due to viscous effects is evenly distributed along the plate, with a fixed value of drag coefficient C_{D}; we can thus study viscous effects on the system dynamics by investigating the influence of the parameter C_{D}. Finally, it should be mentioned that it may be possible to take into account the viscous effects using viscous-inviscid interaction techniques (Lock and Williams, 1987) or Navier-Stokes solvers (e.g., see the work by Visbal and Gordnier (2004)); however, the heavy computational load involved in these methods precludes their use in the current comprehensive investigation on the dynamics of cantilevered flexible plates in axial flow in various parameter spaces, which is the main subject of this thesis.

2.6. Summary on modelling

It can be seen in this chapter that the dynamics of cantilevered flexible plates in axial flow is indeed a challenging problem. Some aspects of this problem, for example the large amplitude vibrations of a cantilevered beam and the unsteady aero/hydrodynamics with moving boundaries are currently attracting extensive attention and research effort. The model developed in this thesis may be better regarded as a

shortcut solution which needs further improvement; although it is relatively simple and comes into place with considerable limitations, as one will see in the chapters that follow, the present model to some extent indeed captures successfully most of the inherent physics of the fluid-structure interaction system under investigation with acceptable time consumption and computational expense. Moreover, the current model also has the advantage of convenience in lending itself to modification or elimination of certain parts of the model in order to examine their consequence, which therefore gives us a unique opportunity to examine various factors influencing the system dynamics and to develop further insights into the mechanisms underlying its dynamical behaviour.

Chapter 3

Solution Methods and Preliminary Validation of the Model

3.1. Introduction

In this chapter the solution methods for the models of cantilevered flexible plates in axial flow developed in Chapter 2 are summarized. The lumped-vortex model for the aero/hydro-dynamics part of the fluid-structure interaction system does not need a discretization process; while the equations of motion of the plate are discretized using the traditional Galerkin expansion (Bishop and Johnson, 1979). The resulting nonlinear ordinary differential equations for the plate are coupled with the lumped-vortex model. There are various numerical parameters in the discretized aero/hydro-elastic model of the system; the convergence of simulation results with respect to these numerical parameters is tested. Some special treatments applied in the solutions are discussed in detail. Moreover, preliminary simulation results are compared with published experimental observations for the purpose of validating the fluidelastic model developed.

3.2. The Galerkin expansion

The nondimensional equation of motion of an inextensible cantilevered flexible plate and the associated boundary conditions are, respectively, given in Eqs. (2.7)

and (2.9), which can be discretized using the conventional Galerkin method. To do this, the transverse displacement of the plate w is expanded as

$$w(s,\tau) = \sum_{m=1}^{M} q_m(\tau)\phi_m(s), \tag{3.1}$$

where M is the number of modes utilized in the analysis, $q_m(\tau)$ is the generalized coordinate, and $\phi_m(s)$ are the *in vacuo* eigenmodes of a linear cantilevered beam defined by

$$\phi_m(s) = [\cosh(\beta_m s) - \cos(\beta_m s)] - \varsigma_m [\sinh(\beta_m s) - \sin(\beta_m s)], \tag{3.2}$$

where β_m is the dimensionless eigenvalue associated with the eigenmode $\phi_m(s)$, and ς_m is defined by

$$\varsigma_m = \frac{\cosh(\beta_m) - \cos(\beta_m)}{\sinh(\beta_m) - \sin(\beta_m)}. \tag{3.3}$$

Both ς_m and β_m are known sets of constants. Note that the normal modes of the nonlinear equation of motion defined in Eq. (2.7) can be calculated exactly; it has been shown by Hsieh et al. (1993) and Nayfeh et al. (1995) that, in the case no material damping, they are very close to the linear modes defined in Eq. (3.2).

It should be mentioned that the values of ς_m are very close to unity for higher-order modes (say, $m \geq 8$), and that the evaluation of $\phi_m(s)$ according to Eq. (3.2) with a numerical scheme of finite significant-figure precision loses accuracy due to round-off errors. To avoid this numerical problem, Eq. (3.2) should be rewritten in an alternative form as follows (Tang, 2003):

$$\begin{aligned}
\phi_m(s) \;=\; & \frac{1}{\sinh(\beta_m) + \sin(\beta_m)} \\
& \times \{[\cosh(\beta_m s)\sinh(\beta_m) - \cosh(\beta_m)\sinh(\beta_m s)] \\
& - [\cos(\beta_m s)\sinh(\beta_m) + \cos(\beta_m)\sinh(\beta_m s)] \\
& + [\cosh(\beta_m s)\sin(\beta_m) + \cosh(\beta_m)\sin(\beta_m s)] \\
& - [\cosh(\beta_m s)\sin(\beta_m) - \cos(\beta_m)\sin(\beta_m s)]\}.
\end{aligned} \tag{3.4}$$

Substituting Eq. (3.1) into Eq. (2.7), multiplying both sides by ϕ_i, and then taking the integration from $s = 0$ to $s = 1$, one obtains a set of nonlinear ordinary differential equations in terms of q_i as follows

$$\ddot{q}_i + \left(1 + \alpha\frac{\partial}{\partial\tau}\right)\left(A_i q_i + B_{imnl} q_m q_n q_l\right) + C_{imnl} q_m \left(\dot{q}_n \dot{q}_l + q_n \ddot{q}_l\right) = f_i, \tag{3.5}$$

where Einstein's scientific notion has been used (i.e., repeating indices denote summations), and the range of all indices i, m, n and l is from 1 to M. The generalized load f_i is given by

$$f_i = \int_0^1 \phi_i f_{\text{eff}}\, ds. \tag{3.6}$$

Moreover, the numerical constants A_i, B_{imnl} and C_{imnl} are defined by

$$A_i = \beta_i^4, \tag{3.7}$$

$$B_{imnl} = \int_0^1 \phi_i \left(\phi_m'''' \phi_n' \phi_l' + 4\phi_m' \phi_n'' \phi_l''' + \phi_m'' \phi_n'' \phi_l''\right) ds, \tag{3.8}$$

$$C_{imnl} = \int_0^1 \phi_i \phi_m' \left(\int_0^s \phi_n' \phi_l'\, d\zeta\right) ds - \int_0^1 \phi_i \phi_m'' \left[\int_s^1 \left(\int_0^\eta \phi_n' \phi_l'\, d\zeta\right) d\eta\right] ds. \tag{3.9}$$

Integrating by parts and utilizing Eq. (A.22), one can prove that

$$\begin{aligned} &\int_0^1 \phi_i \phi_m'' \left[\int_s^1 \left(\int_0^\eta \phi_n' \phi_l'\, d\zeta\right) d\eta\right] ds \\ &= -\int_0^1 \left\{\phi_i' \phi_m' \left[\int_s^1 \left(\int_0^\eta \phi_n' \phi_l'\, d\zeta\right) d\eta\right]\right\} ds + \int_0^1 \phi_i \phi_m' \left(\int_0^s \phi_n' \phi_l'\, d\zeta\right) ds, \end{aligned} \tag{3.10}$$

where $\left\{\phi_i \left[\int_s^1 \left(\int_0^\eta \phi_n' \phi_l'\, d\zeta\right) d\eta\right]\right\}_0^1 = 0$ has been used. Therefore, the expression for C_{imnl} can be simplified to

$$C_{imnl} = \int_0^1 \phi_i' \phi_m' \left[\int_s^1 \left(\int_0^\eta \phi_n' \phi_l'\, d\zeta\right) d\eta\right] ds. \tag{3.11}$$

Note that $C_{imnl} = C_{minl} = C_{imln}$ according to Eq. (3.11). It should be mentioned that the size of these numerical constants may be very large; for example, C_{imnl} contains the number 20 736 when $M = 12$. Therefore, these numerical constants are precalculated and then loaded into the simulation code.

3.3. The Houbolt method

Eq. (3.5) can be rewritten as

$$\begin{aligned} & \ddot{q}_i + C_{imnl} q_m q_n \ddot{q}_l + \alpha A_i \dot{q}_i + \alpha \left(B_{imnl} + B_{inml} + B_{ilnm} \right) \dot{q}_m q_n q_l \\ + \; & C_{imnl} q_m \dot{q}_n \dot{q}_l + A_i q_i + B_{imnl} q_m q_n q_l = f_i. \end{aligned} \tag{3.12}$$

To formulate a stable, accurate and efficient time-integration scheme for the solution of Eq. (3.12) is by no means a trivial task, due to the nonlinear inertial terms (Semler et al., 1996). The Houbolt method (Houbolt, 1950; Semler et al., 1996) seems to be the most suitable for obtaining reliable simulation results. Having been proved to be unconditionally stable (Johnson, 1966), the Houbolt method is based on the following two multistep backward finite-difference approximations at time step $k+1$:

$$\ddot{q}_i^{k+1} = \frac{\sum_{j=1}^{4} a_j q_i^{k-j+2}}{\Delta\tau^2} = \frac{a_1 q_i^{k+1} + \lambda_{1i}^{k+1}}{\Delta\tau^2}, \tag{3.13a}$$

$$\dot{q}_i^{k+1} = \frac{\sum_{j=1}^{4} b_j q_i^{k-j+2}}{\Delta\tau} = \frac{b_1 q_i^{k+1} + \lambda_{2i}^{k+1}}{\Delta\tau^2}, \tag{3.13b}$$

where $a_{j,j=1,2,3,4} = (2, -5, 4, -1)$ and $b_{j,j=1,2,3,4} = (11/6, -3, 3/2, -1/3)$ are coefficients for the fourth-order scheme of the Houbolt method, and $\Delta\tau$ is the time step. Substituting Eqs. (3.13a) and (3.13b) into Eq. (3.12), a set of nonlinear equations for the unknown q_i^{k+1} are obtained, namely

$$D_i q_i + E_{imnl} q_m q_n q_l + F_{imnl} \lambda_{2m} q_n q_l + C_{imnl} q_m \left(q_n \lambda_{1l} + \lambda_{2n} \lambda_{2l} \right) + \lambda_{3i} = \Delta\tau^2 f_i, \tag{3.14}$$

where the superscript $k+1$ has been dropped for clarity; the time-dependent coefficients λ_{1i}, λ_{2i} and λ_{3i}, at time step $k+1$, are defined by

$$\lambda_{1i}^{k+1} = \sum_{j=2}^{4} a_j q_i^{k-j+2}, \quad \lambda_{2i}^{k+1} = \sum_{j=2}^{4} b_j q_i^{k-j+2}, \quad \lambda_{3i}^{k+1} = \lambda_{1i}^{k+1} + \Delta\tau \alpha A_i \lambda_{2i}^{k+1}; \tag{3.15}$$

and the numerical constants D_i, E_{imnl} and F_{imnl} are defined by

$$D_i = a_1 + (\Delta\tau^2 + \Delta\tau \alpha b_1) A_i, \tag{3.16}$$

$$E_{imnl} = (\Delta\tau^2 + 3\Delta\tau \alpha b_1) B_{imnl} + (a_1 + b_1^2) C_{imnl}, \tag{3.17}$$

$$F_{imnl} = \Delta\tau\alpha\left(B_{imnl} + B_{inml} + B_{ilnm}\right) + b_1\left(C_{ilnm} + C_{inml}\right). \tag{3.18}$$

Note that, although the time step $\Delta\tau$, the material damping coefficient α and the coefficients of the Houbolt method a_1 and b_1 are involved in their definitions, the values of D_i, E_{imnl} and F_{imnl} do not vary with time.

The subroutine DLSARG provided by IMSL (Visual Numerics Inc, 1998) is used to solve Eq. (3.12); when f_i at the current time step $k+1$ is regarded as a known, the *Jacobian* of Eq. (3.14) can be calculated according to

$$\begin{aligned}\mathbb{J}_{ij}^{k+1} &= D_i\delta_{ij} + \left(E_{ijmn} + E_{imjn} + E_{imnj}\right) q_m^{k+1} q_n^{k+1} + \left(F_{imjn} + F_{imnj}\right) \lambda_{2m}^{k+1} q_n^{k+1} \\ &+ \left(C_{ijmn} + C_{imjn}\right) q_m^{k+1} \lambda_{1l}^{k+1} + C_{ijmn} \lambda_{2m}^{k+1} \lambda_{2n}^{k+1}.\end{aligned} \tag{3.19}$$

To start the solution of Eq. (3.12), initial conditions should be set. Usually, it is assumed that $q_i^{k=0}$ and $\dot{q}_i^{k=0}$ are prescribed at time instant $\tau = 0$. Therefore, it is necessary to solve $q_i^{k=-1,-2}$ and $\dot{q}_i^{k=-1,-2}$. The scheme adopted in this thesis is to solve $\ddot{q}_i$ from a modified version of Eq. (3.12) with $f_i = 0$, as follows:

$$\begin{aligned}&\left(C_{imnj} q_m q_n + \delta_{ij}\right) \ddot{q}_j^k \\ =\ & -\left[A_i q_i^k + B_{imnl} q_m^k q_n^k q_l^k + \alpha A_i \dot{q}_i^k\right. \\ +\ & \left.\alpha\left(B_{imnl} + B_{inml} + B_{ilnm}\right) \dot{q}_m^k q_n^k q_l^k + C_{imnl} q_m^k \dot{q}_n^k \dot{q}_l^k\right].\end{aligned} \tag{3.20}$$

Hence, q_i^{k-1} and $\dot{q}_i^{k-1}$ are calculated using

$$q_i^{k-1} = q_i^k - \dot{q}_i^k \Delta\tau, \qquad \dot{q}_i^{k-1} = \dot{q}_i^k - \ddot{q}_i^k \Delta\tau; \tag{3.21}$$

this process can be repeated once again to obtain q_i^{k-2} and $\dot{q}_i^{k-2}$.

3.4. The solution schemes

In this thesis, the structural model and the aero/hydro-dynamics model are not fully coupled: as illustrated in Figs. 1.6 and 3.1(a), the structural model generates the deformed shapes and vibration velocities of the cantilevered flexible plate to be

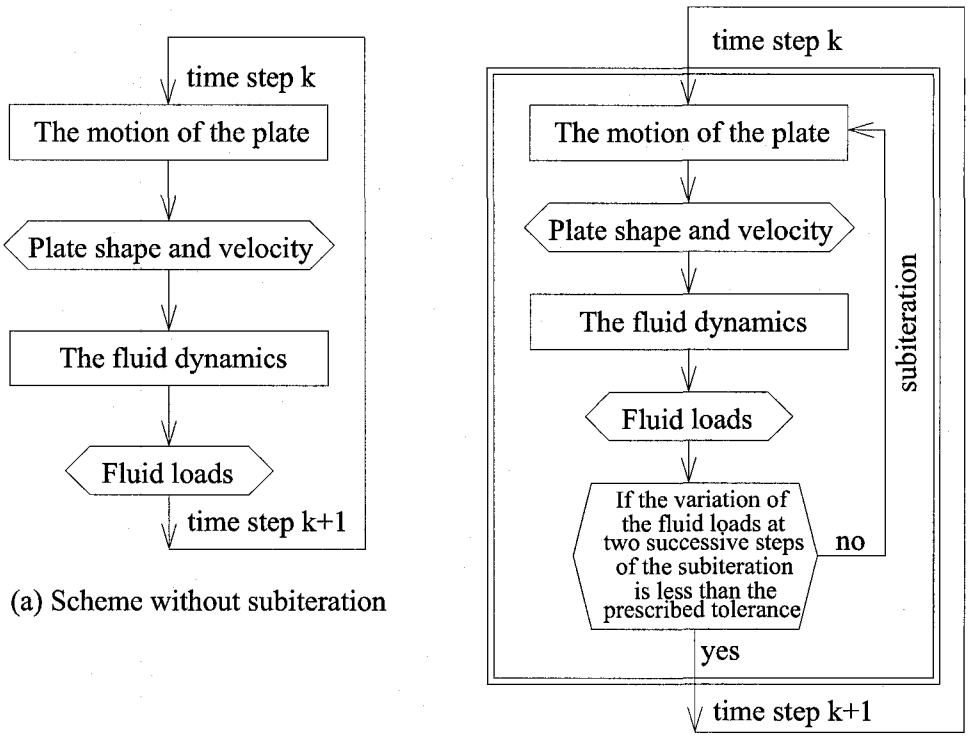

(a) Scheme without subiteration

(b) Scheme with subiteration

FIGURE 3.1. Two solution schemes.

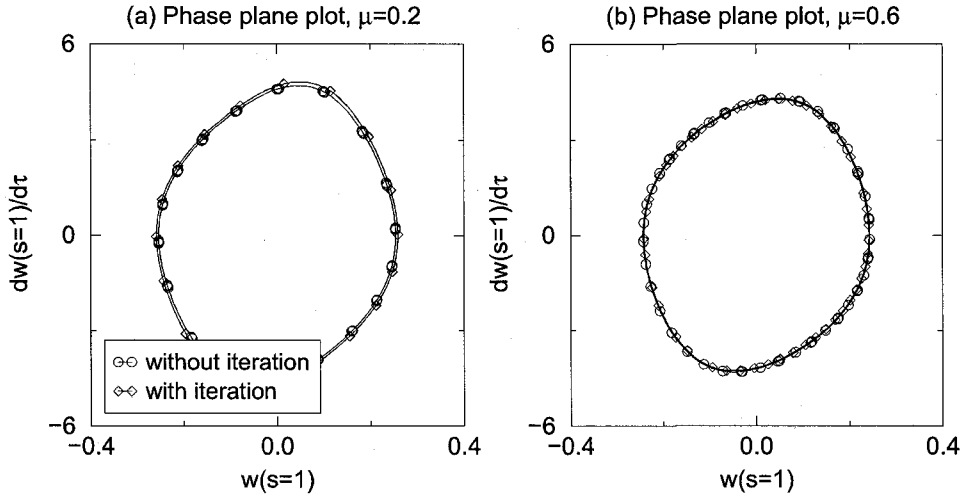

FIGURE 3.2. The simulation results obtained by using or without using the subiteration scheme. The time step used is $\Delta\tau = 0.001$.

used in the aero/hydro-dynamics model; while the latter calculates the fluid loads for the structural one. Note that the fluid loads are regarded as constants in the solution of the equation of motion of the plate. As illustrated by Fig. 3.1(b), one can also use a subiteration scheme to eliminate the lagging between the solutions of the

structural model and the aero/hydro-dynamics model. In particular, at each time step, the subiteration is carried out to drive the variation in the generalized load f_i (see Eq. (3.6)) to a prescribed small value. However, as shown in Fig. 3.2, it is found through extensive tests that the subiteration scheme is not necessary when the mass ratio μ is small, say $\mu \leq 0.6$, if the parameters of the system are properly chosen and the time step is sufficiently small.

Another important issue involved in the solution is that, when $\mu > 0.6$, the solution may become unstable, even when using the subiteration scheme. This difficulty can be overcome by using the added-mass compensation method (Bélanger et al., 1995). A virtual added-mass is defined by

$$\overline{M}_{\mathrm{A}} = \overline{\beta}_{\mathrm{A}} \rho_{\mathrm{F}} L, \tag{3.22}$$

where $\overline{\beta}_{\mathrm{A}}$ is the nondimensional virtual added-mass coefficient. To apply the added-mass compensation method, an additional constant inertia term $\overline{M}_{\mathrm{A}} \ddot{W}$ is added to both sides of Eq. (2.1). Theoretically, the value of $\overline{\beta}_{\mathrm{A}}$ will not influence the solution result; in this thesis, $\overline{\beta}_{\mathrm{A}} = 0.5$ is consistently used.

It should be noted that, with the added-mass compensation, the nondimensional equation of motion of the plate Eq. (2.7) becomes

$$\begin{aligned} &\left(1 + \overline{\beta}_{\mathrm{A}} \mu\right) \ddot{w} + \left(1 + \alpha \frac{\partial}{\partial \tau}\right) \left[w'''' \left(1 + w'^2\right) + 4 w' w'' w''' + w''^3\right] \\ + \; & w' \int_0^s \left(\dot{w}'^2 + w' \ddot{w}'\right) ds - w'' \int_s^1 \left[\int_0^s \left(\dot{w}'^2 + w' \ddot{w}'\right) ds\right] ds = \overline{f}_{\mathrm{eff}}, \end{aligned} \tag{3.23}$$

where the effective force $\overline{f}_{\mathrm{eff}}$ (refer to Eq. (2.10)) is defined by

$$\overline{f}_{\mathrm{eff}} = \mu {U_{\mathrm{R}}}^2 \left(f_{\mathrm{L}} - w' f_{\mathrm{D}} + w'' \int_s^1 f_{\mathrm{D}} \, ds\right) + \overline{\beta}_{\mathrm{A}} \mu \ddot{w}. \tag{3.24}$$

It follows that in the solution the generalized load f_i (see Eq. (3.6)) should be accordingly changed to

$$f_i = \int_0^1 \phi_i \overline{f}_{\mathrm{eff}} \, ds. \tag{3.25}$$

Moreover, the numerical constant D_i (see Eq. (3.16)) and the time-dependent coefficient λ_{3i} (see Eq. (3.15)) should, respectively, be accordingly renewed as

$$D_i = (1 + \overline{\beta}_{\mathrm{A}}\mu)a_1 + (\Delta\tau^2 + \Delta\tau\alpha b_1)A_i, \tag{3.26}$$

$$\lambda_{3i}^{k+1} = (1 + \overline{\beta}_{\mathrm{A}}\mu)\lambda_{1i}^{k+1} + \Delta\tau\alpha A_i\lambda_{2i}^{k+1}. \tag{3.27}$$

3.5. Convergence tests

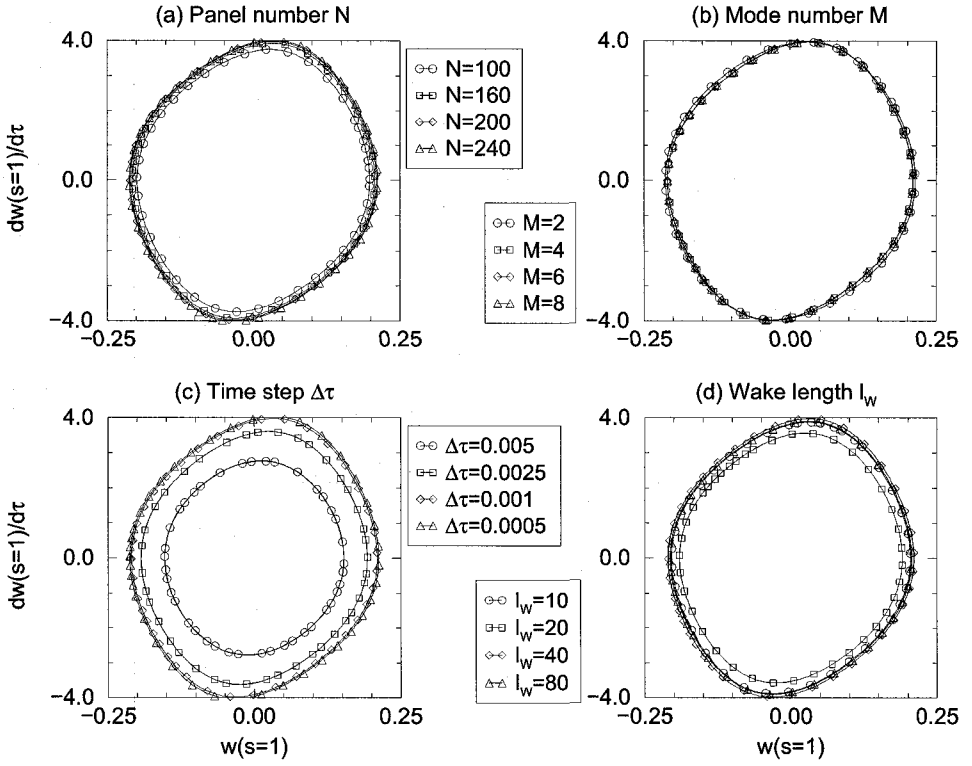

FIGURE 3.3. The convergence tests presented by means of phase plane plots for the following numerical parameters: (a) the number of panels N, (b) the number of Galerkin modes M, (c) the time step $\Delta\tau$, and (d) the length of truncated wake street l_{W}. The system parameters are: $\mu = 0.2$, $U_{\mathrm{R}} = 10$, $l_0 = 1$, $\alpha = 0.004$ and $C_{\mathrm{D}} = 0$. The reference set of numerical parameters is: $N = 200$, $M = 6$, $\Delta\tau = 1.0 \times 10^{-3}$ and $l_{\mathrm{W}} = 40$.

There are four numerical parameters that arise form the discretization of the model of cantilevered flexible plates in axial flow: the number of panels N, the length of the truncated wake street l_{W}, the number of Galerkin modes M and the time step $\Delta\tau$. Note that N and l_{W} come from the aero/hydro-dynamics model; M comes from the structural model; $\Delta\tau$ is the same for both models. The convergence of simulation

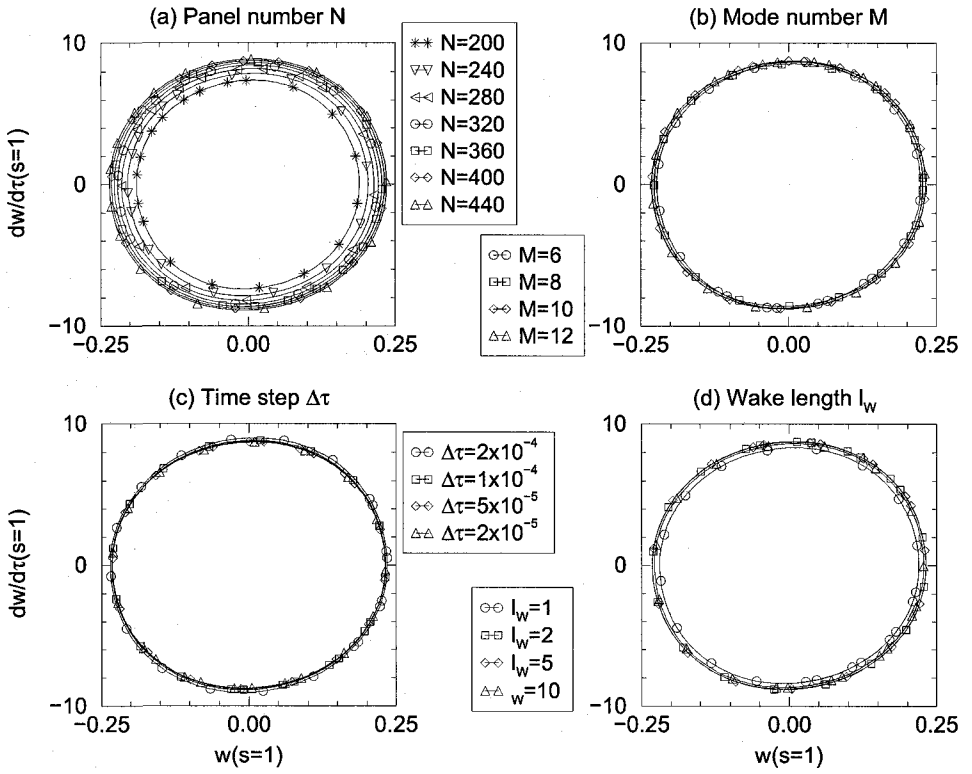

FIGURE 3.4. The convergence tests presented by means of phase plane plots for the following numerical parameters: (a) the number of panels N, (b) the number of Galerkin modes M, (c) the time step $\Delta\tau$, and (d) the length of truncated wake street l_{W}. The system parameters are: $\mu = 20$, $U_{\mathrm{R}} = 9.487$, $l_0 = 0.01$, $\alpha = 0.004$ and $C_{\mathrm{D}} = 0$. The reference set of numerical parameters is: $N = 400$, $M = 8$, $\Delta\tau = 5.0 \times 10^{-5}$ and $l_{\mathrm{W}} = 10$.

results with respect to these four numerical parameters is examined, as shown in Figs. 3.3 and 3.4, for two different values of mass ratio μ.

The convergence of the simulation results depends on the value of mass ratio μ of the system. It is found that when $\mu \leq 0.6$, as shown in Fig. 3.3 for the case $\mu = 0.2$ as an example, satisfactory convergence can be achieved with $N = 200$, $M = 6$, $\Delta\tau = 1.0 \times 10^{-3}$ and $l_{\mathrm{W}} = 40$. However, when $\mu > 0.6$, for convergence the values of the numerical parameters should be chosen as $N = 400$, $M = 8$, $\Delta\tau = 5.0 \times 10^{-5}$ and $l_{\mathrm{W}} = 10$, as shown in Fig. 3.3 for the case $\mu = 20$ as an example. As compared to the convergence tests presented in Fig. 3.3 for $\mu = 0.2$, one can see in Fig. 3.4 that when μ increases to $\mu = 20$, more panels are necessary in the aero/hydro-dynamics model of the system, while the truncated length of the wake l_{W} becomes less important. Moreover, as μ increases, it is interesting to note that the increase of the number of

Galerkin modes is moderate, in contrast to the increase in the number of panels. That is, when higher-order modes become significant in the dynamics of the cantilevered flexible plate, the required value of the number of panels N for convergence should be considerably increased in order to accurately predict the fluid loads acting on the plate.

3.6. Preliminary validation of the model

The preliminary validation of the model is carried out through comparisons between simulation results obtained using the present theory with specific parameter sets and the corresponding published experimental observations. It can be seen in Fig. 3.5 that the present theory can well predict the vibration modes of the cantilevered flexible plate for various systems with different values of mass ratio μ. Moreover, as shown in Table 3.1, the critical reduced flow velocity U_{Rc} and the critical flutter frequency $f_{\mathrm{c}}^{\star}$ predicted by the present theory agree with experimental measurements made by Kornecki et al. (1976) much better than with their own theory. Note that, in this thesis, the dynamics of the system is studied in the time-domain; therefore, the values U_{Rc} and $f_{\mathrm{c}}^{\star}$ presented in Table 3.1 for the present theory are obtained through examining the time histories, as shown in Fig. 3.6.

TABLE 3.1. A test for the present theory

		Kornecki et al. (1976)	
	Present theory	Experiment	Theory
μ	0.232	0.232	0.232
l_0	1.125	1.125	not considered
α	0.002	not available	not considered
C_{D}	0.8	not available	not considered
U_{Rc}	8.78	8.77	5.84
$f_{\mathrm{c}}^{\star}$	3.2	3.26	3.22

It should be mentioned that, in the comparisons presented herein, the parameter sets used in the numerical simulations are not exactly identical to those of the corresponding previous experiments. For example, as shown in Table 3.1, in the experiment by Kornecki et al. (1976), no information about the material damping α and

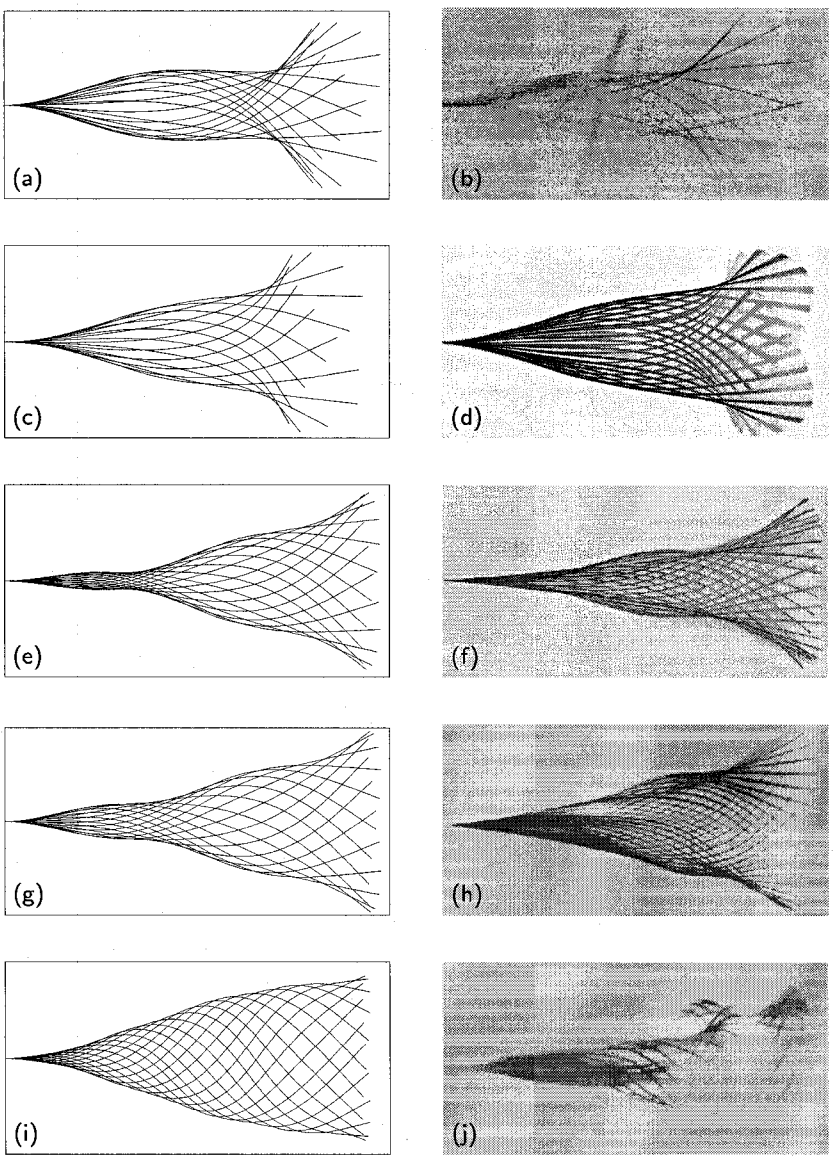

FIGURE 3.5. The vibration modes at various values of mass ratio μ predicted by the present theory and observed in previous experiments: (a, c, e, g, i) predicted by the present theory; (b, d, f, h, j) observed in previous experiments. (a, b) For the system with a small μ studied by Tang et al. (2003), $\mu = 0.30$; (c, d) for the system with a small μ studied by Souilliez et al. (2006), $\mu = 0.68$; (e, f) for the system with a medium μ studied by Souilliez et al. (2006), $\mu = 1.8$; (g, h) for the system with a medium μ studied by Watanabe et al. (2002b), $\mu = 2.7$; (i, j) for the system with a large μ studied by Watanabe et al. (2002b), $\mu = 35.7$.

the viscous drag C_{D} acting on the plate was available; nevertheless, $\alpha = 0.002$ and $C_{\mathrm{D}} = 0.8$ have arbitrarily been used in the numerical simulations with the present theory, and this achieves an excellent agreement between the theoretical prediction and the experimental observations in terms of U_{Rc} and $f_{\mathrm{c}}^{\star}$, which do depend indeed

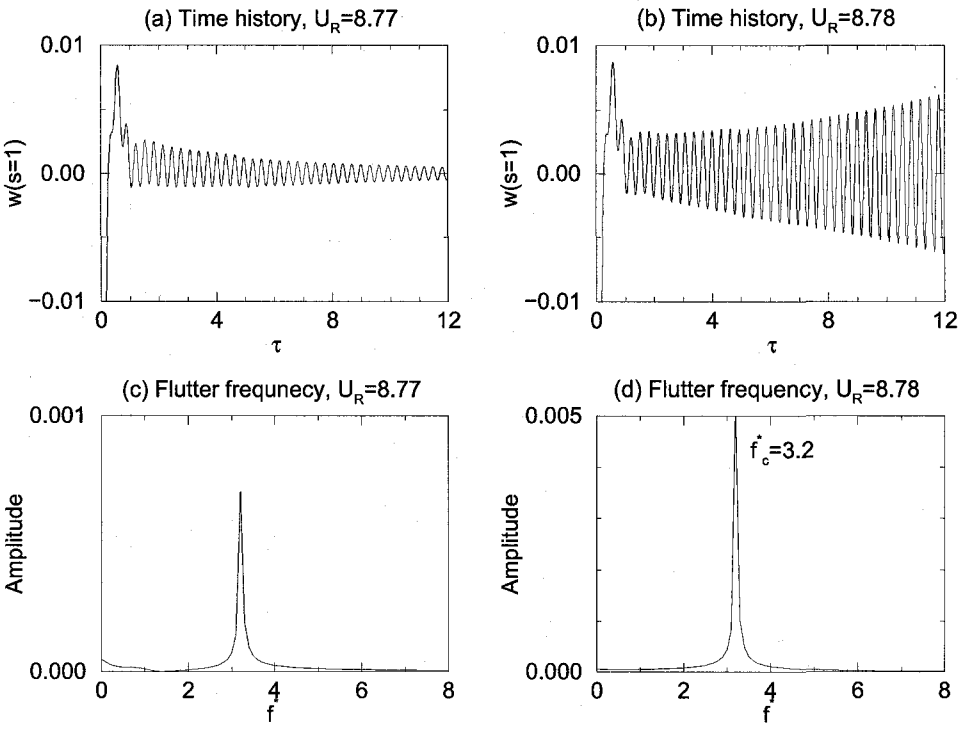

FIGURE 3.6. The onset of flutter detected through time histories for the studied by Kornecki et al. (1976). The other system parameters are: $\mu = 0.232$, $l_0 = 1.125$, $\alpha = 0.002$ and $C_D = 0.8$.

on the values of α and C_D. The excellence of this agreement may be fortuitous; however, it can be concluded through the comparisons between simulation results and previous experimental observations that the present theory is capable of capturing the inherent properties of the dynamics of cantilevered flexible plates in axial flow. The influence of various control parameters on the system dynamics will be further discussed in Chapter 4.

Chapter 4

The Dynamics of the Basic Configuration

4.1. Introduction

In this chapter, we systematically study the dynamics of cantilevered flexible plates in axial flow in the vertical configuration as shown in Fig. 1.3(a), i.e., the basic configuration. The influence of various nondimensional control parameters (in contrast to the numerical parameters discussed in Chapter 3) on the dynamics of the fluid-structure interaction system, not only the onset of flutter but also the post-critical behaviour, are investigated in detail using the numerical model developed in Chapters 2 and 3. In particular, when the plate is assumed to be inextensible, these nondimensional control parameters are: the mass ratio μ, the reduced flow velocity U_{R}, the length of the upstream rigid segment l_0, the material damping coefficient α and the viscous drag coefficient C_{D}.

Moreover, the theoretical predictions of the system dynamics obtained using the present theory are compared with previous theoretical results as well as experimental observations; it can be seen in this chapter that the present theory indeed captures the principal properties of the global dynamics of the system and achieves a better agreement with experimental observations than previous theories.

Finally, the dynamics of the system in the basic configuration discussed in this chapter can also be regarded as the benchmark for the dynamics of the system with modified configurations, which will be addressed in Chapter 5.

4.2. Onset of flutter and post-critical vibrations

There are five nondimensional control parameters in the fluid-structure interaction system: μ, U_{R}, l_0, α and C_{D}. When the other control parameters are fixed, the system dynamics with respect to U_{R} is shown in Figs. 4.1 and 4.2 for $\mu = 0.2$ and in Fig. 4.3 for $\mu = 2.0$.

When the mass ratio of the system is $\mu = 0.2$, it can be seen in Fig. 4.1(a) that the critical reduced flow velocity is $U_{\mathrm{Rc}} = 9.92$; U_{Rc} is also referred to in short as the critical point in this thesis. When $U_{\mathrm{R}} < U_{\mathrm{Rc}}$, the plate remains in the stable flat state; any small disturbance to the system is attenuated. Flutter occurs when $U_{\mathrm{R}} \geq U_{\mathrm{Rc}}$. With increasing U_{R}, the flutter amplitude increases monotonically, as shown in Figs. 4.1(a) and 4.3(a). For the case $\mu = 0.2$, as shown in Fig. 4.1(b), the flutter frequency first decreases, and then somewhat recovers at large U_{R}. The decrease in flutter frequency with increasing U_{R} is qualitatively contrary to what is observed in previous experiments by Taneda (1968), Watanabe et al. (2002b), Tang et al. (2003) and Shelley et al. (2005). This discrepancy may be attributed to the absence of a proper model for the (viscous) drag acting on the oscillating plate; further investigation on this aspect will be conducted later in this chapter. It should be mentioned that the dynamics of the system depends on the value of μ. For example, when $\mu = 2.0$, as seen in Figs. 4.3(a) and (b), the critical point is located at $U_{\mathrm{Rc}} = 10.88$ and the overall flutter frequency is higher than for $\mu = 0.2$. Moreover, when $\mu = 2.0$, the flutter frequency predicted using the present theory monotonically increases in a stepped fashion with increasing U_{R}.

The time histories, phase plane plots and modes of the post-critical vibrations of the case $\mu = 0.2$ at $U_{\mathrm{R}} = 9.95$ and 13.78 are shown in Figs. 4.1(c) through (h). Moreover, for the same case, i.e., $\mu = 0.2$, the system dynamics at a intermediate

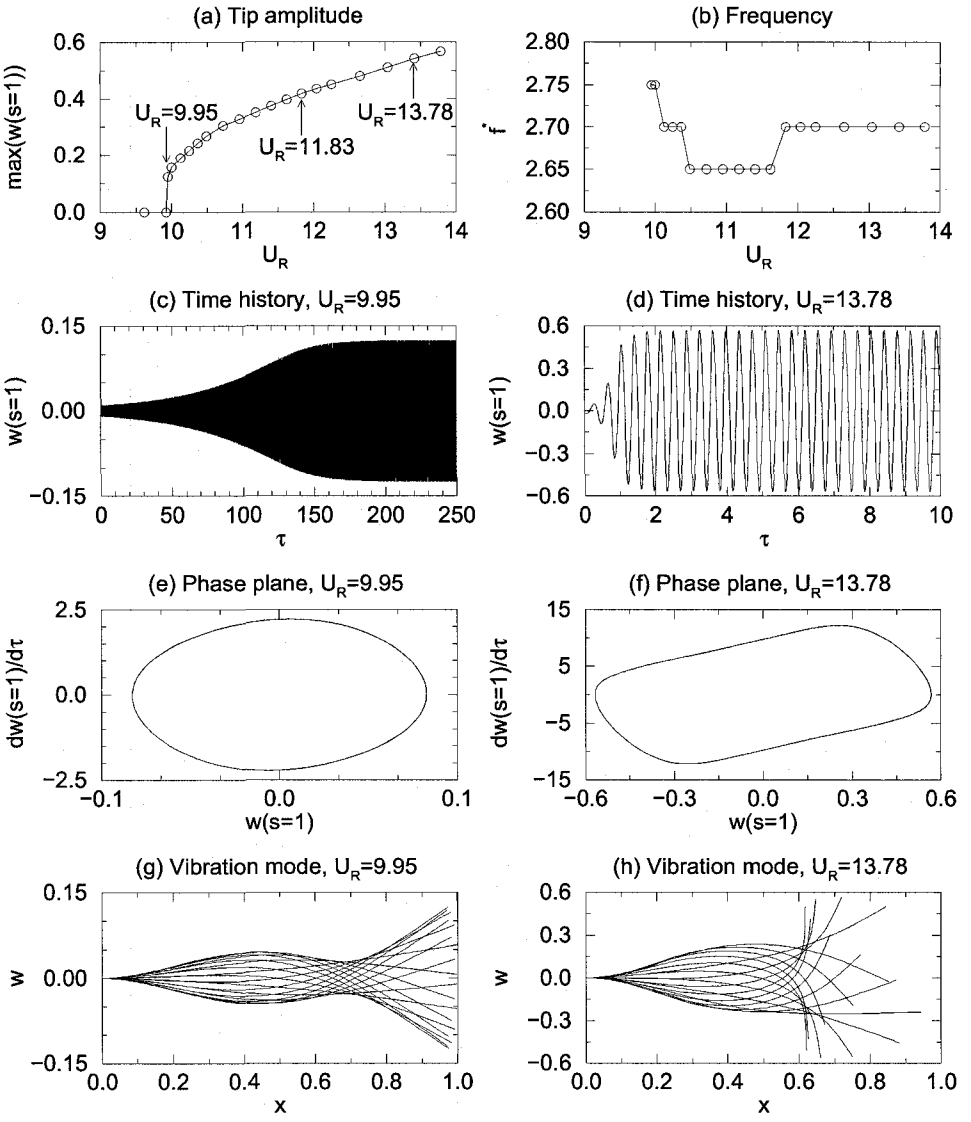

FIGURE 4.1. The instability and post-critical vibrations of cantilevered flexible plates in axial flow. The parameters of the system are $\mu = 0.2$, $l_0 = 0.01$, $\alpha = 0.004$ and $C_D = 0$.

reduced flow velocity $U_R = 11.83$ is presented in Fig. 4.2. It is observed in Figs. 4.1(c) and (e) that when U_R is close to U_{Rc}, the transient is very long; the flutter amplitude is relatively small; and, the system dynamics is almost linear. Note that the behaviour of the system at a U_R close to U_{Rc}, i.e., the long transient together with the small amplitude, may explain the small amplitude oscillations preceding the large amplitude flutter observed in the experiments conducted by Tang et al. (2003).

For the specific case of $\mu = 0.2$, the modal form of the oscillation involves travelling waves (no stationary nodes) of roughly second-beam-mode shape; there is a

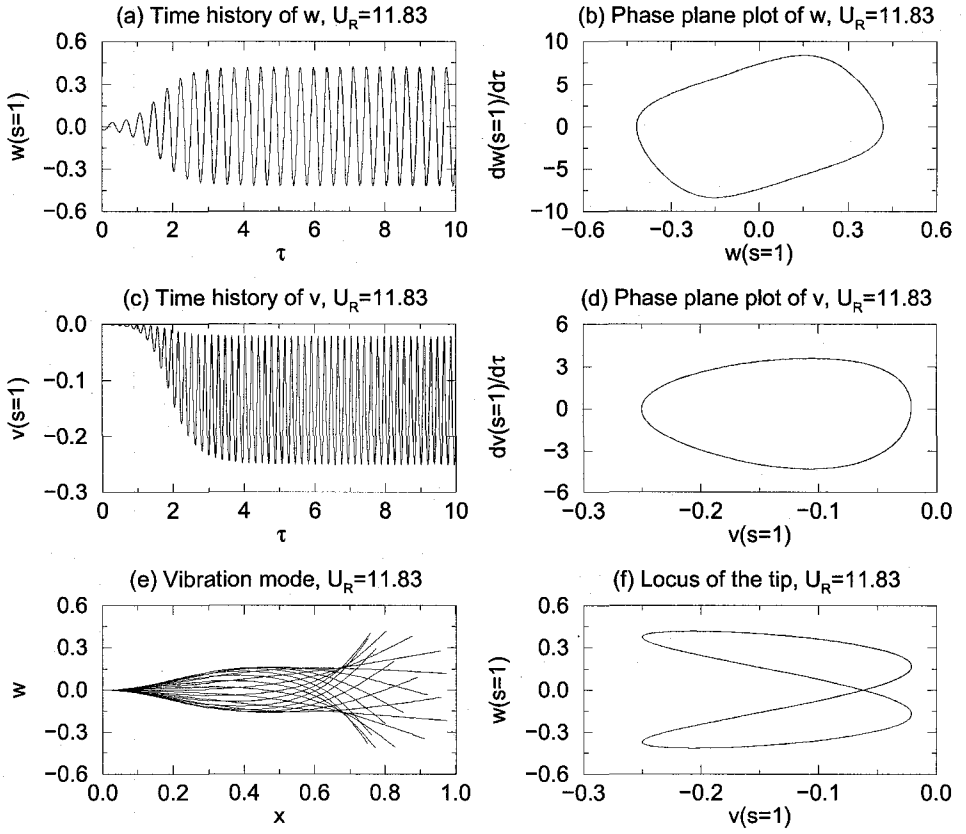

FIGURE 4.2. The post-critical vibrations of cantilevered flexible plates in axial flow with the consideration of longitudinal displacements. The parameters of the system are $\mu = 0.2$, $U_{\mathrm{R}} = 11.83$, $l_0 = 0.01$, $\alpha = 0.004$ and $C_{\mathrm{D}} = 0$.

quasi-node located at about three-quarters of the plate length. Here, the *beam mode* refers to one of the linear modes of a cantilevered beam as defined in Eqs. (3.2) and (3.3); and, the term *second-beam-mode shape* means that the beam modes up to the second one, as compared to the higher modes, are significant in the vibrations of the plate. The second-beam-mode shape can clearly be observed at low U_{R}, as shown in Fig. 4.1(g), where the flutter amplitude and the corresponding longitudinal displacements are relatively small. It can be seen in Figs. 4.1(g), 4.2(e) and 4.1(h) that, as U_{R} increases, the quasi-node becomes less distinct, while the vibration modes remain qualitatively the same. As shown in Fig. 4.4, a further observation of the vibration modes can be made in terms of the magnitudes of individual generalized coordinates q_i, which is defined in Eq. (3.1). It can be seen in Fig. 4.4 that the ratios of the generalized coordinates of the higher modes to that of the first mode, in terms of their magnitudes $\max(|q_i|)$, are $1 : 1.18 : 0.0236 : 0.00392$ and $1 : 0.606 : 0.0381 : 0.00981$,

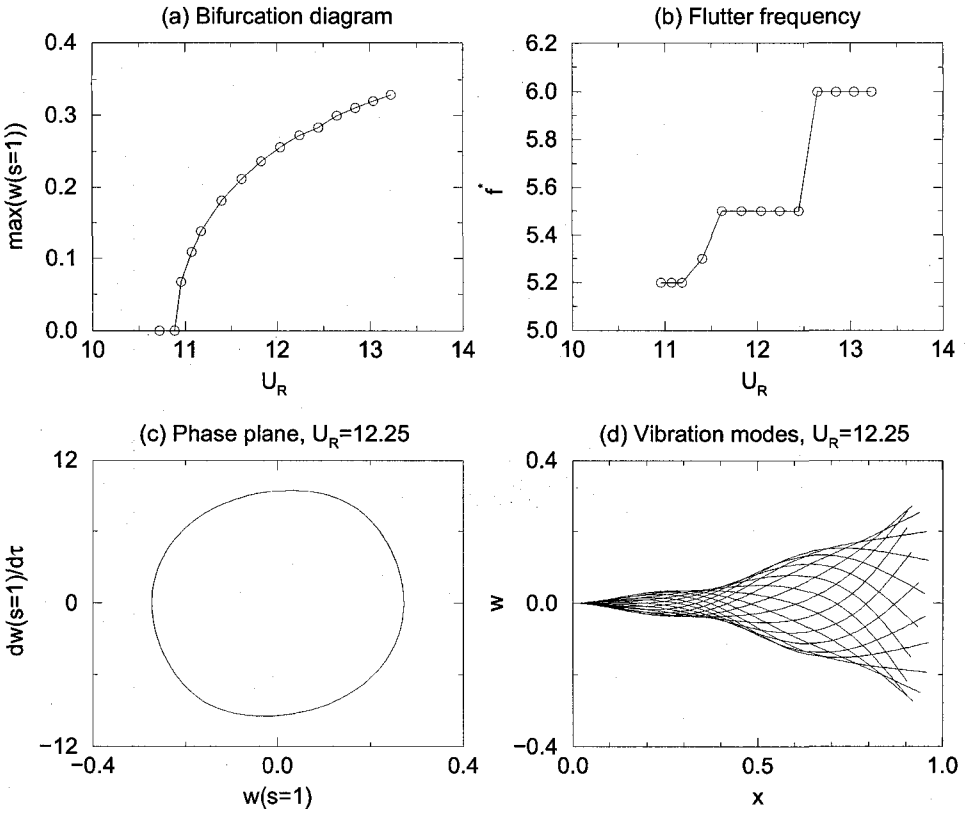

FIGURE 4.3. The instability and post-critical vibrations of cantilevered flexible plates in axial flow. The parameters of the system are $\mu = 2.0$, $l_0 = 0.01$, $\alpha = 0.004$ and $C_D = 0$.

respectively, for the cases $U_R = 9.95$ and $U_R = 13.78$. That is, the first two beam modes are dominant in both cases, and the vibration of the plate thus exhibits a pronounced second-beam-mode shape. It should be noted that the vibration modes also depend on the value of μ; a third-beam-mode shape is observed in the vibrations of the plate when $\mu = 2.0$, as shown in Fig. 4.3(d).

The time history and phase plane plot of the longitudinal displacements of the plate tip are, respectively, shown in Figs. 4.2(c) and (d); as expected, it can be seen that the longitudinal displacement is always negative and the frequency of the longitudinal vibration is twice that of the transverse vibration, as always. The locus of the plate tip exhibits a figure-of-eight shape as shown in Fig. 4.2(f), which was clearly observed before in the experiments by Zhang et al. (2000) (see also Fig. 2.3(c)). Another important conclusion that can be drawn from Fig. 4.2 is that the magnitudes of the transverse and longitudinal displacements, when observed in the fixed X-Y

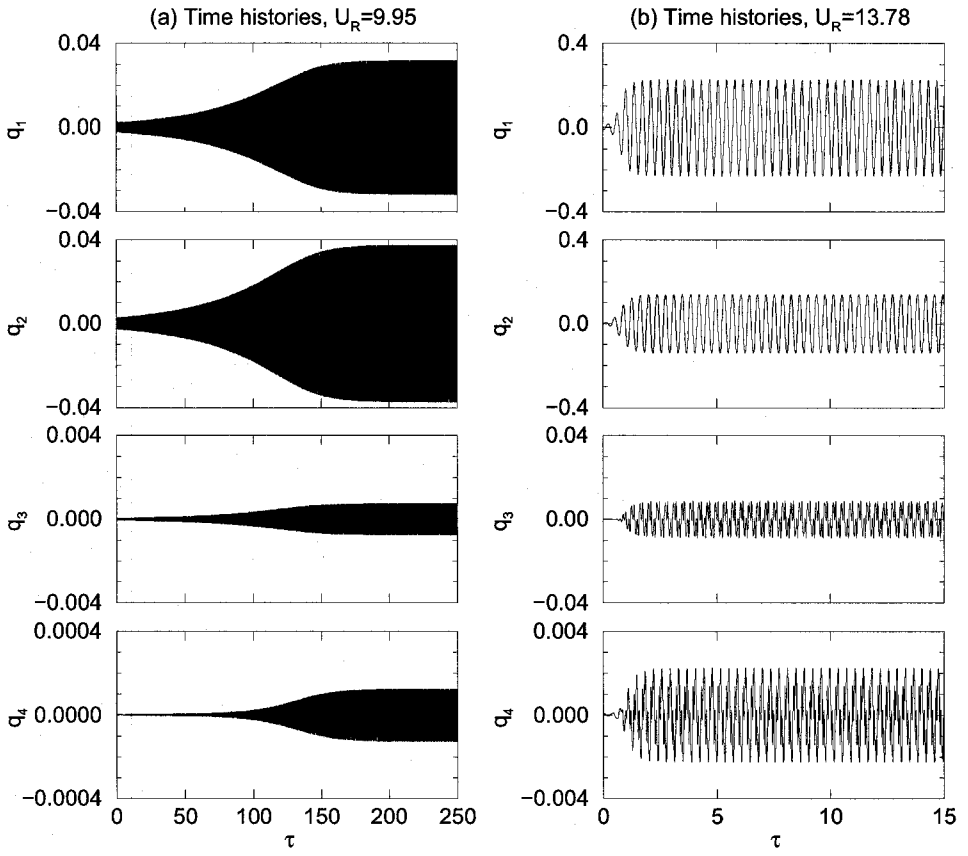

FIGURE 4.4. The time histories of the generalized coordinates q_i. The parameters of the system are $\mu = 0.2$, $l_0 = 0.01$, $\alpha = 0.004$ and $C_D = 0$.

coordinate system, are of the same order; for the present case, one can find that $\max(|\, w(s=1)\,|) = 0.418$ and $\max(|\, v(s=1)\,|) = 0.250$. It can further be seen in Fig. 4.2(f) that the maxima of the longitudinal and transverse displacements arise almost concurrently in the vibration, while the minimum of the longitudinal displacement does not occur simultaneously as that in the transverse displacement.

From the bifurcation diagrams shown in Figs. 4.1(a) and 4.3(a), respectively for $\mu = 0.2$ and $\mu = 2.0$, it is seen that the present theory predicts a supercritical bifurcation, leading to flutter. In experiments, however, flutter is more likely to occur in a subcritical manner (Zhang et al., 2000; Watanabe et al., 2002b; Tang et al., 2003; Shelley et al., 2005). It should be emphasized that all theories to date fail to capture this characteristic; they all predict a supercritical bifurcation. Normally, a subcritical bifurcation is accompanied by the hysteresis phenomenon; two stable states of the system (Zhang et al., 2000) may co-exist in a certain range of U_R in the bifurcation

diagram. In other words, the system dynamics in this range of U_R depends on initial conditions. To this end, the influence of initial conditions on the system dynamics has been extensively examined, as shown in Fig. 4.5 for some of the tests: from very small initial deformations to relatively large ones, as well as from initial deformations in a single mode to those of combined modes. In regard to both the onset of flutter and the post-critical behaviour, no dependence of the system dynamics on initial conditions has been observed.

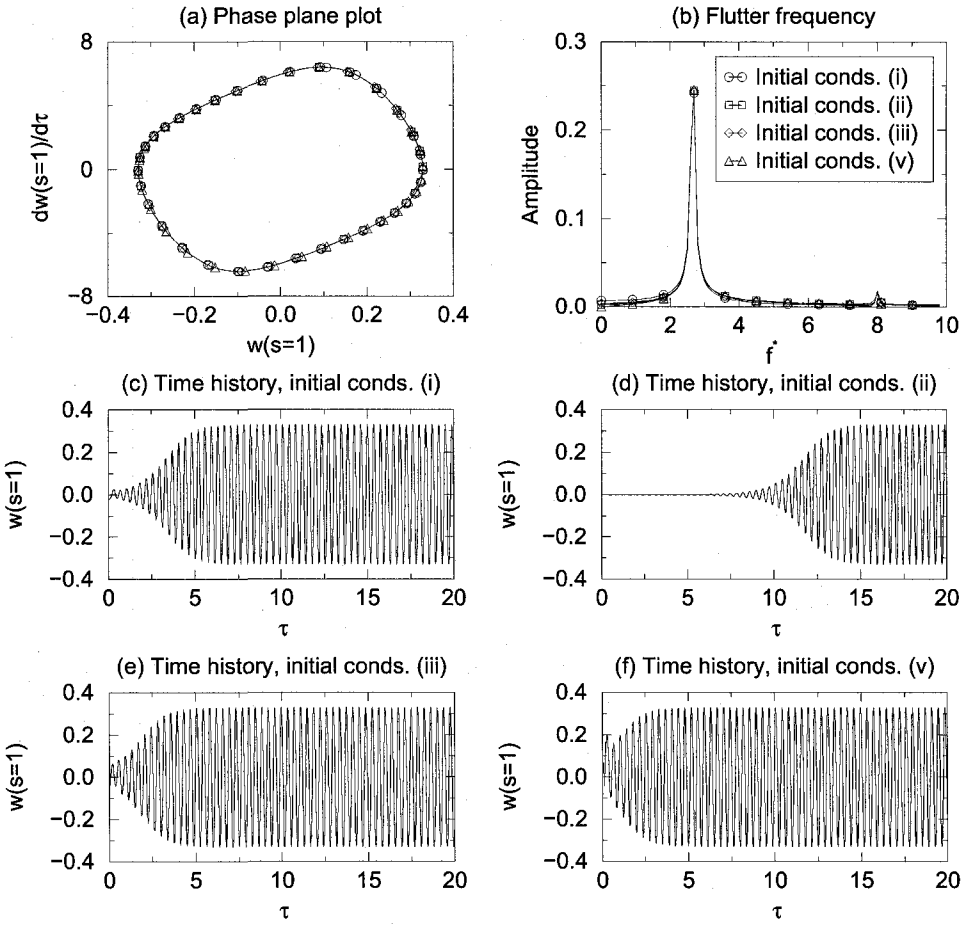

FIGURE 4.5. The system dynamics with various initial conditions: (i) $q_1^0 = -1.0 \times 10^{-2}$; (ii) $q_2^0 = 2.0 \times 10^{-5}$; (iii) $q_3^0 = -5.0 \times 10^{-2}$; and, (v) $q_3^0 = -5.0 \times 10^{-2}$ and $q_4^0 = 1.0 \times 10^{-2}$. The parts of the initial conditions not specified are all zeros, i.e., $q_i^0 = 0$ and $\dot{q}_i^0 = 0$. The parameters of the system are $\mu = 0.2$, $U_R = 10.95$, $l_0 = 0.01$, $\alpha = 0.004$ and $C_D = 0$.

4.3. On some issues of the present theory

4.3.1. The longitudinal displacements. The longitudinal displacements of the plate were neglected in all previous theoretical studies on the dynamics of cantilevered flexible plates in axial flow. In this thesis, the longitudinal displacement v is calculated according to Eq. (2.2), and the longitudinal deformations and velocities of the plate are taken into account in the calculation of the aero/hydro-dynamic loads (see Eqs. (2.18), (2.19), (2.21b) and (2.22)).

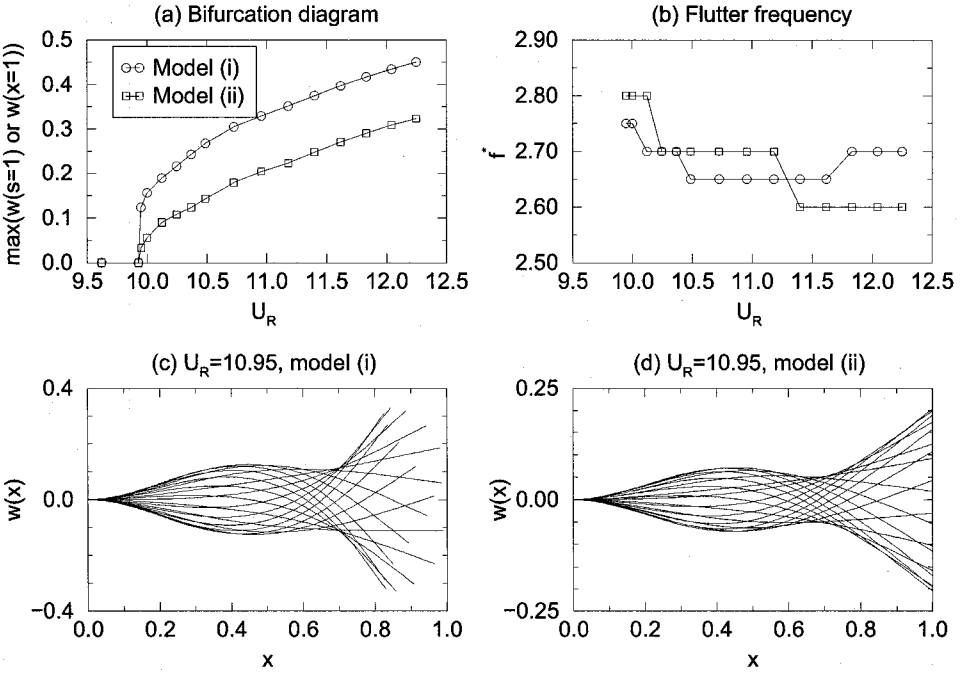

FIGURE 4.6. The comparison of two models: (i) the model adopted in the present theory; (ii) the model neglecting the longitudinal displacement. The parameters of the system are $\mu = 0.2$, $l_0 = 0.01$, $\alpha = 0.004$ and $C_D = 0$.

The dynamics of the system obtained using (i) the original model adopted in the present theory, and (ii) a modified model, which neglects the longitudinal deformations and velocities, are shown in Fig. 4.6 for the case of $\mu = 0.2$. It can be observed in Fig. 4.6(a) that the two models predict the same critical point U_{Rc}; however, the onset of flutter predicted by model (i) is in such a manner that the curve in the bifurcation diagram, in the immediate vicinity of the critical point, is much steeper than that obtained using model (ii). Without considering the longitudinal displacements in the model, the flutter amplitude still increases with increasing U_R; but, at a fixed

U_R, model (ii) predicts a smaller flutter amplitude than model (i). Although the vibration amplitudes predicted by the two models are different, as shown in Figs. 4.6(c) and (d), the vibration modes are qualitatively similar. In Fig. 4.6(b), one can find that the flutter frequency predicted by model (ii) monotonically decreases as U_R is increased. Moreover, when $U_R < 11.18$, model (ii) predicts higher flutter frequencies than model (i); but this relation is reversed when $U_R > 11.40$. It should be noted that all the results from here on are with the longitudinal displacement taken into account.

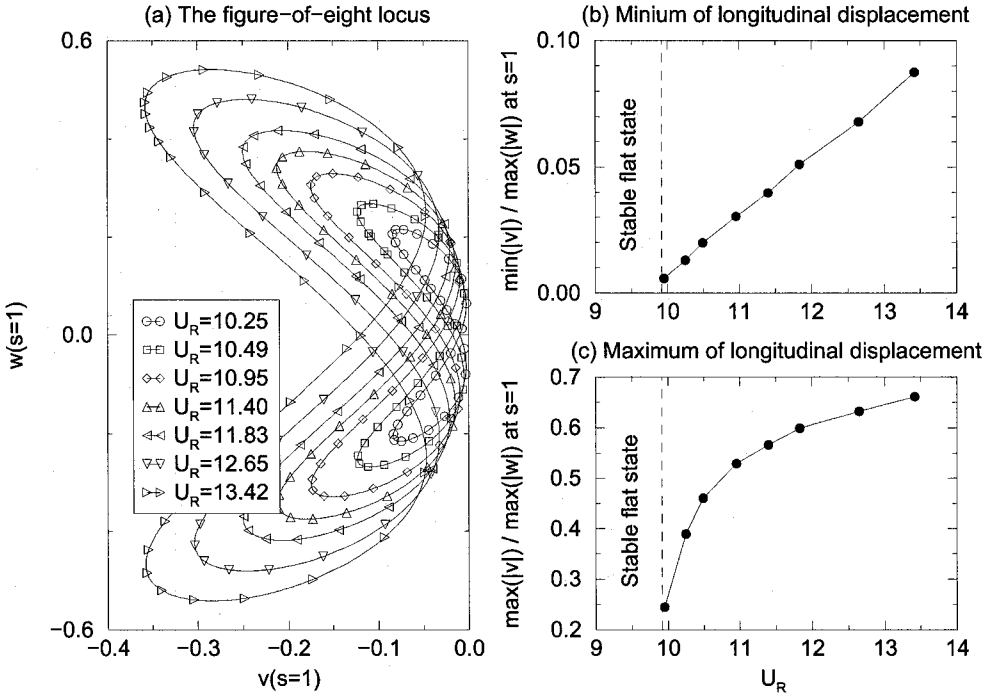

FIGURE 4.7. The relationship between the longitudinal and transverse displacements at various U_R. The parameters of the system used are $\mu = 0.2$, $l_0 = 0.01$, $\alpha = 0.004$ and $C_D = 0$.

The longitudinal displacements of the system at various U_R are studied in Fig. 4.7 in terms of the ratios of the minima and maxima of the longitudinal displacements at the trailing edge of the plate to the corresponding maxima of the transverse displacements, i.e., the values of $\min(|v(s=1)|)/\max(|w(s=1)|)$ and $\max(|v(s=1)|)/\max(|w(s=1)|)$, respectively. It can be seen in Figs. 4.7(b) and (c) that as U_R approaches the critical point U_{Rc}, both ratios become increasingly small. That is, the longitudinal displacements become less important in the system dynamics when

U_R is close to U_{Rc}; this observation may explain why the models with or without the consideration of the longitudinal displacements predict the same critical point.

4.3.2. The model of the vortical wake. The system dynamics has been studied using two wake models: (i) the model adopted by the present theory, and (ii) a refined model; results are presented in Fig. 4.8. In the present theory, the wake vortices are assumed to be shed off from the trailing edge of the plate and then move downstream with the undisturbed flow velocity. Obviously, in a better model of the vortical wake, i.e., model (ii), one can assume that the latest wake vortex, when it is shed off from the plate, has the same velocity as the trailing edge of the plate; and, the specific wake vortex will then move downstream with the local flow velocity, which is determined by the undisturbed flow velocity and the induced flow velocity by all the bound vortices as well as all the other wake vortices. It should be emphasized that considerable computational loads are involved in the calculation of the local flow velocity. For example, when the parameters used are $l_w = 40$, $\Delta\tau = 0.001$ and $U_R = 10.95$, the number of wake vortices can be approximately calculated as $N_W = l_w/U_R\Delta\tau = 3\,640$. Therefore, the calculation of the induced flow velocity by all the other wake vortices at the instantaneous location of the current wake vortex need 3 640 manipulations; and, 3 640 $\times$ 3 640 manipulations are required for all the wake vortices.

It can be seen in Figs. 4.8(a) through (d) that the system dynamics in terms of the time history and the vibration modes obtained using wake models (i) and (ii) are very close to each other. For example, the flutter amplitude and frequency predicted using wake model (i) are, respectively, 0.3294 and 2.7; the corresponding quantities when using wake model (ii) are, respectively, 0.3008 and 2.6. Moreover, it is found that these two wake models predicted the same critical point at $U_{Rc} = 9.92$. Therefore, it can reasonably be concluded that the performance of wake model (i) is equivalent to wake model (ii), although the former is a considerably simplified version of the latter. It should be noted that all the results from here on are obtained with wake model (i).

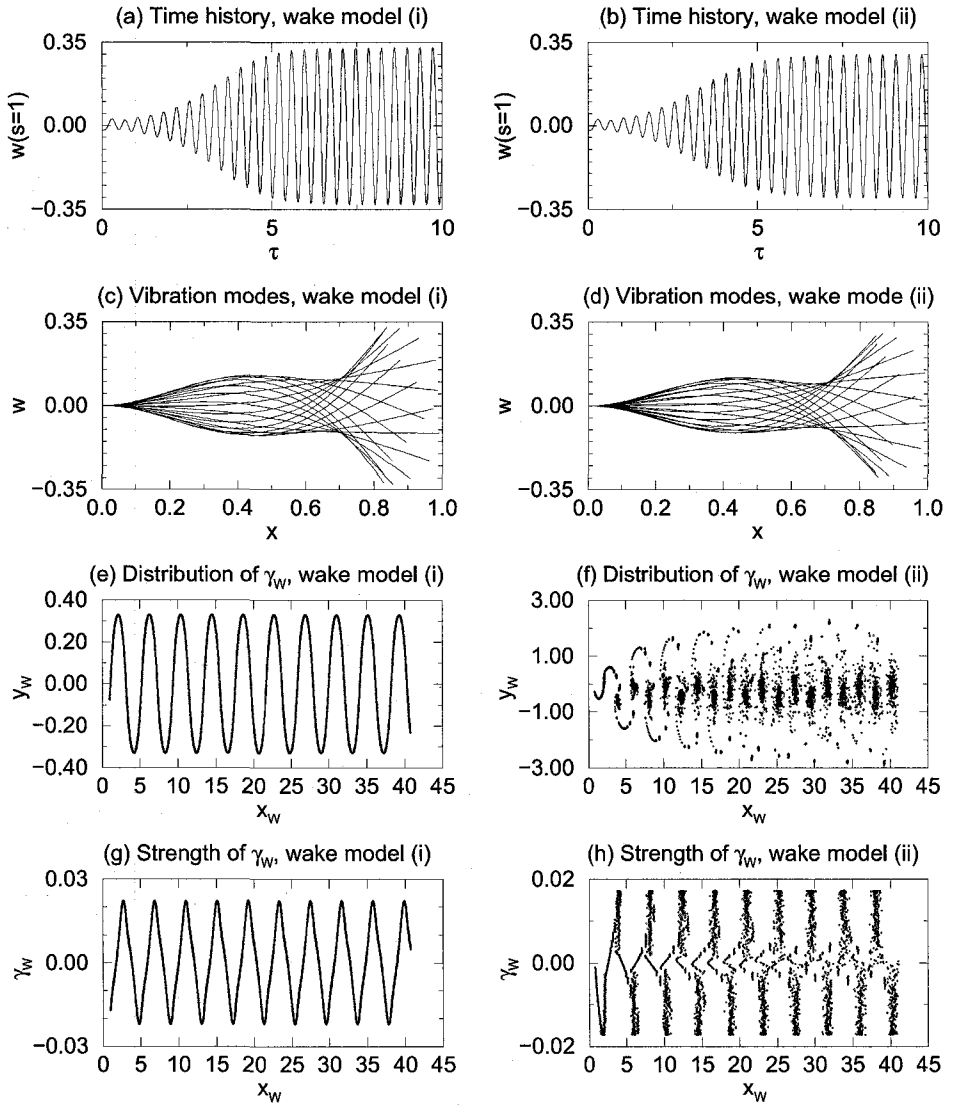

FIGURE 4.8. The system dynamics obtained using two wake models: (i) the model adopted by the present theory, where all wake vortices are assumed to move downstream with the same velocity as the undisturbed fluid flow; (ii) the wake model where each individual wake vortex moves downstream with the local flow velocity. Note that the distributions and strengthes of the wake vortices are, respectively, presented in subfigures (e,f) and (g,h) for a specific time instant $\tau = 20$. The parameters of the system are $\mu = 0.2$, $U_R = 10.95$, $l_0 = 0.01$, $\alpha = 0.004$ and $C_D = 0$. The numerical parameters relating to the generation of the vortical wake used in the simulations are $\Delta\tau = 0.001$ and $l_W = 40$.

As shown in Figs. 4.8(e) and (g), when using wake mode (i), the vortical wake has a wavy form, not only in terms of the distribution but also in terms of the strength of individual wake vortices. When examining the wavy form of the vortical wake in conjunction with the vibrations of the plate, one can find that the wake

vortices generated by a single stroke of the plate are of the same sign, as observed in the experiments conducted by Zhang et al. (2000). When the wake model (ii) is considered, as shown in Figs. 4.8(f) and (h), the wavy form of the vortical wake is still visible, although it becomes less distinct due to the accumulation of wake vortices in some regions.

4.4. The influence of l_0, α and C_D

The effect of varying the length of the upstream rigid segment l_0 and the material damping coefficient α on the system dynamics is shown in Figs. 4.9 and 4.10.

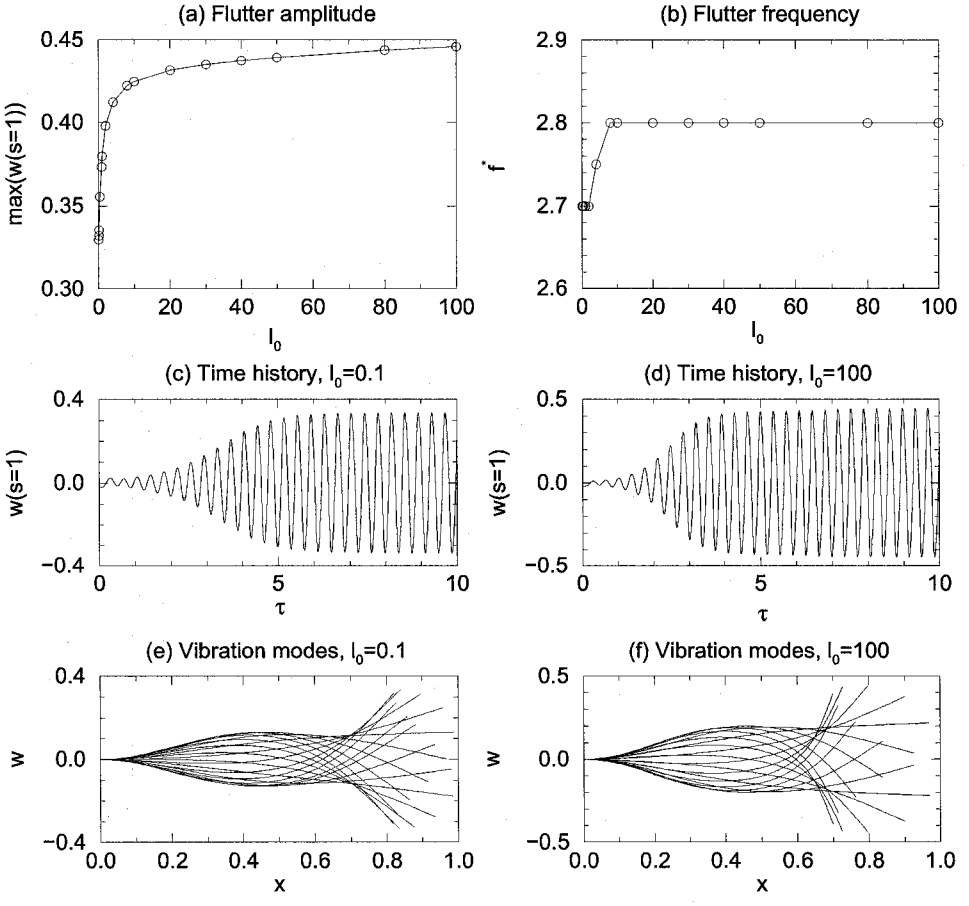

FIGURE 4.9. The influence of l_0 on the system dynamics. The other parameters of the system are $\mu = 0.2$, $U_R = 10.95$, $\alpha = 0.004$ and $C_D = 0$.

When the rigid segment is short, disturbances in the flow due to plate motion and the associated wake affect the flow upstream; i.e., the upstream flow cannot be treated as a steady uniform flow. As shown in Fig. 4.9(a), when l_0 is small, say $l_0 < 5$,

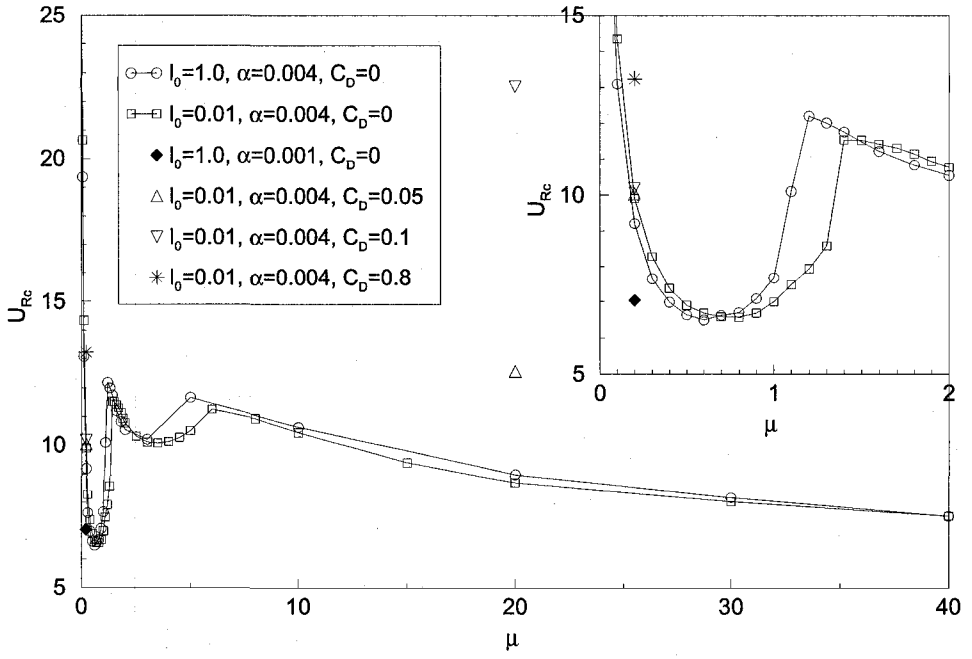

FIGURE 4.10. The influence of l_0, α and C_D on the critical point U_{Rc} at various values of mass ratio μ.

significant changes occur in the flutter amplitude with small variations of l_0. However, it can be seen in Figs. 4.9(b) through (f) that, excepting the flutter amplitudes, the other aspects of the post-critical behaviour of the system (i.e., the flutter frequency, the time history and the modes) are not sensitive to the variations in l_0.

The critical point U_{Rc} also depends on the value of l_0. In particular, as shown in Fig. 4.10 for the case $\mu = 0.2$, $U_{Rc} = 9.20$ when $l_0 = 1.0$; while $U_{Rc} = 9.92$ when $l_0 = 0.01$. When l_0 is sufficiently large, the dependence of the system dynamics on it becomes unimportant; eventually, the dynamics converges to that of the case $l_0 = \infty$. It is also found that the influence of l_0 on the system dynamics becomes less important when the mass ratio μ is large, as shown in Fig. 4.10. For example, for the case $\mu = 20.0$, $U_{Rc} = 8.71$ when $l_0 = 0.01$; while, $U_{Rc} = 8.89$ when $l_0 = 1.0$. It should be emphasized that the dependence of the system dynamics on the mass ratio μ exhibits a rather complicated pattern. For a specific case of μ, the critical point U_{Rc} may either increase or decrease as the value of l_0 become larger. For example, it can be observed in Fig. 4.10 that the critical point U_{Rc} of the case $l_0 = 1.0$ is higher than the case $l_0 = 0.01$ in the ranges $0.7 < \mu < 1.5$ and $\mu > 3.0$; while, in the other ranges of μ, a longer rigid segment l_0 results in a lower critical point U_{Rc}.

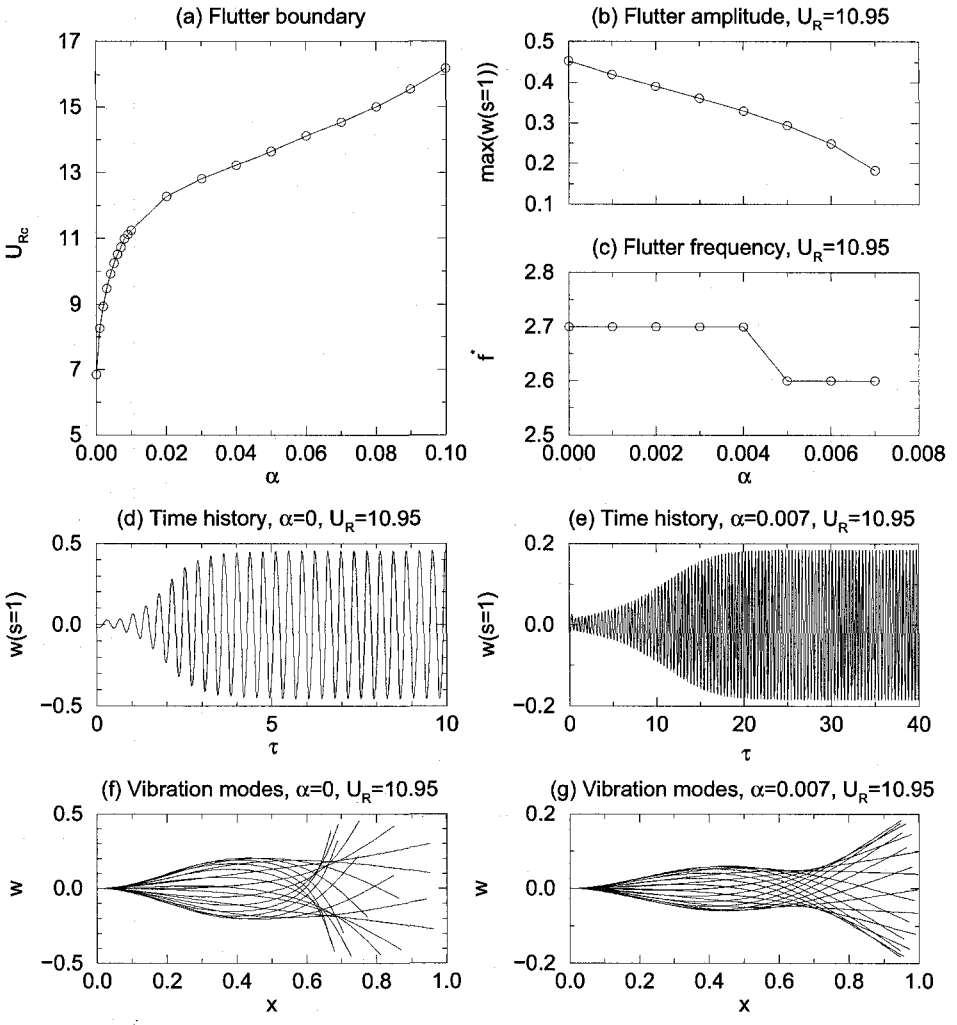

FIGURE 4.11. The influence of α on the system dynamics. The other parameters of the system are $\mu = 0.2$, $l_0 = 0.01$ and $C_D = 0$.

As shown in Fig. 4.11(a), the system becomes more stable with increasing value of material damping α; for example, $U_{Rc} = 8.26$ and 9.92 when $\alpha = 0.001$ and $\alpha = 0.004$, respectively. At a fixed value of U_R beyond the critical point U_{Rc}, it can be seen in Fig. 4.11(b) that the flutter amplitude decreases as α increases. However, one can see in Figs. 4.11(c) through (g) that the post-critical dynamics of the system (the flutter frequency, the time history and the vibration modes) with different values of α is qualitatively the same.

When taking into account the viscous drag C_D, as shown in Fig. 4.12(a), the system becomes more stable and the flutter amplitude decreases with increasing C_D at a fixed value of U_R beyond the critical point U_{Rc}. It was measured in the experiments

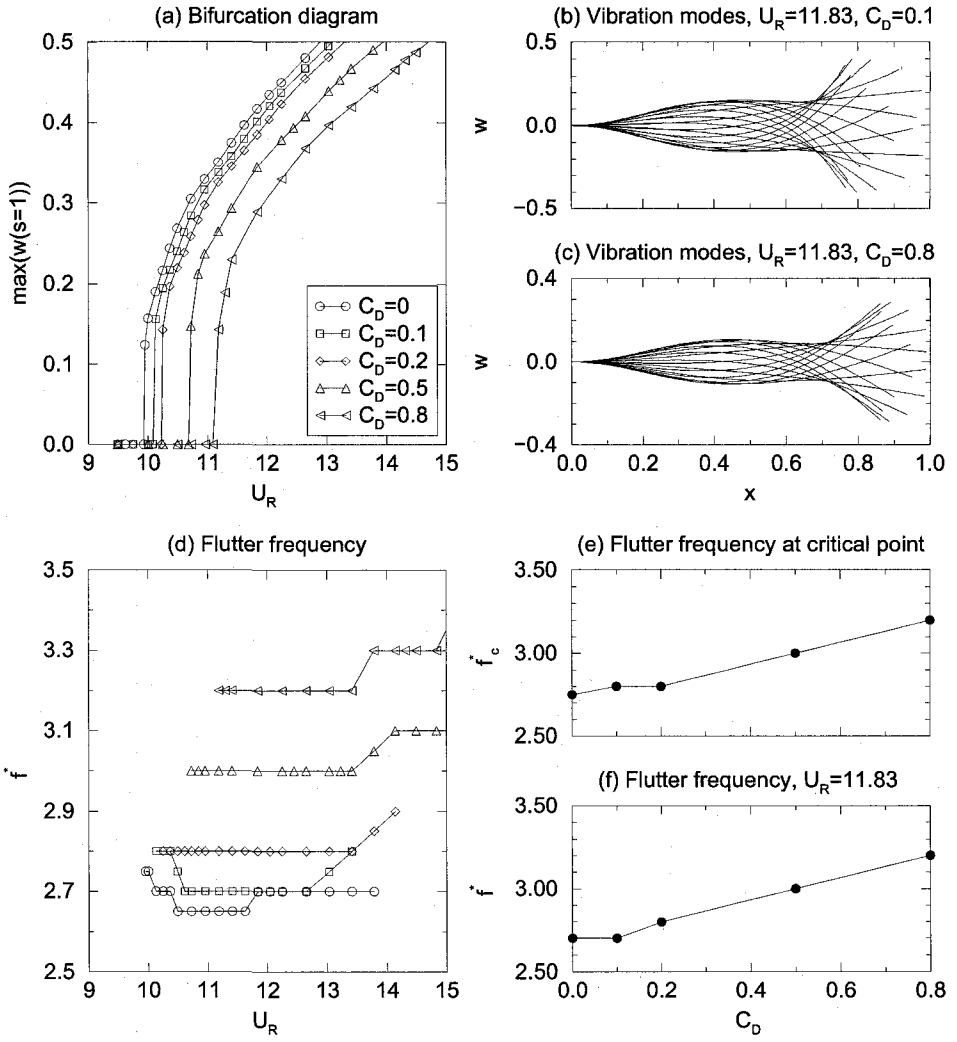

FIGURE 4.12. The influence of C_D on the system dynamics. The other parameters of the system are $\mu = 0.2$, $l_0 = 0.01$ and $\alpha = 0.004$.

conducted by Taneda (1968) that the value of the *total* aero/hydro-dynamic drag (i.e., the summation of the inviscid drag and the viscous drag defined in Eq. (2.24)), if evaluated in terms of an equivalent drag coefficient C_D, was about 0.07 before flutter took place and it jumped to about 1.0 at the critical point, but this very large jump was never explained (perhaps it involved also the resolved inviscid drag). Omitting the viscous drag will considerably underestimate the value of the critical point. In particular, one can obtain from Fig. 4.12(a) that $U_{Rc} = 9.92$ when $C_D = 0$; while $U_{Rc} = 11.08$ when $C_D = 0.8$. As shown in Figs. 4.12(b) and (c), at a fixed value of the reduced flow velocity $U_R = 11.83$, the vibration modes of the the two cases,

which have different values of viscous drag ($C_D = 0.1$ and 0.8, respectively), are quite similar.

Another important role of the viscous drag C_D, as shown in Fig. 4.12(d), is to increase the flutter frequency; this is expected, because the tension in the plate is related to the viscous drag C_D according to Eqs. (2.5) and (2.24). It is noticed that when a system is studied with a fixed value of C_D and when $C_D > 0.2$, the flutter frequency of the system monotonically increases with increasing U_R; this trend agrees with previous experimental observations (Taneda, 1968; Watanabe et al., 2002b; Tang et al., 2003; Shelley et al., 2005). However, when $C_D < 0.2$, this trend cannot be observed; see the curves for $C_D = 0$ and $C_D = 0.1$ in Fig. 4.12(d).

It has been shown in Figs. 4.9(b) and 4.11(c) that varying l_0 and α has little effect on the flutter frequency; but C_D does have a significant effect. As shown in Fig. 4.12(e), the flutter frequency at the critical point is $f_c^\star = 2.75$ when $C_D = 0$; it grows monotonically to $f_c^\star = 3.15$ when $C_D = 0.8$. Moreover, as shown in Fig. 4.12(f), the flutter frequency $f^\star$ at a fixed value of U_R beyond the critical point U_{Rc} also increases considerably with increasing C_D. However, it is noticed that, when C_D is fixed, the flutter frequency may be invariant or even decrease with increasing U_R, as shown in Fig. 4.11(d). This observation suggests that the value of C_D should be dependent on the flutter amplitude: the larger the U_R, the larger is the flutter amplitude (see Fig. 4.1(a)), and the larger the value of C_D.

In previous work, Blasius-type solutions have been used by Datta and Gottenberg (1975) and Yadykin et al. (2000) as a first approximation to the viscous drag ${F_D}^\star$ acting on the plate (White, 1991),

$$ {F_D}^\star = \begin{cases} 1.328\rho_F U^2 \mathrm{Re}_X^{-1/2} & \text{for a laminar boundary layer,} \\ 0.054\rho_F U^2 \mathrm{Re}_X^{-1/7} & \text{for a turbulent boundary layer,} \end{cases} \tag{4.1} $$

where the variable Reynolds number Re_X is defined by

$$ \mathrm{Re}_X = \mathrm{Re}\frac{L_0 + X}{L}. \tag{4.2} $$

In Eq. (4.2), Re is the Reynolds number defined with the length of the flexible plate L, i.e., $\mathrm{Re} = UL/\nu_F$, where ν_F is the kinematic viscosity of the fluid. Therefore, when taking into account $F_D{}^\star$ and setting $C_D = 0$, Eq. (2.24) becomes

$$f_{Di} = \Delta p_i \sin\alpha_i + \begin{cases} 1.328[\mathrm{Re}(l_0 + x_{Ci})]^{-1/2} & \text{for laminar boundary layer,} \\ 0.054[\mathrm{Re}(l_0 + x_{Ci})]^{-1/7} & \text{for turbulent boundary layer.} \end{cases} \tag{4.3}$$

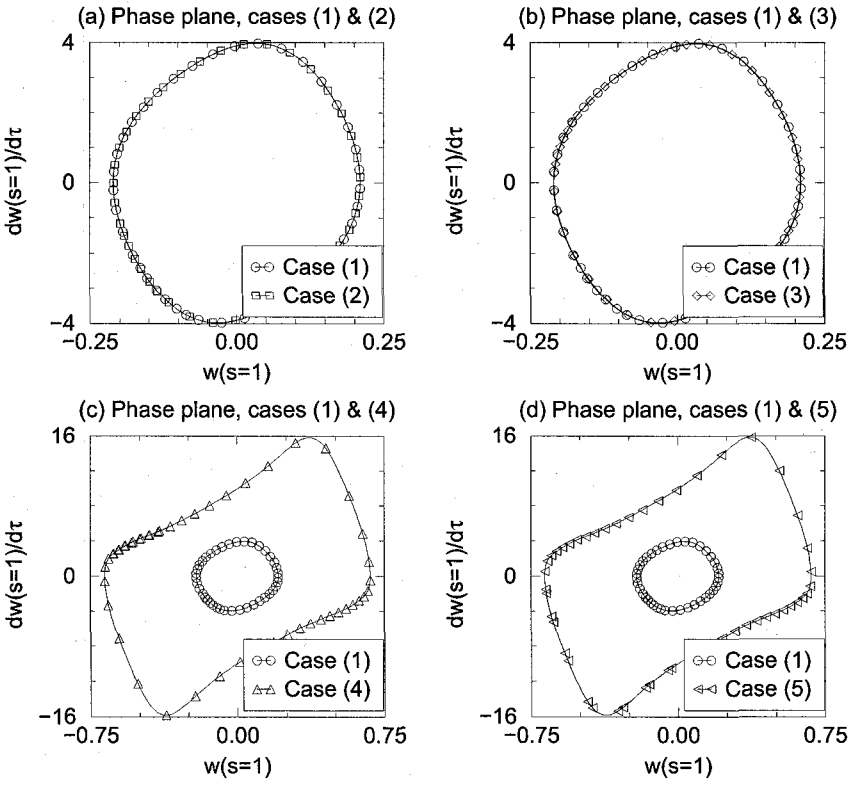

FIGURE 4.13. The influence of the viscous drag, modelled using the Blasius-type solutions, on the system dynamics. With $C_D = 0$, the drag considered is composed of: (i) the inviscid drag; (ii) the viscous drag modelled using the Blasius-type solution for the laminar boundary layer; and (iii) the viscous drag modelled using the Blasius-type solution for the turbulent boundary layer. The cases tested are as follows. Case (1): only (i) is considered; case (2): the summation of (i) and (ii) is considered; case (3): the summation of (i) and (iii) is considered; case (4): only (ii) is considered; and case (5): only (iii) is considered. The parameters of the system are $\mu = 0.2$, $U_R = 10.25$, $\alpha = 0.004$ and $l_0 = 0.01$. For the calculation of the viscous drag modelled using the Blasius-type solutions, $\mathrm{Re} = 5 \times 10^5$ is used (see Appendix C for the value of Re).

The influence of the viscous drag modelled using the Blasius-type solutions on the system dynamics is studied in Fig. 4.13. It can be seen in Figs. 4.13(a) and (b) that, with such a model, no matter whether the formula for the laminar boundary

layer or the turbulent boundary layer is used, the system dynamics is almost the same as without taking the viscous drag into account. On the other hand, as shown in Figs. 4.13(c) and (d), if one considers only the viscous drag (modelled using the Blasius-type solutions) but otherwise omits the inviscid drag, the system dynamics is significantly different. It is therefore concluded that the viscous drag modelled using the Blasius-type solutions according to Eq. (4.1) have negligible effects on the system dynamics, at lease for the modest value of μ in these calculations.

4.5. On the hysteresis phenomenon

Hysteresis phenomena have repeatedly been reported in previous experimental observations conducted by Zhang et al. (2000), Watanabe et al. (2002b), Tang et al. (2003) and Shelley et al. (2005). In general, it has been observed that flutter takes place in an abrupt manner: once the flow velocity reaches a critical point, vibration develops suddenly with a large amplitude. On the other hand, when the plate is already in vibration and the flow velocity is gradually reduced, the plate may return to rest at another critical point, lower than the former one. Therefore, a hysteresis loop is formed; i.e., the bifurcation leading to flutter is subcritical. This hysteresis phenomenon also implies that the dynamics depends on initial conditions; two stable states coexist between the lower and the upper critical points.

As already remarked, no existing theory is capable of predicting subcritical dynamic behaviour for the flow-induced flutter. Clearly, this must be due to either a systemic weakness in all the theoretical models, or because a particular aspect of all (or virtually all) experiments, is not taken into account in the theoretical models.

In all experiments, the plate is of course three-dimensional. Thus, the theoretical assumption that the flow is two-dimensional ignores all edge-effects, e.g. edge-vortices, the overall effect of which may not be negligible; there may indeed be a phase lag between their generation and the plate motion. Also, most of the aero/hydro-dynamics models employed are linear, and the observed hysteresis may be due to fluid nonlinearities. However, simulations using Navier-Stokes solvers (Watanabe et al., 2002a;

Balint and Lucey, 2005; Tetlow et al., 2006) have not shown any hysteresis effects either; still, this may have been insufficiently explored.

On the purely experimental side of things, it is noted that all experiments have been conducted in a wind or water tunnel; yet, the effect of confinement was not considered. Furthermore, this effect is not a straightforward blockage when the plate is fluttering. Recently, for the problem of vortex-induced vibrations of an oscillating cylinder (in cross flow), Prasanth et al. (2006) have shown that a blockage of 5% as compared to 1% has a profound effect on the dynamics - affecting lock-in and the existence of hysteresis; but both 1% and 5% are normally considered *small*! Clearly, this is not a static effect of increasing the effective flow velocity around the cylinder, but a more profound effect on the vortical dynamics. In the case of the plate, the amplitudes of motion are larger at the trailing edge than for the cylinder, and so also is the dynamic blockage; hence this effect could well be more pronounced. Another possibility is that, due to quasi-ubiquitous imperfections, spanwise bending would stiffen a plate in experiments prior to the onset of flutter, but such bending could be partly ironed out at post-critical flows, thus generating a hysteresis.

In the remarkable experiments conducted by Zhang et al. (2000), it has been observed that the onset of the flutter of a cantilevered plate in axial flow is accompanied by the evolution of the vortical wake from a von Kármán type to an undulating one. To demonstrate how a hysteresis might occur due to vortical effects, we have investigated (as a preliminary exercise) the effect of adding a steady von-Kármán-type vortex street to the undulating wake vortices shed at the trailing edge of the plate while in motion. As shown in Fig. 4.14, it is assumed that $\Gamma_V = UL$ for small motions (when $W(S = L)/L \leq 0.02$) and $\Gamma_V = 0$ for larger motions (when $W(S = L)/L > 0.02$), where Γ_V is the strength of a single von Kármán wake vortex. The geometry of the von Kármán wake street is set as $S_V/L = 0.1$ and $D_V/L = 0.02$ (refer to the experimental observations made by Taneda (1958) and Zhang et al. (2000)), where S_V is the distance between two successive vortices in the same row and D_V is the distance between either of the two vortex rows to the neutral plane. It should be mentioned that the distance between two successive von Kármán wake vortices S_V is normally

much larger than that of two successive vortices belonging to the undulating wake $U\Delta t$, as shown in Fig. 4.14. As the first vortex (the latest one) in the undulating wake street has a longitudinal clearance of $0.25U\Delta t$ to the trailing edge of the plate, the distance between the first vortex of the von Kármán wake street and the trailing edge of the plate is supposed to be $0.5S_{\mathrm{V}}$. Moreover, as the strength of each individual vortex in the undulating wake depends on the magnitudes of the deformations and velocities of the plate at the time instant when it was generated, the strengths of the vortices in the von Kármán wake street are assumed to be a fixed quantity $\Gamma_{\mathrm{V}} = UL$ (or in the nondimensional form $\gamma_{\mathrm{V}} = \Gamma_{\mathrm{V}}/(UL) = 1$) whenever the deformation of the plate is small; that is, when the amplitude of the plate vibrations is small, the von Kármán wake is dominant.

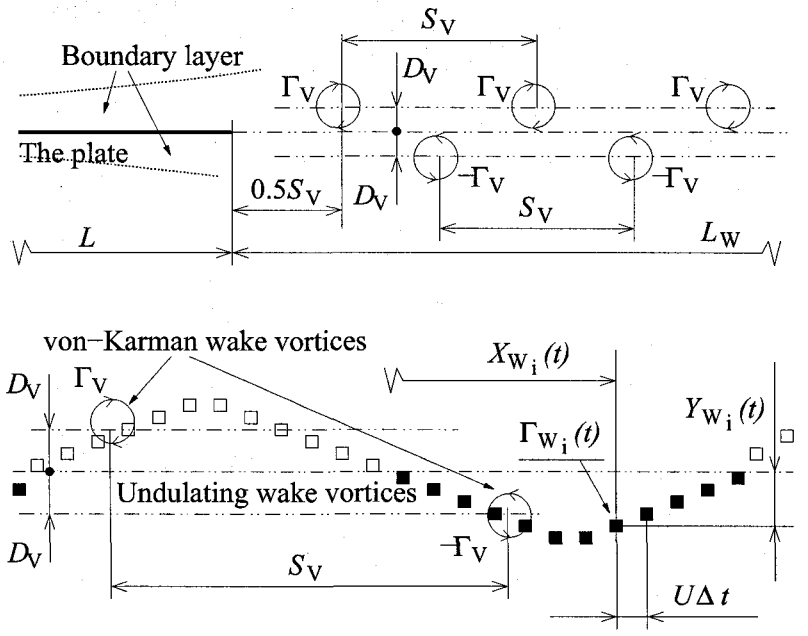

FIGURE 4.14. An illustration of the superposition of the von Kármán vortical wake street and the flutter wake street.

When superimposing the von Kármán wake street onto the undulating vortical wake, the dynamics of the system is shown in Fig. 4.15, demonstrating that a hysteresis may be obtained. It can be seen in Fig. 4.15(a) that, as compared to the results presented in Fig. 4.5, the system dynamics depend on the initial conditions when $9.92 < U_{\mathrm{R}} < 10.95$. When $U_{\mathrm{R}} < 9.92$, no matter what initial condition is used, the system is stable. When $9.92 < U_{\mathrm{R}} < 10.95$, as shown in Figs. 4.15(b) and (c) for the case $U_{\mathrm{R}} < 10.49$, when the initial disturbance imparted to the plate is relatively

large, flutter takes place; while, when a very small initial deformation of the plate is used for the simulation, the system is still stable. With further increasing U_R and when $U_R > 10.95$, the dependence of the system dynamics on the initial conditions disappears; although the transient may be different, as shown in Figs. 4.15(d) and (e), the properties of the obtained stable limit cycle oscillations using two different initial conditions are exactly the same.

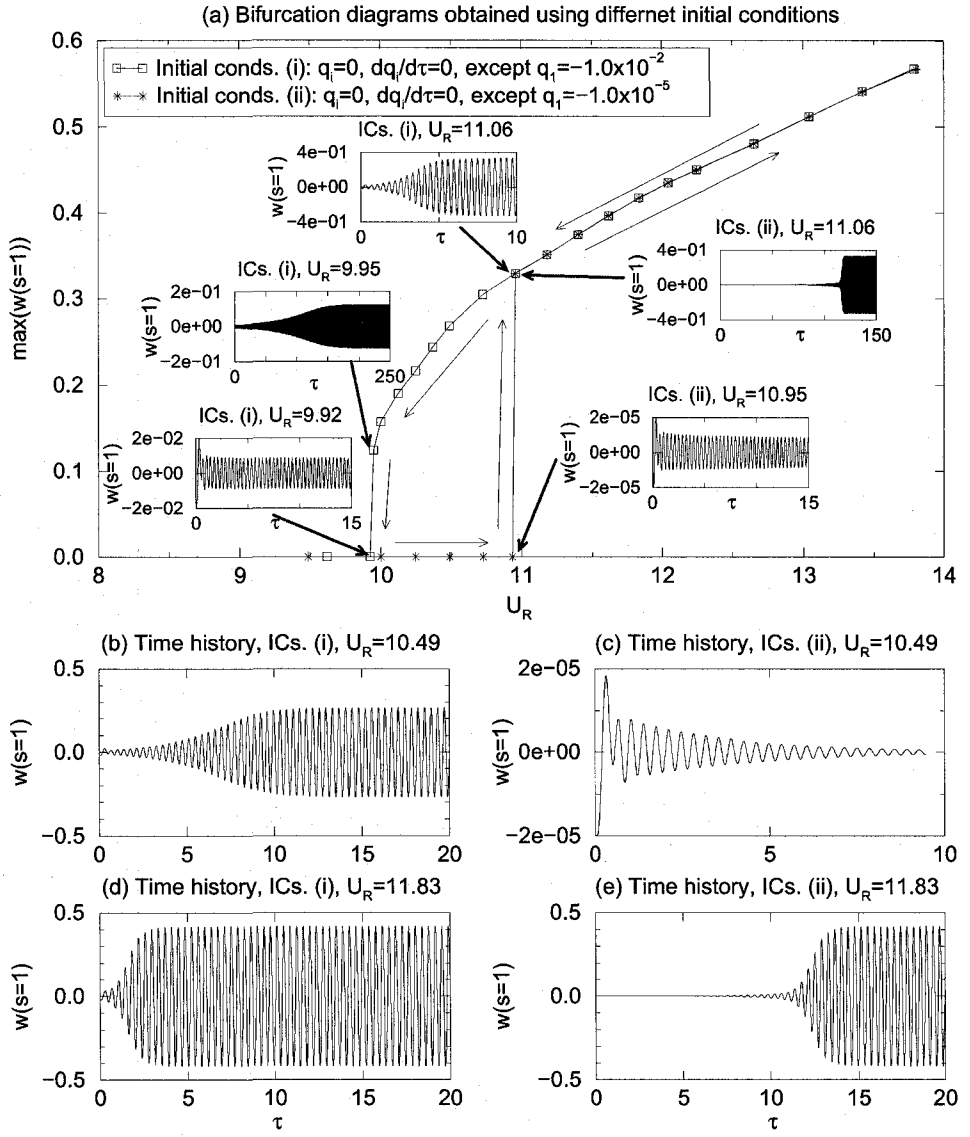

FIGURE 4.15. The bifurcation diagram of the system with the additional consideration of a von Kármán wake obtained using two different sets of initial conditions: (i) $q_1^0 = -1.0 \times 10^{-2}$; and (ii) $q_1^0 = -1.0 \times 10^{-5}$. The other parts of the initial conditions not specified are all zeros, i.e., $q_{i,i\neq 1}^0 = 0$ and $\dot{q}_i^0 = 0$. The other parameters of the system are $\mu = 0.2$, $l_0 = 0.01$, $\alpha = 0.004$ and $C_D = 0$.

It should be emphasized that the mechanism discussed here of superimposing a von Kármán wake street to the undulating vortical wake is non-physical, and only exploratory from the phenomenological point of view. In particular, both the vortex strength and the geometrical pattern used for the von Kármán wake street are arbitrarily determined and the evolution of the wake from the von-Kármán-type to the undulating-type cannot be accounted. However, it is very interesting to find the wake beyond the trailing edge of the plate has a profound effect indeed on the dynamics of the system, as has been observed in the experiments by Zhang et al. (2000).

4.6. Dynamics of the system with various μ

In Fig. 4.16, we examine the flutter boundary in terms of the mass ratio μ. The flutter boundaries predicted by other theories by Huang (1995), Guo and Païdoussis (2000), Yamaguchi et al. (2000b), Watanabe et al. (2002a), Shelley et al. (2005) and Argentina and Mahadevan (2005) for two-dimensional plates and by Eloy et al. (2007) for plates with the aspect ratio $\mathcal{R} = \infty$ (i.e., two-dimensional plates) as well as $\mathcal{R} = 1$, as well as the corresponding experimental data published by Kornecki et al. (1976), Huang (1995), Yamaguchi et al. (2000a), Watanabe et al. (2002b), Tang et al. (2003) and Souilliez et al. (2006) are all presented. One can see from Fig. 4.16 that, from a viewpoint of global dynamics of the system, the flutter boundary predicted by the present theory agrees very well with experimental measurements (excepting the abnormal data published by Watanabe et al. (2002b)). Moreover, further examination of Fig. 4.16 reveals that the present theory achieves better agreement with the experimental data than that achieved by other theories.

In Fig. 4.16, U_{R}/μ is used as the ordinate, which can be written as $U_{\mathrm{R}}/\mu = [(\rho_{\mathrm{P}}h)^{3/2}/(\rho_{\mathrm{F}}D^{1/2})]U$ (or, $U_{\mathrm{R}}/\mu = \left[{\rho_{\mathrm{P}}}^{3/2}{\rho_{\mathrm{F}}}^{-1}E^{-1/2}/\sqrt{12(1-\nu^2)}\right]U$ if the expression for D is substituted therein). Moreover, the mass ratio μ can be written as $[\rho_{\mathrm{F}}/(\rho_{\mathrm{P}}h)]L$. Therefore, Fig. 4.16 actually reveals the relation between the critical

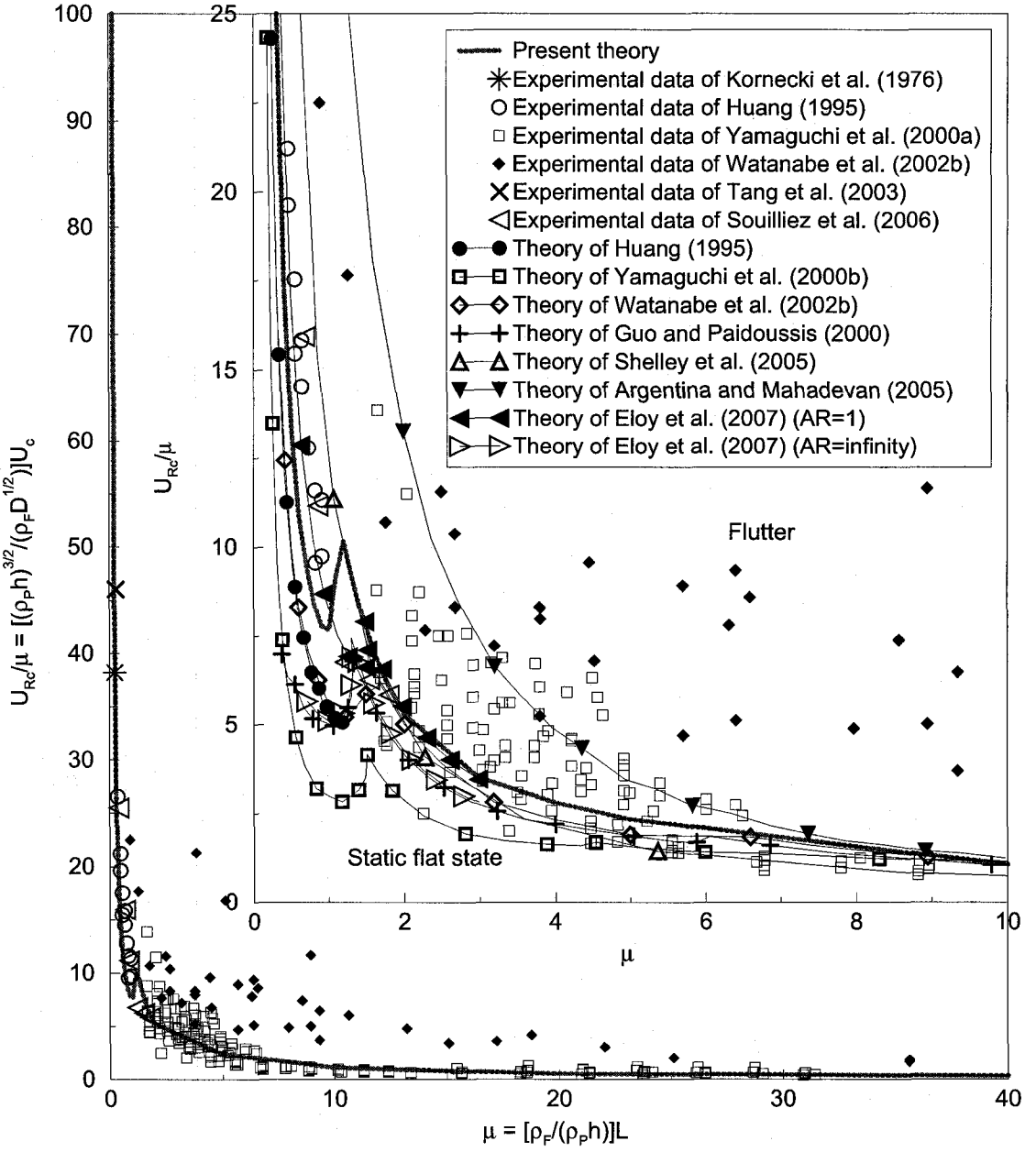

FIGURE 4.16. The flutter boundary of cantilevered flexible plates in axial flow: theoretical predictions and experimental measurements from various sources. Note that AR denotes the aspect ratio $\mathcal{A}$R. For the results obtained using the present theory, the parameters of the system are: $l_0 = 0.01$, $\alpha = 0.004$ and $C_D = 0$.

flow velocity U_c and the plate length L, the most controllable parameter in experiments, when the other physical parameters (ρ_P, ρ_F, h and D) of the fluid-structure system are fixed.

All the theoretical and experimental data presented in Fig. 4.16 clearly indicate the same trend for the flutter boundary: when the plate is short (say $\mu < 1$), U_c

is very sensitive to L; while, when the plate is sufficiently long (say $\mu > 4$), U_c is almost a constant, varying very gradually with changing L. In general, U_c decreases with increasing L. However, within the range $1.0 < \mu < 1.2$, there is a local rise and then subsidence in U_c as L increases; a subtle transition in the flutter mode shape occurs in this interval (refer to Figs. 4.18(c) and (d) to see the difference between the vibration modes when $\mu = 1.1$ and $\mu = 1.2$).

Another important observation that can be made in Fig. 4.16 is that the differences in the flutter boundaries obtained using various theories are quite large for short plates ($\mu < 1$). Gradually and monotonically, this difference is diminished as L is increased, and all theories converge towards one another for long plates ($\mu > 4$). The same phenomenon can also be observed regarding the agreement between experimental data (excepting those by Watanabe et al. (2002b)) and theoretical predictions. As for the large scatter in the experimental data shown in Fig. 4.16, we attribute this to the difficulty encountered in setting up the experiments. Moreover, the plates used in different experiments have different aspect ratios, different lengths of upstream rigid segment, different levels of material damping, and the experiments themselves have been carried out in different wind or water tunnels with different geometries; all these factors will cause variations in U_c. Nevertheless, it is very interesting to notice that most theoretical predictions are in better agreement with most experimental data when μ is large. This implies that all the possible factors mentioned above have much less influence on the stability of the system when the plate is long. For example, one can show that the vortical wake beyond the trailing edge of the plate indeed has less influence on system stability for long plates than it does for short plates; see Appendix D for details.

It should be emphasized that Fig. 4.16 reveals inherent properties of the global stability of cantilevered flexible plates in axial flow. Both the trend of a single flutter boundary and the relation between different ones (no matter whether they be theoretical or experimental) are neither distorted by scale factors in the axes used nor qualitatively changed by other factors that influence the system dynamics (i.e., the length of upstream rigid segment l_0, the material damping coefficient α and the

viscous drag coefficient C_D). The actual values of the scale factors $[\rho_F/(\rho_P h)]$ and $[(\rho_P h)^{3/2}/(\rho_F D^{1/2})]$ for the experimental data of Kornecki et al. (1976), Huang (1995), Tang et al. (2003) and Souilliez et al. (2006) are listed in Table 4.1; the absence of the other studies (Yamaguchi et al., 2000a; Watanabe et al., 2002b) from the Table is due to the lack of published information which would have enabled calculation of these scale factors. Although the scale factors for L and U_c may not always be close to unity nor be the same for individual experiments, it is easy to check that they will not qualitatively change the key properties of the flutter boundaries shown in Fig. 4.16.

TABLE 4.1. The values of $\rho_F/(\rho_P h)$ and $(\rho_P h)^{3/2}/(\rho_F D^{1/2})$ in various experiments

Experiments by	$\rho_P h$ (kg/m^2)	ρ_F (kg/m^3)	D (N $\cdot$ m)	$\rho_F/(\rho_P h)$ (m^{-1})	$\frac{(\rho_P h)^{3/2}}{\rho_F D^{1/2}}$ (s/m)
Kornecki et al. (1976)	1.343	1.226	8.47×10^{-1}	0.913	1.397
Huang (1995)	0.142	1.226	7.29×10^{-4}	8.634	1.616
Tang et al. (2003)	1.108	1.226	3.83×10^{-1}	1.107	1.50
Souilliez et al. (2006)	0.2	1.226	6.15×10^{-3}	6.31	0.93

It should be mentioned that Lemaitre et al. (2005) have recently also reported that U_c is insensitive to L for long plates, in their work on hanging plates in axial flow (i.e., with gravity in the positive X direction of Fig. 2.1); they attributed the observed trend to the axial tension caused by the distributed weight of the plate. However, for all the theoretical analyses and experiments presented in Fig. 4.16, both the plate and the upstream support are vertical (i.e., the gravity is in the negative Z direction of Fig. 2.1); therefore, the gravitational force needs not to be taken into account in these studies, and is hence neglected.

If, instead of U_{Rc}/μ one plots U_{Rc} versus μ (refer to Fig. 4.10), neither the global trend for a single flutter boundary nor the correlation between different ones as described in the foregoing would be discernible. Therefore, a discussion of the global properties of a flutter boundary has to be conducted in terms of dimensional parameters U_c and L in a U_{Rc}/μ versus μ plot. The scale factor $[\rho_F/(\rho_P h)]$ for different systems is not always the same, and a system with a larger μ does not necessarily correspond to a longer plate than another system with a smaller μ. However, for a

specific system of which the physical parameters ρ_P, h and ρ_F are fixed, μ is directly proportional to L. In particular, in light of the flutter boundary predicted by the present theory, one can consider that a plate is long when $\mu \geq 4$, and that it is a short one when $\mu \leq 1$.

Along the flutter boundary shown in Fig. 4.16, the flutter frequencies $f_c^\star$ at various values of μ have been obtained and presented in Fig. 4.17. Similar to Fig. 4.16, the purpose here is to reveal the relation between f_c and L when the other physical parameters (ρ_P, ρ_F, h and D) of the system are fixed; therefore, Fig. 4.17 uses $f_c^\star/\mu^2 = [(\rho_P h)^{5/2}/(\rho_F{}^2 D^{1/2})]f_c$ as ordinate, and μ is written as $[\rho_F/(\rho_P h)]L$. It can be seen in Fig. 4.17 that $f_c^\star$ has the same trend as U_c in Fig. 4.16: f_c is very sensitive to L for short plates, and it is almost invariant for long plates; f_c generally decreases as L increases, but there is a local rise and then subsidence for $1.0 < \mu < 1.2$. The experimental measurements of the frequencies at the flutter boundary made by Kornecki et al.

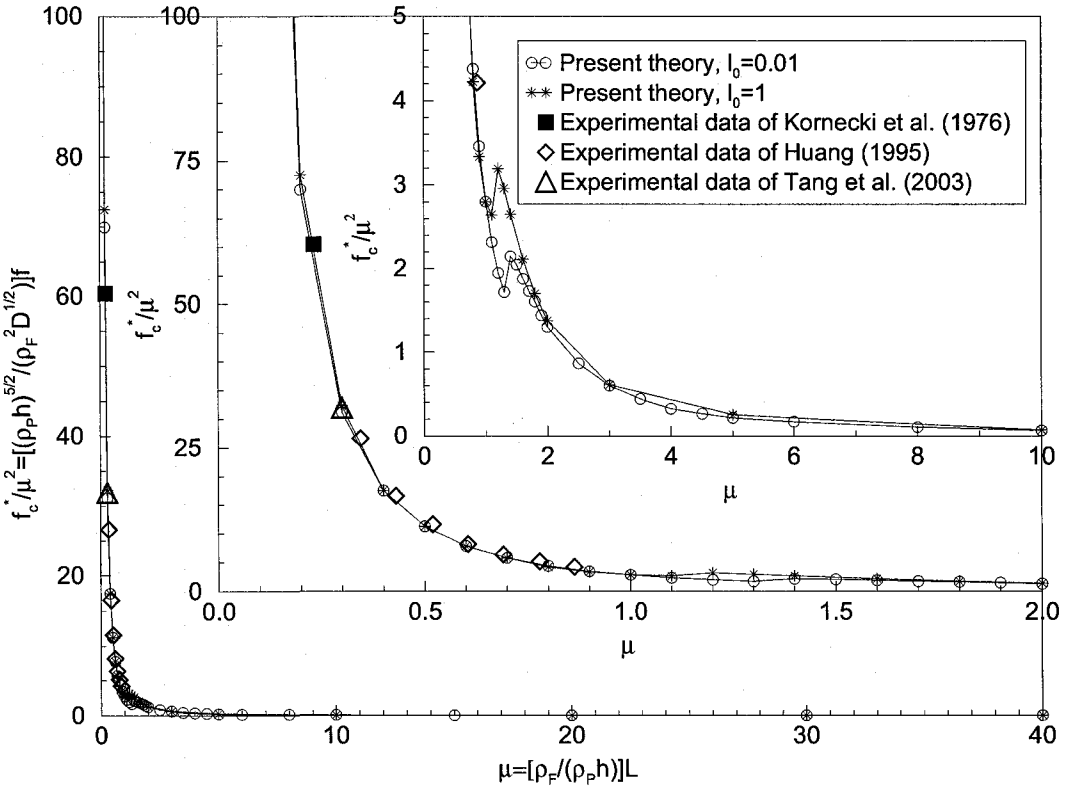

FIGURE 4.17. The flutter frequencies of the system along the boundary of instability in terms of mass ratio μ. The data obtained in the experiments by Kornecki et al. (1976), Huang (1995) and Tang et al. (2003) are also presented. The other parameters of the system are: $\alpha = 0.004$ and $C_D = 0$.

(1976), Huang (1995) and Tang et al. (2003) are also presented in Fig. 4.17; it can be seen that the present theory agrees with experimental observations, surprisingly perhaps, very well indeed. It should be noted that, due to the difference in the normalization methods used and the lack of exact values for the physical parameters of the system, the experimental results obtained by Yamaguchi et al. (2000a) and Watanabe et al. (2002b), as well as all the previous theoretical predictions for f_c, cannot be included in Fig. 4.17.

Vibration modes of the system with different values of μ, obtained at the corresponding critical points U_{Rc}, are shown in Fig. 4.18. It is seen that, for a fixed μ, the vibration modes of the system at different post-critical flow velocities are qualitatively similar, although the vibration amplitude and some other aspects (for example, the location and girth of the quasi-node) may vary. As already shown in Fig. 3.5 for the purposes of validation of the present theory, when comparing these vibration modes

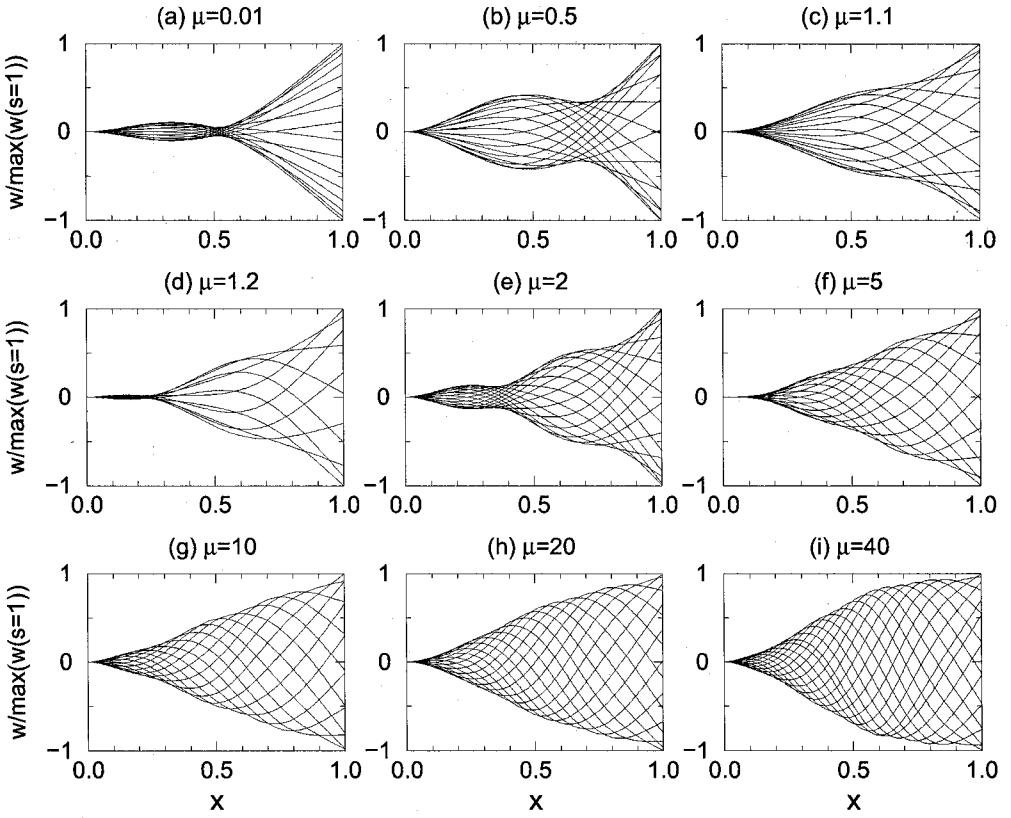

FIGURE 4.18. Vibration modes of the system with different values of mass ratio μ obtained at the corresponding critical points U_{Rc}. The other parameters of the system are $l_0 = 0.01$, $\alpha = 0.004$ and $C_D = 0$.

with the experimental observations by Tang et al. (2003) for $\mu = 0.30$, by Souilliez et al. (2006) for $\mu = 0.68$ and $\mu = 1.8$, and by Watanabe et al. (2002b) for $\mu = 2.7$ and $\mu = 35.7$, good agreement is found. It can be seen from Fig. 4.18 that, as μ increases more and more, higher-order beam modes participate in the dynamics and they become increasingly significant. It is also interesting to see that a pure first-mode flutter never happens for any value of μ; cf. Païdoussis (2004).

Chapter 5

The Dynamics of Modified Configurations

5.1. Introduction

In this chapter, the dynamics of cantilevered flexible plates in axial flow in various modified configurations is investigated. The results obtained may be regarded as addenda to the dynamics of the basic system (i.e., the plain plate in a vertical configuration, as shown in Fig. 1.3(a)) extensively studied in the preceding chapters. When one considers modified configurations of the basic one, new system parameters are introduced; it is of interest to examine the effect of these parameters on the dynamics of the system, not only the onset of instability but also the post-critical behaviour. Moreover, as one can see in Chapter 6, some of the modified configurations of the system are closely related to the design of a flutter-mill discussed therein.

We first consider a plate in an arrangement such that the gravitational force must be taken into account; that is, for the system in either the horizontal configuration or hanging configuration, as shown in Figs. 1.3(b) and (c), respectively. Then, as all previous experiments of cantilevered flexible plates in axial flow were conducted in a wind tunnel or water channel, the presence of parallel solid walls on either side of the flexible plate is considered in the calculation of fluid loads acting on the plate, and the influence of the parallel solid walls on the dynamics of the system is investigated. Also, if an additional linear or nonlinear spring support is installed on the cantilevered flexible plate, of variable spring stiffness and location along the

length of the plate, the dynamics of the system with this new feature is investigated. Similarly, the dynamics of the system with an additional concentrated mass of varying magnitude and at different locations along the length of the plate is also studied. Finally, we also investigate the case where there exists a small oscillating component in the undisturbed flow, in particular a small oscillating angle of incidence with respect to the leading edge of the cantilevered plate; the influence of this oscillating component on the system dynamics is examined. The final modified system investigated is the case of two identical cantilevered flexible plates aligned parallel to each other in axial flow.

When a modified configuration of the system is under investigation, the effects of the new system parameters have to be studied together with those shared with the basic configuration, i.e., μ, U_{R}, l_0, α and C_{D}. It should be noted that we by no means intend to cover all the possible combinations of these parameters. Instead, the investigations carried out in this chapter focus on the influence of the new parameters (one at a time) on the system with, in most cases, a small value of mass ratio μ and a fixed reference set of l_0, α and C_{D}. The main reason for doing so is that, for a system with a large value of μ, the computational load is too heavy to obtain sufficient simulation results for meaningful analysis; besides, as one can see in Chapter 6, the design of a flutter-mill is more likely to be based on a system with a small mass ratio μ.

5.2. With gravity

The effect of gravitational forces should be taken into account when one examines the dynamics of a cantilevered flexible plate in axial flow in the horizontal or hanging configuration, as illustrated in Figs. 1.3(b) and (c), respectively. All realistic problems that have been modelled as cantilevered flexible plates in axial flow are actually in either the horizontal configuration (for example, the flexible control surface studied by De Breuker et al. (2006)) or the hanging configuration (for example, the human snoring problem studied by Huang (1995) and the paper flutter problem

studied by Watanabe et al. (2002b,a)); the vertical configuration is indeed a rather artificial case, which is deliberately adopted in both theoretical/experimental studies to simplify matters by eliminating the influence of the gravitational force.

No previous publications can be found for the horizontal configuration, although the importance of gravity is manifested in the design of a flexible control surface proposed by De Breuker et al. (2006). Taneda (1968), Datta and Gottenberg (1975), Aurégan and Depollier (1995) and Zhang et al. (2000) conducted experiments for systems in the hanging configuration; while Datta and Gottenberg (1975) and Aurégan and Depollier (1995) omitted the gravitational force in their theories, although they did compare the theoretical predictions to their own experimental observations. Yadykin et al. (2001) modelled the gravitational force in their theoretical work, but did not analyze its influence on the system dynamics. Hanging strips were experimentally/theoretically studied by Lemaitre et al. (2005); they found that the variation of the critical flow velocity becomes small when the plate (strip) is sufficiently long.

5.2.1. Equation of motion. In this thesis, we regard the horizontal and hanging configurations as modified cases of the basic configuration, i.e., the vertical configuration (see Fig. 1.3(a)). The gravitational force is, respectively, taken into account as an additional force component in the *lift* for the horizontal configuration, and in the *drag* direction for the hanging configuration. Therefore, the third line of Eq. (2.1) becomes

$$F_{\mathrm{L}} - W' F_{\mathrm{D}} + W'' \int_S^L F_{\mathrm{D}}\, dS - F_{\mathrm{G}} \tag{5.1}$$

for the horizontal configuration, and

$$F_{\mathrm{L}} - W'(F_{\mathrm{D}} + F_{\mathrm{G}}) + W'' \int_S^L (F_{\mathrm{D}} + F_{\mathrm{G}})\, dS \tag{5.2}$$

for the hanging configuration. In Eqs. (5.1) and (5.2), F_{G} is the distribution of the gravitational force along the length of the plate, and is defined by

$$F_{\mathrm{G}} = (\rho_{\mathrm{P}} - \rho_{\mathrm{F}}) h g, \tag{5.3}$$

where the buoyancy force of the fluid has been considered, and g is the gravitational acceleration.

Using the nondimensionalization scheme defined in conjunction with Eq. (2.6), Eqs. (5.1) and (5.2), the new versions of the third line of Eq. (2.7) become

$$\mu {U_{\mathrm{R}}}^2 \left(f_{\mathrm{L}} - w' f_{\mathrm{D}} + w'' \int_s^1 f_{\mathrm{D}}\, ds \right) - \gamma_{\mathrm{G}} \tag{5.4}$$

for the horizontal configuration, and

$$\mu {U_{\mathrm{R}}}^2 f_{\mathrm{L}} - w'(\mu {U_{\mathrm{R}}}^2 f_{\mathrm{D}} + \gamma_{\mathrm{G}}) + w'' \int_s^1 (\mu {U_{\mathrm{R}}}^2 f_{\mathrm{D}} + \gamma_{\mathrm{G}})\, ds \tag{5.5}$$

for the hanging configuration. In Eqs. (5.4) and (5.5), γ_{G} is the gravity parameter defined by

$$\gamma_{\mathrm{G}} = \frac{(\rho_{\mathrm{P}} - \rho_{\mathrm{F}}) h g L^3}{D} = \frac{12(1-\nu^2)(\rho_{\mathrm{P}} - \rho_{\mathrm{F}}) g L^3}{E h^2}, \tag{5.6}$$

which accounts for the ratio of the gravitational force to the restoring force of the plate.

TABLE 5.1. The mass ratio and gravity parameter of the system

L (m)	h (m)	$\mu = [\rho_F/(\rho_P h)]L$	$\gamma_{\mathrm{G}} = [(\rho_P - \rho_F)gh/D]L^3$
0.181	3.9×10^{-4}	0.2	0.1670
0.452	3.9×10^{-4}	0.5	2.610
1.81	3.9×10^{-4}	2	167.0
9.03	3.9×10^{-4}	10	2.088×10^4

To determine the value of the gravity parameter, the experiments conducted by Tang et al. (2003) are considered (see Appendix C for details); supposing that only the plate length L varies, one obtains the corresponding values of μ and γ_{G} as listed in Table 5.1. It should be noted that, when the parameters ρ_{P}, ρ_{F}, h and D of the system are fixed, the mass ratio μ is proportional to L; while, the gravity parameter γ_{G} is proportional to L^3.

5.2.2. Dynamics of the system in horizontal configuration. When the system is set up in the horizontal configuration, the influence of the gravitational force on the stability of the system is first examined using the parameters listed in

Table 5.1. It can be seen in Table 5.2 that the system in the horizontal configuration generally has a higher critical point $U_{\mathrm{Rc}}^{\star}$ than its counterpart U_{Rc} for the vertical configuration. Moreover, when the mass ratio μ is small (i.e., the plate is short), the gravity parameter γ_{G} is also small and thus the influence of the gravitational force is small. However, as the value of γ_{G} increases very quickly with increasing L, for systems with a relatively large value of μ (i.e., the plate is relatively long), the gravitational force has a significant effect on the system dynamics. For example, when $\mu = 2$, the values of the critical point of the system in the horizontal and vertical configurations are, respectively, $U_{\mathrm{Rc}}^{\star} = 11.88$ and $U_{\mathrm{Rc}} = 10.89$; the variation is as large as 9.09%.

TABLE 5.2. The influence of the gravitational force on the stability of the system in the horizontal configuration

μ	γ_{G}	$U_{\mathrm{Rc}}^{\star}$	U_{Rc}	$(U_{\mathrm{Rc}}^{\star} - U_{\mathrm{Rc}})/U_{\mathrm{Rc}}$
0.2	0.167	9.92	9.92	0%
0.5	2.610	6.95	6.91	0.58%
2	167.0	11.88	10.89	9.09%

When $\mu = 0.2$, the dynamics of the system in the horizontal configuration is studied in Fig. 5.1, where the gravity parameter used is $\gamma_{\mathrm{G}} = 2.5$ (considerably larger than $\gamma_{\mathrm{G}} = 0.167$ in Table 5.2). It can be seen in Figs. 5.1(a) and (b) that the plate is buckled, by the effect of gravity alone, when $U_{\mathrm{R}} = 0$; it remains buckled for all values of U_{R} until the onset of flutter. Note that, when U_{R} is close to zero, say $U_{\mathrm{R}} = 0.02$ as shown in Fig. 5.1(b), one actually obtains the static deflection of the cantilevered flexible plate without flow. It is found that the shape of the buckled plate is always of the first beam mode for this case. With increasing U_{R}, the amplitude of the static deflection decreases; that is, the plate is elevated by the aero/hydro-dynamic *lift*. Obviously, the buckled form of the plate is defined by the balance among the gravitational force, the restoring force and the aero/hydro-dynamic *lift* achieved for the buckled shape of the plate. As U_{R} is increased further, flutter takes place; the critical reduced flow velocity is $U_{\mathrm{Rc}}^{\star} = 9.98$, as obtained from Fig. 5.1(a), which is a little higher then $U_{\mathrm{Rc}} = 9.92$ for the vertical configuration. Moreover, it is interesting to find that the flutter occurs directly from the buckled state; a stable flat state

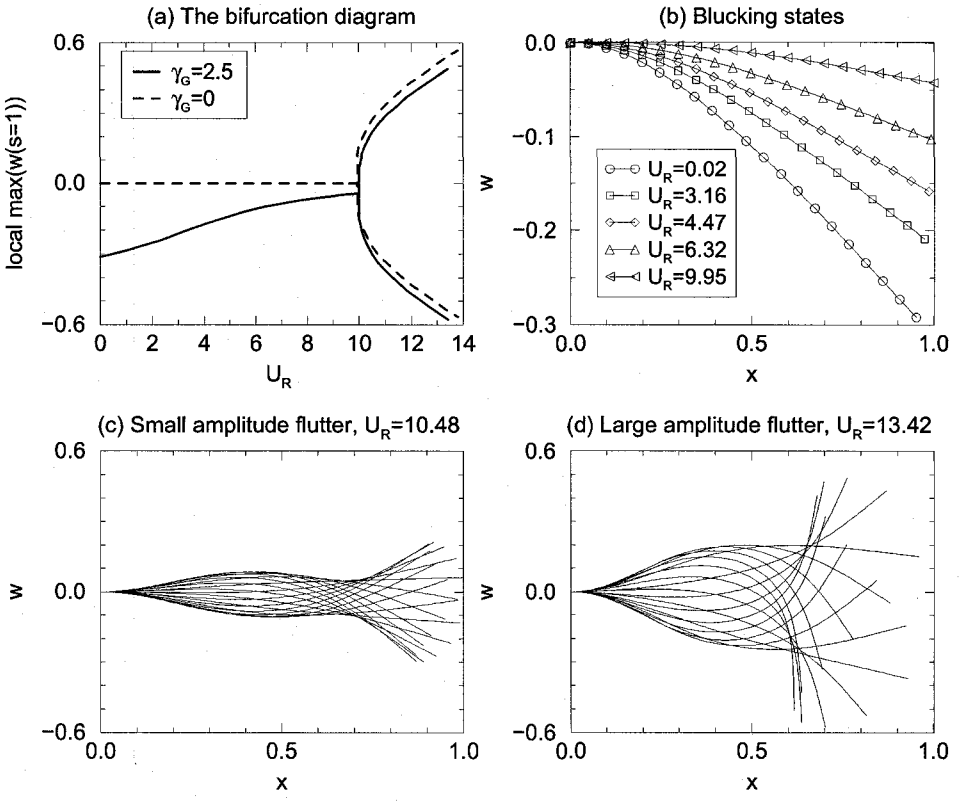

FIGURE 5.1. The dynamics of the system in the horizonal configuration. The other parameters are: $\mu = 0.2$, $l_0 = 0.01$, $\alpha = 0.004$, $C_D = 0$ and $\gamma_G = 2.5$.

does not occur. Finally, when U_R exceeds the critical point, the flutter amplitude increases with increasing U_R. Due to the influence of the gravitational force, the vibration modes of the system in the horizontal configuration are not symmetric with respect to the mean flow axis. However, for the case of a small μ investigated here, the gravity effect is rather small; and the vibration modes in Figs. 5.1(c) and (d) are very similar to those in Figs. 4.1(g) and (h).

As one can see in Table 5.1, the value of the gravity parameter γ_G (being proportional to L^3) increases very quickly as μ (being proportional to L) increases. The dynamics of the system in the horizontal configuration with $\mu = 2$ and $\gamma_G = 167$ are shown in Fig. 5.2. The dynamics of the system with large values of μ and γ_G are qualitatively similar to that shown in Fig. 5.2 for small values of μ and γ_G. From the bifurcation diagram shown in Fig. 5.2(a), the critical value of U_R in this case

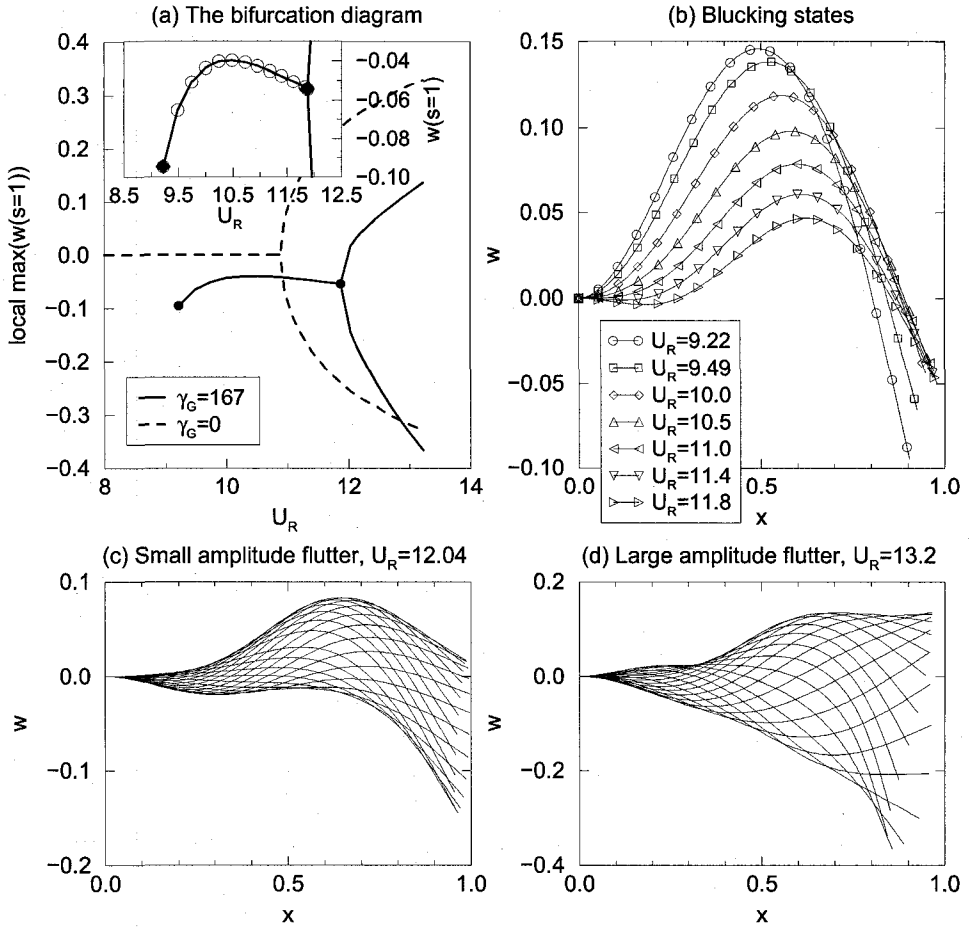

FIGURE 5.2. The dynamics of the system in the horizonal configuration. The other parameters are: $\mu = 2$, $l_0 = 0.01$, $\alpha = 0.004$, $C_D = 0$ and $\gamma_G = 167.0$.

is $U_{Rc}^{\star} = 11.88$, which is considerably larger than $U_{Rc} = 10.89$ for the vertical configuration. When $U_R > U_{Rc}^{\star}$, flutter takes place. As shown in Figs. 5.2, the flutter amplitude increases with increasing U_R, and the vibration modes of the system are strongly asymmetric. The buckled states of the plate for $U_R < U_{Rc}^{\star}$ are shown in Fig. 5.2(b). It is very interesting to see that, when U_R approaches to $U_{Rc}^{\star}$ from below, the plate is buckled in the second beam mode, in contrast to the case shown in Fig. 5.1(b) where the plate buckled with a predominantly first-beam-mode shape. Moreover, in this case also, the deflection of the plate is diminished with increasing U_R. But as the amplitude of the buckling decreases, its shape becomes more complex, with the appearance of a third-beam-mode component. Corresponding to this behaviour, in the bifurcation diagram of the amplitude of the plate tip versus U_R

in Fig. 5.2(a), the curve first goes up and then somewhat drops with increasing U_{R} before the onset of flutter.

It should be mentioned that, unlike the case shown in Fig. 5.1 for $\mu = 0.2$ and $\gamma_{\mathrm{G}} = 2.5$ where the static deflection of the plate as $U_{\mathrm{R}} \to 0$ can be obtained, for the case $\mu = 2$ and $\gamma_{\mathrm{G}} = 167$ shown in Fig. 5.2, the present theory fails when $U_{\mathrm{R}} < 8.94$. Moreover, the present theory does not work for the case $\mu = 10$ and $\gamma_{\mathrm{G}} = 2.088 \times 10^4$.

5.2.3. Dynamics of the system in the hanging configuration. When the system is set up in the hanging configuration, the effect of the gravitational force is equivalent to an additional *drag*. Again, the parameters listed in Table 5.1 are used to examine the influence of the gravitational force on the stability of the system in this configuration. The results are given in Table 5.3. It can be seen in Table 5.3 that the system in the hanging configuration generally has a higher critical point $U_{\mathrm{R_c}}^{\star}$ than its counterpart $U_{\mathrm{R_c}}$ for the vertical configuration. When μ is small, γ_{G} is also small and thus the influence of the gravitational force is small. While, for the system with a relatively large μ, the gravitational force has a significant effect on the system dynamics. For example, when $\mu = 2$, one obtains $U_{\mathrm{R_c}}^{\star} = 15.66$, and the difference between $U_{\mathrm{R_c}}^{\star}$ and $U_{\mathrm{R_c}}$ is large (43.8%).

TABLE 5.3. The influence of the gravitational force on the stability of the system in the hanging configuration

μ	γ_{G}	$U_{\mathrm{R_c}}^{\star}$	$U_{\mathrm{R_c}}$	$(U_{\mathrm{R_c}}^{\star} - U_{\mathrm{R_c}})/U_{\mathrm{R_c}}$
0.2	0.1670	9.93	9.92	0.202%
0.5	2.610	7.01	6.91	1.45%
2	167.0	15.66	10.89	43.8%

The influence of the gravitational force on the post-critical dynamics of the system in the hanging configuration is further studied in Figs. 5.3 and 5.4 for the two cases: $\mu = 0.2$ and $\gamma_{\mathrm{G}} = 2.5$; and, $\mu = 2$ and $\gamma_{\mathrm{G}} = 167$. It can be found in Fig. 5.3 that when the values of μ and γ_{G} are small, the influence of the gravitational force is also small (as compared to the dynamics of the system in the vertical configuration shown in Fig. 4.1); while, as shown in Fig. 5.4, the effect is quite significant (as compared to Fig. 4.3) for the system with large values of μ and γ_{G}. Moreover, for a system in

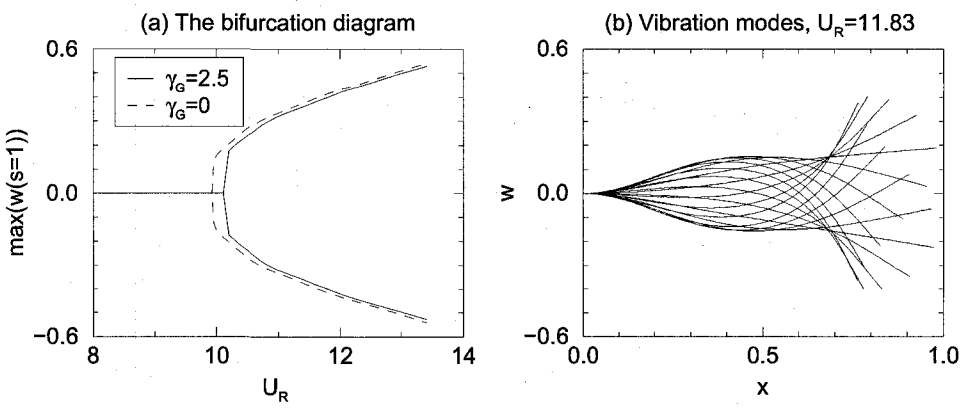

FIGURE 5.3. The dynamics of the system in the hanging configuration. The other parameters are: $\mu = 0.2$, $l_0 = 0.01$, $\alpha = 0.004$, $C_D = 0$ and $\gamma_G = 2.5$.

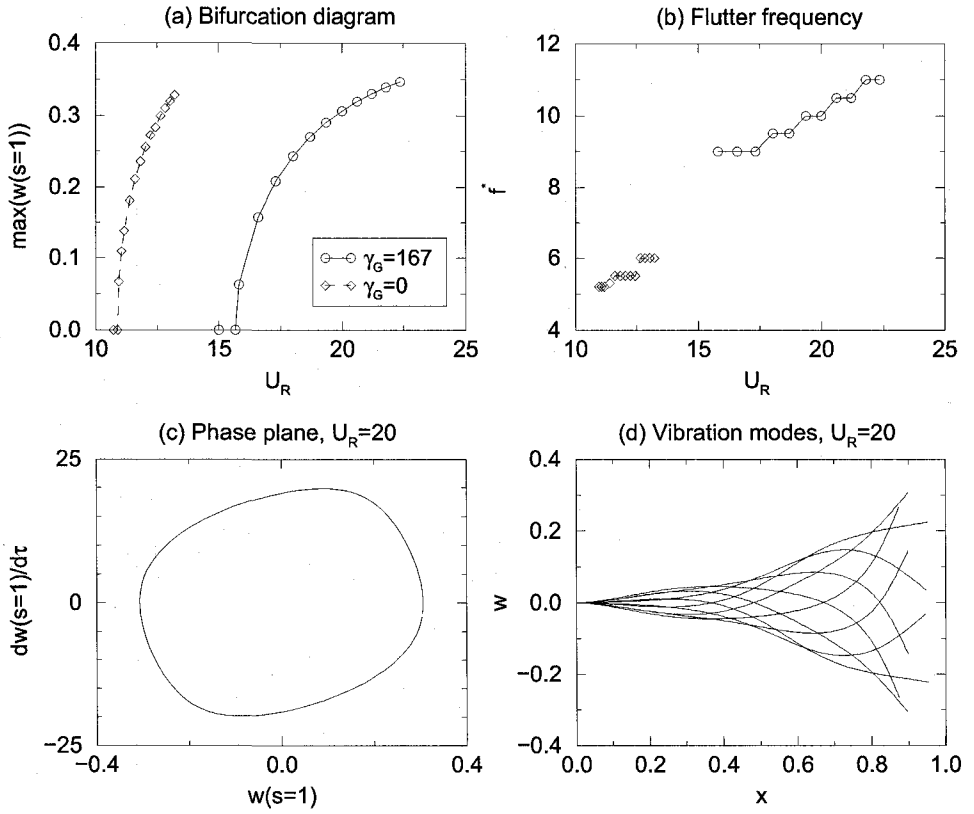

FIGURE 5.4. The dynamics of the system in the hanging configuration. The other parameters are: $\mu = 2$, $l_0 = 0.01$, $\alpha = 0.004$, $C_D = 0$ and $\gamma_G = 167$.

the hanging configuration, since the gravitational force contributes to the total drag acting on the plate and thus always increases the tension in the plate, one can expect the system in the hanging configuration to have higher flutter frequencies than its counterpart in the vertical configuration, as shown in Fig. 5.4(b).

5.3. With parallel solid walls

All previous experiments with cantilevered flexible plates in axial flow (Taneda, 1968; Datta and Gottenberg, 1975; Kornecki et al., 1976; Huang, 1995; Aurégan and Depollier, 1995; Yamaguchi et al., 2000a; Zhang et al., 2000; Watanabe et al., 2002b; Tang et al., 2003; Shelley et al., 2005; Lemaitre et al., 2005; Souilliez et al., 2006) were conducted in a wind tunnel or water channel. The presence of the parallel solid tunnel/channel walls of course affects the dynamics of the system; and this influence depends on the the distances between the upper/lower walls to the neutral plane of the plate, i.e., H_1 and H_2 as shown in Fig. 5.5. The effect of the parallel solid walls was usually neglected in previous theoretical studies (Datta and Gottenberg, 1975; Kornecki et al., 1976; Shayo, 1980; Huang, 1995; Yamaguchi et al., 2000b; Yadykin et al., 2001; Watanabe et al., 2002a; Tang et al., 2003; Attar et al., 2003; Argentina and Mahadevan, 2005; Shelley et al., 2005; Lemaitre et al., 2005; De Breuker et al., 2006; Eloy et al., 2007) except in the work by Aurégan and Depollier (1995) who assumed conservation of mass for the fluid flow between the plate and a channel wall, Guo and Païdoussis (2000) who analyzed the system on the basis of a direct solution of the axial channel flow, Wu and Kaneko (2005) with a leakage flow model, Balint and Lucey (2005) and Tetlow et al. (2006) who utilized Navier-Stokes solvers for the viscous channel flow, and Howell et al. (2006) who adopted the boundary-element method taking into account the parallel solid walls.

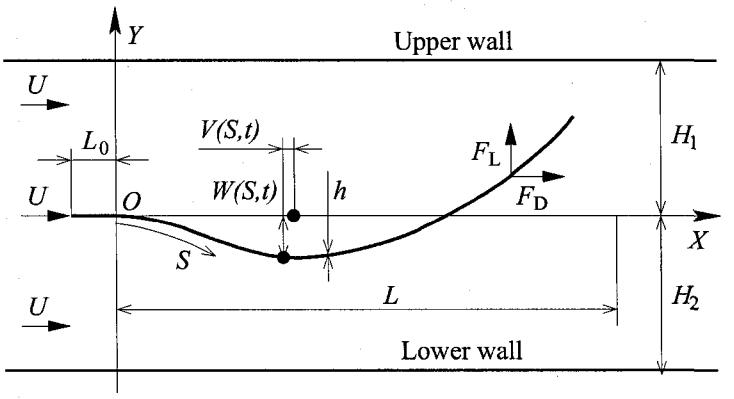

FIGURE 5.5. A cantilevered flexible plate in axial channel flow.

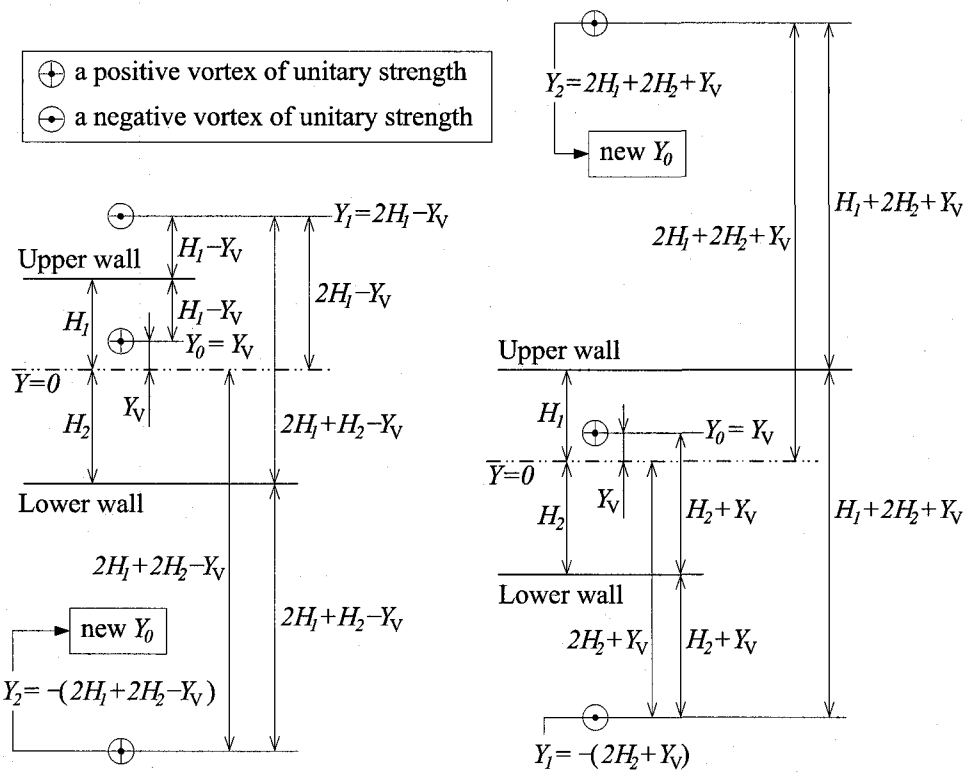

(a) The upward mirroring process. (b) The downward mirroring process.

FIGURE 5.6. A schematic diagram of the mirroring process.

5.3.1. Modelling and solution method. In this thesis, we incorporate the parallel solid walls into the basic configuration of the system, i.e., the vertical configuration shown in Fig. 1.3(a), using the mirroring process (Mateescu, 1995), as illustrated in Fig. 5.6. Regarding the lumped-vortex method and the associated wake model discussed in Chapter 2, when a parallel solid wall is present, each individual original bound/wake vortex should be considered together with its mirror images. As shown in Fig. 5.6(a), taking the upward mirroring process for example, when a vortex of unit strength is located at $Y_0 = Y_V$, the first mirror image with respect to the upper wall will be located at $Y_1 = 2H_1 - Y_V$, and this mirror vortex itself will have a mirror image with respect to the lower wall at $Y_2 = -(2H_1 + 2H_2 - Y_V)$; the strengths of the first and second images are, respectively, -1 and 1. Therefore, the mirror image at Y_2 can be treated as a new original vortex; and further levels of the upward mirroring process can be continued. Taking into account the original vortex and its images obtained through both the upward and downward mirroring processes, the influence coefficient defined by Eq.(2.18) becomes

$$
\begin{aligned}
\alpha_{ij} = & \frac{(y_{Ci}-y_{Vj})\sin\alpha_i+(-x_{Ci}+x_{Vj})\cos\alpha_i}{2\pi\left[(y_{Ci}-y_{Vj})^2+(x_{Ci}-x_{Vj})^2\right]} \\
& - \sum_{k=1}^{N_M}\frac{\left\{y_{Ci}-\left[2h_1+2(k-1)(h_1+h_2)-y_{Vj}\right]\right\}\sin\alpha_i+(-x_{Ci}+x_{Vj})\cos\alpha_i}{2\pi\left\{\left\{y_{Ci}-\left[2h_1+2(k-1)(h_1+h_2)-y_{Vj}\right]\right\}^2+(x_{Ci}-x_{Vj})^2\right\}} \\
& + \sum_{k=1}^{N_M}\frac{\left\{y_{Ci}+\left[2k(h_1+h_2)-y_{Vj}\right]\right\}\sin\alpha_i+(-x_{Ci}+x_{Vj})\cos\alpha_i}{2\pi\left\{\left\{y_{Ci}+\left[2k(h_1+h_2)-y_{Vj}\right]\right\}^2+(x_{Ci}-x_{Vj})^2\right\}} \\
& - \sum_{k=1}^{N_M}\frac{\left\{y_{Ci}+\left[2h_2+2(k-1)(h_1+h_2)+y_{Vj}\right]\right\}\sin\alpha_i+(-x_{Ci}+x_{Vj})\cos\alpha_i}{2\pi\left\{\left\{y_{Ci}+\left[2h_2+2(k-1)(h_1+h_2)+y_{Vj}\right]\right\}^2+(x_{Ci}-x_{Vj})^2\right\}} \\
& + \sum_{k=1}^{N_M}\frac{\left\{y_{Ci}-\left[2k(h_1+h_2)+y_{Vj}\right]\right\}\sin\alpha_i+(-x_{Ci}+x_{Vj})\cos\alpha_i}{2\pi\left\{\left\{y_{Ci}-\left[2k(h_1+h_2)+y_{Vj}\right]\right\}^2+(x_{Ci}-x_{Vj})^2\right\}},
\end{aligned}
\tag{5.7}
$$

where N_M is the number of levels of mirroring process, and $h_1 = H_1/L$ and $h_2 = H_2/L$ are, respectively, the nondimensional distances of the upper/lower parallel solid walls to the neutral plane of the plate, normalized using the length of the flexible plate L.

A new numerical parameter N_M has been introduced in Eq. (5.7); the convergence tests with respect to this parameter are shown in Fig. 5.7. The convergent value of N_M depends on the values of h_1 and h_2. As shown in Fig. 5.7, when $h_1 = h_2 \geq 5$, $N_M = 2$ can be used to get good convergent simulation results; while $N_M = 10$ and $N_M = 40$ should be used, respectively, for $h_1 = h_2 = 2$ and $h_1 = h_2 = 1$. It should be noted that the dependence of the convergent value of N_M on the values of h_1 and h_2 is actually determined by the distances of the bound/wake vortices to the parallel walls. That is, when the amplitude of the plate vibration is large and the bound/wake vortices approach one of the two solid walls, a larger value should be considered for N_M. On the other hand, when the plate is studied at the flutter boundary where the vibration amplitude is small, the convergent values of N_M mentioned above become safer.

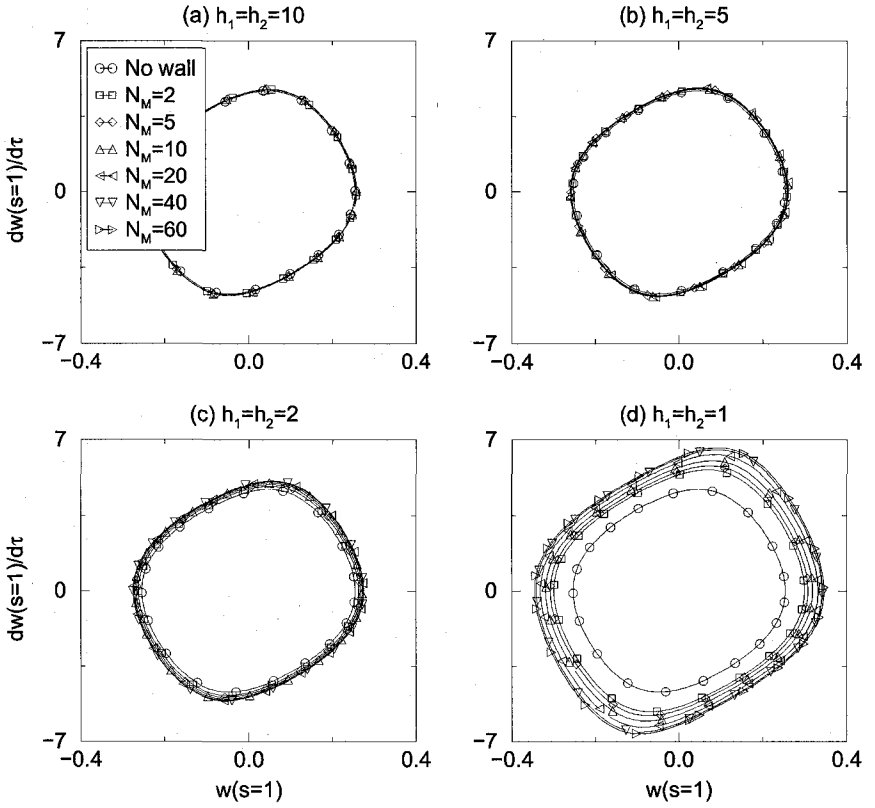

FIGURE 5.7. Convergence tests of the number of levels of mirroring process N_{M} for various h_1 and h_2. It is assumed that $h_1 = h_2$. The other parameters are: $\mu = 0.2$, $U_{\mathrm{R}} = 10.95$, $l_0 = 0.01$, $\alpha = 0.004$, and $C_{\mathrm{D}} = 0$.

The new system parameters h_1 and h_2 are used for examining the influence of parallel solid walls on the dynamics of the system; it is assumed that $h_1 = h_2$, that is, the mid-plane of the channel coincides with the neutral plane of the plate. In this thesis, a lumped-vortex model associated with a simplified wake model is used for the aero/hydro-dynamics part of the system; neither the interaction between individual wake vortices nor the interaction between the original bound/wake vortices and their mirror images has been taken into account. Therefore, in the current quasi-steady analysis (see Chapter 2), only the cases with $h_1 = h_2 > \max(w)$ are investigated; i.e., it is assumed that no contact of the deformed flexible plate with either of the parallel solid walls takes place.

5.3.2. Influence of parallel solid walls. The influence of the parallel solid walls on system stability and post-critical dynamics is shown in Figs. 5.8 and 5.9.

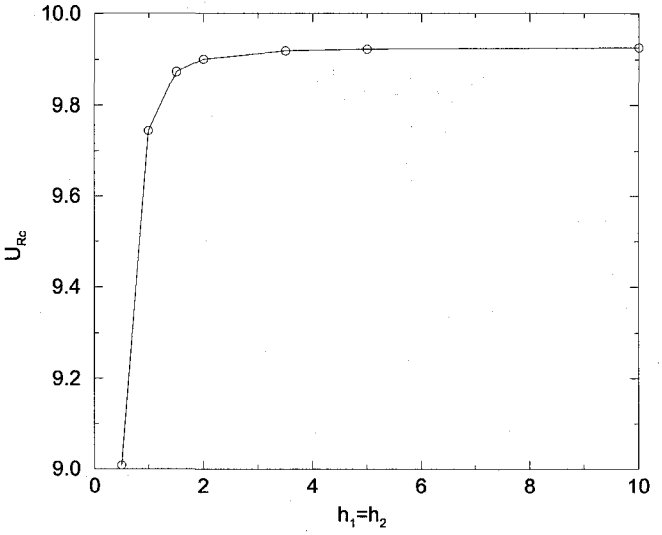

FIGURE 5.8. The influence of the parallel solid walls on system stability. The convergent values of N_M used for $h_1 = h_2 = 10$, 5, 3.5, 2, 1.5, 1 and 0.5 are, respectively, 2, 2, 5, 10, 10, 20 and 20. The other parameters are: $\mu = 0.2$, $l_0 = 0.01$, $\alpha = 0.004$, and $C_D = 0$.

It can be seen in Fig. 5.8 that the influence of the parallel solid walls on system stability is small when $h_1 = h_2$ is large. In particular, when $h_1 = h_2 = 10$, $U_{Rc} = 9.92$, which is identical to the unconfined flow case (i.e., the basic configuration with $h_1 = h_2 = \infty$). However, as $h_1 = h_2$ decreases, the value of U_{Rc} becomes smaller; it is found that $U_{Rc} = 9.9$, 9.87, 9.74 and 9.01 for $h_1 = h_2 = 2$, 1.5, 1 and 0.5, respectively. That is, the presence of the parallel solid walls has a destabilizing effect; this effect becomes more significant when $h_1 = h_2 < 1$. It should be mentioned that, although not shown in Fig. 5.8, the decreasing trend of U_{Rc} with decreasing value of $h_1 = h_2$ continues for $h_1 = h_2 = 0.1$; a preliminary simulation with $N_M = 20$ (without confirmation by convergence tests) identifies a critical point well below $U_{Rc} = 9.01$ obtained for the case $h_1 = h_2 = 0.5$.

Recall that the values of the critical point U_{Rc} observed in previous experiments (where the value of $h_1 = h_2$ is usually around 1, see Appendix C for details) is normally larger than the corresponding theoretical predictions, as one can bee in Fig. 4.16. Therefore, the destabilizing effect of the solid walls does not aid in explaining the discrepancy between experimental measurements and theoretical predictions.

Little previous work can be found regarding the influence of the parallel solid walls on the dynamics of cantilevered flexible plates in axial flow, and the conclusions made in various studies conducted by different authors are somewhat controversial. Aurégan and Depollier (1995) studied a system with very small mass ratios ($0.015 < \mu < 0.023$) and narrow channels ($0.04 < h_1 = h_2 < 0.2$); a destabilizing effect of the parallel solid walls was found and confirmed by their own experimental observations. Wu and Kaneko (2005) worked on a system with $\mu = 0.14$ and leakage flow ($2.0 \times 10^{-3} < h_1 = h_2 < 2.25 \times 10^{-3}$); it was found that the parallel solid walls had a stabilizing effect. Howell et al. (2006) investigated a system with $\mu = 0.42$, and two cases $h_1 = h_2 = 0.5$ and 0.05 were considered; it was reported that the latter case has a higher critical point, i.e., the presence of the parallel solid walls has a stabilizing effect. As indicated by Païdoussis (2004, Section 7.5), when the *confinement* (i.e., the size of the channel) becomes very small, inviscid theories have to be replaced by viscous theories. Note that, both the present theory (with C_D) and that of Aurégan and Depollier (1995) assume that the fluid is inviscid; while the theories of Wu and Kaneko (2005) and Howell et al. (2006) (respectively using a leakage flow model and a Navier-Stokes model) are inherently viscous ones. Therefore, a general assessment of the influence of the parallel solid walls on the system stability is: when $h_1 = h_2$ is relatively large, inviscid theories can be used, and a destabilizing effect can be observed; while, when $h_1 = h_2$ is very small, viscous theories should be used and the parallel solid walls have a stabilizing effect.

As shown in Fig. 5.9, the confinement by parallel solid walls will result in higher amplitude of plate vibrations at any fixed U_R beyond the critical point; the smaller the value of $h_1 = h_2$, the larger is the flutter amplitude. However, as one can see in Fig. 5.9, the post-critical dynamics of the system is qualitatively the same, regardless the value of $h_1 = h_2$; this can also be confirmed by the excellent agreement between the vibration modes observed in experiments (with parallel solid walls) and those predicted for the system in the basic configuration (ignoring the presence of the parallel solid walls) using the present theory (see Fig. 3.5).

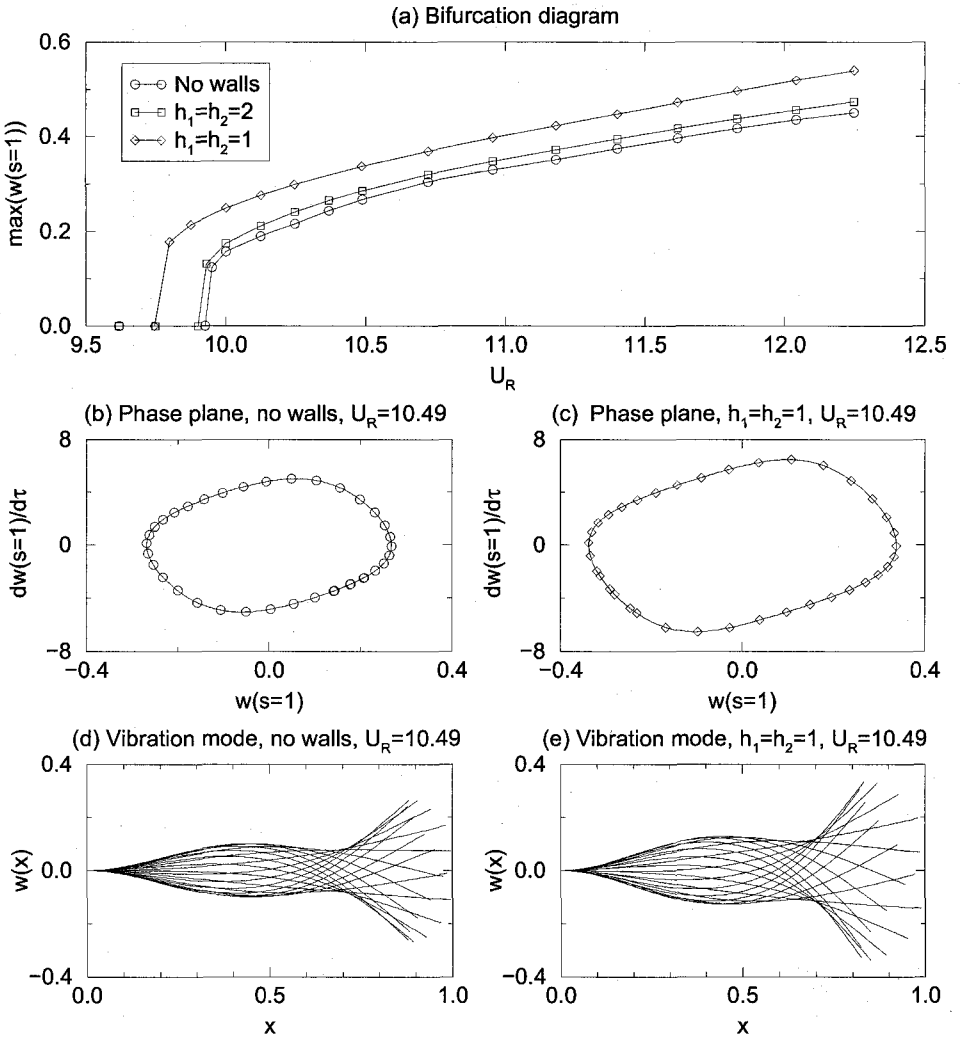

FIGURE 5.9. The influence of the parallel solid walls on the post-critical dynamics of the system. The other parameters are: $\mu = 0.2$, $l_0 = 0.01$, $\alpha = 0.004$, and $C_D = 0$.

It can also be seen in Fig. 5.9 that the presence of the parallel solid walls does not change the nature of the bifurcation point; it is still of the supercritical type. Various initial conditions have been tested at the flutter boundary; no dependence of the critical point U_{Rc} on initial conditions is found. Moreover, we also consider a small misalignment between the neutral plane of the plate and the mid-plane of the channel, which may easily happen in an experimental set-up. In particular, the case with $h_1 = 0.95$ and $h_2 = 1.05$ has been studied. It is found that the value of U_{Rc} so obtained is almost identical to the case with $h_1 = h_2 = 1$; moreover, the system stability is still independent of initial conditions. Therefore, it can be concluded that the subcritical bifurcation observed in experiments is not caused by a

blockage effect (Prasanth et al., 2006). However, it should be emphasized that such a conclusion from a relatively simple incompressible and inviscid aero/hydro-dynamics model, which may not fully be able to reveal the complicated interactions among the plate, the fluid flow and the parallel solid walls, is not totally reliable.

5.4. With an additional spring support

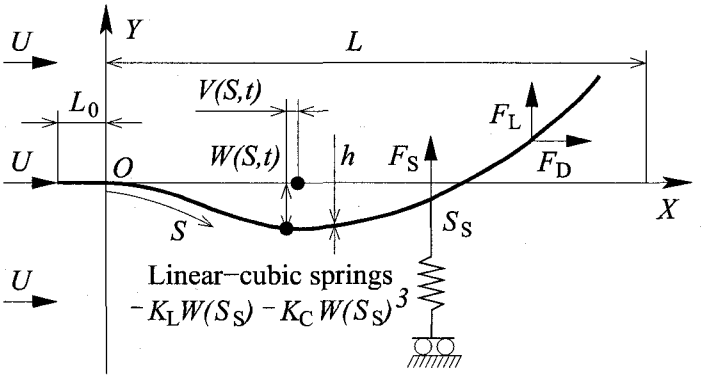

FIGURE 5.10. A cantilevered flexible plate with an additional spring support in axial flow.

5.4.1. Equation of motion. A schematic diagram of a cantilevered flexible plate with an additional (linear or cubic) spring support in axial flow is shown in Fig. 5.10, where S_S is the location of the spring, $F_S = -K_L W(S_S) - K_C W(S_S)^3$ is the spring force acting the plate, and K_L and K_C are the stiffnesses of the linear spring or the cubic spring, as the case may be. When the vibration amplitude is large, the longitudinal displacement of the plate, V, becomes important. In this thesis, the additional spring support is assumed to be able to move longitudinally with the plate; only transverse spring forces are considered. Therefore, the equation of motion of the plate is identical to Eq. (2.7). However, instead of Eq. (2.10), the effective force acting on the plate should be calculated by

$$f_{\text{eff}} = \mu U_R{}^2 \left(f_L - w' f_D + w'' \int_s^1 f_D \, ds \right) + f_S \delta(s - s_S), \tag{5.8}$$

where $s_S = S_S/L$ is the location of the additional spring support normalized by the length of the flexible plate L. The nondimensional spring force f_S is given by

$$f_S = \frac{L^3}{D} F_S = -k_L w - k_C w^3, \tag{5.9}$$

where, k_{L} and k_{C} are, respectively, the nondimensional stiffnesses of the linear and the cubic spring, defined by

$$k_{\mathrm{L}} = \frac{L^4}{D} K_{\mathrm{L}}, \qquad k_{\mathrm{C}} = \frac{L^6}{D} K_{\mathrm{C}}, \tag{5.10}$$

which represent the ratios of the spring forces to the restoring force of the plate.

5.4.2. Dynamics of the system with an additional linear spring support. When a linear spring support is added, the plate may lose stability statically (buckling or divergence instability) rather than by flutter. Stability diagrams of a cantilevered flexible plate in axial flow with an additional linear spring support at $s_{\mathrm{S}} = 1$ and $s_{\mathrm{S}} = 0.8$ are shown in Figs. 5.11 and 5.13, respectively. It is clear that the system dynamics is dependent not only on the stiffness but also on the location of the spring.

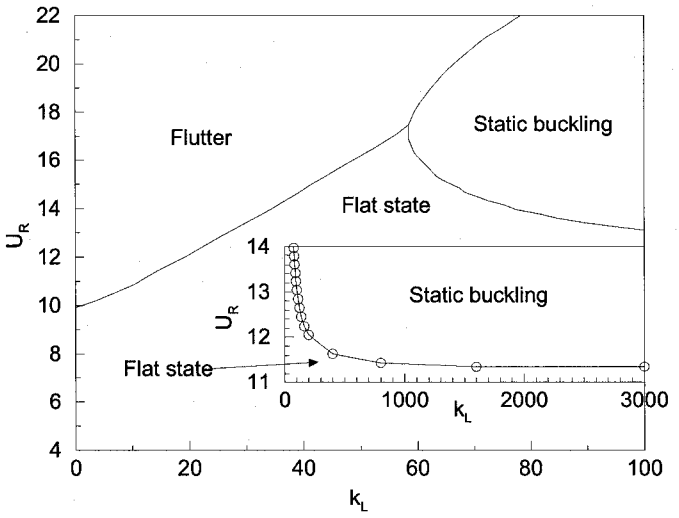

FIGURE 5.11. Stability diagram of a cantilevered flexible plate in axial flow with an additional linear spring support at the plate trailing edge, i.e., $s_{\mathrm{S}} = 1$. The system parameters are: $\mu = 0.2$, $l_0 = 0.01$, $\alpha = 0.004$ and $C_{\mathrm{D}} = 0$. The spring force is given by $f_{\mathrm{S}} = -k_{\mathrm{L}} w(s = 1)$.

When the linear spring support is located at $s_{\mathrm{S}} = 1$, it can be seen in Fig. 5.11 that the plate loses stability through flutter at various values of U_{R}, provided $k_{\mathrm{L}} < 59$; the loss of stability through divergence (buckling) when $k_{\mathrm{L}} > 59$. For $k_{\mathrm{L}} < 59$, the value of U_{Rc} increases with increasing spring stiffness. On the other hand, when $k_{\mathrm{L}} > 59$, U_{Rc} decreases as k_{L} increases. However, with further increase in k_{L}, U_{Rc} converges to

a constant $U_R = 11.30$, as shown in the inset of Fig. 5.11. This observation implies a clamped/simply-supported plate in axial will lose stability through buckling (Dowell, 1975; Païdoussis, 2004) at $U_{Rc} = 11.30$ for the particular values of μ, l_0, α and $C_D = 0$ used in the calculations (see the caption of Fig. 5.11), since the linear spring support is equivalent to a simple support when $k_L \to \infty$.

As shown in Fig. 5.11, when $k_L > 59$, the plate may develop flutter at higher values of U_R, beyond the onset of buckling. It can be shown that all the limit cycle oscillations observed in the flutter region are of the symmetric type. At a given value of k_L, the flutter amplitude grows with increasing U_R. The plate cannot develop divergence (buckling) again, beyond the flutter threshold in this range of k_L.

The three sable states (i.e., stable flat state, static buckling and limit cycle oscillations) of a cantilevered flexible plate in axial flow with an additional linear spring support at the plate trailing edge are shown in Fig. 5.12 for the case $k_L = 70$. It is of interest to see in Fig. 5.12(b) that the overall effect of the distributed fluid load f_L is indeed a *lift*, which balances the point spring force applied on the plate at $s_L = 1$, although the upstream part of the deformed plate shape has a negative angle of incidence in the axial flow. Moreover, due to the presence of the spring support, the vibration modes shown in Fig. 5.12(c) becomes more complicated as compared to those shown in Figs. 4.1(g) and (h) for the system in the basic configuration.

As shown in Fig. 5.13 for the case of the additional linear spring support at $s_S = 0.8$, the plate loses stability through flutter when $k_L < 193$. For a range of k_L around $k_L = 193$, divergence may succeed flutter at higher U_R. On the other hand, when $k_L > 193$, the primary instability is buckling; flutter never takes place, no matter how large U_R is. Again, only symmetric limit cycle oscillations are found in the flutter region; at a fixed value of k_L, the flutter amplitude increases as U_R increases.

A very interesting phenomenon that can be observed in Fig. 5.13 is that the system with an additional linear spring support mounted at $s_S = 0.8$ loses stability at a lower critical reduced flow velocity U_{Rc} when $0 < k_L < 106$ than when $k_L = 0$.

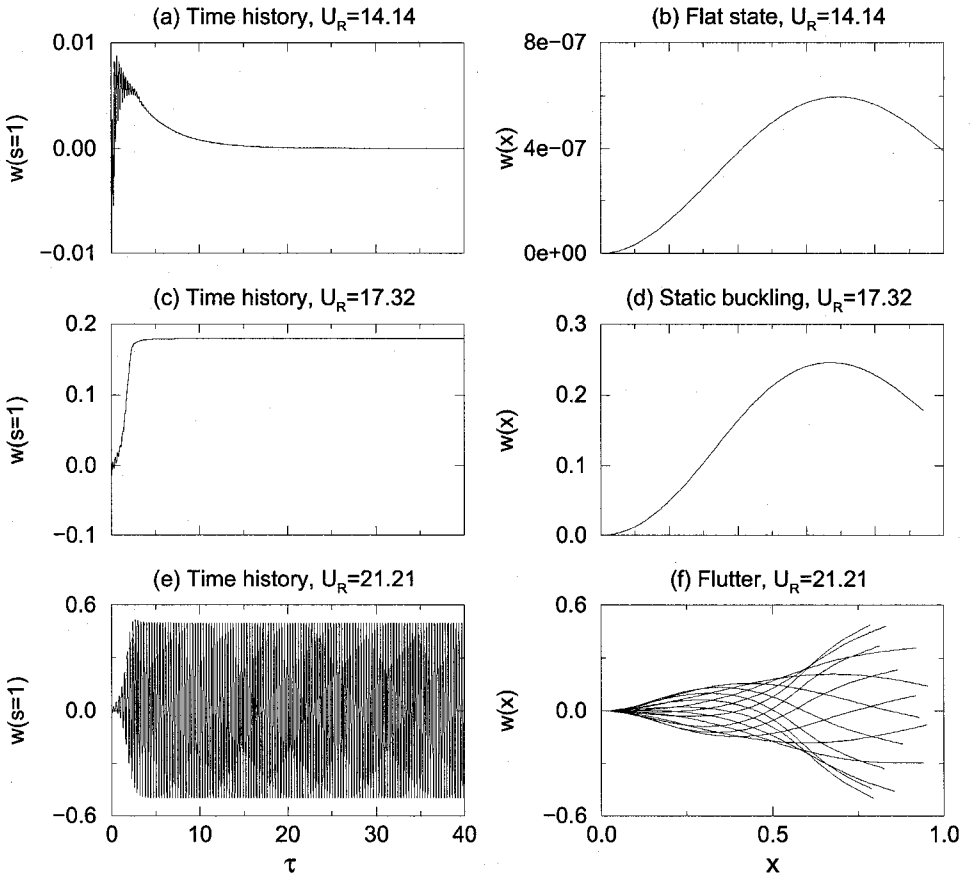

FIGURE 5.12. The dynamics of a cantilevered flexible plate in axial flow with an additional linear spring support at the plate trailing edge, i.e., $s_S = 1$. The system parameters are: $\mu = 0.2$, $l_0 = 0.01$, $\alpha = 0.004$ and $C_D = 0$. The spring force is given by $f_S = -k_L w(s = 1)$, where $k_L = 70$.

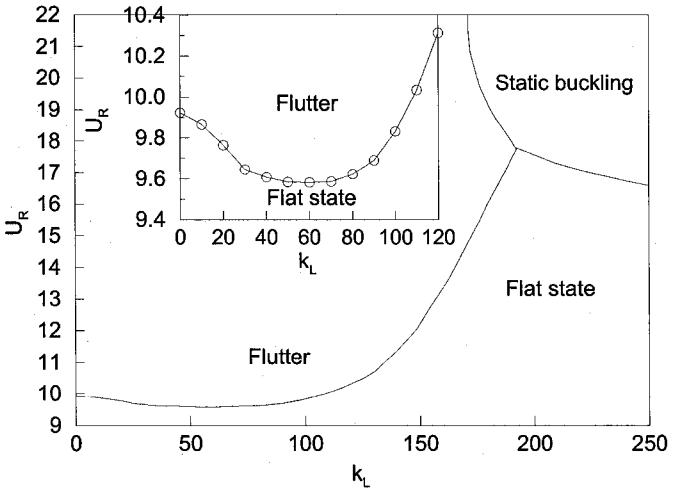

FIGURE 5.13. Stability diagram of a cantilevered flexible plate in axial flow with an additional linear spring support at $s_S = 0.8$. The system parameters are: $\mu = 0.2$, $l_0 = 0.01$, $\alpha = 0.004$ and $C_D = 0$. The spring force is given by $f_S = -k_L w(s = 0.8)$.

In fact, when $0 < k_{\mathrm{L}} < 56$, the value of U_{Rc} decreases as k_{L} increases. A similar stronger-constraint/less-stable phenomenon has been observed in cantilevered pipes conveying fluid (Chen, 1971; Païdoussis, 1998), where the pipe may become buckled when an additional support is applied at a point somewhere in the downstream part of the pipe. Similarly to the system considered in this thesis, the cantilevered pipe with an additional spring support may lose stability by either divergence or flutter, depending on the location and the stiffness of the spring. This and other *strange* phenomena have been found to arise in such "circulatory nonconservative" systems according to the classification of Ziegler (1977) (see also the discussion regarding this topic in Païdoussis (1998)). However, this is the first time that the stronger-constraint/less-stable phenomenon has been observed for the onset of flutter in plate dynamics.

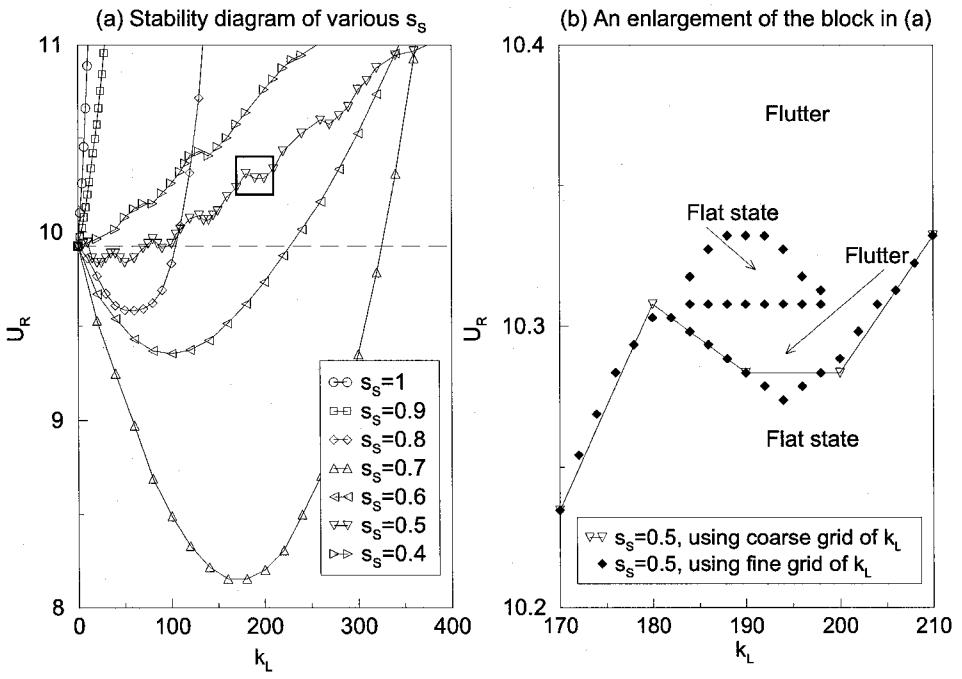

FIGURE 5.14. The stronger-constraint/less-stable phenomenon: stability diagrams of a cantilevered flexible plate in axial flow with an additional linear spring support at various locations. The system parameters are: $\mu = 0.2$, $l_0 = 0.01$, $\alpha = 0.004$ and $C_{\mathrm{D}} = 0$. The spring force is given by $f_{\mathrm{S}} = -k_{\mathrm{L}} w(s = s_{\mathrm{S}})$.

The stability diagrams of the system with an additional linear spring support at various locations are shown in Fig. 5.14(a). The stronger-constraint/less-stable phenomenon can be observed for the cases $s_{\mathrm{S}} = 0.5$ through $s_{\mathrm{S}} = 0.8$, but not for

the other cases (i.e., $s_S = 0.4$, 0.9 and 1); and the most remarkable case is $s_S = 0.7$, where a minimum value of U_{Rc} is predicted to occur at $k_L \approx 170$. Note that, when the system is in the basic configuration without the additional spring support, the plate loses stability in the second-beam-mode shape; it is speculated that the additional spring support located at a point close to the quasi-node of the vibration modes of the plate (see Figs. 4.1(g) and (h)) may aid the plate to choose the second beam mode for the instability. When the location of the additional spring support lies closer to the upstream clamping constraint, i.e., when $s_S \leq 0.5$, the stability diagram will not be a smooth curve; an S-shaped curve, as shown in Fig. 5.14(b), may be observed.

5.4.3. Dynamics of the system with an additional cubic spring support.

The system exhibits richer dynamics when the additional spring support is a cubic one. Two bifurcation diagrams are shown in Figs. 5.15 and 5.17 for the cubic spring support located at $s_S = 1$ and $s_S = 0.8$, respectively. It is again found that the dynamics of the system depends on the location of the spring, as in the case of a linear spring support.

As shown in Figs. 5.15(e) and (f), when the additional cubic spring support is at the trailing edge, the plate first loses stability through flutter at $U_{Rc} = 9.9247$; symmetric limit cycle oscillations take place beyond this critical point, as shown in Fig. 5.15(a) for $U_R = 14.14$, the amplitude of which grows as U_R increases. The symmetry of the limit cycle oscillations is broken when the reduced flow velocity reaches $U_R = 14.8997$, as shown in Fig. 5.15(b) for $U_R = 15.81$. It can be shown that, whenever a solution of asymmetric limit cycle oscillations is obtained, there must exist the other asymmetric one, in the origin-symmetry sense, in the phase plane plot (or in the axis-symmetry sense with respect to $w = 0$ in the bifurcation diagram). The asymmetric limit cycle oscillations experience a series of period-doubling bifurcations, which take place at $U_R = 16.5831$, 16.8701, 16.9381 and 16.9536. As an illustration, Figs. 5.15(c), (g) and (h) show the period-2 limit cycle oscillations at $U_R = 16.73$, period-4 at $U_R = 16.93$ and period-8 at $U_R = 16.954$, respectively. As shown in Fig. 5.15(d), large amplitude period-4 limit cycle oscillations may be observed in a small region around $U_R = 16.89$.

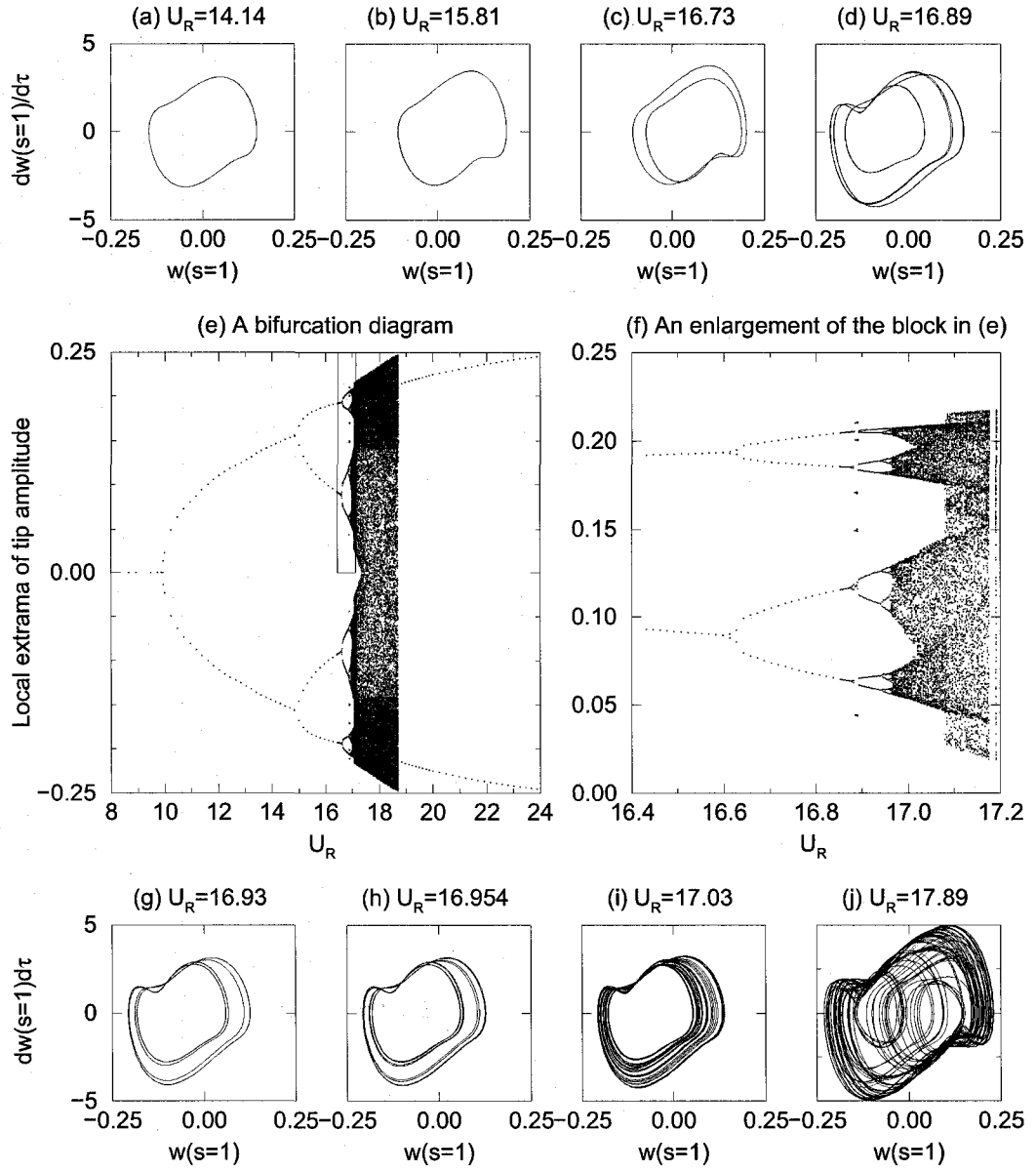

FIGURE 5.15. The dynamics of a cantilevered flexible plate in axial flow with an additional cubic spring support at the plate trailing edge, i.e., $s_S = 1$. The system parameters are: $\mu = 0.2$, $l_0 = 0.01$, $\alpha = 0.004$ and $C_D = 0$. The spring force is given by $f_S = -k_C w^3(s = 1)$, where $k_C = 1000$.

A further period-doubling bifurcation seems to occur at $U_R = 16.9570$; beyond this point, the dynamics becomes more chaotic than periodic, as shown in Fig. 5.15(i) for $U_R = 17.03$. According to these period-doubling bifurcation points, a series of Feigenbaum numbers (Moon, 1992; Païdoussis, 2004) can be obtained: $\delta_F = 5.87$, 4.22, 4.39 and 4.56, which trends to converge towards the universal value of 4.6692, indicating that a period-doubling route to chaos has been followed. This

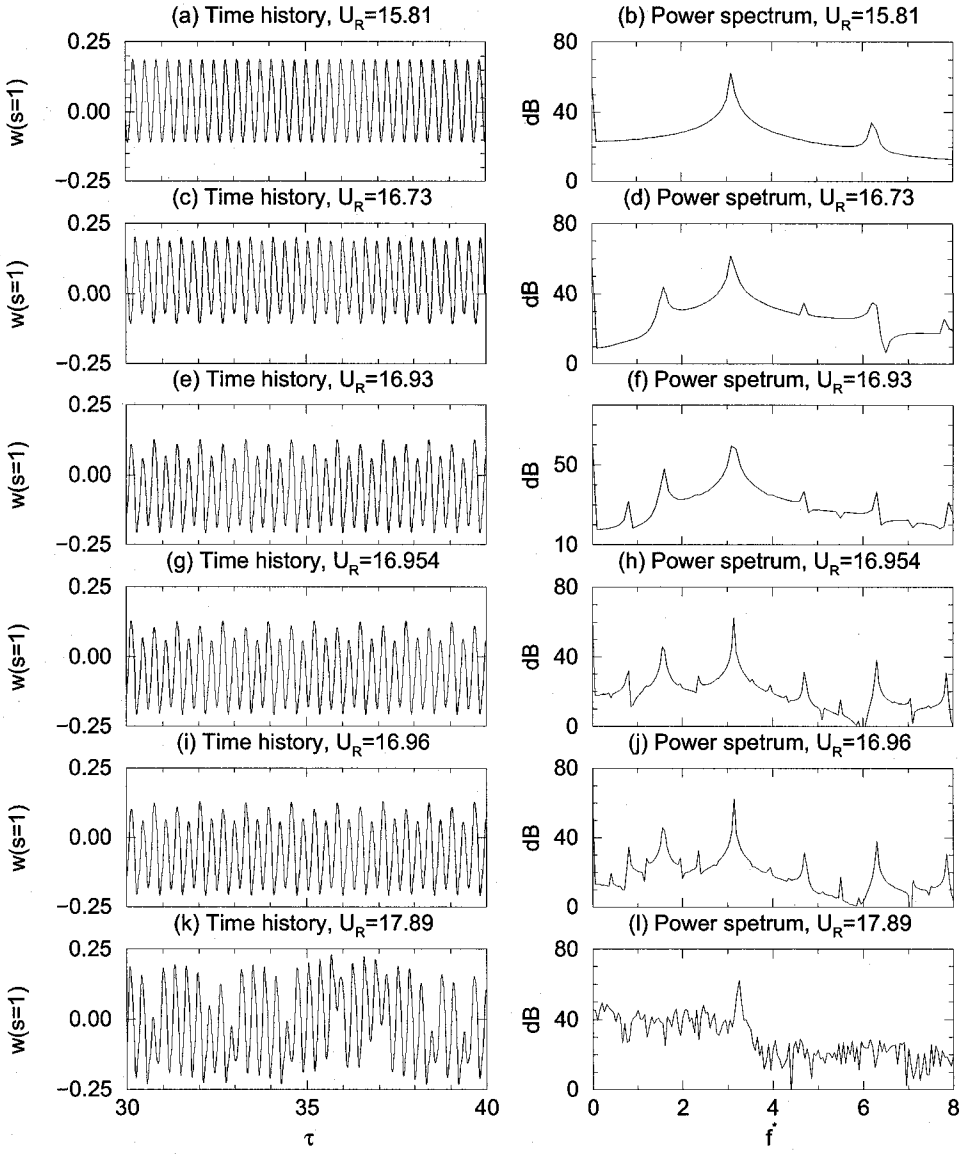

FIGURE 5.16. Time histories and power spectra of the dynamics of a cantilevered flexible plate in axial flow at various values of U_{R} for the system studied in Fig. 5.15. The system parameters are: $\mu = 0.2$, $l_0 = 0.01$, $\alpha = 0.004$ and $C_{\mathrm{D}} = 0$. An additional cubic spring support at $s_{\mathrm{S}} = 1$ has been considered; the spring force is given by $f_{\mathrm{S}} = -k_{\mathrm{C}} w^3(s = 1)$, where $k_{\mathrm{C}} = 1000$.

period-doubling process can also be seen in Fig. 5.16, where the time histories and the power spectra of the dynamics at various values of U_{R} are presented. The region of chaotic motion (as shown in a typical case in Fig. 5.15(j) as well as in Figs. 5.16(k) and (l) for $U_{\mathrm{R}} = 17.89$) is between $U_{\mathrm{R}} = 16.96$ and $U_{\mathrm{R}} = 18.71$; the very high low-frequency content in Fig. 5.16(l) is particularly indicative of chaos.

Finally, when $U_R > 18.71$, the chaotic motions disappear all of a sudden; the plate becomes statically buckled. With increasing U_R, the tip amplitude of the buckled plate increases. It is interesting to see in Fig. 5.15(e) that the locus of increasing tip amplitude in the buckling region looks like the continuation of that in the region of symmetric limit cycle oscillations between $U_R = 9.9247$ and $U_R = 14.8997$; this observation suggests the possible existence of (unstable) solutions in the interval $14.8997 < U_R < 18.71$.

Figs. 5.17(a) and (b) show the bifurcation diagram in terms of U_R when the additional cubic spring support is located at $s_S = 0.8$. It can be seen in Fig. 5.17(a) that the system loses stability still through flutter, but in this case very abruptly, at $U_{Rc} = 9.92$. After the primary bifurcation, the system develops symmetric limit cycle oscillations, as shown in Fig. 5.17(c) as well as in Figs. 5.18(a) and (b) for $U_R = 14.14$, before a secondary bifurcation takes place at $U_R = 15.33$; beyond this point, the limit cycle oscillations become asymmetric (see Fig. 5.17(d) for $U_R = 17.32$). In the region of period-1 asymmetric limit cycle oscillation (i.e., $15.33 < U_R < 17.86$), it is interesting to see that, with increasing U_R, the flutter amplitude of the plate trailing edge decreases and the contour of the fluttering plate becomes narrower, as shown in Fig. 5.17(a) as well as in Figs. 5.18(d) and (f).

A series of period-doubling bifurcations take place at $U_R = 17.86$, 18.49 and 18.74; asymmetric limit cycle oscillations of various periods are shown in Figs. 5.17(e) through (g). A region of chaotic motions can be found when $18.81 < U_R < 19.62$, as shown in Fig. 5.17(h) for $U_R = 19.49$. However, as U_R is increased further, regular limit cycle oscillations re-emerge; another period doubling route to chaos can be observed in the region $19.62 < U_R < 21.10$, as shown in Figs. 5.17(i) through (k), respectively, for period-2 motions at $U_R = 20.74$, period-4 at $U_R = 20.95$ and period-8 at $U_R = 21.02$. The main region of chaos is observed for $21.10 < U_R < 23.45$ (see Figs. 5.17(l) and (m) for $U_R = 21.21$ and 21.91, respectively); there is a periodic window between $U_R = 22.36$ and $U_R = 22.56$, as illustrated in Fig. 5.17(n) for $U_R = 22.47$. Finally, the plate becomes statically buckled at $U_R > 23.45$, as shown in Fig. 5.17(a) as well as in Figs. 5.18(g) and (h) for $U_R = 24.90$.

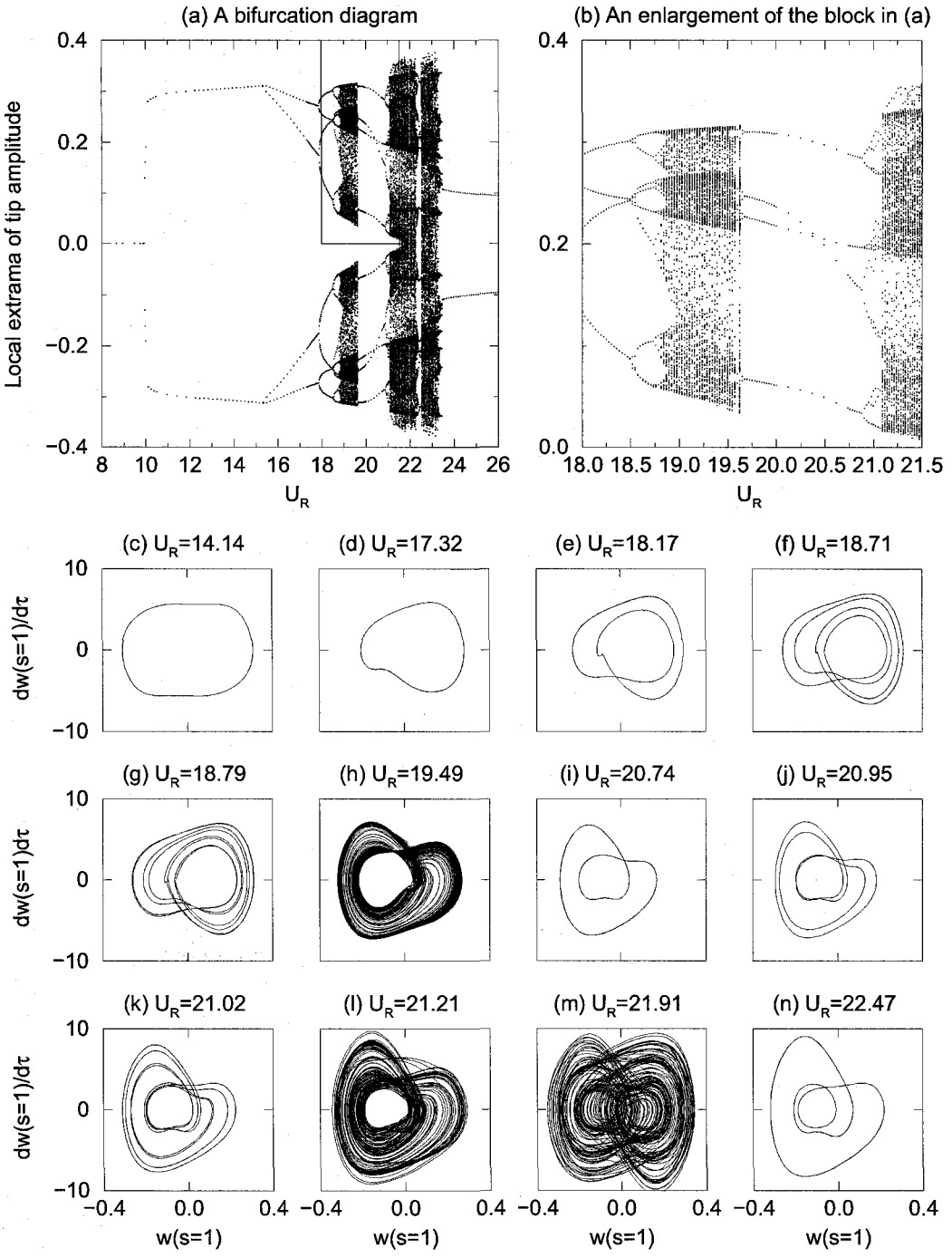

FIGURE 5.17. The dynamics of a cantilevered flexible plate in axial flow with an additional cubic spring support at $s_S = 0.8$. The system parameters are: $\mu = 0.2$, $l_0 = 0.01$, $\alpha = 0.004$ and $C_D = 0$. The spring force is given by $f_S = -k_C w^3(s = 0.8)$, where $k_C = 6000$.

The static buckling states of the cantilevered flexible plates at high reduced flow velocities U_R observed in Figs. 5.15 and 5.17 are summarized in Fig. 5.19. Although the two cases studied have different values of k_C, which affects the amplitude of the

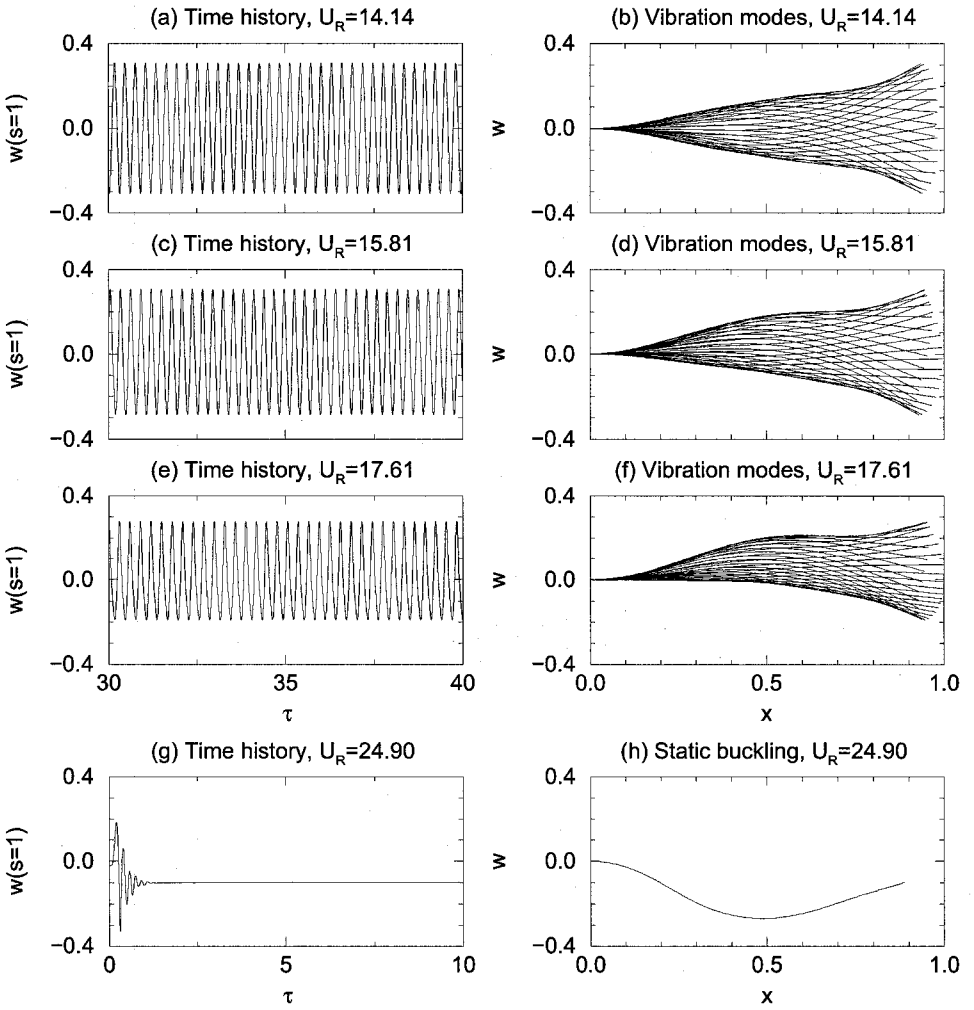

FIGURE 5.18. Time histories and vibration modes of a cantilevered flexible plate in axial flow at various values of U_{R} for the system studied in Fig. 5.17. The system parameters are: $\mu = 0.2$, $l_0 = 0.001$, $\alpha = 0.004$ and $C_{\mathrm{D}} = 0$. An additional cubic spring support at $s_{\mathrm{S}} = 0.8$ has been considered; the spring force is given by $f_{\mathrm{S}} = -k_{\mathrm{C}} w^3(s = 0.8)$, where $k_{\mathrm{C}} = 6000$.

deformations, one can still see the influence of the location of the additional cubic spring support, s_{S}, on the buckled shapes. As shown in Fig. 5.19(a), when $s_{\mathrm{S}} = 1$, as U_{R} increases, the deformation amplitude everywhere along the whole length of the plate increases. While, as shown in Fig. 5.19(b), when $s_{\mathrm{S}} = 0.8$, the deformation amplitude of the plate between the clamped support and the additional spring support grows as U_{R} is increased, but it decreases at locations beyond the spring support; therefore, a quasi-node (not an exact node due to the longitudinal deformations of the plate) can be observed at the point of attachment of the spring.

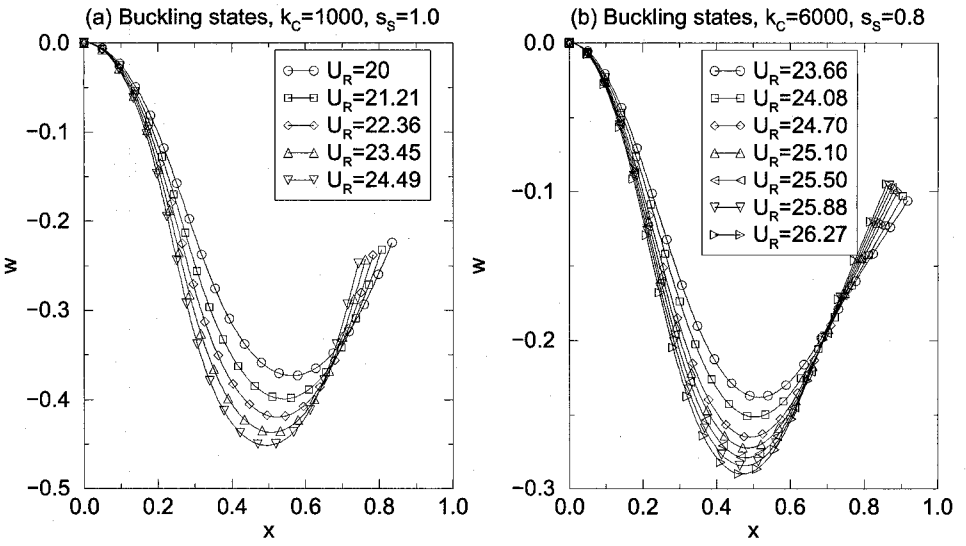

FIGURE 5.19. Static buckling states of the cantilevered flexible plates at high reduced flow velocities U_{R} observed in Figs. 5.15 and 5.17.

5.5. With an additional concentrated mass

5.5.1. Equation of motion and solution method. When there is an additional concentrated mass m_{A} located at S_{M} on the plate, as illustrated in Fig. 5.20, one can obtain the equation of motion of the plate following the procedure discussed in Appendix A; wherever the term $\rho_{\mathrm{P}}h$ is present, it should be replaced by $\rho_{\mathrm{P}}h+m_{\mathrm{A}}\delta(S-S_{\mathrm{M}})$. Therefore, accounting for the additional concentrated mass, the nondimensional equation of motion, Eq. (2.7), becomes

$$\begin{aligned}
&\left[1+\sigma_{\mathrm{M}}\delta(s-s_{\mathrm{M}})\right]\ddot{w}+\left(1+\alpha\frac{\partial}{\partial\tau}\right)\left[w''''\left(1+w'^2\right)+4w'w''w'''+w''^3\right]\\
+\;&\left[1+\sigma_{\mathrm{M}}\delta(s-s_{\mathrm{M}})\right]w'\int_0^s\left(\dot{w}'^2+w'\ddot{w}'\right)\,ds\\
-\;&w''\int_s^1\left[1+\sigma_{\mathrm{M}}\delta(s-s_{\mathrm{M}})\right]\left[\int_0^s\left(\dot{w}'^2+w'\ddot{w}'\right)\,ds\right]\,ds=f_{\mathrm{eff}},
\end{aligned}\tag{5.11}$$

where the nondimensional concentrated mass parameter σ_{M} is defined by

$$\sigma_{\mathrm{M}}=\frac{m_{\mathrm{A}}}{\rho_{\mathrm{P}}hL},\tag{5.12}$$

representing the ratio of the additional concentrated mass to the mass of the plate itself (in the sense of the per-unit-width mass); s_{M} $(0<s_{\mathrm{M}}\leq 1)$ is the nondimensional

location of the additional concentrated mass, which is normalized using the length of the flexible plate L, i.e., $s_{\mathrm{M}} = S_{\mathrm{M}}/L$.

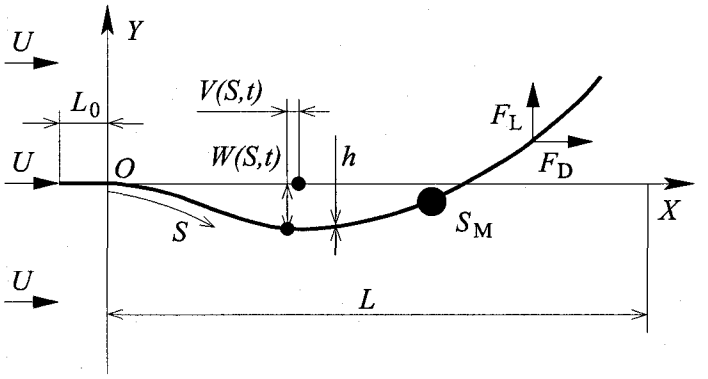

FIGURE 5.20. A cantilevered flexible plate in axial flow with an additional concentrated mass.

When the additional concentrated mass is located at the tailing edge of the plate, $s_{\mathrm{M}} = 1$, and Eq. (5.11) becomes

$$\begin{aligned}
&[1+\sigma_{\mathrm{M}}\delta(s-1)]\,\ddot{w} + (1+\alpha\frac{\partial}{\partial\tau})\left[w''''\left(1+w'^2\right)+4w'w''w'''+w''^3\right] \\
+\;& [1+\sigma_{\mathrm{M}}\delta(s-1)]\,w'\int_0^s \left(\dot{w}'^2+w'\ddot{w}'\right)\,ds \\
-\;& w''\int_s^1\left[\int_0^s\left(\dot{w}'^2+w'\ddot{w}'\right)\,ds\right]\,ds - \sigma_{\mathrm{M}}w''\int_0^1\left(\dot{w}'^2+w'\ddot{w}'\right)\,ds = f_{\mathrm{eff}}. \qquad (5.13)
\end{aligned}$$

However, when the additional concentrated mass is located somewhere along the plate rather than at the tailing edge, i.e., $0 < s_{\mathrm{M}} < 1$, it is more convenient to rewrite Eq. (5.11) as

$$\begin{aligned}
&[1+\sigma_{\mathrm{M}}\delta(s-s_{\mathrm{M}})]\,\ddot{w} + (1+\alpha\frac{\partial}{\partial\tau})\left[w''''\left(1+w'^2\right)+4w'w''w'''+w''^3\right] \\
+\;& [1+\sigma_{\mathrm{M}}\delta(s-s_{\mathrm{M}})]\,w'\int_0^s \left(\dot{w}'^2+w'\ddot{w}'\right)\,ds - w''\int_s^1\left[\int_0^s\left(\dot{w}'^2+w'\ddot{w}'\right)\,ds\right]\,ds \\
=\;& f_{\mathrm{eff}} + \begin{cases} \sigma_{\mathrm{M}}w''\int_0^{s_{\mathrm{M}}}\left(\dot{w}'^2+w'\ddot{w}'\right)\,ds & \text{when} \quad s \le s_{\mathrm{M}}, \\ 0 & \text{when} \quad s > s_{\mathrm{M}}. \end{cases} \qquad (5.14)
\end{aligned}$$

Applying the same Galerkin expansion as used in Chapter 3 to Eq. (5.13) or Eq. (5.14), one obtains

$$\ddot{q}_i + \sigma_{\mathrm{M}}\phi_i(s_{\mathrm{M}})\phi_m(s_{\mathrm{M}})\ddot{q}_m + \left(1 + \alpha\frac{\partial}{\partial\tau}\right)(A_i q_i + B_{imnl}q_m q_n q_l) + C^{\mathrm{new}}_{imnl}q_m\left(\dot{q}_n\dot{q}_l + q_n\ddot{q}_l\right) = f_i^{\mathrm{new}}, \tag{5.15}$$

where, C^{new}_{imnl} and f_i^{new} are, respectively, the new versions of the numerical constant C_{imnl} and the generalized force f_i; they are, respectively, defined by

$$C^{\mathrm{new}}_{imnl} = C_{imnl} + \begin{cases} \sigma_{\mathrm{M}}(G_{imnl} - H_{imnl}) & \text{when} \quad s_{\mathrm{M}} = 1, \\ \sigma_{\mathrm{M}} I_{imnl} & \text{when} \quad 0 < s_{\mathrm{M}} < 1, \end{cases} \tag{5.16}$$

$$f_i^{\mathrm{New}} = f_i + \begin{cases} 0 & \text{when} \quad s_{\mathrm{M}} = 1, \\ \sigma_{\mathrm{M}} J_{imnl}q_m\left(\dot{q}_n\dot{q}_l + q_n\ddot{q}_l\right) & \text{when} \quad 0 < s_{\mathrm{M}} < 1 \text{ and } s < s_{\mathrm{M}}, \\ 0 & \text{when} \quad 0 < s_{\mathrm{M}} < 1 \text{ and } s > s_{\mathrm{M}}. \end{cases} \tag{5.17}$$

In Eqs. (5.16) and (5.17), the numerical constants G_{imnl}, H_{imnl}, I_{imnl} and J_{imnl} are defined by

$$G_{imnl} = \phi_i(1)\phi'_m(1)\int_0^1 \phi'_n\phi'_l\, ds, \tag{5.18}$$

$$H_{imnl} = \left(\int_0^1 \phi_i\phi''_m\, ds\right)\left(\int_0^1 \phi'_n\phi'_l\, ds\right), \tag{5.19}$$

$$I_{imnl} = \phi_i(s_{\mathrm{M}})\phi'_m(s_{\mathrm{M}})\int_0^1 \phi'_n\phi'_l\, ds, \tag{5.20}$$

$$J_{imnl} = \left(\int_0^1 \phi_i\phi''_m\, ds\right)\left(\int_0^{s_{\mathrm{M}}} \phi'_n\phi'_l\, ds\right). \tag{5.21}$$

Note that in the evaluation of $\int_0^1 \phi_i\phi''_m\, ds$ in Eqs. (5.19) and (5.21), the following expression (Païdoussis, 1998, Chapter 3) can be used:

$$\int_0^1 \phi_i\phi''_j\, ds = \begin{cases} [4(\beta_j\varsigma_j - \beta_i\varsigma_i)]/[(-1)^{i+j} - (\beta_i/\beta_j)^2] & \text{when} \quad i \neq j, \\ \beta_i\varsigma_i(2 - \beta_i\varsigma_i) & \text{when} \quad i = j, \end{cases} \tag{5.22}$$

where the constants β_i and ς_i are defined in conjunction with the eigenmodes of a linear *in vacuo* cantilevered beam (see Eqs. (3.2) and (3.3)).

Substituting these formulae of the Houbolt method, i.e., Eq. (3.13b), into Eq. (5.15), one obtains

$$D_i q_i + \sigma_{\mathrm{M}} \phi_i(s_{\mathrm{M}}) \phi_m(s_{\mathrm{M}})(a_1 q_m + \lambda_{1m}) + E^{\mathrm{new}}_{imnl} q_m q_n q_l + F^{\mathrm{new}}_{imnl} \lambda_{2m} q_n q_l$$
$$+ \; C^{\mathrm{new}}_{imnl} q_m \left(q_n \lambda_{1l} + \lambda_{2n} \lambda_{2l}\right) + \lambda_{3i} = \Delta\tau^2 f_i^{\mathrm{new}}, \tag{5.23}$$

where the numerical constants E^{new}_{imnl} and F^{new}_{imnl} are, respectively, the new versions of E_{imnl} and F_{imnl} according to the renewal of C_{imnl} involved, that is

$$E^{\mathrm{new}}_{imnl} = (\Delta\tau^2 + 3\Delta\tau\alpha b_1) B_{imnl} + (a_1 + b_1^2) C^{\mathrm{new}}_{imnl}, \tag{5.24}$$

$$F^{\mathrm{new}}_{imnl} = \Delta\tau\alpha \left(B_{imnl} + B_{inml} + B_{ilnm}\right) + b_1 \left(C_{ilnm} + C^{\mathrm{new}}_{inml}\right). \tag{5.25}$$

5.5.2. Dynamics of the system with an additional concentrated mass.

The influence of an additional concentrated mass, corresponding to various values of σ_{M} at different locations s_{M}, on system stability is studied. It can be seen in Fig. 5.21(a) that a small additional concentrated mass $\sigma_{\mathrm{M}} = 0.01$ at a variety of locations along the plate has a different effect on the critical point. When there is no additional concentrated mass, i.e., the case $s_{\mathrm{M}} = 0$ which is equivalent to the basic configuration, $U_{\mathrm{Rc}} = 9.92$. When $s_{\mathrm{M}} < 0.4$, the value of U_{Rc} decreases slightly with increasing s_{M}. When $0.4 < s_{\mathrm{M}} < 0.7$, U_{Rc} grows with increasing values of s_{M} and reaches the maximum $U_{\mathrm{Rc}} = 9.97$ at $s_{\mathrm{M}} = 0.7$. Beyond this maximum point, U_{Rc} decreases again, more rapidly this time, as s_{M} further increases; finally, the minimum $U_{\mathrm{Rc}} = 9.70$ is observed when the additional concentrated mass is located at the trailing edge of the plate, i.e., $s_{\mathrm{M}} = 1$.

When the additional concentrated mass is placed at $s_{\mathrm{M}} = 0.75$ or $s_{\mathrm{M}} = 1$ while σ_{M} is varied, the flutter boundaries obtained are, respectively, shown in Figs. 5.21(b) and (c). It can be seen in Fig. 5.21(b) that, when $s_{\mathrm{M}} = 0.75$, the value of U_{Rc} increases monotonically from $U_{\mathrm{Rc}} = 9.92$ with $\sigma_{\mathrm{M}} = 0$ to $U_{\mathrm{Rc}} = 12.96$ with $\sigma_{\mathrm{M}} = 1$. When $s_{\mathrm{M}} = 1$, the relation between U_{Rc} and σ_{M} becomes more complicated. In particular, as shown in Fig. 5.21(c), U_{Rc} decreases significantly with increasing σ_{M} when $0 < \sigma_{\mathrm{M}} < 0.1$. However, for $0.1 < \sigma_{\mathrm{M}} < 0.2$, the variation in U_{Rc} is negligibly

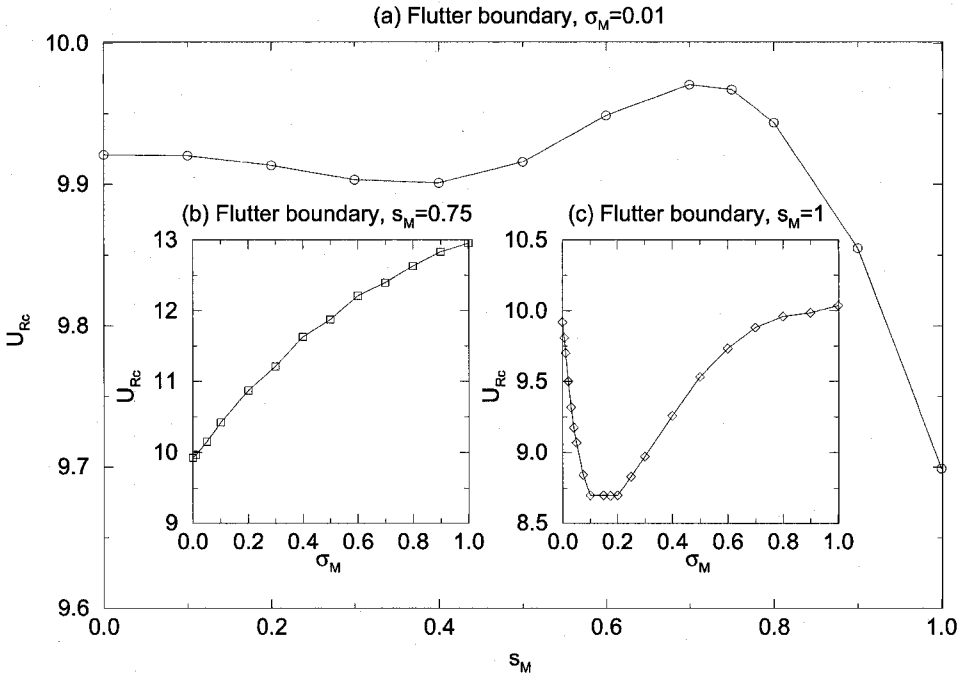

FIGURE 5.21. The influence of an additional concentrated mass on the system stability. The other parameters of the system are $\mu = 0.2$, $l_0 = 0.01$, $\alpha = 0.004$ and $C_D = 0$.

small, and a plateau is formed where $U_{Rc} = 8.70$. As σ_M is increased further, the trend for U_{Rc} is reversed; and, finally $U_{Rc} = 10.04$ when $\sigma_M = 1$.

The underlying mechanism of the pattern of the flutter boundary in terms of the value of σ_M presented in Fig. 5.21(c) for the system with an additional concentrated mass located at the trailing edge of the plate (i.e., $s_M = 1$) is not yet fully understood. However, as shown in Fig. 5.22, when examining the vibration modes of the plate along the flutter boundary in Fig. 5.21(c), one can find that, when the value of σ_M is small, say $\sigma_M < 0.2$, the mode shapes of the plate shown in Figs. 5.22(a) through (e) are qualitatively the same as that of the basic configuration shown in Fig. 4.1(g). In particular, as shown in Fig. 4.4, these vibration modes are a combination of the first and second beam-mode shapes. In contrast, when $\sigma_M \geq 0.3$, as shown in Figs. 5.22(f) through (h), the vibration modes are solely determined by the second-beam-mode shape, in that a quasi-stationary node becomes more prominent.

It has been observed in Fig. 5.21(a) that a small additional concentrated mass $\sigma_M = 0.01$ located at $s_M = 1$ significantly reduces the value of critical point; moreover,

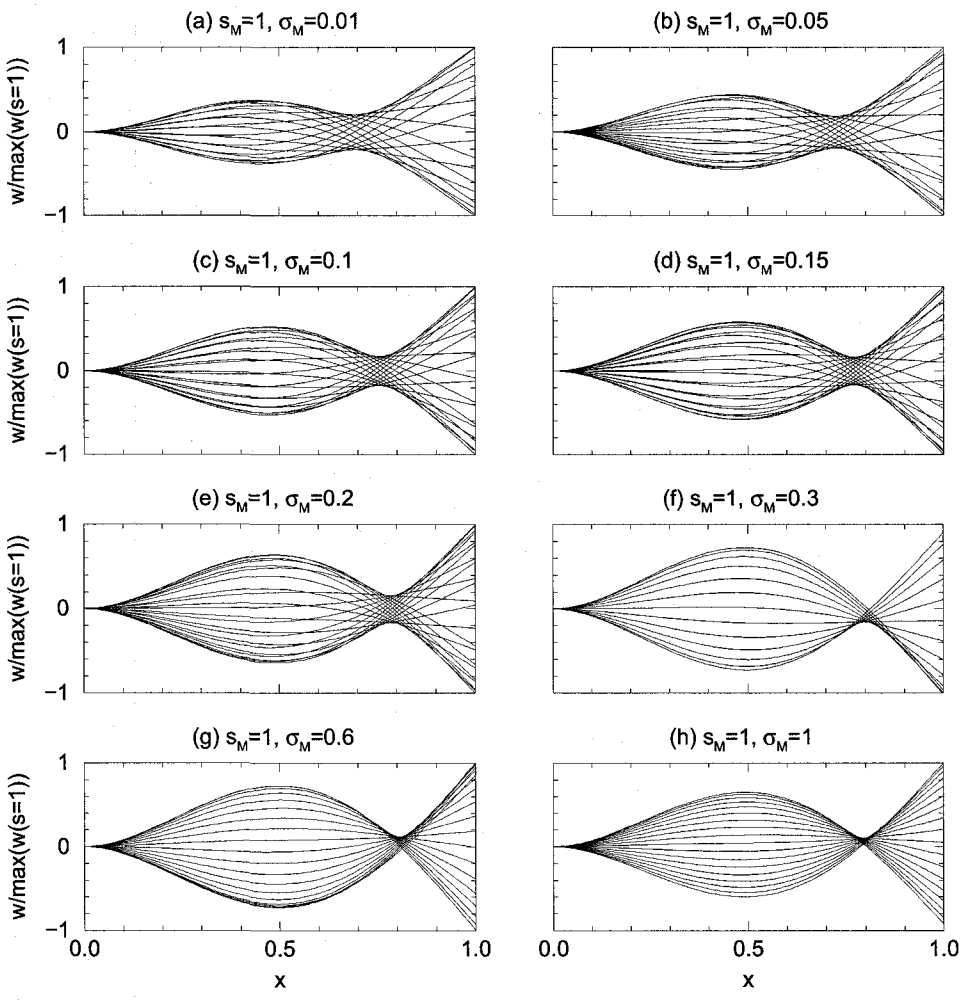

FIGURE 5.22. The vibration modes of the systems with various additional concentrated masses located at the trailing edge of the plate. Note that the vibrations modes are obtained at the corresponding critical point of each individual case. The other parameters of the system are $\mu = 0.2$, $l_0 = 0.01$, $\alpha = 0.004$ and $C_D = 0$.

as shown in Fig. 5.23, it will also affect the manner of the onset of the flutter and the post-critical dynamics of the system. It can be seen in Fig. 5.23(a) that, as compared to the bifurcation diagram of the system in the basic configuration, flutter takes place in a more abrupt manner; and, once the critical point is exceeded, the flutter amplitude is rather large. This phenomenon may imply the occurrence of a subcritical bifurcation instead of a supercritical one. That is, an imperfection in the distribution of mass along the plate length may account for the abrupt onset of flutter, which is commonly observed in experiments but cannot be captured by the present theories (neither by any other theory).

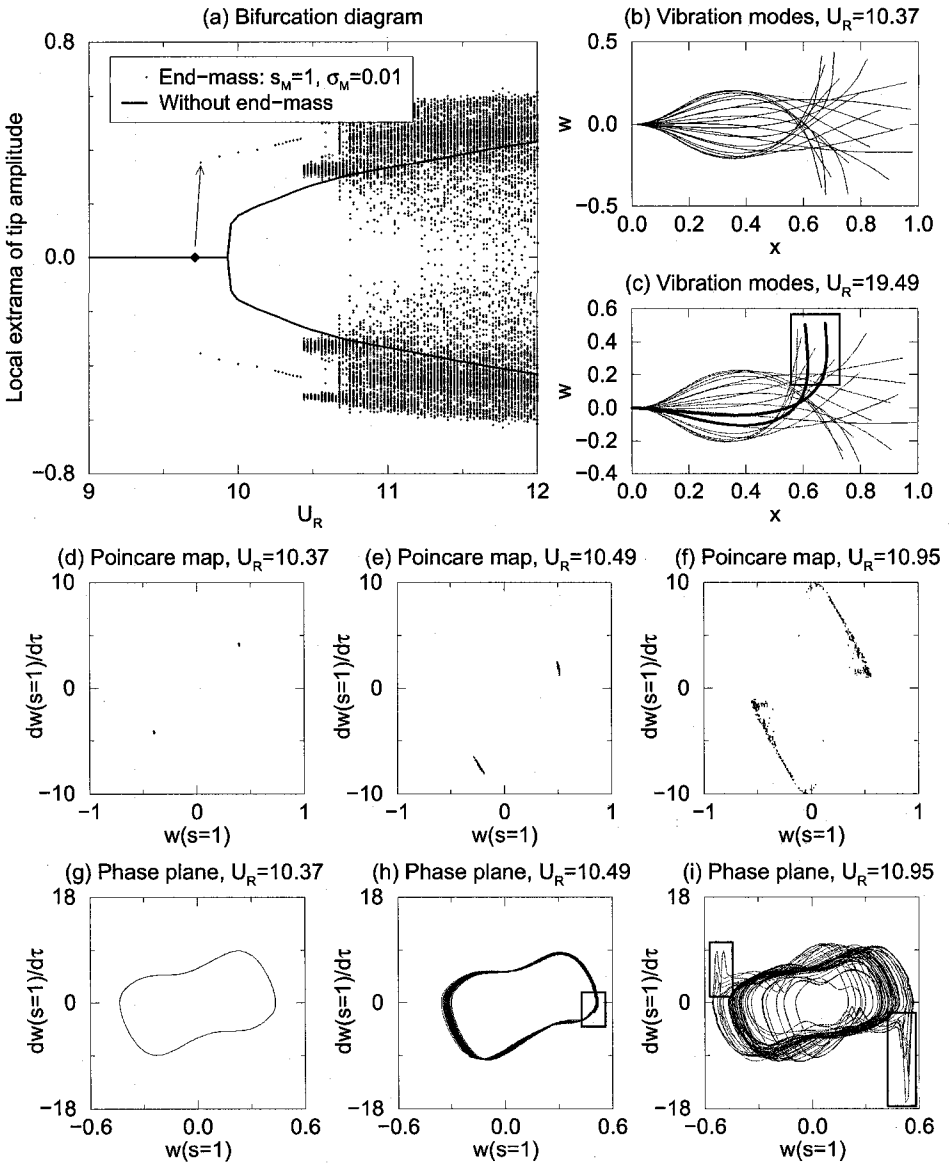

FIGURE 5.23. The dynamics of the system with a small concentrated mass located at the trailing edge of the plate, i.e., $\sigma_{\mathrm{M}} = 0.01$ and $s_{\mathrm{M}} = 1$. The other parameters of the system are $\mu = 0.2$, $l_0 = 0.01$, $\alpha = 0.004$ and $C_{\mathrm{D}} = 0$. Note that the Poincaré maps (Moon, 1987) are obtained by simultaneously recording the position and the velocity of the trailing edge of the plate with $w(s = 0.5) = 0$ as the controlling event.

With the small additional concentrated mass $\sigma_{\mathrm{M}} = 0.01$ located at $s_{\mathrm{M}} = 1$, symmetric limit cycle oscillations can still be observed at higher U_{R} beyond the critical point $U_{\mathrm{Rc}} = 9.70$, as shown in Figs. 5.23(b), (d) and (g) for the case $U_{\mathrm{R}} = 10.37$ for example. Note that the flutter amplitude of the system with an additional concentrated mass is significantly larger than that of the system in the basic configuration, even though σ_{M} is so small ($\sigma_{\mathrm{M}} = 0.01$). As U_{R} increases further and exceeds the

point $U_R = 10.43$, chaos takes place, as shown in Figs. 5.23(e) and (h) for the case $U_R = 10.49$ where chaotic motions start to emerge, and in Figs. 5.23(f) and (i) for the case $U_R = 10.95$ where the dynamics of the system is fully chaotic.

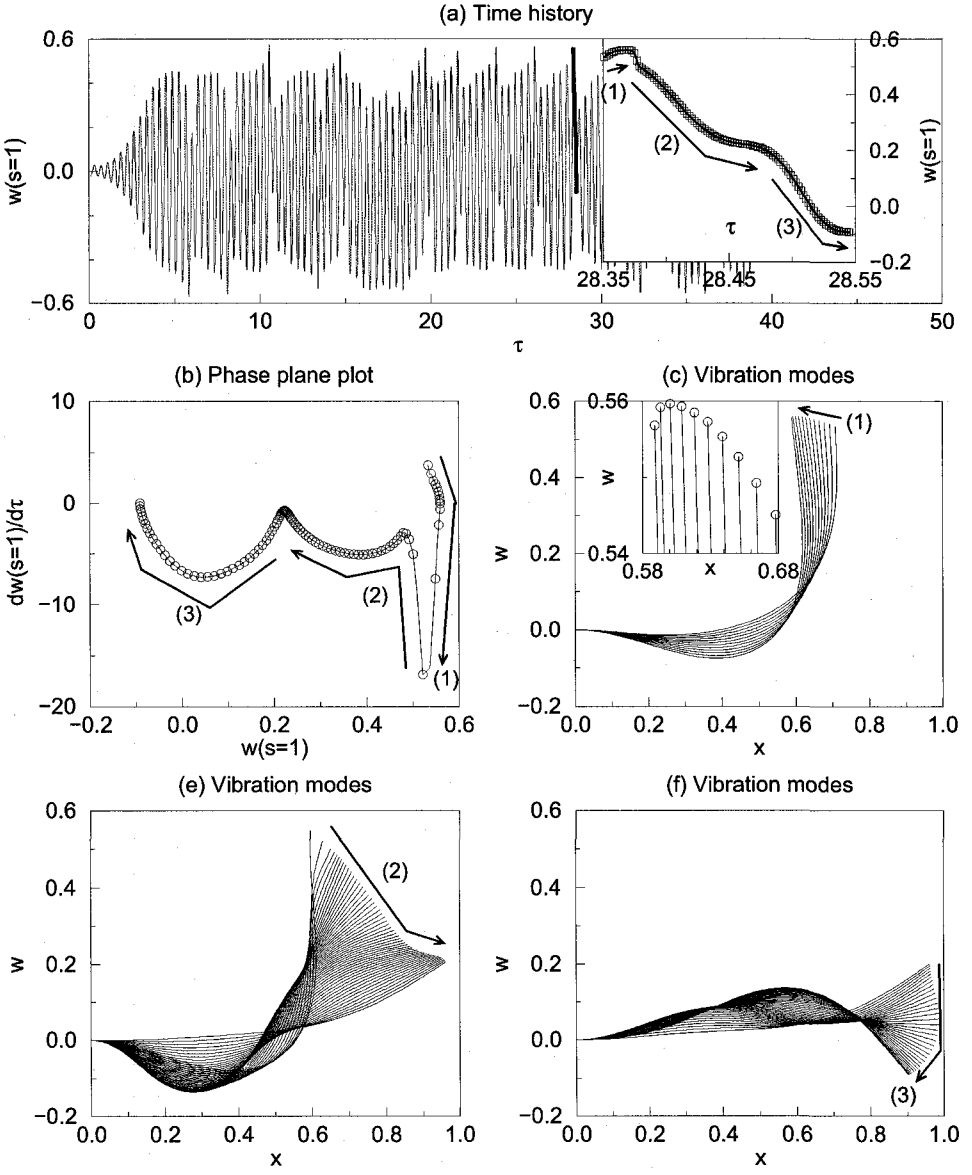

FIGURE 5.24. The occurrence of the spurs observed in Fig. 5.21. The parameters of the system are $\sigma_M = 0.01$, $s_M = 1$, $\mu = 0.2$, $U_R = 10.95$, $l_0 = 0.01$, $\alpha = 0.004$ and $C_D = 0$.

A conventional route to chaos cannot be identified from the bifurcation diagram of Fig. 5.23(a) for the system with a small additional concentrated mass at the trailing edge of the plate. Closer examination of the system dynamics regarding the onset of chaotic motions reveals that the rear part of the plate may whip forward, as illustrated

by the two deformed shapes of the plate shown in thicker lines in Fig. 5.23(c) for the vibration modes of the system at $U_{\mathrm{R}} = 10.49$; corresponding spikes in the phase plane plot can be observed in the blocked region in Fig. 5.23(h). The spikes in the phase plane plot can be more clearly observed in the two blocked regions in Fig. 5.23(i) for $U_{\mathrm{R}} = 10.95$; the occurrence of one of these spikes is carefully studied in Fig. 5.24, where the time history, a section of phase plane plot and the vibration modes of the system are presented. It can be seen in Fig. 5.24(b) that a spike occurs, at the point of the intersection of segments (1) and (2) in the section of the phase plane plot. Note that, segments (1) through (3) can also be identified in Figs. 5.24(a) and (c) through (f); no spike-like phenomena are observed in the time history and the vibration modes. That is, the spikes are likely not caused by numerical errors, as no corresponding jump or discontinuity is found in the time history and the vibration modes. Instead, as one can see from Figs. 5.24(c) and (d), the spike is caused by a jerk in the motion when the trailing edge of the plate is close to its local maximum amplitude (in positive sense for the specific spike studied in Fig. 5.24). That is, the small variations in the vibration modes are accompanied by large changes in the vibration velocity. Finally, it should be mentioned that the wrapped-around mode shapes predicted by the present theory may not be physically entirely correct in terms of modelling of the fluid flow in this case; nevertheless, the analysis herein provides a very interesting case of chaotic motions in conjunction with complex evolutions of the mode shapes of the system.

5.6. With a small oscillating incidence angle

One may already have noticed that the flapping motions of a real flag in wind is dynamically much richer than those predicted by the model of cantilevered flexible plates in axial flow in the basic configuration (see Chapter 4); it is therefore of interest to study the dynamics of the system when the undisturbed flow has some kind of an unsteady component, specifically a small oscillating component. For example, as shown in Fig. 5.25, the undistributed flow is considered to be not exactly parallel to the neutral plane of the plate (as compared to Fig. 2.1); although the velocity

of the undisturbed flow is still U, the angle of incidence between the plate and the undisturbed flow has the magnitude α_U and the frequency $f_{\alpha U}$.

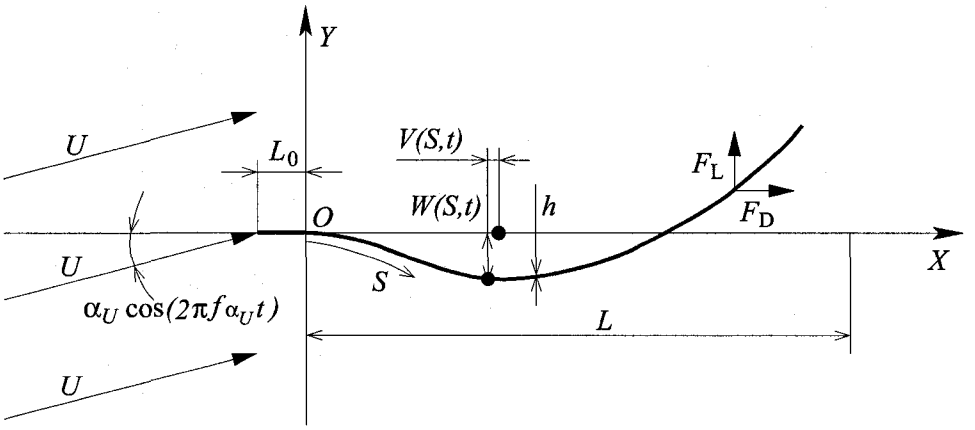

FIGURE 5.25. A cantilevered flexible plate in axial flow with a small oscillating incidence angle.

5.6.1. Modelling. With a small oscillating incidence angle, the undistributed flow velocity can be decomposed into two parts in the fixed X-Y coordinate system as shown in Fig. 5.25, i.e.,

$$\begin{cases} u_x = \cos\left[\alpha_U \cos\left(2\pi f^{\star}_{\alpha U}\tau\right)\right] & \text{in the } x \text{ direction,} \\ u_y = \sin\left[\alpha_U \cos\left(2\pi f^{\star}_{\alpha U}\tau\right)\right] & \text{in the } y \text{ direction,} \end{cases} \tag{5.26}$$

where u_x and u_y are, respectively, the flow velocity components in the x and y directions normalized by U; $f^{\star}_{\alpha U} = f_{\alpha U} T_{\mathrm{S}}$ (refer to Eq. (2.6)) is the nondimensional frequency of the oscillating incidence angle normalized using the solid time T_{S} defined in Eq. (2.11).

It follows that, when calculating the fluid loads, Eqs. (2.19) and (2.22) should respectively be modified to take into account both u_x and u_y as

$$\mathrm{rhs}_i = \left(\frac{\dot{v}_i}{U_{\mathrm{R}}} - u_x - v_{\mathrm{W}i}\right)\sin\alpha_i + \left(\frac{\dot{w}_i}{U_{\mathrm{R}}} - u_y - w_{\mathrm{W}i}\right)\cos\alpha_i, \tag{5.27}$$

$$\begin{aligned} \Delta p_i \;=\; & \left[\left(-\frac{\dot{v}_i}{U_{\mathrm{R}}} + u_x + v_{\mathrm{W}i}\right)\cos\alpha_i + \left(\frac{\dot{w}_i}{U_{\mathrm{R}}} - u_y - w_{\mathrm{W}i}\right)\sin\alpha_i\right]\frac{\gamma_i}{\Delta s} \\ & + \frac{1}{U_{\mathrm{R}}}\frac{\partial}{\partial\tau}\left(\sum_{j=1}^{i}\gamma_j\right). \end{aligned} \tag{5.28}$$

It should be emphasized that a simplified model of the vortical wake behind the cantilevered flexible plate, as discussed in Chapters 2 and 4, is adopted in this thesis. In the current investigation on an oscillating incidence angle, it is assumed for simplicity that the magnitude of the incidence angle α_U is so small that each individual wake vortex, once it is shed off the trailing edge of the plate, still moves downstream with the velocity of the undisturbed flow as if the angle of incidence were steady (zero).

5.6.2. Dynamics of the system when $f^{\star}_{\alpha_U} = 0$. Using the model developed for cantilevered flexible plates in axial flow with a small oscillating angle of incidence, it is convenient to first examine the dynamics of the system with $f^{\star}_{\alpha_U} = 0$, i.e., a fixed small angle of incidence. It should be mentioned that the current case may find its application in the design of the flexible control surface attached to a rigid wing (De Breuker et al., 2006), as illustrated in Fig. 1.1(c), where the cantilevered flexible plate is not always parallel to the undisturbed flow.

It can be seen in Fig. 5.26(a) that, as compared to the system in the basic configuration, the plate first buckles at low reduced flow velocities U_{R} before flutter takes place at a sufficiently high U_{R}, in the sense that a static deformation of the plate is found to arise. In the present case of a small incidence angle $\alpha_U = 5^{\circ}$, the critical reduced flow velocity is found to be $U_{\mathrm{Rc}} = 9.87$, which is slightly below the critical point of the case $\alpha_U = 0^{\circ}$ (i.e., the system in the basic configuration, when $U_{\mathrm{Rc}} = 9.92$). As shown in Fig. 5.26(b), before the onset of flutter, the amplitude of the static buckling grows as U_{R} increases; and the plate deforms in the first beam mode (see Chapter 4). On the other hand, when $U_{\mathrm{R}} > U_{\mathrm{Rc}}$, the vibration modes of the system, shown in Figs. 5.26(c) and (d), are found to be qualitatively the same as those of the system in the basic configuration (see Figs. 4.1(g) and 4.2(e)). However, in the current case, the vibration of the plate is not symmetric with respect to its neutral plane; instead, the buckling component can be observed in the vibration modes.

5.6.3. Dynamics of the system with a small oscillating incidence angle. When $f^{\star}_{\alpha_U} \neq 0$, rich dynamics of the system can be observed. The influence of

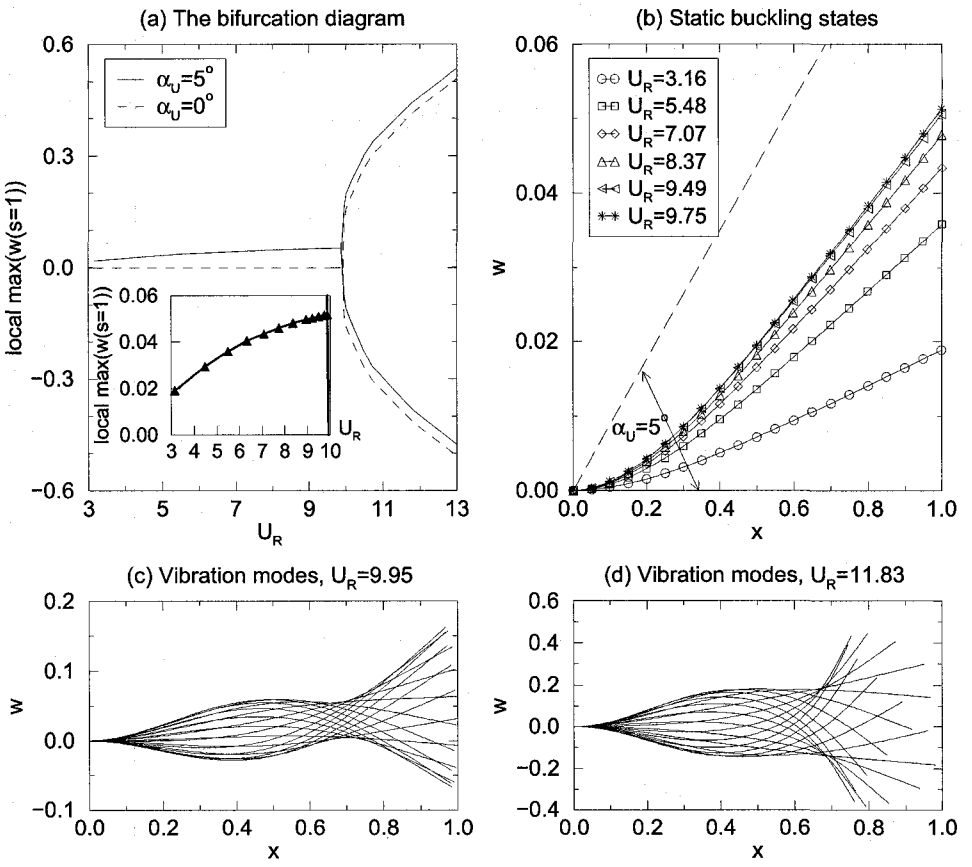

FIGURE 5.26. The dynamics of a cantilevered flexible plate in axial flow with a fixed small incidence angle, where $\alpha_U = 5°$ and $f^\star_{\alpha U} = 0$. The other parameters of the system are: $\mu = 0.2$, $l_0 = 0.01$, $\alpha = 0.004$ and $C_D = 0$.

α_U is studied in Fig. 5.27, in which the magnitude of the incidence angle is $\alpha_U = 5°$ and the frequency is swept from $f^\star_{\alpha U} = 0$ to $f^\star_{\alpha U} = 20.0$. Note that the reduced flow velocity U_R used in the frequency sweeping is $U_R = 8.94$, which is about 10% below the critical point of either the case where there is a fixed incidence angle of $\alpha_U = 5°$ (as seen in Fig. 5.26(a), $U_{Rc} = 9.87$) or the case where the system is in the basic configuration (i.e., the case of $\alpha_U = 0°$ and $f^\star_{\alpha U} = 0$, of which $U_{Rc} = 9.92$).

In Fig. 5.27(a), resonance phenomena in the frequency-response of the system can be observed. If the vibration amplitude of the system is evaluated at the tailing edge of the plate, i.e. the point $s = 1$, three local peaks can be found at $f^\star_{\alpha U} = 1.15$, 2.8 and 9.4. However, when observed at the mid-length point of the plate $s = 0.5$, the first two peaks shift to $f^\star_{\alpha U} = 0.95$, 2.81, respectively; moreover, the third peak disappears. It is evident that the primary resonance of the system occurs at $f^\star_{\alpha U} = 2.8$

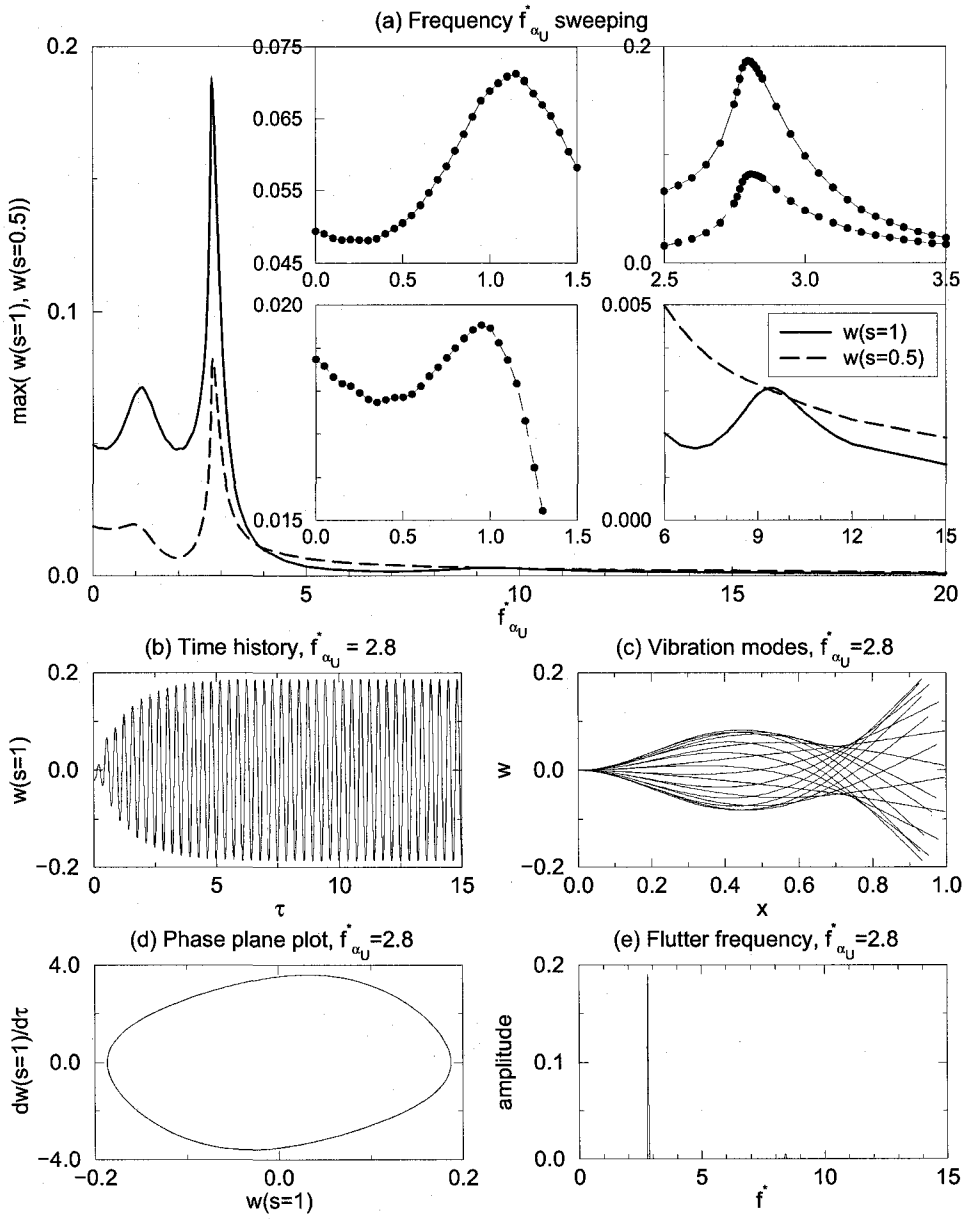

FIGURE 5.27. The vibration amplitudes of a cantilevered flexible plate in axial flow with a small oscillating incidence angle, where $\alpha_U = 5^{\circ}$ and the value of $f^{\star}_{\alpha_U}$ is swept from 0 to 12.0. The other parameters of the system are: $\mu = 0.2$, $U_{\mathrm{R}} = 8.94$, $l_0 = 0.01$, $\alpha = 0.004$ and $C_{\mathrm{D}} = 0$.

(or, $f^{\star}_{\alpha_U} = 2.81$ in terms of the amplitude at $s = 0.5$), where the plate vibrates with quite a large amplitude. The pattern of the frequency-response shows that an external excitation (Thomsen, 1997), i.e., the small oscillating incidence angle of the undisturbed flow, has been applied to the system. However, it should be noticed that, although the oscillation of the incidence angle is an external mechanism, the undisturbed flow and the plate are two inseparable parts of an integrated system; the

aero/hydro-dynamic forces caused by the fluid flow (with a small oscillating angle of incidence) depend on the motions of the plate. Therefore, it does not make sense to talk about the natural frequency of the plate without taking into account the fluid flow. Under these circumstances, one cannot expect the secondary resonances of the system to be related to the primary one *via* an integer relationship (either subharmonic or superharmonic). In particular, in the current case, the secondary resonances of the system can be found at $f^{\star}_{\alpha_U} = 1.15$ and 9.4 in terms of the amplitude at $s = 1$, and the ratios to the primary resonance of $f^{\star}_{\alpha_U} = 2.8$ are, respectively, 0.4107 and 3.357.

The dynamics of system is shown in Figs. 5.27(b) through (e) for the case $f^{\star}_{\alpha_U} = 2.8$; one can see that the vibration of the plate, at the primary resonance point, is very similar to that of the system in the basic configuration, shown in Fig. 4.1. Additionally, it is found that the system vibrates with only one frequency which is exactly the same as the excitation frequency, i.e., $f^{\star}_{\alpha_U}$.

The vibration modes of the system at various values of $f^{\star}_{\alpha_U}$ are shown in Fig. 5.28, where the deformed shapes of the plate are normalized by the maximum amplitude it can reach (not necessarily at $s = 1$ or $s = 0.5$). It is interesting to see that the vibration modes of the plate depend on the frequency of the oscillating angle of incidence. When $f^{\star}_{\alpha_U}$ is small, the plate vibrates in the first beam mode; however, beam modes of higher order participate in the vibration and become increasingly important in the dynamics as $f^{\star}_{\alpha_U}$ increases. Moreover, when the first and second beam modes are dominant in the dynamics of the system, the maximum amplitude of the plate takes place at $s = 1$; while, when beam modes of higher order become important, the maximum amplitude is observed somewhere in the middle part of the plate. It should be remarked that the complexity of these vibration modes of cantilevered flexible plates in axial flow with a small oscillating angle of incidence, as shown in Fig. 5.28, may give a good explanation for the rich dynamics observed for real flags in wind; that is a small unsteady component in the undisturbed flow may well be the underlying mechanism.

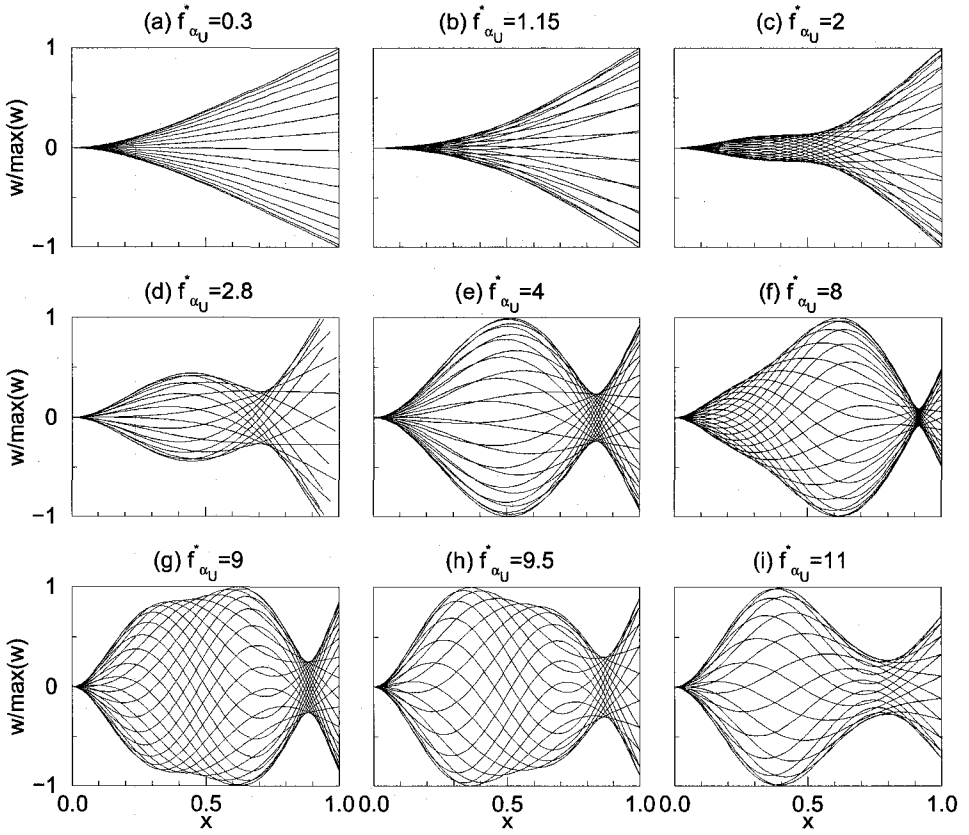

FIGURE 5.28. The vibration modes of a cantilevered flexible plate in axial flow with a small oscillating incidence angle, where $\alpha_U = 5^\circ$ and $f^\star_{\alpha_U}$ has various values. The other parameters of the system are: $\mu = 0.2$, $U_{\mathrm{R}} = 8.94$, $l_0 = 0.01$, $\alpha = 0.004$ and $C_{\mathrm{D}} = 0$.

When examining the frequency-response in conjunction with the vibration modes of the system, as respectively shown in Figs. 5.27(a) and 5.28, more important observations with regard to the dynamics of the system can be made. First, since the vibration mode of the system changes with varying $f^\star_{\alpha_U}$, the resonance points of the system depend on the point of observation. For example, the secondary resonance occurs at $f^\star_{\alpha_U} = 1.15$ if it observed at the point $s = 1$, while it is located at $f^\star_{\alpha_U} = 0.95$ if the point $s = 0.5$ is chosen for observing the frequency-response of the system. Second, at the primary resonance point $f^\star_{\alpha_U} = 2.8$ (or $f^\star_{\alpha_U} = 2.81$ in terms of the vibration amplitude at $s = 0.5$), the plate vibrates in the second beam mode, and the frequency-response curve slightly bends to the left, which implies a weak softening-type nonlinearity in the fluid-structure interaction system. In contrast, at the secondary resonance point $f^\star_{\alpha_U} = 1.15$ (or $f^\star_{\alpha_U} = 0.95$ in terms of the vibration

amplitude at $s = 0.5$), the frequency-response curve slightly bends to the right; therefore, a hardening-type nonlinearity arises when the plate vibrates in the first beam mode at low $f^{\star}_{\alpha U}$. It should be mentioned that investigations on the properties of the nonlinearity in a two-dimensional cantilevered flexible plate (modelled using the inextensible assumption), instead of the whole fluid-structure interaction system, were previously conducted by Anderson et al. (1996) and Tang et al. (2003), and similar conclusions to the current ones have been reached (see Chapter 2). Finally, when $f^{\star}_{\alpha U}$ is close to zero, the plate vibrates in the first beam mode with an amplitude smaller than that of the static buckling state obtained using $f^{\star}_{\alpha U} = 0$.

5.7. Two identical plates aligned parallel to each other

It is of interest to examine the dynamics of cantilevered flexible plates in axial flow in the case of a multiple-plates assembly; for example, as illustrated in Fig. 5.29, we see two identical plates aligned parallel to each other in axial flow and separated by a distance D_{P}. In the experiments by Zhang et al. (2000), it was observed that the two plates may flutter in-phase when D_{P} is small; while they are locked in out-of-phase oscillations for relatively large values of D_{P}. As D_{P} increases further, the coupling between the two plates diminishes, and each plate flutters independently. Some of these experimental observations were preliminarily confirmed by the theoretical work of Farnell et al. (2004), who used a Navier-Stokes solver for the aero/hydro-dynamics

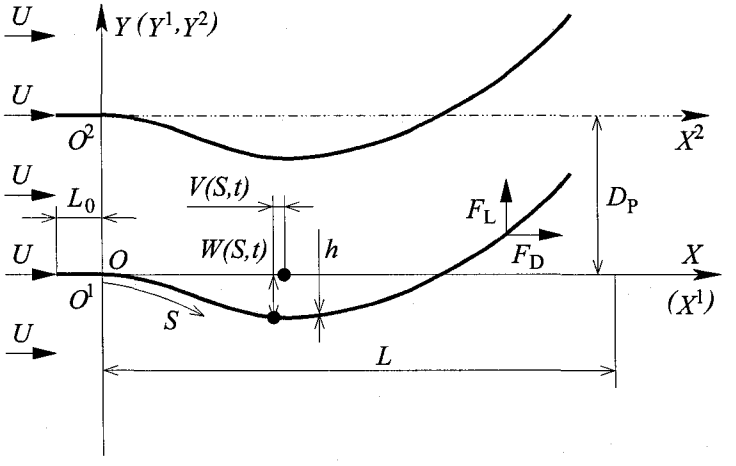

FIGURE 5.29. Two identical cantilevered flexible plates aligned parallel to each other in axial flow.

and modelled each flexible plate as a so-called *N-tuple pendulum.* In the experiments of Zhang et al. (2000) and the theoretical work of Farnell et al. (2004), the two plates are actually placed in an axial channel. Instead, in this thesis, the case of two cantilevered flexible plates aligned parallel to each other in *open* (unconfined) axial flow is studied.

5.7.1. Modelling and solution method. The current system involving multiple cantilevered flexible plates in axial flow may be categorized as the blade-blade interaction problem (Yao and Liu, 1998), which concerns the interactions of multiple airfoils/wings in either the aligned-in-parallel configuration or the tandem configuration. Jones and Platzer (1995) solved their two airfoil in tandem problem without considering the impingement of the vortices shed from the upstream airfoil upon the downstream one. Improved schemes were developed by Jones and Platzer (1997) and Yao and Liu (1998) to prevent any moving vortex from penetrating into the body of the (downstream) airfoil of finite thickness. However, in the current problem of two thin plates of zero thickness aligned parallel to each other in axial flow, it is not necessary to consider the vortex impingement because the vortices shed from the trailing edge of either one of the two plates never approaches the other plate.

As shown in Fig. 5.29, it is assumed that the two identical cantilevered flexible plates originally lie along the X^1 and X^2 axes, respectively; the distance between X^1 and X^2 is D_{P}, or d_{P} when normalized using the length of the flexible plate L. The fixed X-Y coordinate system is based on the first plate, coinciding with the X^1-Y^1 system. The two plates have the same equation of motion, namely Eq. (2.7) in the nondimensional form (see Chapter 2), except that the transverse displacements of the second plate $w^2(s)$ include a fixed constant part d_{P}. As for the aero/hydrodynamics part of the system, following the scheme utilized by Yao and Liu (1998), the bound vortices and the latest wake vortices of both plates are simultaneously solved, regarding the satisfaction of the Kutta-Joukowski condition and the respect

of Kelvin's theorem for either plate, from

$$\begin{bmatrix} \mathbb{A}^{1,1} & \mathbb{A}^{1,2} \\ \mathbb{A}^{2,1} & \mathbb{A}^{2,2} \end{bmatrix} \begin{Bmatrix} \mathbf{V}^1 \\ \mathbf{V}^2 \end{Bmatrix} = \begin{Bmatrix} \mathbf{R}^1 \\ \mathbf{R}^2 \end{Bmatrix}, \tag{5.29}$$

where, $\mathbb{A}^{m,n}$ $(m = 1, 2,\ n = 1, 2)$ is the matrix of influence coefficients of plate n to plate m, which is defined by (refer to Eq. (2.17))

$$\mathbb{A}^{m,n} = \begin{bmatrix} \alpha_{m_1,n_1} & \alpha_{m_1,n_2} & \cdots & \alpha_{m_1,n_N} & \alpha_{m_1,n_{N+1}} \\ \alpha_{m_2,n_1} & \alpha_{m_2,n_2} & \cdots & \alpha_{m_2,n_N} & \alpha_{m_2,n_{N+1}} \\ \vdots & \vdots & \ddots & \vdots & \vdots \\ \alpha_{m_N,n_1} & \alpha_{m_N,n_2} & \cdots & \alpha_{m_N,n_N} & \alpha_{m_N,n_{N+1}} \\ \delta_{m,n} & \delta_{m,n} & \cdots & \delta_{m,n} & \delta_{m,n} \end{bmatrix}. \tag{5.30}$$

In Eq. (5.30), $\delta_{m,n}$ is the Dirac delta, and α_{m_i,n_j} is calculated by

$$\alpha_{m_i,n_j} = \frac{(y_{\mathrm{C}i}^m - y_{\mathrm{V}j}^n)\sin\alpha_i^m + (-x_{\mathrm{C}i}^m + x_{\mathrm{V}j}^n)\cos\alpha_i^m}{2\pi\left[(y_{\mathrm{C}i}^m - y_{\mathrm{V}j}^n)^2 + (x_{\mathrm{C}i}^m - x_{\mathrm{V}j}^n)^2\right]}. \tag{5.31}$$

In Eq. (5.29), $\mathbf{V}^m$ $(m = 1, 2)$ is the vector consisting of the bound vortices γ_i^m $(i = 1, 2, \cdots, N)$ and the latest wake vortex γ_{N+1}^m of plate m, and $\mathbf{R}^m$ is the right-hand-side vector of plate m; they are, respectively, defined by

$$\mathbf{V}^m = (\gamma_1^m, \gamma_2^m, \cdots, \gamma_N^m, \gamma_{N+1}^m)^{\mathrm{T}}, \tag{5.32}$$

$$\mathbf{R}^m = (\mathrm{rhs}_1^m, \mathrm{rhs}_2^m, \cdots, \mathrm{rhs}_N^m, \gamma^{\star m})^{\mathrm{T}}, \tag{5.33}$$

where

$$\mathrm{rhs}_i^m = (\frac{\dot{v}_i^m}{U_{\mathrm{R}}} - 1 - {v_{\mathrm{W}}}_i^m)\sin\alpha_i^m + \left(\frac{\dot{w}_i^m}{U_{\mathrm{R}}} - {w_{\mathrm{W}}}_i^m\right)\cos\alpha_i^m, \tag{5.34}$$

$$\gamma^{\star m;k+1} = \sum_{i=1}^{N} \gamma_i^{m;k}. \tag{5.35}$$

In Eq. (5.34), $(v,w)_{\mathrm{W}_i}^{m}$ is the wake-induced flow velocity at the ith collocation point of plate m, which should be calculated by

$$(v,w)_{\mathrm{W}_i}^{m}=\sum_{n=1}^{2}\sum_{j=1}^{N_{\mathrm{W}}}\frac{\gamma_{\mathrm{W}_j}^{n}}{2\pi}\frac{(y_{\mathrm{C}_i}^{m}-y_{\mathrm{W}_j}^{n},-x_{\mathrm{C}_i}^{m}+x_{\mathrm{W}_j}^{n})}{(y_{\mathrm{C}_i}^{m}-y_{\mathrm{W}_j}^{n})^2+(x_{\mathrm{C}_i}^{m}-x_{\mathrm{W}_j}^{n})^2};\tag{5.36}$$

that is, the wakes of both plates should be considered in the calculation of the wake-induced flow velocity $(v,w)_{\mathrm{W}_i}^{m}$.

When the distribution of the discrete vortices on each plate is available, the pressure difference across plate m can be calculated by (refer to Eq. (2.22))

$$\begin{aligned}\Delta p_i^m &= \left[\left(-\frac{\dot{v}_i^m}{U_{\mathrm{R}}}+1+v_{\mathrm{W}_i}^m+v_{\Gamma_i}^m\right)\cos\alpha_i^m+\left(\frac{\dot{w}_i^m}{U_{\mathrm{R}}}-w_{\mathrm{W}_i}^m-w_{\Gamma_i}^m\right)\sin\alpha_i^m\right]\frac{\gamma_i^m}{\Delta s}\\ &+\frac{1}{U_{\mathrm{R}}}\frac{\partial}{\partial\tau}\left(\sum_{j=1}^{i}\gamma_j^m\right),\end{aligned}\tag{5.37}$$

and then Eq. (2.23) is used to calculate the fluid loads $f_{\mathrm{L}_i}^{m}$ and $f_{\mathrm{D}_i}^{m}$ acting on plate m. Note that, in Eq. (5.37), the wake-induced flow velocity $(v,w)_{\mathrm{W}_i}^{m}$ should be calculated according to Eq. (5.36), and the flow velocity induced by the bound vortices on the other plate n, i.e., $(v,w)_{\Gamma_i}^{m}$, which is calculated by

$$(v,w)_{\Gamma_i}^{m}=\sum_{j=1}^{N}\frac{\gamma_{\mathrm{V}_j}^{n}}{2\pi}\frac{(y_{\mathrm{C}_i}^{m}-y_{\mathrm{V}_j}^{n},-x_{\mathrm{C}_i}^{m}+x_{\mathrm{V}_j}^{n})}{(y_{\mathrm{C}_i}^{m}-y_{\mathrm{V}_j}^{n})^2+(x_{\mathrm{C}_i}^{m}-x_{\mathrm{V}_j}^{n})^2},\tag{5.38}$$

should also be considered.

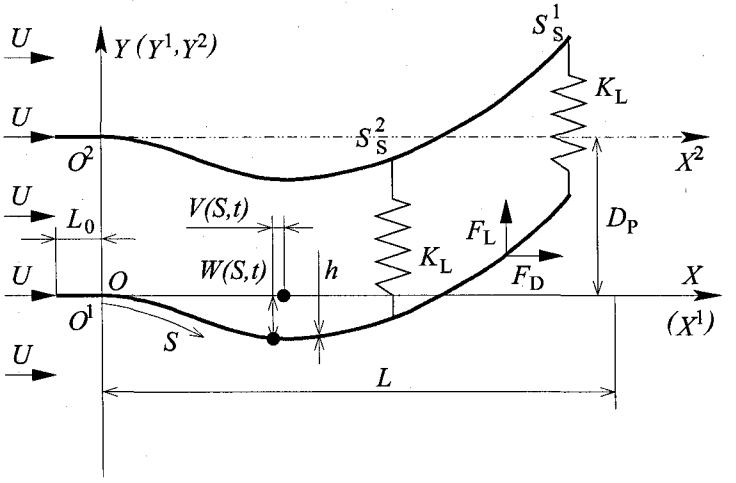

FIGURE 5.30. Two identical cantilevered flexible plates aligned parallel to each other in axial flow with virtual spring connections.

Besides the original model developed for two identical cantilevered flexible plates aligned parallel to each other in axial flow, an in-phase model is also considered. That is, as shown in Fig. 5.30, two virtual spring connections are taken into account, and the *lift* force acting on plate m should be calculated by

$$\overline{f}_{\mathrm{L}i}^{\,m} = f_{\mathrm{L}i}^{\,m} \pm k_{\mathrm{L}} \left(w^2 - w^1 - d_{\mathrm{P}}\right) \delta\left(s - s_{\mathrm{S}}^1\right) \pm k_{\mathrm{L}} \left(w^2 - w^1 - d_{\mathrm{P}}\right) \delta\left(s - s_{\mathrm{S}}^2\right), \quad (5.39)$$

where k_{L} is the nondimensional stiffness of the spring (of the linear type, see Eq. (5.10) for the definition); $s_{\mathrm{S}}^{1,2}$ are the locations of the spring connections. Note that, the "+" sign is used when $m = 1$; while, the "−" sign when $m = 2$.

The consideration of the virtual spring connections is supposed to force the two plates to always oscillate in-phase. When they indeed oscillate in-phase, the distance between the two plates everywhere along the whole length of the plates is exactly d_{P}, and $w^2 - w^1 - d_{\mathrm{P}} \equiv 0$. That is, no spring force acts on the plates. The value of the spring stiffness should be sufficiently large in order to avoid the influence of the springs on the dynamics of the system. In the current investigation, $k_{\mathrm{L}} = 1.0 \times 10^6$ is used; refer to the dynamics of the cantilevered flexible plate with an additional spring support studied in Figs. 5.11 and 5.13, where much smaller values of k_{L} are considered. Moreover, the number and locations of spring connections are determined by the dynamics of a single cantilevered flexible plate in axial flow as studied in Chapter 4. When the mass ratio μ of the single-plate system is small, say $\mu < 0.6$, the plate vibrates in the second beam mode and a quasi-node can be observed at about three-quarters of the plate length (see Figs. 4.1(g) and (h)). Therefore, two virtual connections can be respectively placed at $s_{\mathrm{S}}^1 = 1$ and $s_{\mathrm{S}}^2 = 0.75$.

5.7.2. Dynamics of the system with two identical plates aligned-in-parallel. The flutter boundaries of the system with two identical plates aligned parallel to each other, respectively obtained using the "original" model (without constraining springs) and the in-phase model (with springs), are presented in Fig. 5.31(a).

It can be seen that the system oscillating in-phase is always more stable than the system oscillating out-of-phase, as the original model predicts a flutter boundary below the one obtained using the in-phase model.

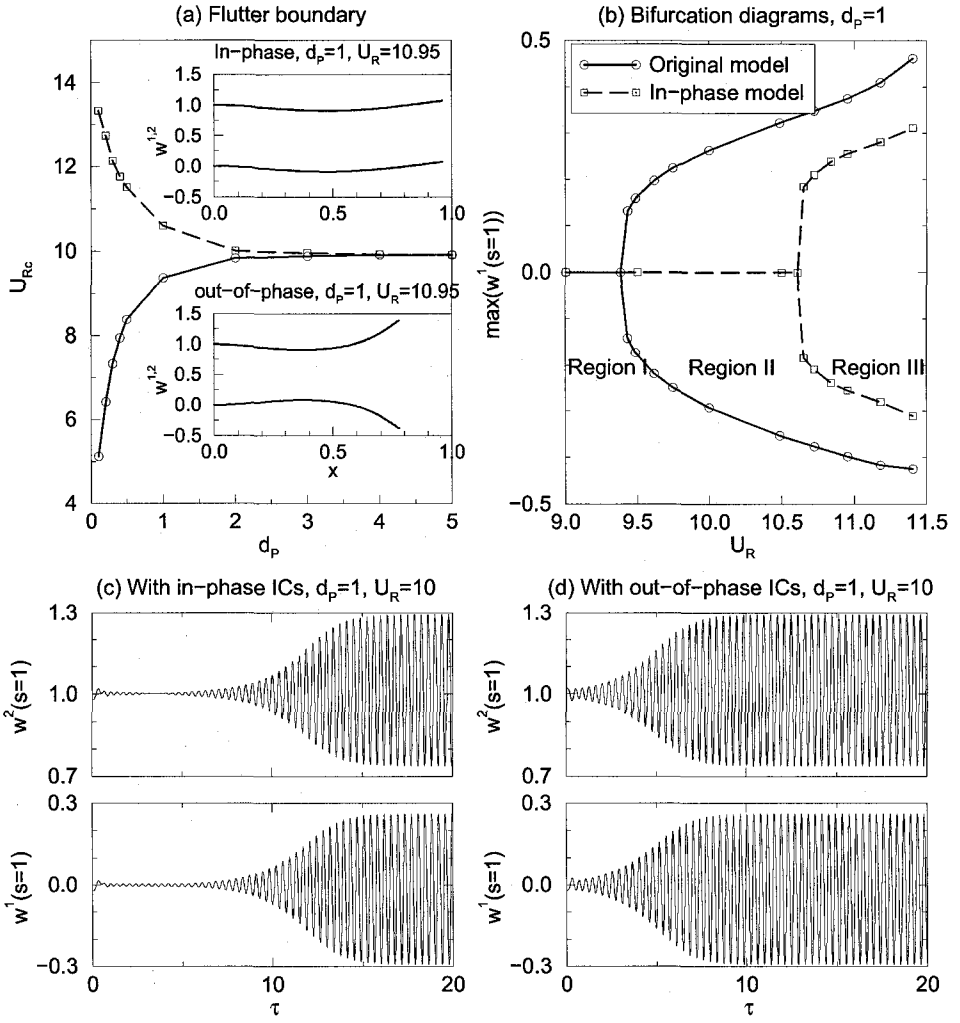

FIGURE 5.31. The instability boundary and the bifurcation diagram of two identical cantilevered flexible plates aligned parallel to each other in axial flow. The in-phase initial conditions are: $q_1^{1,2;k=0} = -1.0 \times 10^{-2}$, $q_{i\neq 1}^{1,2;k=0} = 0$ and $\dot{q}_i^{1,2;k=0} = 0$. The out-of-phase initial conditions are: $q_1^{1;k=0} = -1.0 \times 10^{-2}$, $q_1^{2;k=0} = 1.0 \times 10^{-2}$, $q_{i\neq 1}^{1,2;k=0} = 0$ and $\dot{q}_i^{1,2;k=0} = 0$. The other parameters of the system are: $\mu = 0.2$, $l_0 = 0.01$, $\alpha = 0.004$ and $C_D = 0$.

When d_P is small, the stability of the system depends on the separation distance of the two plates; the smaller the value of d_P, the more significant is its influence. On the other hand, when $d_P = 5$, no difference can found between the original model and the in-phase model, as well as between the models of the two-plate system and

the model of the system in its basic configuration (i.e., a single plate) in that all of them predict the same critical reduced flow velocity at $U_{\mathrm{Rc}} = 9.92$.

One can also see in Fig. 5.31(a) that, as compared to the system in the basic configuration, with decreasing values of d_{P}, the two-plate system becomes increasingly less stable when it is oscillating in the out-of-phase modes; while, on the contrary, increasingly more stable in the in-phase modes. It should be mentioned that the two plates vibrating out-of-phase can be viewed as a case of a single plate in the presence of ground, with the ground surface coinciding with the mid-plane of the two plates, i.e., the $y = d_{\mathrm{P}}/2$ plane; the other plate is just the mirror-image of the first one with respect to the ground surface. With ground effects (Mateescu, 1995), a larger aero/hydro-dynamic load (*lift*) can be expected; and, the plate becomes less stable.

It should be emphasized that the spring connections considered in the in-phase model are virtual ones; no spring forces act on the plates when the plate vibrates in-phase because the separation distance between the two plates are always d_{P} (the original lengths of the springs). Through extensive tests, it is found that in-phase solutions cannot be obtained using the original model. Moreover, if while working with the in-phase model of the system the virtual spring connections are broken in the middle of the simulation after a stable in-phase solution has already been achieved, one finds that the dynamics of system (in-phase oscillations) is altered and finally converges to the dynamics of the system obtained by using the original model (out-of-phase oscillations). As shown in Fig. 5.31(b), two bifurcation diagrams are obtained using (i) the original model and (ii) the in-phase model. Because the spring connections considered are virtual ones, the in-phase model is indeed identical to the original model when the two plates vibrate in-phase. Therefore, the two bifurcation diagrams shown in Fig. 5.31(b) can be viewed as a combined one for the system with two plates. That is, the in-phase state of the system is the unstable branch (denoted by the dashed-line) of its dynamics, which cannot be predicted by the original model, but which can nevertheless be captured with the aid of the virtual spring connections (i.e., using the in-phase model).

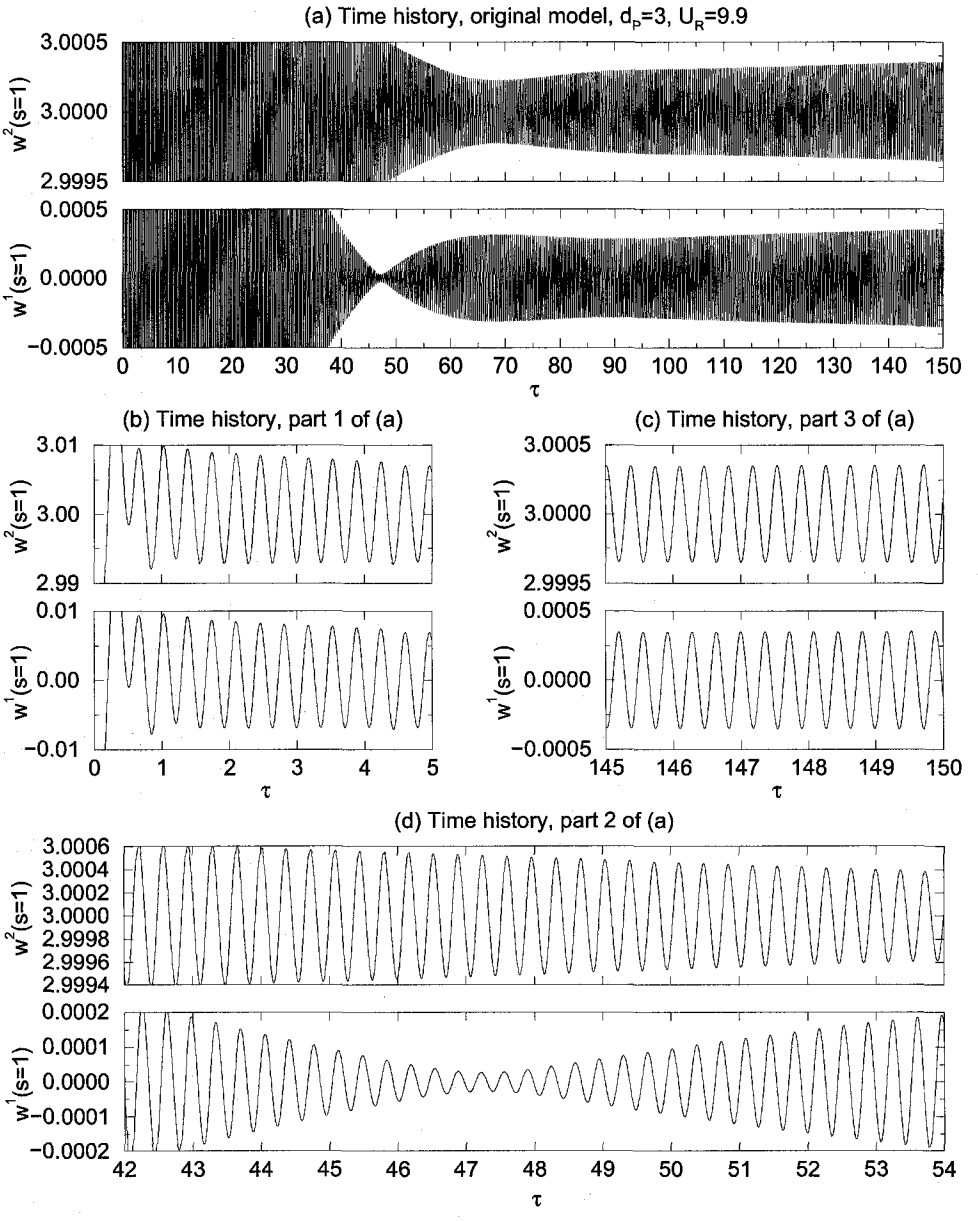

FIGURE 5.32. The time history of two identical cantilevered flexible plates parallel-aligned in axial flow at critical point. The other parameters of the system are: $\mu = 0.2$, $l_0 = 0.01$, $\alpha = 0.004$ and $C_D = 0$. The in-phase initial conditions used are the same as those defined in the caption of Fig. 5.31.

Both the original model and the in-phase model are studied with various initial conditions, either in-phase or out-of-phase. With out-of-phase initial conditions, the virtual springs in the in-phase model become effective, and after the transients have died out, in-phase vibrations result, as expected. On the other hand, without the virtual springs, the original model always predicts out-of-phase vibrations, no matter what initial conditions are used, as shown in Figs. 5.31(c) and (d) for $U_R = 10$. It

is of interest to observe in Fig. 5.31(d) that the two plates always vibrate out-of-phase if they are started with out-of-phase initial conditions. In contrast, as shown in Fig. 5.31(c), when in-phase initial conditions are used, the two plates gradually reorganize the phase relationship between them and at last out-of-phase vibration results; a longer transient, as compared to the dynamics shown in Fig. 5.31(d), can be observed in Fig. 5.31(c) due to the phase reorganization.

The evolution of the phase relationship between the two plates can be seen more clearly in Fig. 5.32, in the case of $d_{\mathrm{P}} = 3$ and $U_{\mathrm{R}} = 9.9$, obtained by means of the original model with in-phase initial conditions. Note that, when $d_{\mathrm{P}} = 3$, the critical points of original model and the in-phase model are, respectively, $U_{\mathrm{Rc}} = 9.87$ and 9.95. These two critical points are very close to each other in that the coupling between the two plates is attenuated for the value of d_{P} involved. For the results of Fig. 5.32, the reduced flow velocity U_{R} is close to the critical point; as one can see in Fig. 5.32(a), there is a long transient as expected. At the beginning, since in-phase initial conditions have been used (see the caption of Fig. 5.31), the two plates vibrate in-phase with the same amplitude, as shown in Fig. 5.32(b). Moreover, because $U_{\mathrm{R}} = 9.9$ is below the in-phase critical point, the vibration amplitudes of both plates decrease. As time elapses, a phase difference between the two plates emerges and grows, as shown in Fig. 5.32(d). During the process of phase reorganization, the vibration amplitudes of the two plates are different. Additionally, as the vibration amplitude of one plate decreases with time, that of the other one increases. A close examination of Fig. 5.32(d) reveals that the transition from in-phase motions to out-of-phase motions is not achieved at one stroke from 0 to π in terms of phase difference. For example, a significant phase difference can be observed for $42 < \tau < 43$ and $53 < \tau < 54$, while the two plates vibrate almost in-phase for $47 < \tau < 48$. Nevertheless, when a sufficiently long time has elapsed, the two plates at last vibrate out-of-phase (a phase difference of π) with the same amplitude, as shown in Fig. 5.32(c). Moreover, because the current U_{R} is larger than the out-of-phase critical point, the vibration amplitudes of both plates grow (note that the time histories of Fig. 5.32(a) show that the system is still in a transient state).

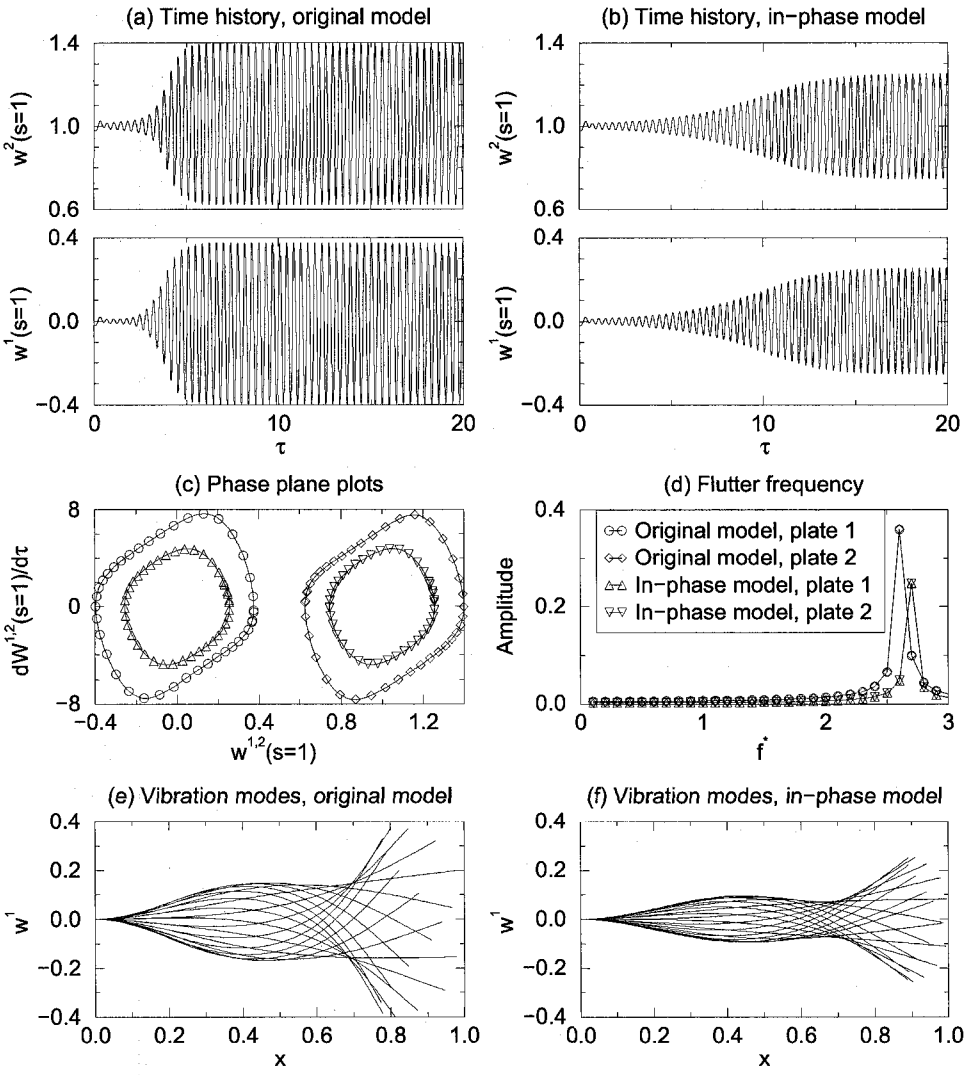

FIGURE 5.33. The post-critical behavior of two identical cantilevered flexible plates parallel-aligned in axial flow. The parameters of the system are: $d_{\mathrm{P}} = 1$, $\mu = 0.2$, $U_{\mathrm{R}} = 10.95$, $l_0 = 0.01$, $\alpha = 0.004$ and $C_{\mathrm{D}} = 0$.

The post-critical dynamics of the two-plate system are studied in Fig. 5.33 for $d_{\mathrm{P}} = 1$ and $U_{\mathrm{R}} = 10.95$, where both the original model and the in-phase model predict stable limit cycle oscillations. As one can observe in Figs. 5.33(a) and (b), the amplitude of the out-of-phase vibrations is larger than that of the in-phase vibrations. This is because the value of the out-of-phase critical point is smaller than the in-phase one, as shown in Figs. 5.31(a) and (b). When vibrating in-phase, the dynamics of either of the two plates is exactly the same, except that the transverse displacements of plate 2 have a constant part d_{P}; moreover, either plate undergoes symmetrical vibrations with respect to its own neutral plane. On the other hand, when the two

plates vibrate out-of-phase, the dynamics of either plate is the mirror image of the other one. However, as one can see in Figs. 5.33(a), (c) and (e), as well as more clearly in Figs. 5.31(c), the vibrations of either plate are not symmetrical with respect to its own neutral plane; a small buckling in the direction away from the other plate can be observed superposed on the limit cycle oscillations. Regardless of the difference discussed above, one can see in Fig. 5.33 that the dynamics of the two-plate system, obtained with either the original model or the in-phase model, is qualitatively the same in terms of the time history, flutter frequency and vibration modes. Moreover, as compared to the system in the basic configuration (a single plate) shown in Fig. 4.1, the dynamics of either of the two plates in Fig. 5.33 is qualitatively the same.

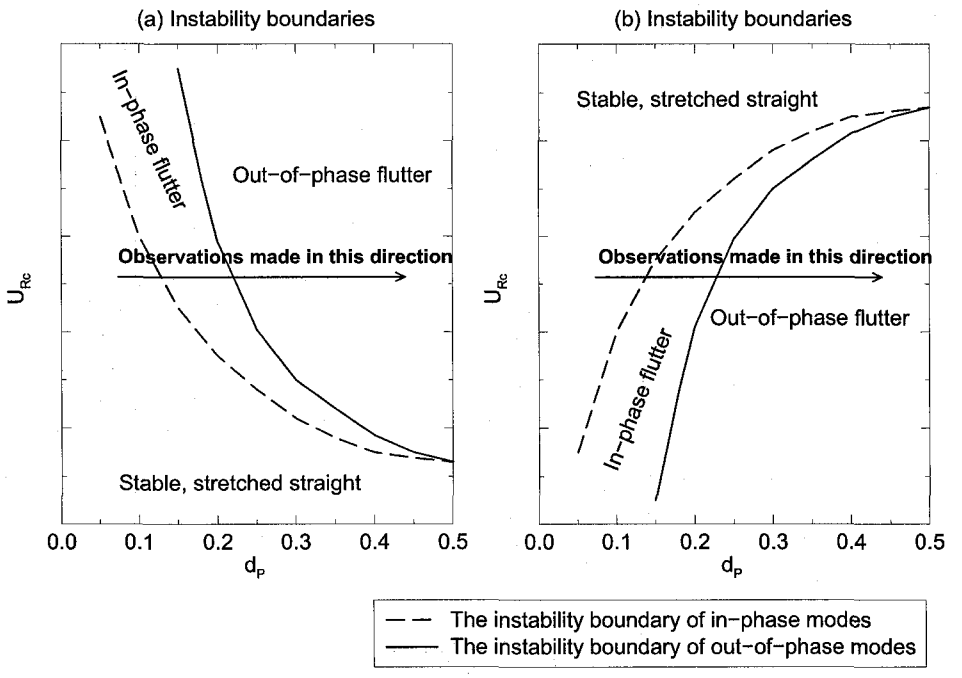

FIGURE 5.34. The sketches of the instability boundaries of the work by Zhang et al. (2000) and Farnell et al. (2004).

It is of interest to compare the results obtained with the present theory with previous experimental observations (Zhang et al., 2000) and theoretical predictions (Farnell et al., 2004). In the work by Zhang et al. (2000) and Farnell et al. (2004), both in-phase vibrations (without the aid of the virtual springs) and out-of-phase vibrations were reported; and, from their published data, two possible sets of bifurcation diagrams can be sketched as shown in Figs. 5.34(a) and (b), respectively. That is, with a fixed value of U_R (as Zhang et al. (2000) and Farnell et al. (2004) did in their

work), in-phase vibrations are first observed when the separation distance d_P is small, while the two plates are locked in out-of-phase vibrations when d_P exceeds a relatively larger value. Although not explicitly specified by Zhang et al. (2000) and Farnell et al. (2004), it is not likely that the two-plate system, with a fixed value of d_P, remains in the stretched-straight state at higher values of U_R and that it undergoes flutter at lower ones. Therefore, the sketch of bifurcation diagrams shown in Fig. 5.34(b) can be excluded. Under these circumstances, one can conclude from the sketch of the bifurcation diagrams in Fig. 5.34(a) that the system oscillating out-of-phase is more stable than the system oscillating in-phase, which is completely opposite to the observations made in this thesis. The underlying mechanism of this qualitative difference may be very complicated; however, a possible explanation is that, in the present computations, the fluid flow is supposed to be inviscid and the two plates are in unconfined axial flow. In the experiments conducted by Zhang et al. (2000) and the theory of Farnell et al. (2004), which was based on a Navier-Stokes solver, however, both viscosity and confinement are naturally in place in the experiments or taken into account in the analytical model. Moreover, the size of the channel in the work by Zhang et al. (2000) and Farnell et al. (2004) is indeed small, say, not as large as 1 when normalized by the plate length; this lateral width is fixed when the separation distance between the two plates is altered. Therefore, the viscosity of the fluid and the separation between the two plates, as well as between each plate and either of the two parallel solid walls, may well have profound and complex influence on the dynamics of the system.

Chapter 6

Energy Transfer and Design of Flutter-Mill

6.1. Introduction

In this chapter, we go back to cantilevered flexible plates in axial flow set up in the basic configuration and we investigate the dynamics of the system from the point of view of energy transfer between the plate and the surrounding fluid flow. When flutter takes place, energy is pumped into the plate from the fluid flow, and this can be used as a criterion of the onset of the (dynamic) instability (Balint and Lucey, 2005). Moreover, when stable limit cycle oscillations are observed in the dynamics of the system, balanced states of the energy transfer process, over the whole length of the plate and in the time-averaged sense, are attained between the energy extracted by the plate from the fluid flow and internal dissipation within the plate. We first examine the energy transfer under various flow conditions: with the reduced flow velocity U_{R} well below the critical point U_{Rc}, then around U_{Rc}, and finally above U_{Rc}. The energy transfer, first at various locations along the length of the plate, and then in terms of various vibration modes, is studied.

Based on the analysis of energy transfer, a new energy-harvesting concept, the flutter-mill, utilizing the self-induced vibrations (the flutter motions) of a cantilevered thin flexible plate in axial flow is proposed. As illustrated in Fig. 6.1, a plate made of

flexible material with embedded conductors is placed between two parallel magnetic panels. When flutter takes place, the motion of each conductor in the magnetic field generates an electric potential difference between its upstream and downstream ends. At this stage, the performance of the energy-harvesting device is preliminarily studied, without extensive optimization in the multiparameter space of the system. However, design considerations in the light of the dynamics of cantilevered flexible plates in axial flow, which may be in the basic plain configuration or in modified versions (for example, with an additional spring support and/or concentrated mass), are touched upon.

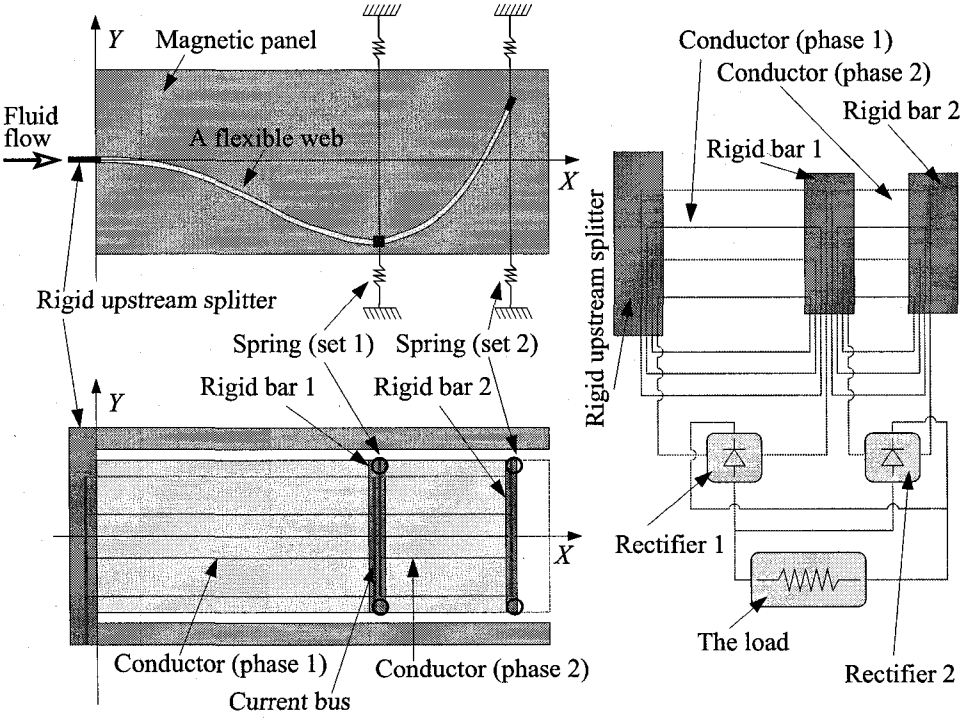

FIGURE 6.1. A schematic diagram of a flutter-mill.

6.2. Energy transfer

6.2.1. The quantities used in the analysis of energy transfer. To study the energy transfer between the cantilevered flexible plate and the surrounding fluid flow, it is convenient to use the equation of motion of the plate in the form of Eq. (2.4). That is, the fluid load f_D in the longitudinal direction is incorporated into the tension

term in the equation of motion. To this end, the nondimensional equation of motion of the plate, i.e., Eq. (2.7), is rewritten as

$$\frac{1}{\mu {U_{\mathrm{R}}}^2}\left\{\ddot{w}+\left(1+\alpha\frac{\partial}{\partial\tau}\right)\left[w''''\left(1+w'^2\right)+4w'w''w'''+w''^3\right]-\left(T^\star w'\right)'\right\}=f_{\mathrm{L}}, \quad (6.1)$$

where $T^\star$ is the nondimensional tension (refer to Eq. (2.5)) in the plate, defined by

$$T^\star=\int_s^1\left(\mu {U_{\mathrm{R}}}^2 f_{\mathrm{D}}-\ddot{v}\right)\,ds. \quad (6.2)$$

Note that v in Eq. (6.2) is the nondimensional longitudinal displacement of the plate defined in Eq. (2.8). Moreover, as defined in Eq. (2.24), the longitudinal fluid load f_{D} should take into account both the inviscid drag originating from the decomposition of the pressure difference across the plate and the viscous drag.

From Eq. (6.1), the nondimensional power $P^\star_{\mathrm{F}i}$ of the work done by the transverse fluid load $f_{\mathrm{L}i}$ on the ith panel, in the sense of per unit length along the spanwise dimension of the plate, can be calculated from

$$P^\star_{\mathrm{F}i}=\left[f_{\mathrm{L}i}\Delta s\right]\dot{w}(s_i); \quad (6.3)$$

and the nondimensional (accumulated) work $W^\star_{\mathrm{F}i}$ on the ith panel from

$$W^\star_{\mathrm{F}i}=\int_0^\tau\left[f_{\mathrm{L}}\Delta s\right]\dot{w}(s_i)\,d\tau. \quad (6.4)$$

It follows that, over the whole length of the plate, the nondimensional total power $\widehat{P}^\star_{\mathrm{F}}$ and the nondimensional (accumulated) total work $\widehat{W}^\star_{\mathrm{F}}$ can, respectively, be calculated by

$$\widehat{P}^\star_{\mathrm{F}}=\sum_{i=1}^{N}P^\star_{\mathrm{F}i}, \qquad \widehat{W}^\star_{\mathrm{F}}=\sum_{i=1}^{N}W^\star_{\mathrm{F}i}. \quad (6.5)$$

According to the nondimensionalization scheme defined in Eq. (2.6), the fluid load is normalized by $\rho_{\mathrm{F}}U^2$. Moreover, the length of the flexible plate L and the characteristic solid time T_{S} are, respectively, uniformly used as the length and time scales of the fluid-structure interaction system. Therefore, the dimensional versions

of $P^{\star}_{\mathrm{F}i}$ and $W^{\star}_{\mathrm{F}i}$ are, respectively, given by

$$P_{\mathrm{F}i} = F_{\mathrm{L}i}\Delta S\frac{dW(S_i)}{dt} = \rho_{\mathrm{F}}U^2\frac{L^2}{T_{\mathrm{S}}}P^{\star}_{\mathrm{F}i} = \rho_{\mathrm{F}}U^2\sqrt{\frac{D}{\rho_{\mathrm{P}}h}}P^{\star}_{\mathrm{F}i} = \zeta_{\mathrm{P}}P^{\star}_{\mathrm{F}i}, \tag{6.6}$$

$$W_{\mathrm{F}i} = \int_0^t F_{\mathrm{L}i}\Delta S\frac{dW(S_i)}{dt}\,dt = \rho_{\mathrm{F}}U^2L^2W^{\star}_{\mathrm{F}i} = \zeta_{\mathrm{W}}P^{\star}_{\mathrm{F}i}, \tag{6.7}$$

where the power coefficient ζ_{P} and the work coefficient ζ_{W} are, respectively, defined by

$$\zeta_{\mathrm{P}} = \rho_{\mathrm{F}}U^2\sqrt{\frac{D}{\rho_{\mathrm{P}}h}}, \qquad \zeta_{\mathrm{W}} = \rho_{\mathrm{F}}U^2L^2. \tag{6.8}$$

Using ζ_{P} and ζ_{W}, it is straightforward to write the dimensional versions of $\widehat{P}^{\star}_{\mathrm{F}}$ and $\widehat{W}^{\star}_{\mathrm{F}}$ as

$$\widehat{P}_{\mathrm{F}} = \zeta_{\mathrm{P}}\widehat{P}^{\star}_{\mathrm{F}}, \qquad \widehat{W}_{\mathrm{F}} = \zeta_{\mathrm{W}}\widehat{W}^{\star}_{\mathrm{F}}, \tag{6.9}$$

respectively.

In this thesis, the Galerkin method is used in the solution of the equation of motion of the plate (see Chapter 3); according to Eq. (3.1), the vibration velocity of the plate $\dot{w}(s_i)$ can be expanded as

$$\dot{w}(s_i,\tau) = \sum_{m=1}^{M}\dot{q}_m(\tau)\phi_m(s_i). \tag{6.10}$$

Therefore, substituting Eq. (6.10) into the second of Eqs. (6.5), one can calculate the (accumulative) total work $\Psi^{\star}_{\mathrm{F}m}$ done by the transverse fluid load f_{L} in terms of each individual beam mode ϕ_m (see Eq. (3.2)), which is defined by

$$\Psi^{\star}_{\mathrm{F}m} = \sum_{i=1}^{N}\int_0^{\tau} f_{\mathrm{L}}\Delta s\dot{q}_m(\tau)\phi_m(s_i)\,d\tau. \tag{6.11}$$

It should be noted that, no matter how one evaluates the energy transfer between the plate and the fluid flow, in terms of various locations along the the length of the plate or various vibration modes, the total work done by the fluid is the same, i.e.,

$$\widehat{W}^{\star}_{\mathrm{F}} = \sum_{i=1}^{N}W^{\star}_{\mathrm{F}i} = \sum_{m=1}^{M}\Psi^{\star}_{\mathrm{F}m}. \tag{6.12}$$

Another thing that should be made clear is the determination of the point s_i. In this thesis, s_i is chosen at the collocation point of the ith panel. That is, for example, when the number of panels is $N = 200$ in the numerical simulation and the energy transfer at location $s_i = 0.7$ is considered, we actually calculate all the quantities relating to the fluid load, the motion of of the plate, the work and the power at the collocation point of the 140th panel.

6.2.2. Energy transfer at various values of U_{R}. The energy transfer between the cantilevered flexible plate and the fluid flow is first examined at various values of reduced flow velocity U_{R} in Fig. 6.2. For a specific system with parameters $\mu = 0.2$, $l_0 = 0.01$, $\alpha = 0.004$ and $C_{\mathrm{D}} = 0$, the dynamics is discussed in detail in Chapter 4 (see Figs. 4.1 and 4.2); the critical point of the system is at $U_{\mathrm{Rc}} = 9.925$. When $U_{\mathrm{R}} < U_{\mathrm{Rc}}$, any disturbance to the system dies away with time and the plate always returns to the static flat state. However, as one can see in Fig. 6.2(a), when $U_{\mathrm{R}} = 9.823 = 99.0\%U_{\mathrm{Rc}}$, the total work $\widehat{W}_{\mathrm{F}}^{\star} = \sum_{i=1}^{N} W_{\mathrm{F}i}^{\star}$ done by the fluid load f_{L} is positive; the positive fluid work done on the plate is consumed by the dissipation mechanism inside the plate, i.e., the material damping, and the non-conservative drag. As time elapses, the vibration amplitude of the system decreases and the increase of $\widehat{W}_{\mathrm{F}}^{\star}$ gradually saturates; that is, the power $\widehat{P}_{\mathrm{F}}^{\star}$ (or the time derivative of $\widehat{W}_{\mathrm{F}}^{\star}$) approaches to zero. It is found that when U_{R} is well below U_{Rc}, say $U_{\mathrm{R}} = 8.660 = 87.3\%U_{\mathrm{Rc}}$, $\widehat{W}_{\mathrm{F}}^{\star}$ is still positive. Nevertheless, when U_{R} is very low, as is the case for $U_{\mathrm{R}} = 7.756 = 78.1\%U_{\mathrm{Rc}}$ shown in Fig. 6.2(a), $\widehat{W}_{\mathrm{F}}^{\star}$ becomes negative; that is, the effect of the fluid load f_{L} acting on the plate is equivalent to an additional damping mechanism.

When $U_{\mathrm{R}} > U_{\mathrm{Rc}}$, flutter takes place. It can be seen in Fig. 6.2(b) for the case $U_{\mathrm{R}} = 10 = 100.8\%U_{\mathrm{Rc}}$ that $\widehat{W}_{\mathrm{F}}^{\star}$ is positive and its value continuously grows, as compared to the case $U_{\mathrm{R}} = 9.823$ shown in Fig. 6.2(a). Moreover, as shown in Fig. 6.2(c), with increasing U_{R}, the flutter amplitude of the system increases and more work is done by f_{L}.

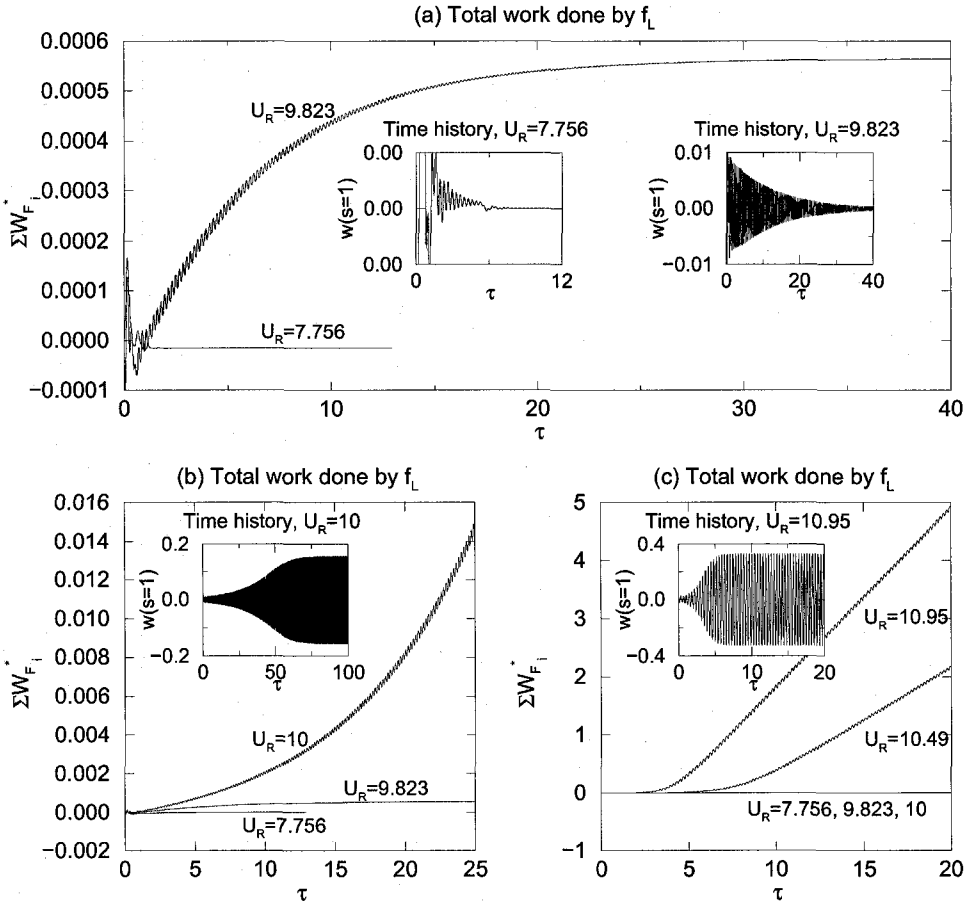

FIGURE 6.2. The work done by the fluid load f_{L} at various values of U_{R}. The other parameters of the system are: $\mu = 0.2$, $l_0 = 0.01$, $\alpha = 0.004$ and $C_{\mathrm{D}} = 0$.

It should be noted that the total work done by the fluid load f_{L}, i.e., $\widehat{W}_{\mathrm{F}}^{\star}$, is the time integral of the power $\widehat{P}_{\mathrm{F}}^{\star}$. When the plate vibrates, $\widehat{P}_{\mathrm{F}}^{\star}$ also oscillates about zero, as shown in Fig. 6.3(a); that is, in a cycle of the vibration of the plate, f_{L} does both positive work (the energy transferred from the fluid flow to the plate) and negative work (the energy transferred from the plate to the fluid). Since $\widehat{P}_{\mathrm{F}}^{\star}$ is oscillating, the plot of $\widehat{W}_{\mathrm{F}}^{\star}$ versus time is not smooth, as one can see in Fig. 6.3(b) (also in Fig. 6.2). The oscillating $\widehat{P}_{\mathrm{F}}^{\star}$ may be evaluated in terms of the time-averaged power $\overline{P}_{\mathrm{F}}^{\star}$, for example, the time-averaged power in a cycle of vibration of the system. In this thesis, as illustrated in Fig. 6.3(b), we conveniently use the slope of the $\widehat{W}_{\mathrm{F}}^{\star}$ versus time plot, in terms of the line connecting the local maxima (or the local minima), to calculate $\overline{P}_{\mathrm{F}}^{\star}$.

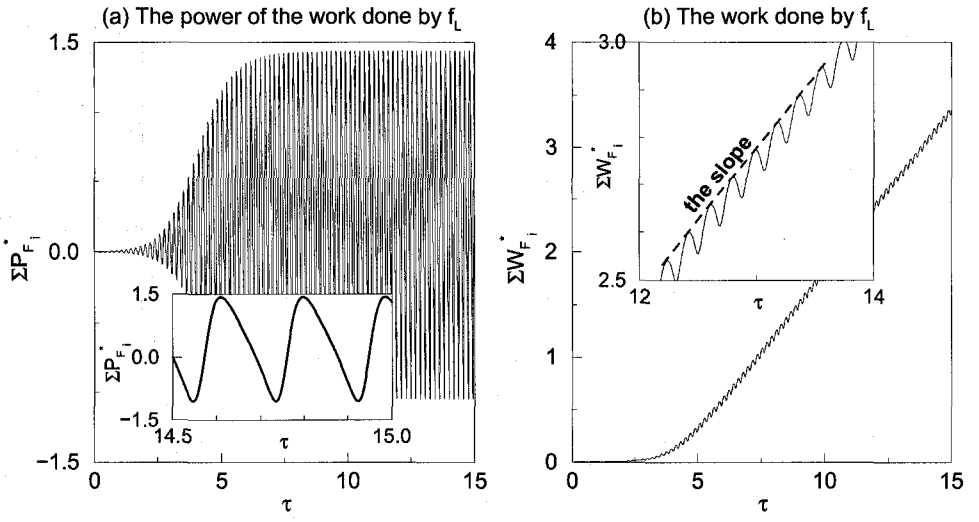

FIGURE 6.3. The work done by by the fluid load f_{L} and the associated power. The parameters of the system are: $\mu = 0.2$, $U_{\mathrm{R}} = 10.95$, $l_0 = 0.01$, $\alpha = 0.004$ and $C_{\mathrm{D}} = 0$.

It is of interest to examine the slopes of the $\widehat{W}_{\mathrm{F}}^{\star}$ versus time plots (i.e., the values of $\overline{P}_{\mathrm{F}}^{\star}$) presented in Figs. 6.2(b) and (c) for the cases $U_{\mathrm{R}} > U_{\mathrm{Rc}}$. One finds that, firstly, at a fixed value of U_{R}, as the flutter amplitude grows with time, $\overline{P}_{\mathrm{F}}^{\star}$ continuously increases; when limit cycle oscillations are attained, $\overline{P}_{\mathrm{F}}^{\star}$ becomes a constant. This observation reveals that, with the increase of the flutter amplitude, more energy is pumped into the plate from the fluid flow; at the same time, more energy is dissipated by the plate. Nevertheless, in the end, a balance between the input energy and the dissipation of the plate can be attained, and a constant flutter amplitude of the stable limit cycle oscillations is obtained. Secondly, with increasing U_{R}, the flutter amplitude grows, so does the value of $\overline{P}_{\mathrm{F}}^{\star}$; that is, at higher U_{R}, the balance between input energy and dissipation is attained at a higher level of energy transfer between the plate and the fluid flow.

6.2.3. Energy transfer at various locations. It has been shown in Chapter 4 that cantilevered flexible plates in axial flow vibrate in various modes; the points at different locations along the length of the plate do not oscillate in phase (as some parts of the plate move upwards, and other parts downwards). Moreover, as one can see in Fig. 4.18 for various systems with different values of mass ratio μ, the vibration

modes are qualitatively different. Therefore, it is of interest to examine the energy transfer between the plate and the fluid flow at various locations along the plate.

As shown in Fig. 6.4 for a specific system with parameters $\mu = 0.2$, $U_{\mathrm{R}} = 10.95$ $(110.3\%U_{\mathrm{Rc}})$, $l_0 = 0.01$, $\alpha = 0.004$ and $C_{\mathrm{D}} = 0$, the energy transfer at various locations is not the same: energy is pumped from the fluid flow into the plate (positive slope of the $W^{\star}_{\mathrm{F}i}$ versus time plot) at some locations; while it is transferred from the plate to the fluid flow (negative slope of the $W^{\star}_{\mathrm{F}i}$ versus time plot) at other locations.

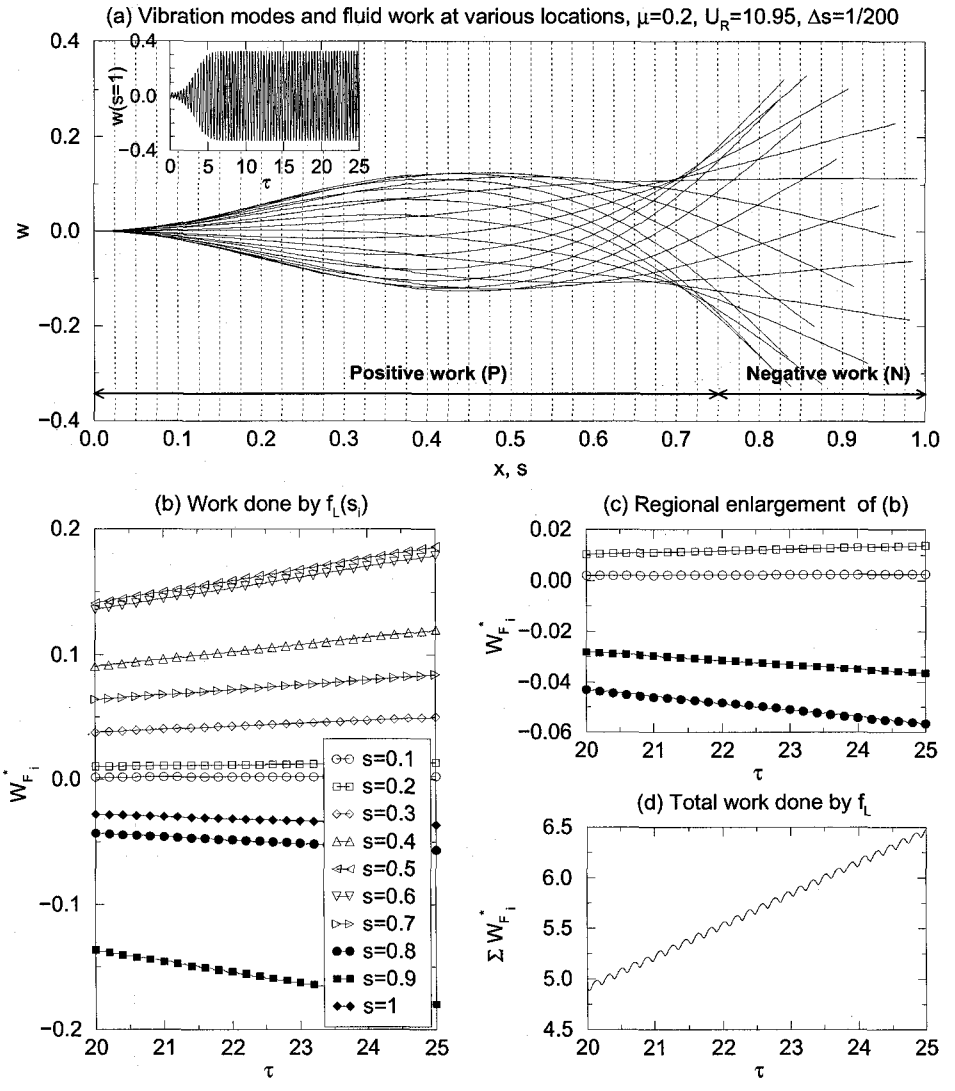

FIGURE 6.4. The work done by the fluid load f_{L} at various locations along the length of the plate. The parameters of the system are: $\mu = 0.2$, $U_{\mathrm{R}} = 10.95$, $l_0 = 0.01$, $\alpha = 0.004$ and $C_{\mathrm{D}} = 0$. Note that, $N = 200$ panels are used in the numerical simulation. The energy transfer at 40 locations (every 5 panels) is recorded and the results at 10 locations (every 20 panels) are presented.

In particular, for this particular case, $W^{\star}_{\mathrm{F}i}$ is positive at points $s_i = 0.025$ through $s_i = 0.675$; while, it is negative at points $s_i = 0.750$ through $s_i = 1$. Note that in this case, the total work done by the fluid load f_{L}, i.e., the sum of all $W^{\star}_{\mathrm{F}i}$ along the whole length of the plate, $\widehat{W}^{\star}_{\mathrm{F}} = \sum_{i=1}^{N} W^{\star}_{\mathrm{F}i}$, is positive, as shown in Fig. 6.4(d). The important finding is that, as energy is pumped into the plate at the upstream section of the plate, it is transferred from the plate to the fluid flow at the downstream section.

The distribution of the positive/negative $W^{\star}_{\mathrm{F}i}$ depends on the reduced flow velocity U_{R}. As shown in Fig. 6.5, for the case with a smaller reduced flow velocity $U_{\mathrm{R}} = 10 = 100.8\%U_{\mathrm{Rc}}$ (the other parameters, especially the mass ratio μ, are the same as those of the case shown in Fig. 6.4), of which $\sum_{i=1}^{N} W^{\star}_{\mathrm{F}i}$ is still positive, $W^{\star}_{\mathrm{F}i}$ is negative at points $s_i = 0.025$ through $s_i = 0.175$, positive in the range $0.2 \leq s_i \leq 0.75$ and negative at points $0.775 \leq s_i \leq 1$; note that the energy is still transferred from the plate to the fluid flow at the downstream section of the plate.

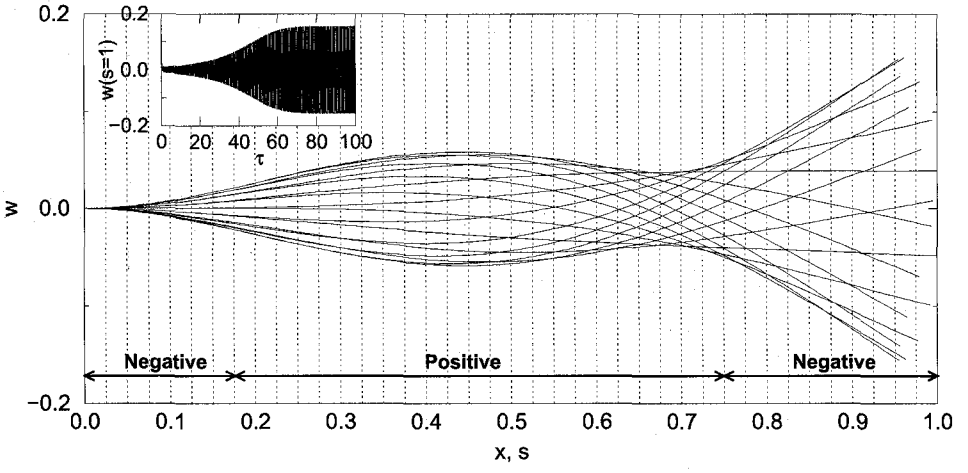

FIGURE 6.5. The work done by the fluid load f_{L} at various locations along the length of the plate. The parameters of the system are: $\mu = 0.2$, $U_{\mathrm{R}} = 10$, $l_0 = 0.01$, $\alpha = 0.004$ and $C_{\mathrm{D}} = 0$. Note that, $N = 200$ panels are used in the numerical simulation. The energy transfer at 40 locations (every 5 panels) is recorded.

An important remark should be made here, particularly. Superficially, the finding that energy is lost to the plate in the downstream part may appear to contradict the findings of Benjamin (1961), Gregory and Païdoussis (1966) and Païdoussis (1998) for a pipe conveying fluid that, for positive work to be done on the plate, the free end

slope and velocity must be in quadrature; i.e., when the slope is negative, the velocity of the free end of the pipe must be positive, and vice versa. Thus, emphasis is placed on the free end, while here we have shown that the downstream end of the plate loses energy uniformly. On closer examination, however, what Benjamin (1961) have found is (i) that positive work is done on the system (energy is transferred from the fluid to the structure) where there is a curvature, which is in the middle of the structure for basically second-beam-mode flutter, (ii) at the downstream end, Coriolis forces dominate, resulting in energy loss, and (iii) the second-beam-mode motion results in the quadrature relationship between slope and velocity at the free end. Thus, there is no contradiction in the basic energy transfer mechanism found here for the plate and that for the pipe, as well as that for a cylinder in axial flow (Païdoussis, 2004).

The distribution of the positive/negative $W^{\star}_{\mathrm{F}i}$ is also examined for various systems with different values of mass ratio μ, as shown in Fig. 6.6. It should be mentioned that different values of U_{R} are used for individual cases of μ for the purpose of obtaining flutter motions; as shown in Table 6.1, for each case of μ, U_{R} is so chosen that it is about 10% above the corresponding critical reduced flow velocity U_{Rc}. It can be seen in Fig. 6.6 that the distribution of the positive/negative $W^{\star}_{\mathrm{F}i}$ depends on μ. When μ is large, say $\mu = 2$ or $\mu = 5$, higher modes become important in the dynamics of the system (see Chapter 4), and the distribution of positive/negative $W^{\star}_{\mathrm{F}i}$ has a complicated pattern. However, when $\mu = 20$, it seems that the pattern of the distribution of positive/negative $W^{\star}_{\mathrm{F}i}$ does not have as many alternations in sign as the cases $\mu = 2$ and $\mu = 5$. Finally, one can see in Fig. 6.6 that, no matter what values of μ and U_{R} are used, the energy is transferred from the plate to the fluid flow at the most downstream section of the plate.

TABLE 6.1. The reduced flow velocities U_{R} used in the examination of energy transfer of various systems with different values of mass ratio μ (see Fig. 6.6)

μ	0.01	0.5	0.5	2	5	20
U_{Rc}	37.08	6.9	6.9	10.78	10.51	8.709
U_{R}	40.62	7.483	7.746	11.83	11.40	9.487
$(U_{\mathrm{R}} - U_{\mathrm{Rc}})/U_{\mathrm{Rc}}$	9.55%	8.45%	12.26%	9.76%	8.47%	8.17%

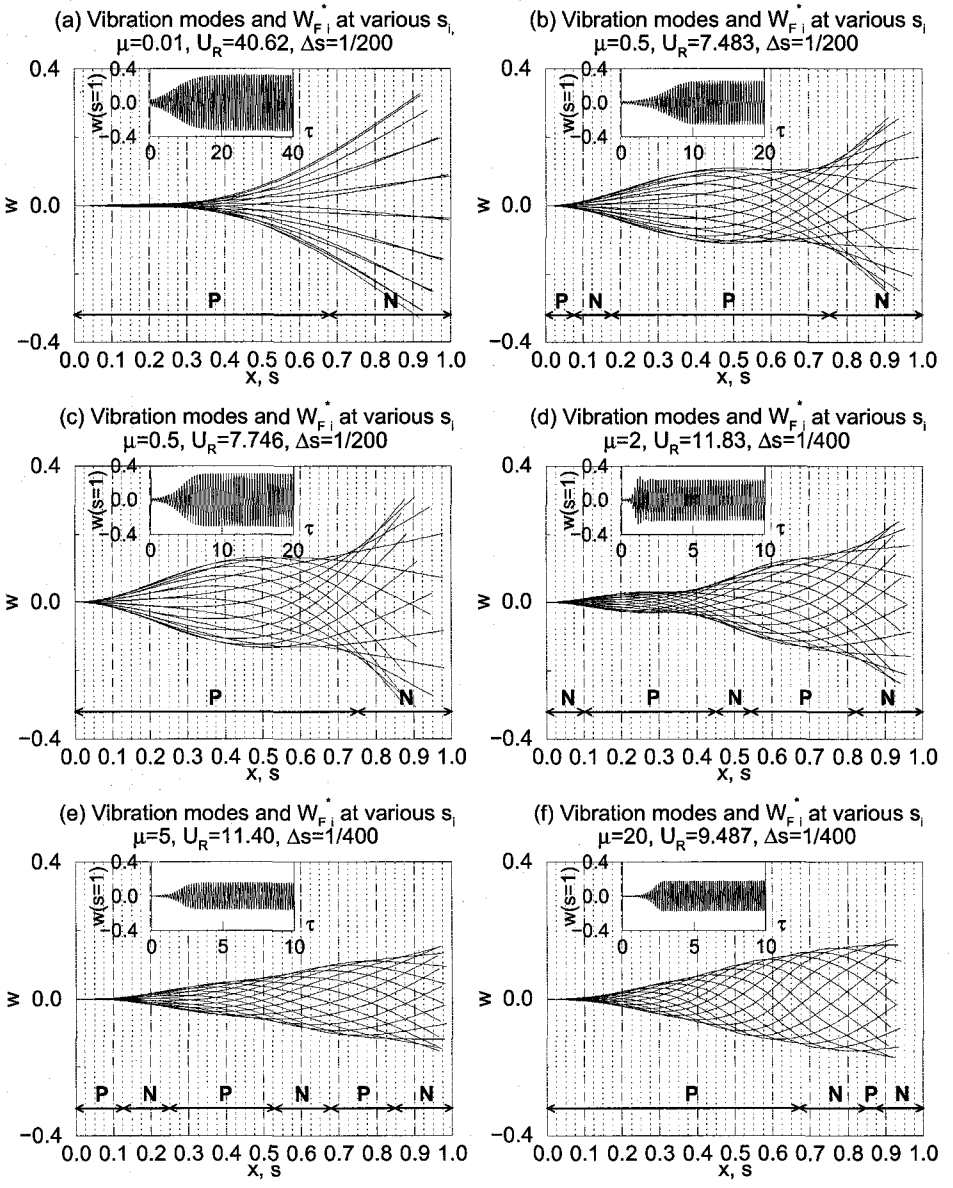

FIGURE 6.6. When flutter takes place, the work done by the fluid load f_{L} at various locations along the length of the plate. The other parameters of the system are: $l_0 = 0.01$, $\alpha = 0.004$ and $C_{\mathrm{D}} = 0$. Note that, the number of panels $N = 200$ is used for the cases $\mu = 0.01$ and $\mu = 0.5$; while, for the other cases $\mu = 2$, $\mu = 5$ and $\mu = 20$, $N = 400$ is used. The energy transfers at 40 locations (every 5 panels in the case of $N = 200$ and every 10 panels when $N = 400$) are recorded.

It is of special interest to examine the case $\mu = 0.5$ in that the design of a flutter-mill may most likely consider such a value of mass ratio. As shown in Figs. 6.6(b) and (c), when $U_{\mathrm{R}} = 7.483 = 108.45\% U_{\mathrm{Rc}}$, the energy transferred from the plate to the fluid flow at locations $0.1 \leq s_i \leq 0.175$ and $0.775 \leq s_i \leq 1$; the reverse energy transfer direction is found at the other locations. As the reduced flow velocity increases to

$U_{\mathrm{R}} = 7.746 = 112.26\%U_{\mathrm{Rc}}$, it has only two sections of the positive/negative $W^{\star}_{\mathrm{F}i}$: at the upstream section $0 \leq s_i \leq 0.75$, energy is pumped into the plate from the fluid flow, while at the downstream section $0.775 \leq s_i \leq 1$, energy is transferred from the plate to the fluid flow. Reduced flow velocities above $U_{\mathrm{R}} = 7.746$ are also examined; only two positive/negative sections are observed, although the boundaries of the two sections may slightly shift from the point $s_i = 0.775$.

6.2.4. Energy transfer in terms of individual beam modes. As the Galerkin method is used in the solution of the equation of motion of the plate, it is convenient to examine the energy transfer between the plate and the fluid flow in terms of individual beam modes.

In Fig. 6.7, the work done by the fluid load f_{L} at various values of U_{R} for a specific system with $\mu = 0.2$ is studied. It can be seen that, at all values of U_{R}, the energy transfer between the plate and the fluid flow occurs largely in the first two beam modes ϕ_1 and ϕ_2 (note that the plate vibrates in the second beam mode when $\mu = 0.2$; see Chapter 4); the magnitudes of $\Psi^{\star}_{\mathrm{F}m,m\geq 3}$ are much smaller than those of $\Psi^{\star}_{\mathrm{F}m,m=1,2}$. Moreover, one finds that, at different values of U_{R}, the work done by f_{L} in terms of ϕ_2 is always positive, while for $\Psi^{\star}_{\mathrm{F}m,m\neq 2}$ it may be either positive or negative.

As shown in Fig. 6.7(a.1), for the case $U_{\mathrm{R}} = 7.756 = 78.1\%U_{\mathrm{Rc}}$, for which $\sum_{m=1}^{M} \Psi^{\star}_{\mathrm{F}m}$ is negative (see Fig. 6.2(a)), $\Psi^{\star}_{\mathrm{F}1}$ is negative and $\Psi^{\star}_{\mathrm{F}2}$ is positive; moreover, the magnitude of $\Psi^{\star}_{\mathrm{F}1}$ is larger than that of $\Psi^{\star}_{\mathrm{F}2}$. That is, when the energy is pumped into the plate in the second beam mode, more energy is transferred from the plate to the fluid flow in the first beam mode. It should be mentioned that the plate is forced to be deformed in the first beam mode with a small amplitude at the starting point of the dynamics, i.e., the initial conditions $q^0_1 = -1.0 \times 10^{-2}, q^0_{i,i\neq 1} = 0$ and $\dot{q}^0_i = 0$ are used in the numerical simulation; that is, at the beginning of the motions of the plate, there is some energy stored in the plate in the first beam mode.

For a relatively higher U_{R}, but still below the critical point U_{Rc}, for example the case $U_{\mathrm{R}} = 9.823 = 99.0\%U_{\mathrm{Rc}}$ shown in Fig. 6.7(b.1), for which $\sum_{m=1}^{M} \Psi^{\star}_{\mathrm{F}m}$ becomes

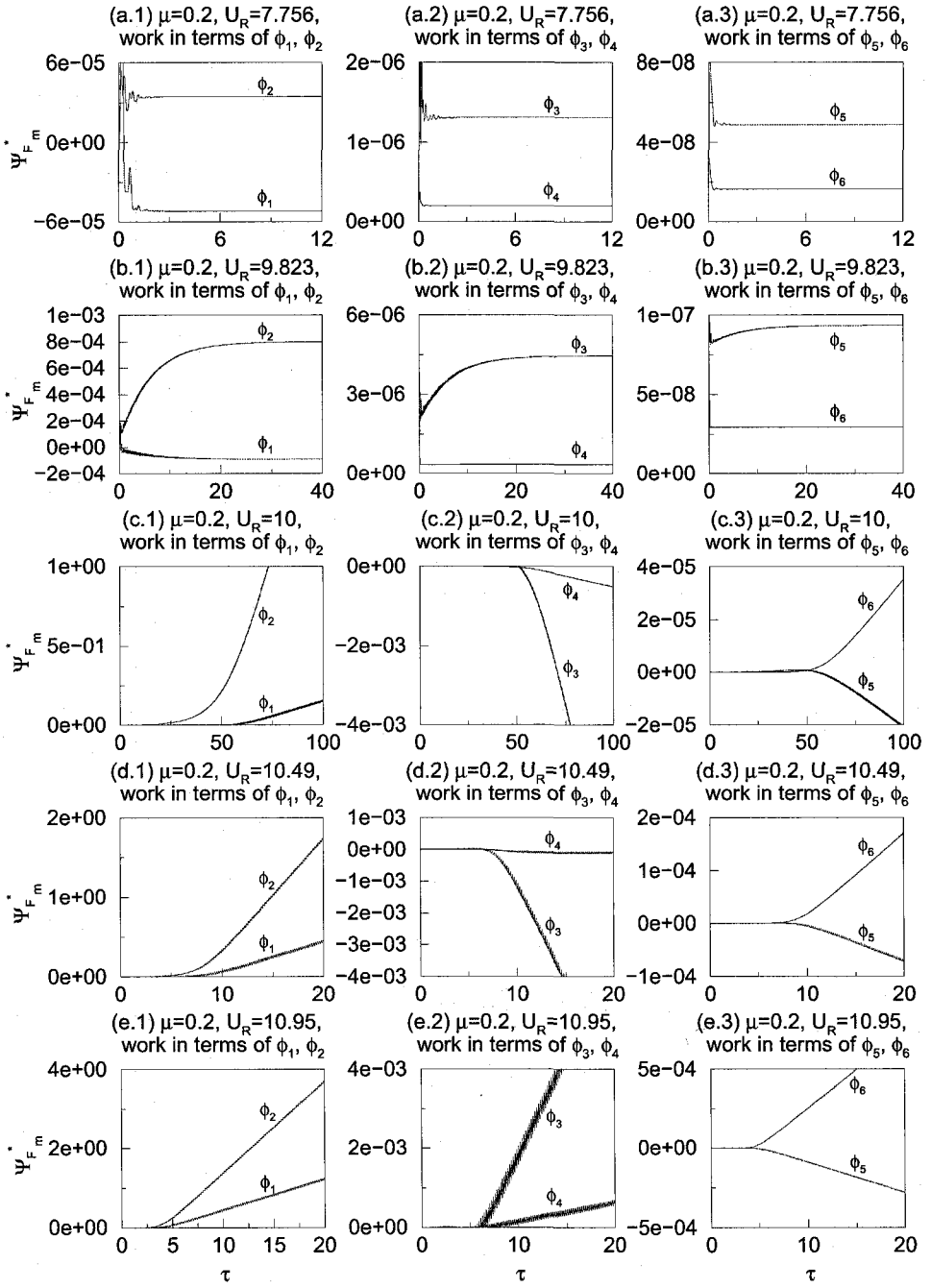

FIGURE 6.7. The work done by the fluid load f_{L} in terms of individual beam modes. The mass ratio of the system is $\mu = 0.2$ and various values of U_{R} are examined. The other parameters of the system are: $l_0 = 0.01$, $\alpha = 0.004$ and $C_{\mathrm{D}} = 0$. Note that $M = 12$ modes are used in the numerical simulation, and only the results of the first six are presented.

positive (see Fig. 6.2(a)), it is found that $\Psi^{\star}_{\mathrm{F}1}$ is still negative. However, when $U_{\mathrm{R}} > U_{\mathrm{Rc}}$, $\Psi^{\star}_{\mathrm{F}1}$ becomes positive, as shown in Fig. 6.7(c.1); the energy is transferred from the fluid flow to the plate in terms of both ϕ_1 and ϕ_2. For higher U_{R}, as one can see

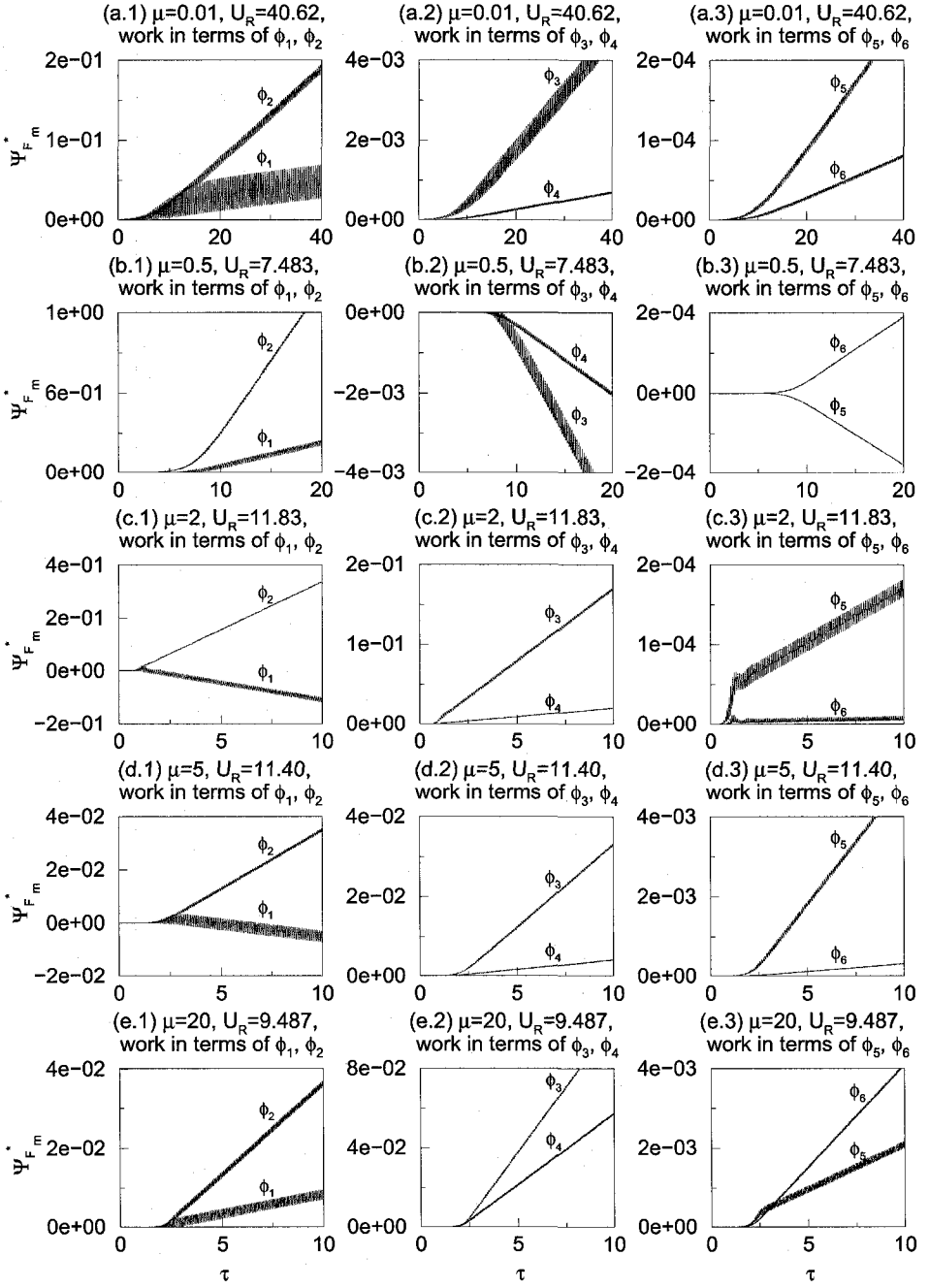

FIGURE 6.8. The work done by the fluid load f_{L} in terms of individual beam modes; various cases of the mass ratio μ are examined. The other parameters of the system are: $l_0 = 0.01$, $\alpha = 0.004$ and $C_{\mathrm{D}} = 0$. Note that $M = 12$ modes are used in the numerical simulation, and only the results of the first six are presented.

in Figs. 6.7(d.1) and (e.1), $\Psi^{\star}_{\mathrm{F}1}$ remains positive; moreover, both slopes of the $\Psi^{\star}_{\mathrm{F}1}$ and $\Psi^{\star}_{\mathrm{F}2}$ versus time plots increase.

When $U_{\mathrm{R}} > U_{\mathrm{Rc}}$, it is interesting to find in Figs. 6.7(c.3), (d.3) and (e.3) that $\Psi^{\star}_{\mathrm{F}5}$ is always positive, but $\Psi^{\star}_{\mathrm{F}6}$ is always negative; note that the magnitudes of $\Psi^{\star}_{\mathrm{F}5}$ and

$\Psi^{\star}_{\mathrm{F}6}$ are very small. However, at a relatively higher level of energy transfer, it can be seen in Figs. 6.7(c.2), (d.2) and (e.2) that both $\Psi^{\star}_{\mathrm{F}3}$ and $\Psi^{\star}_{\mathrm{F}4}$ are negative when U_{R} is just above U_{Rc}; as U_{R} grows, $\Psi^{\star}_{\mathrm{F}4}$ first becomes positive and then both $\Psi^{\star}_{\mathrm{F}3}$ and $\Psi^{\star}_{\mathrm{F}4}$ are positive.

The energy transfer between the plate and the fluid flow in terms of individual beam modes is also studied for the systems with various values of mass ratio μ, as shown in Fig. 6.8. Again, different values of reduced flow velocity U_{R} are used for individual cases of μ in order to examine the energy transfer in the fluttering plate; the values of U_{R} used are listed in Table 6.1. It can be seen in Fig. 6.8 that, when μ is small, say $\mu = 0.01$ or $\mu = 0.5$, the energy transfer occurs largely in the first two beam modes ϕ_1 and ϕ_2. While, when μ is large, as for $\mu = 2$, $\mu = 5$ and $\mu = 20$, the magnitudes of the work done by f_{L} in higher beam modes become comparable with, or even larger than, those for ϕ_1 and ϕ_2. For example, as shown in Figs. 6.8(e.1) and (e.2) for the case $\mu = 20$ and $U_{\mathrm{R}} = 9.487$, one finds that $|\Psi^{\star}_{\mathrm{F}3,4}| > |\Psi^{\star}_{\mathrm{F}1,2}|$.

6.3. Design of flutter-mill

6.3.1. The conceptual design. It has been shown that, over the whole length of the plate and in the time-averaged sense, energy is indeed pumped into the plate from the fluid flow when flutter takes place; we can therefore utilize the energy extracted from the fluid flow to do useful work, for example as shown in Fig. 6.1 in the design of a flutter-mill to generate electricity.

As quite a few of parameters are involved in the dynamics of cantilevered flexible plates in axial flow (see Chapters 4 and 5) as well as in the energy transfer between the plate and the surrounding fluid flow, a starting point should be chosen for the conceptual design. We first notice that, at different sections along the plate, the energy transfer may be from the fluid flow to the plate or vice versa. Therefore, the conductors embedded in the flexible web (the plate) should be correspondingly arranged in several sections, or say phases. Too many phases of conductor arrangement lead to difficulties in the design of the wiring scheme and the rectifier. To this end, in

the light of the vibration modes shown in Fig. 4.18, we consider the system with the mass ratio $\mu < 1$, for which the plate vibrates in the second beam mode; hence, only two phases of conductor arrangement are necessary. It should be mentioned that, no matter whether it is transferred from the fluid flow to the plate at some sections of the plate or vice versa at the other sections, the energy ultimately comes from the fluid flow.

In this chapter, we primarily consider a system with the mass ratio $\mu = 0.5$ and use the case with $\mu = 0.2$ for the purposes of comparison. In the conceptual design of a flutter-mill, dimensional parameters may allow us to evaluate the performance of the device in a more direct manner; to this end, we consider a plate made of aluminium in axial air flow. The reason of considering a metallic plate is that (metal) conductors are supposed to be embedded in the web, otherwise made of a very flexible material; the properties of this *composite* plate would be largely determined by those of the conductors. The parameters of the two systems with $\mu = 0.5$ and $\mu = 0.2$ are, respectively, listed/calculated in Table 6.2 (refer to Appendix C).

Some explanation is necessary for the data in Table 6.2. Firstly, since nondimensional parameters are used in all numerical simulations carried out in this thesis, the physical parameters of the systems listed in Table 6.2 are actually obtained using a reverse approach. In particular, for a aluminium plate in axial air flow, we know the properties of the fluid and the plate material; the thickness of the plate h is determined as $h = 0.0005\,\mathrm{m}$ and then the length of the plate can be calculated for the case $\mu = 0.5$ or $\mu = 0.2$. Secondly, the nondimensional parameters $l_0 = 0.01$, $\alpha = 0.004$ and $C_\mathrm{D} = 0$ are uniformly used in all numerical simulations; the influences of these parameters on the dynamics of the system have already been discussed (see Chapter 4). It should be noted that, as the same material is considered, the material damping coefficients a for both cases $\mu = 0.5$ and $\mu = 0.2$ should be the same. However, the nondimensional material damping coefficient α depends on other physical parameters of the system, and the values for the cases $\mu = 0.5$ and $\mu = 0.2$ are different. Therefore, when we use the uniform value $\alpha = 0.004$ in the numerical simulations, it is indeed overvalued for the case $\mu = 0.5$ and undervalued for $\mu = 0.2$. It has been

TABLE 6.2. Design data of a cantilevered flexible plate in axial flow with the mass ratio $\mu = 0.5$ or $\mu = 0.2$

Parameters	Plate 1 ($\mu = 0.5$)	Plate 2 ($\mu = 0.2$)	Unit
Physical parameters fixed in the design			
ρ_F	1.226	1.226	kg/m^3
ρ_P (Al-7505)	2840	2840	kg/m^3
L_0	0.0058	0.0023	m
h	0.0005	0.0005	m
E	7.056×10^{10}	7.056×10^{10}	Pa
ν	0.3	0.3	
a	0.0005	0.0005	s
Physical parameters varied in the design			
L	0.58	0.232	m
Calculated parameters			
$D = Eh^3/[12(1-\nu^2)]$	0.8077	0.8077	$N \cdot m$
$T_S = \sqrt{\rho_P h L^4/D}$	0.4460	0.0071	s
$U_c = U_{Rc} L/T_S$	8.97 ($U_{Rc} = 6.899$)	32.27 ($U_{Rc} = 9.925$)	m/s
Mass ratio			
$\mu = \rho_F L/(\rho_P h)$	0.5	0.2	
Other nondimensional parameters			
$\alpha = a/T_S$	0.001 (0.004 used)	0.070 (0.004 used)	
$l_0 = L_0/L$	0.01	0.01	
C_D	(0 used)	(0 used)	

shown in Chapter 4 that a larger value of α results in a higher critical point U_{Rc}; that is, at a fixed U_R beyond U_{Rc}, the flutter amplitude (hence the level of energy transfer between the plate and the fluid flow) is underestimated for the case $\mu = 0.5$ and overestimated for $\mu = 0.2$.

The post-critical dynamics of the system with $\mu = 0.5$, in terms of dimensional parameters, are shown in Figs. 6.9 and 6.10; moreover, Fig. 6.10(c) shows the time-averaged power $\overline{P}_F$ of work done by the fluid load f_L at various flow velocities. Note that the dynamics of the system with $\mu = 0.2$ has been discussed in detail in Chapter 4; even so, the dynamics in terms of dimensional parameters and the time-averaged power $\overline{P}_F$ for the case $\mu = 0.2$ are presented in Fig. 6.11, to compare with the case $\mu = 0.5$ shown in Fig. 6.10.

It can be seen in Fig. 6.10(a) that, when the flow velocity $U = U_c = 8.97\,m/s$, flutter takes place; the critical point U_c corresponds to the cut-in point of $\overline{P}_F$, as

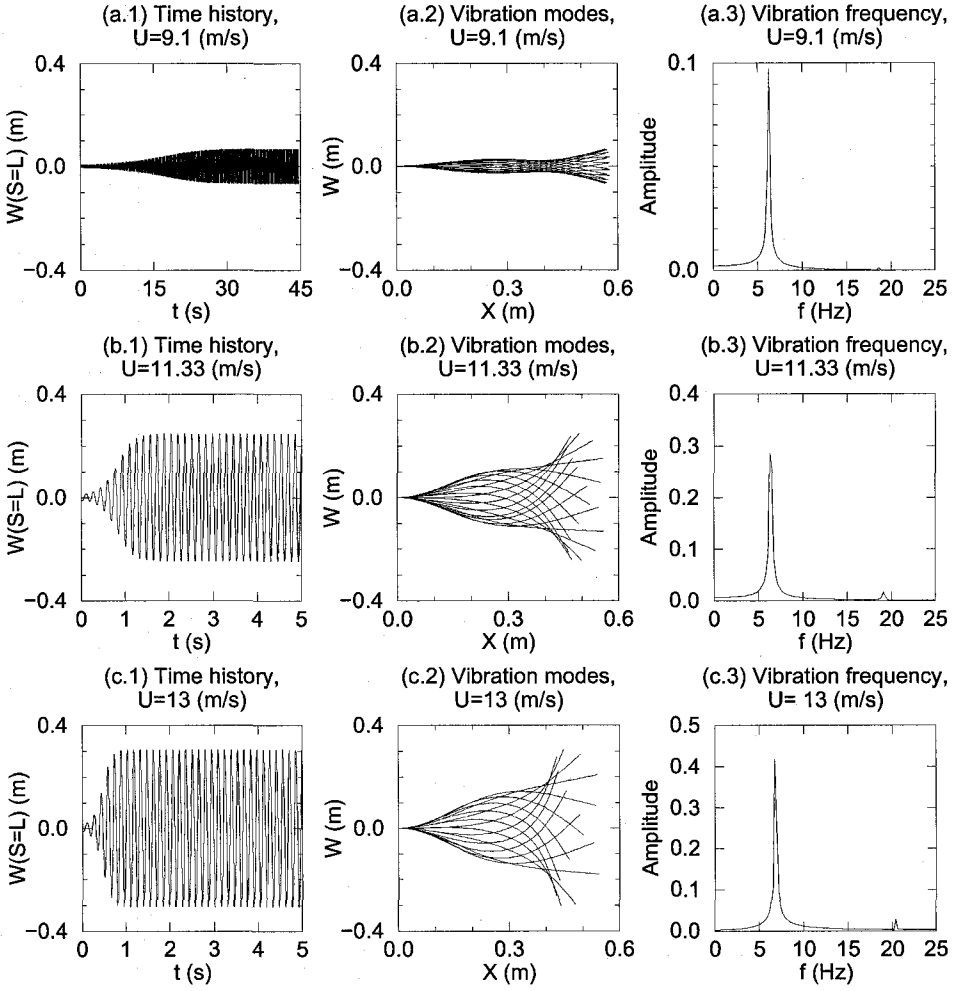

FIGURE 6.9. The dynamics of the system with $\mu = 0.5$. The other parameters of the system are: $l_0 = 0.01$, $\alpha = 0.004$ and $C_D = 0$.

shown in Fig. 6.10(c). With increasing U, the flutter amplitude grows, so does the time-averaged power $\overline{P}_F$ extracted from the fluid flow. However, for a cantilevered flexible plate in axial flow, when the flow velocity is very high, the plate may vibrate wildly in an irregular manner with three-dimensional modes (Taneda, 1968); therefore, we normally consider that there is a maximum flow velocity, at which the flutter amplitude at the trailing edge of the plate is about 50% of the plate length. To this end, a cut-out point can be found in Fig. 6.10(c), where $U = 13\,\mathrm{m/s}$, $\max(W(S = L)) = 0.306\,\mathrm{m} = 52.76\%L$ and $\overline{P}_F = 60.29\,\mathrm{Watt/m}$. If $\mu = 0.2$, one can see in Fig. 6.11 that the cut-in point is as high as $U_c = 32.3\,\mathrm{m/s}$, and at the cut-out point $U = 44.8\,\mathrm{m/s}$, $\max(W(S = L)) = 0.132\,\mathrm{m} = 56.90\%L$ and $\overline{P}_F = 1720\,\mathrm{Watt/m}$.

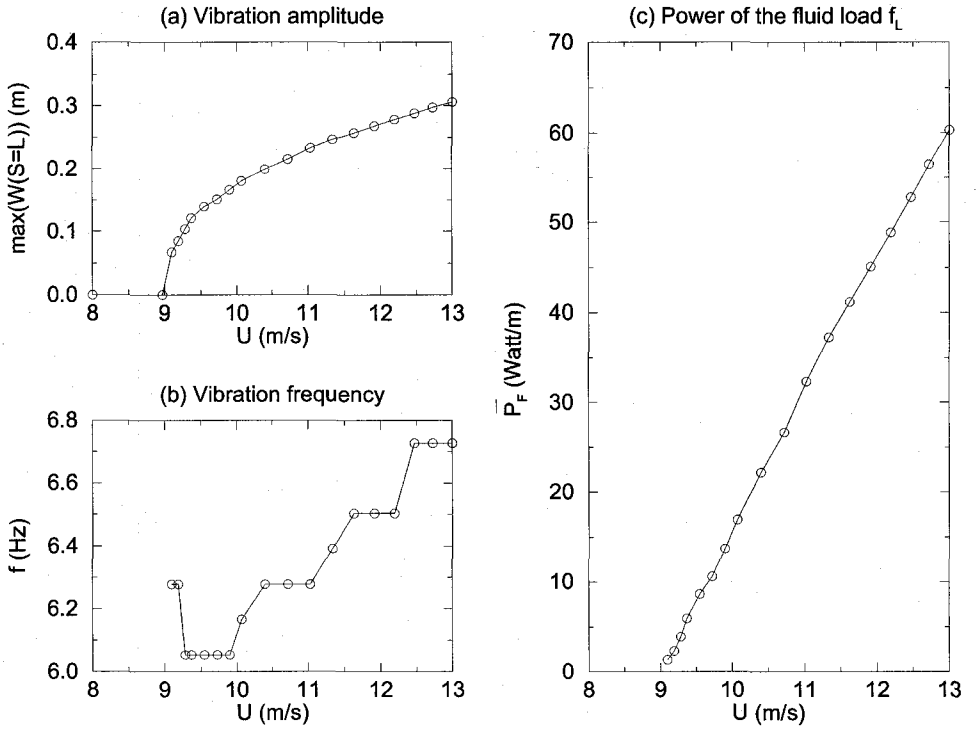

FIGURE 6.10. The dynamics of the system with $\mu = 0.5$ and the time-averaged power $\overline{P}_{\mathrm{F}}$ of the fluid load f_{L}. The other parameters of the system are: $l_0 = 0.01$, $\alpha = 0.004$ and $C_{\mathrm{D}} = 0$.

As shown in Figs. 6.10 and 6.11, preliminary calculations of the power extraction from the fluid flow demonstrate that the proposed flutter-mill is very promising for generation of electrical power. If the system is designed to have a mass ratio $\mu = 0.5$ and plate width $B = 0.2\,\mathrm{m}$, such a compact device of the overall dimensions length $\times$ width $\times$ height $= 0.58\,\mathrm{m} \times 0.2\,\mathrm{m} \times 0.58\,\mathrm{m}$, where the height is considered as twice of the allowed maximum flutter amplitude, can be expected to extract 10 Watt power (at $U = 12\,\mathrm{m/s}$) from the wind; and, if only 10% of the extracted wind energy is ultimately converted to the electrical power, an output of 1 Watt is guaranteed. Higher power output can be expected from the system with $\mu = 0.2$, which works at higher flow velocities. In particular, when $\mu = 0.2$, the power extraction is as high as $\overline{P}_{\mathrm{F}} = 1\,\mathrm{kW/m}$ at $U = 40\,\mathrm{m/s}$.

The working flow velocity of the flutter-mill is relatively high. When $\mu = 0.5$, practical power extraction can be expected within the range $10\,\mathrm{m/s} < U < 13\,\mathrm{m/s}$; although the wind speed at this level agrees with the normal design criteria of commercial wind turbines (above 100 kW rated capacity), it is attained only at high elevations

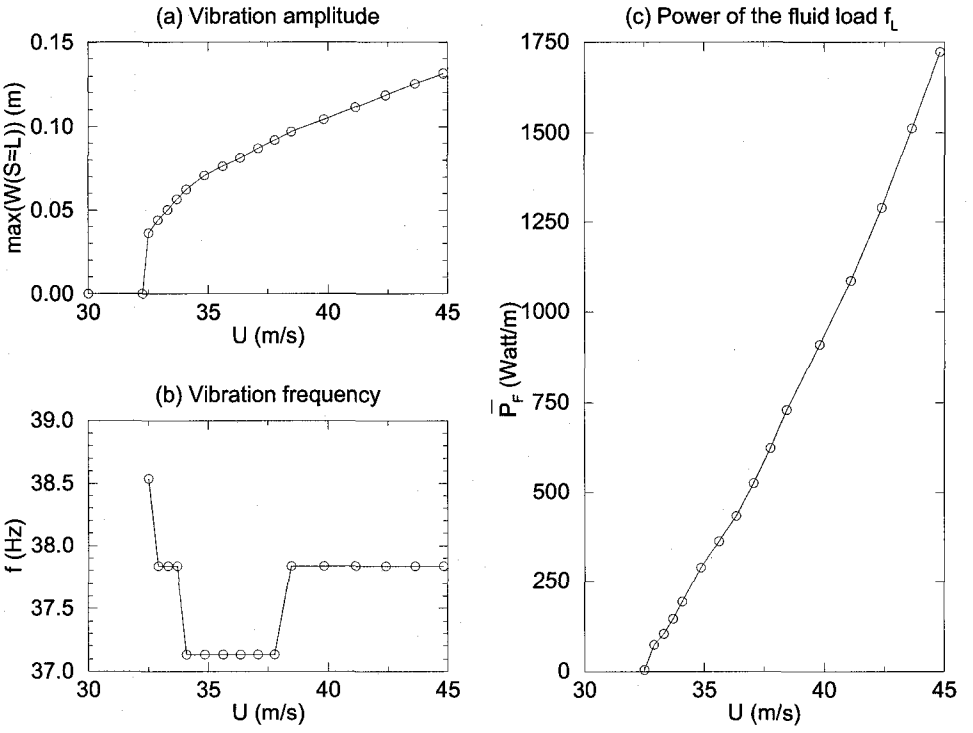

FIGURE 6.11. The dynamics of the system with $\mu = 0.2$ and the time-averaged power $\overline{P}_{\mathrm{F}}$ of the fluid load f_{L}. The other parameters of the system are: $l_0 = 0.01$, $\alpha = 0.004$ and $C_{\mathrm{D}} = 0$.

above the ground. The problem of the high working flow velocity can alternatively be resolved using a concentrator (Manwell et al., 2002). Because the overall dimensions of the flutter-mill are small, say length $\times$ width $\times$ height $= 0.232\,\mathrm{m} \times 0.2\,\mathrm{m} \times 0.232\,\mathrm{m}$ when $\mu = 0.2$ and $B = 0.2\,\mathrm{m}$, the wind receiving area is only $A_2 = 0.0464\,\mathrm{m}^2$; therefore, it is reasonable to consider a concentrator, as illustrated in Fig. 6.12(a), with a large receiving area, say $A_1 = 1\,\mathrm{m}^2$, to substantially increase the flow velocity working on the flutter-mill.

Finally, we consider $B = 0.2\,\mathrm{m}$ in the conceptual design in order to avoid possible difficulties in attaining sufficient strength of the magnetic field between the two magnetic panels. However, it should be mentioned that the choice of the plate width does not affect the analysis of the energy transfer in terms of energy transfer/power density per unit length along the spanwise dimension of the plate. Moreover, as illustrated in Fig. 6.12(b), it is easy to design an array of plates to achieve a desired effective value of B to satisfy a specific design requirement on power capacity.

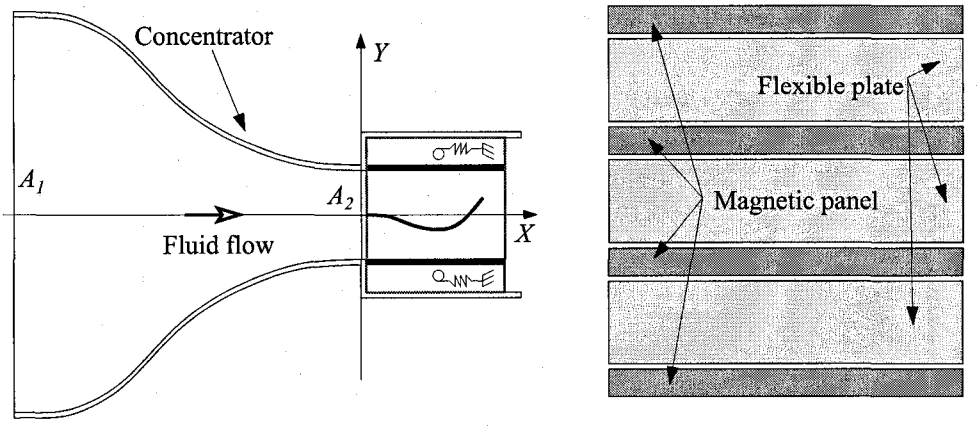

(a) With a concentrator. (b) With a plate array.

FIGURE 6.12. The flutter-mill with (a) a concentrator, and (b) an array of plates.

6.3.2. The performance of the flutter-mill. We first compare the performance of the flutter-mill to a real horizontal axis wind turbine (HAWT), in particular, the Three-blade Stall Regulated Turbine studied by Burton et al. (2001), in terms of electrical power output, as shown in Fig. 6.13. The HAWT has a disk area $227\,\mathrm{m}^2$ and the data for electrical power is collected at the rotational speed 44 rpm. In order to make a comparison, we suppose that the flutter-mill has a same wind receiving area as the HAWT ($227\,\mathrm{m}^2$) and accordingly calculate the effective width B of the plate. Moreover, in the calculation of electrical power output, we assume that only 10% of the energy captured by the plate is ultimately converted to electrical power; the other 90% of the energy is consumed by the plate for sustaining flutter. It can be seen in Fig. 6.13 that when $\mu = 0.5$, the flutter-mill works within the same range of wind speed as the HAWT; however, the electrical power output of the flutter-mill is not as high as that of the HAWT (about 10%). When it is designed with $\mu = 0.2$, the flutter-mill can work at high wind speed and a very high electrical power output can be expected; the capacity is much higher than that of the HAWT.

There are different alternatives for evaluating the performance of a wind energy converter (wind turbine, wingmill or flutter-mill) of a certain design or to compare the characteristics of various designs; among these approaches, the ratio η of the power P_{F} actually extracted by the device to the theoretical/idealized power P_{I} that can be extracted from fluid flow is perhaps the most commonly used indicator; P_{I} is

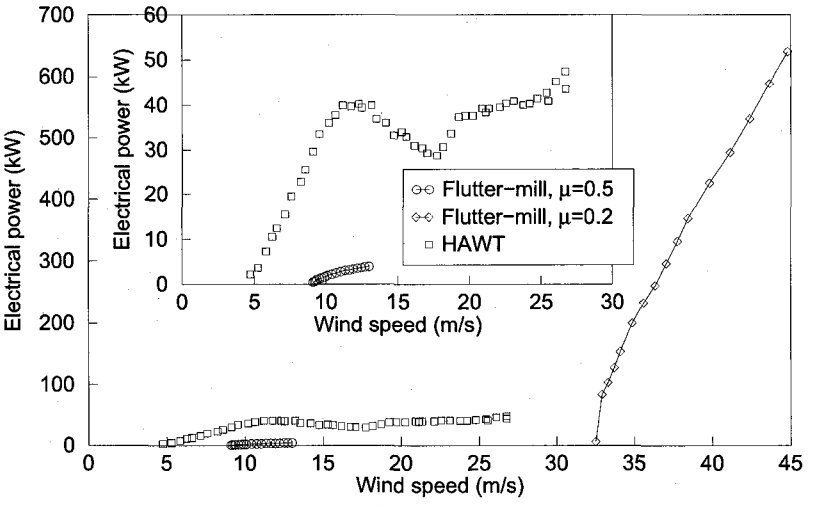

FIGURE 6.13. The performance of the flutter-mill as compared to a real HAWT, i.e., the Three-blade Stall Regulated Turbine studied by Burton et al. (2001).

calculated from

$$P_{\mathrm{I}} = \frac{1}{2} C_{\mathrm{B}} A \rho_{\mathrm{F}} U^3, \tag{6.13}$$

where $C_{\mathrm{B}} \equiv 16/27$ is the Betz limit (Manwell et al., 2002), and A is the disk area in the case of a HAWT. It follows that the primary conversion efficiency

$$\eta = \frac{P_{\mathrm{F}}}{\frac{1}{2} C_{\mathrm{B}} A \rho_{\mathrm{F}} U^3}. \tag{6.14}$$

Note that, for a HAWT, the disk area A is

$$A = \pi {R_{\mathrm{D}}}^2, \tag{6.15}$$

where R_{D} is the radius of the disk or the length of a blade. However, in the design of a flutter-mill, A is redefined as the wind receiving area, calculated by

$$A = 2 \max\left((W(S = L)) \right) B, \tag{6.16}$$

where $W(S = L)$ is the maximum vibration amplitude of the trailing edge of the plate. Moreover, in the design of wingmills proposed by McKinney and DeLaurier (1981), Jones and Platzer (1999) and Isogai et al. (2003) (see Figs. 1.5(a), (b) and (d)), A is defined as the area swept by the leading or trailing edge of the flapping

wing, that is

$$A = H_{\mathrm{W}} B, \tag{6.17}$$

where H_{W} is the maximum distance translated by either the leading edge or the trailing edge of the wing when it is undergoing coupled plunging/pitching motions. It follows that the efficiency η of the flutter-mill can be calculated by

$$\begin{aligned}
\eta &= \frac{P_{\mathrm{F}}}{P_{\mathrm{I}}} = \frac{\overline{P}_{\mathrm{F}} B}{P_{\mathrm{I}}} = \frac{\zeta_{\mathrm{P}} \overline{P}_{\mathrm{F}}^{\star} B}{P_{\mathrm{I}}} \\
&= \frac{\rho_{\mathrm{F}} U^2 \sqrt{D/(\rho_{\mathrm{P}} h)}\, \overline{P}_{\mathrm{F}}^{\star} B}{(1/2) \times (16/27) \times \rho_{\mathrm{F}} U^3 \times 2 \times \max\left((W(S=L)\right) \times B} \\
&= \frac{1.6875 L^2 \sqrt{D/(\rho_{\mathrm{P}} h L^4)}\, \overline{P}_{\mathrm{F}}^{\star}}{U \max\left((W(S=L)\right)} \\
&= \frac{1.6875 \overline{P}_{\mathrm{F}}^{\star}}{U_{\mathrm{R}} \max(w(s=1))}.
\end{aligned} \tag{6.18}$$

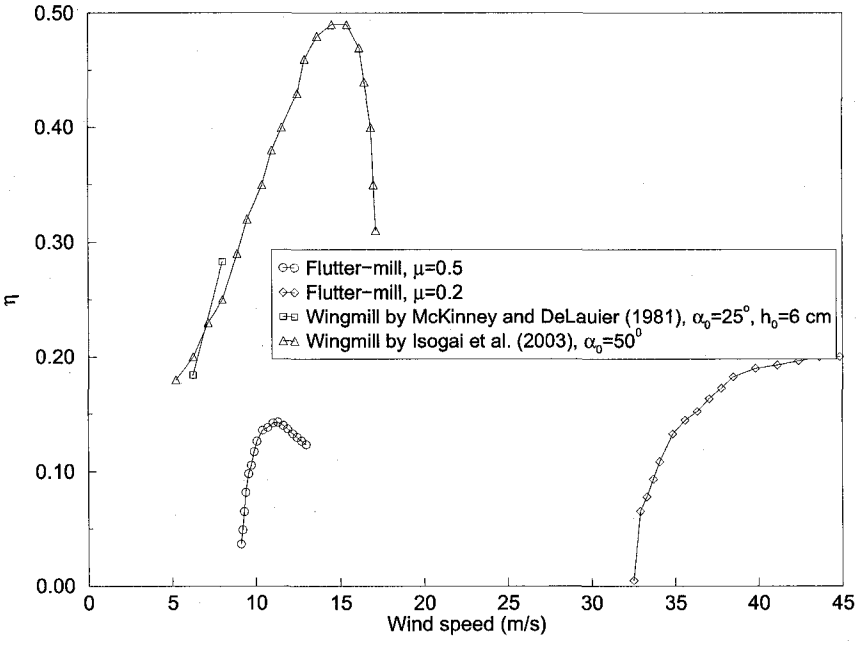

FIGURE 6.14. The efficiency of the flutter-mill as compared to the wingmills proposed by McKinney and DeLaurier (1981) and Isogai et al. (2003).

In Fig. 6.14, the efficiency of the flutter-mill is compared to the wingmills proposed by McKinney and DeLaurier (1981) and Isogai et al. (2003). It can be seen that, when $\mu = 0.5$, the working wind speed of the flutter-mill agrees with that of the wingmill; the efficiency of the flutter-mill is about 30% of the wingmill. Working at higher wind speeds, the flutter-mill with $\mu = 0.2$ achieves a relatively higher efficiency at

about 40% of the wingmill. However, it should be noted that the performance of an energy converter is not fully determined by the primary conversion efficiency η. In the design of a wingmill, an extra mechanism is necessary to couple the plunging/pitching motions, and a transmission gear must be used to convert the plunging/pitching motions to the rotational motion of the generator; energy loss occurs in all these processes. If one assumes that the efficiency of the mechanical transmission of a wingmill is about 70%, the actual power generation efficiencies of the flutter-mill and the wingmill become much closer.

The tip speed ratio λ_T, i.e., the ratio of the rotational speed at the tip of a wind turbine blade to the oncoming wind speed, is one of the key parameters in the design of a wind turbine in that it determines the effective flow velocity to the blade and thus the aerodynamic loads (lift and/or drag), as illustrated in Fig. 6.15(a). In the case of a wingmill, although the term tip speed ratio is still used by Jones and Platzer (1999) and Isogai et al. (2003), as shown in Fig. 6.15(b), it has a very different meaning when it refers to the ratio of the maximum speed of the plunging motion to the wind speed. Because the leading edge of the plate in a flutter-mill is always aligned with the upcoming air flow and the plate itself is flexible, the parameter λ_T does not make any sense in the design of a flutter-mill. Nevertheless, as shown in Fig. 6.15(c), we calculate the ratio of the maximum (transverse) vibration speed at the trailing edge of the plate to the wind speed, i.e., the so-called tip speed ratio λ_T, and put the results of the power extraction efficiency of the flutter-mill in Fig. 6.16, which is a duplicate of a figure given in Jones and Platzer (1999). Regardless of the different meanings of λ_T for various types of wind turbines, windmills, wingmills and flutter-mills, it can be seen in Fig. 6.16 that the efficiency of the flutter-mill is comparable to those of the U.S. multi-blade windmill (commonly found on farms in the United States to pump water out of ground) and the Dutch four-arm windmill (classically used to grind flour). On the other hand, if compared to the wingmills, the efficiency of the flutter-mill is similar to the designs by McKinney and DeLaurier (1981) and Jones and Platzer (1999), although somewhat lower; but the efficiency of the flutter-mill, as well as the efficiencies of the wingmills by McKinney and DeLaurier (1981) and

Jones and Platzer (1999), is well below the claimed exceptional high efficiency of the wingmill studied by Isogai et al. (2003).

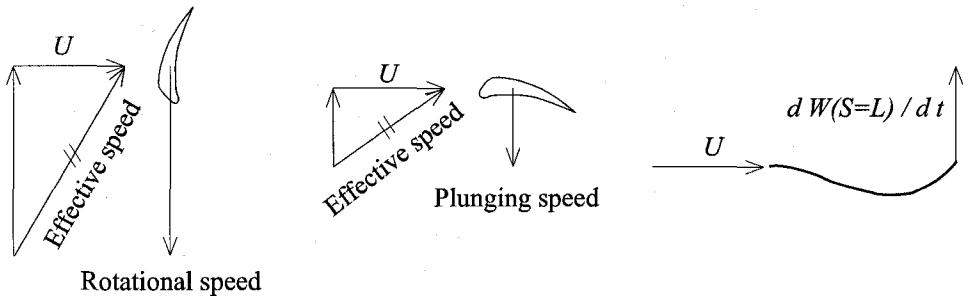

(a) An HAWT (b) A wingmill (c) A flutter–mill

FIGURE 6.15. The meaning of the tip speed ratio.

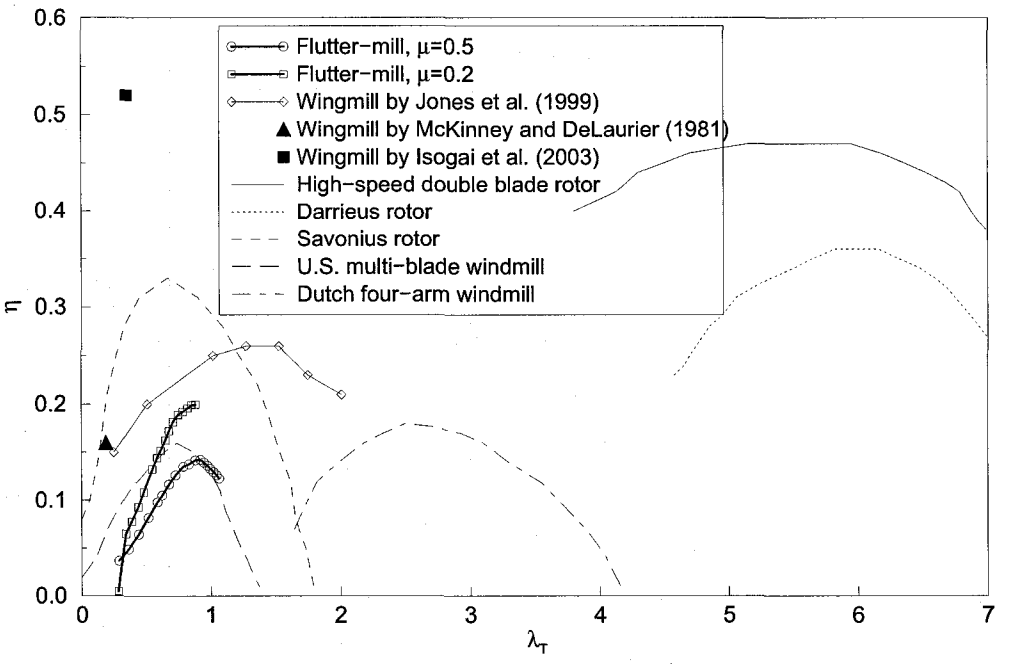

FIGURE 6.16. The efficiencies of various wind energy converters (Jones and Platzer, 1999), where the efficiencies of the flutter-mills with $\mu = 0.5$ and $\mu = 0.2$ and the wingmill proposed by Isogai et al. (2003) are also included.

Finally, it should be mentioned that it is not easy to compare the flutter-mill with the energy-harvesting eels studied by Allen and Smits (2001) and Taylor et al. (2001). However, it is found that the frequency of the wake-induced vibrations of the eel is normally very low, say around 1 Hz, and the low strain level in the thin plate (i.e., the eel) seriously limits the performance of the piezoelectric materials used for generating electrical potentials. It is reported by Taylor et al. (2001) that the goal of

their energy-harvesting eel program is to generate 1 Watt electrical power in about 1 m/s water flow; anyway, this goal can easily be achieved by the flutter-mill working in air flow (see Fig. 6.13).

6.3.3. Other design considerations. In the light of the dynamics of cantilevered flexible plates in axial flow, in the basic plain configuration or various modified configurations, extensively studied in Chapters 4 and 5, other design considerations can be summarized. The main idea here is to reduce the critical flow velocity U_c of the system, so that the flutter amplitude increases at a fixed flow velocity beyond the critical point; thus, a higher level of energy transfer can be achieved.

First, according to the investigations conducted in Chapter 4 on the influence of the parameters l_0 and α, we prefer to use a long upstream rigid splitter ahead of the flexible plate and materials with low damping coefficient for the flexible plate (both the flexible web and the embedded conductors) so that a lower critical point can be achieved.

Second, as discussed in Chapter 5, when the gravitational force is considered in the model, i.e., the system being set up in either the horizontal configuration or the hanging configuration, the value of the critical point of the dynamic instability (flutter) increases. Therefore, we primarily consider the vertical configuration (i.e., the basic configuration) in the design of a flutter-mill. However, if μ is small, as shown in Fig. 5.1 for the case $\mu = 0.2$, it has been found that the increase in the critical point is very small when the system is in the horizontal configuration; thus, the horizontal configuration is also a good choice for the design of a flutter-mill, especially in terms of the possible difficulties involved in setting up a flexible plate in the vertical configuration.

Third, the flutter-mill would normally be placed in a container with upstream and downstream openings; moreover, when a concentrator is considered, this container is indeed necessary. It has been shown in Chapter 5 (see Fig. 5.8) that the presence of parallel solid walls decreases the critical point of the system. Therefore, the presence of this container poses no problems for the flutter-mill.

Fourth, it has been shown in Chapter 5 that the system with an additional spring support exhibits rich dynamics. For a system that has a small value of mass ratio μ and flutters in the second beam mode, with an additional spring being considered at the quasi-node of the vibration (located at about three-quarters of the plate length, for example the cases $s = 0.8$ studied in Figs. 5.14 and 5.17), when the spring is of the linear type, one finds from Fig. 5.14 that the critical point of the system is considerably reduced; this advantage can be taken into account in the design of a flutter-mill. Moreover, if the spring support located at the quasi-node is of the cubic type, although the variation in the critical point is negligible, it has been found in Fig. 5.17 that flutter takes places in a more abrupt manner and the vibration amplitudes/modes have small changes in the range of reduced flow velocity between the primary and secondary bifurcations; this can also be considered in the design so as to allow an almost constant working condition of the flutter-mill over a relatively wide range of flow velocity. On the other hand, if the additional spring support is located at the tailing edge of the plate, i.e., the cases $s = 1$ studied in Figs. 5.11 and 5.15 for, respectively, linear and cubic springs, no useful additional features, emerged that can be directly utilized in the design of a flutter-mill. However, it should be noted that one may consider an additional spring support at the trailing edge of the plate to alter the vibration modes and limit the flutter amplitude at the trailing edge of the plate; this may be necessary if a compact design of flutter-mill is required. For example, when the parallel solid wall is considered and the size of the channel is preferred to be small, an additional spring support should be placed at the trailing edge of plate to prevent it from touching the parallel solid walls.

Besides dynamics considerations, the additional spring supports at the quasi-node and/or the trailing edge aids in setting up the system in the vertical configuration, if this configuration is chosen for the design. It should also be mentioned that, as shown in Fig. 6.1, the additional spring supports are supposed to be a part of the wiring scheme; however, this arrangement is not necessary when the pairing-plate design illustrated in Fig. 6.17 is adopted.

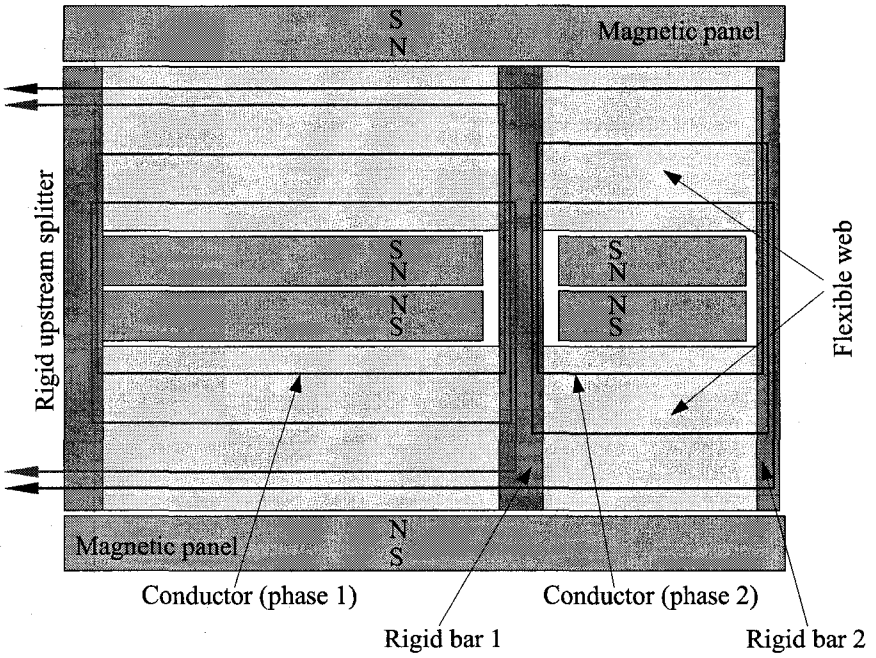

FIGURE 6.17. The pairing-plate design of a flutter-mill and the wiring scheme.

Fifth, additional concentrated masses at the location of the quasi-node and the trailing edge of the plate must be considered in the design of a flutter-mill, as shown in Figs. 6.1 and 6.17, in order to accommodate the wires connecting the ends of conductors to form the conductor coils of the upstream/downstream phases, respectively. The two spanwise rigid bars shown in Figs. 6.1 and 6.17 are actually treated as additional concentrated masses in the two-dimensional model of the system as discussed in Chapter 5. It has been shown in Fig. 5.21(c) that an additional concentrated mass located at the trailing edge of the plate, of the proper magnitude, considerably reduces the critical point of the system; this effect is beneficial for the performance of the flutter-mill. Moreover, as shown in Fig. 5.22 for the case $\mu = 0.2$, when the magnitude of the concentrated mass located at the trailing edge of the plate is relatively large, say $\sigma_M = 0.3$, the size of the quasi-node becomes small and the second beam mode dominates in the dynamics of the system; this characteristic is favourable in the arrangement of the upstream/downsteam phases of the conductors. On the contrary, as shown in Fig. 5.21(b), with an additional concentrated mass located at the quasi-node of the vibration modes (say, $s = 0.75$), the value of the critical point increases with increasing magnitude of the additional concentrated mass; therefore,

one should keep the size of the middle rigid bar, i.e., rigid bar 1 shown in Figs. 6.1 and 6.17, as small as possible. It should be mentioned that, when there is an additional concentrated mass, even of small magnitude, located at the trailing edge of the plate, the plate may vibrate wildly or even whip forward at relatively high flow velocities, as shown in Fig. 5.23; therefore, it is necessary to consider an additional spring support at this location to somewhat suppress the vibration amplitude of the plate.

Sixth, the dynamics of the system with a small oscillating incidence angle in the undisturbed flow has also been studied in Chapter 5. As shown in Fig. 5.28, it was found that the plate may vibrate in higher modes when the frequency of the oscillating incidence angle is relatively large; this effect is not useful for the proposed flutter-mill. Therefore, one should be careful in the design to avoid high frequency unsteady components in the oncoming undisturbed flow, if possible.

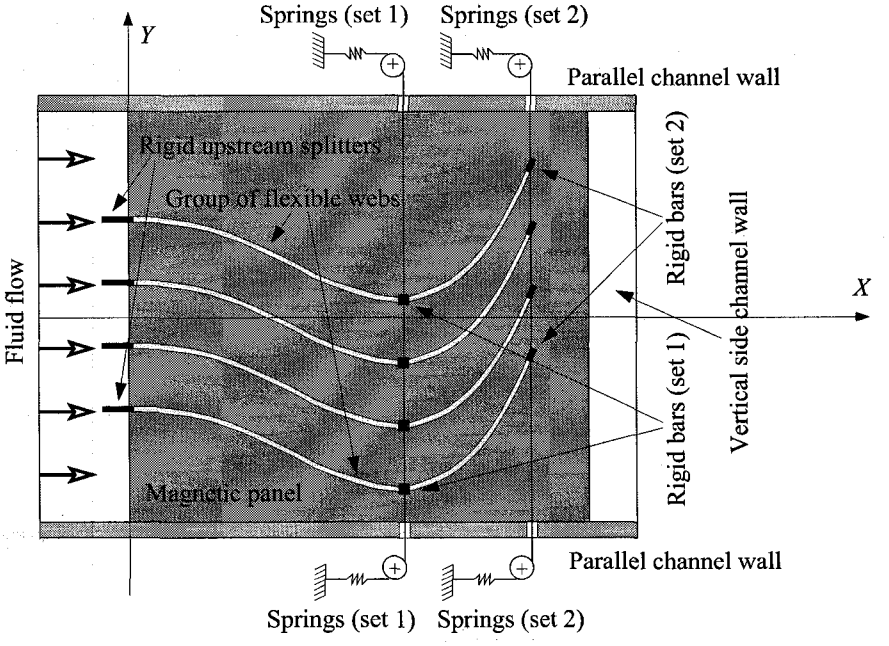

FIGURE 6.18. The design of a flutter-mill with multiple plates aligned in parallel.

Seventh, it is desirable to design a flutter-mill with multiple plates aligned in parallel, as shown in Fig. 6.18, in order to achieve the maximum performance of the device with a compact overall size. The case of two identical parallel plates in open axial flow has been studied in Chapter 5. However, as shown in Fig. 5.31, it

is found that a lower flutter boundary can only be expected from the out-of-phase modes of the two plates; while, when the plates are forced to vibrate in-phase, the critical point of the system substantially increases. The out-of-phase modes are not wanted in the design of a flutter-mill in that when the separation between the two plates is small, the two plates may touch each other at the trailing edges; on the other hand, when the separation is large, the consideration of multiple plates does not help reduce the overall size of the device. As discussed in Chapter 5, according to the work by Zhang et al. (2000) and Farnell et al. (2004), when the plates are placed in channel flow, i.e., when parallel solid walls present, the in-phase modes of the two plates may become less stable than their out-of-phase counterparts. Therefore, it is reasonable to investigate further the design of a flutter-mill with multiple parallel plates combined with the consideration of a container; such an arrangement may achieve a better performance than the single plate design.

Finally, it should be emphasized that, although no extensive optimization has been undertaken in this thesis in the multiparameter space of the system, we have nevertheless been able to outline the design criteria for a flutter-mill in the light of the dynamics of cantilevered flexible plate in axial flow, either in the basic configuration or in various modified configurations, extensively studied in Chapters 4 and 5. Note that the design parameters arising from these design considerations, for example the stiffness/location of the additional spring support, the magnitude/location of the additional concentrated mass, the separation of the two parallel solid walls and so on, should be determined in a more quantitative and extensive manner so as to achieve the best performance of the flutter-mill.

Chapter 7

Experiments

7.1. Introduction

Experiments with cantilevered flexible plates in axial *water* flow are discussed in this chapter. The experiments were conducted in a closed-circulation vertical type water tunnel in the Fluid-Structure Interactions Laboratory at McGill University; an elastomer (silicone rubber) plate has been specially cast for the experiments. Details about the water tunnel and its recent refurbishment, set-up of the support fixture and the elastomer plate, flow velocity calibration, casting process for making the plate, determination of its material properties, and set-up/calibration of displacement-measuring laser system are summarized in Appendix E.

Previous experiments on cantilevered flexible plates in axial flow can be found in the work by Taneda (1968), Datta and Gottenberg (1975), Aurégan and Depollier (1995), Zhang et al. (2000) and Lemaitre et al. (2005) for the system in the hanging configuration (see Fig. 1.3(c)), and by Kornecki et al. (1976), Huang (1995), Yamaguchi et al. (2000a), Watanabe et al. (2002b), Tang et al. (2003), Shelley et al. (2005) and Souilliez et al. (2006) for the vertical configuration (see Fig. 1.3(a)). All previous experiments were conducted in axial *air* flow, except those by Shelley et al. (2005). However, it should be emphasized that, unlike all the other pervious experiments in which homogenous flexible plates (filaments in the experiments by Zhang et al. (2000)) made from a single material were used, the flexible plate investigated in the

water-flow experiments by Shelley et al. (2005) was a "composite" one with copper strips glued onto a Mylar sheet, which may be better described as an articulated flexible plate.

In this thesis, experiments on cantilevered flexible plates in axial flow, in a hanging configuration, are for the first time carried out in a water tunnel. The experiments presented in this thesis are the first phase of a more ambitious and extensive program on the same topic. The purpose of this first phase (i) to explore the suitability of the system (plates, supports and water tunnel), (ii) to investigate methods of measurement, (iii) to obtain enough observations for qualitative description of the dynamics of cantilevered flexible plates in *water flow*, and most importantly (iv) to obtain sufficient experimental data at the high values of the mass ratio μ involved in these experiments to compare with theory; say for $\mu = 80$, which is well beyond the range of μ studied experimentally by other researchers or theoretically in the preceding chapters of this thesis (refer to Figs. 4.16 and 4.17).

7.2. Experimental observations

The physical parameters of the system studied in the current experiments are listed in Table 7.1 (see Appendix E for details). The maximum effective length of the elastomer plate is 240 mm. Pieces of elastomer plate are cut off to yield shorter lengths step by step, and five samples are thus obtained with lengths of 240, 150, 120, 90 and 60 mm. Accordingly, as shown in Table 7.2, the nondimensional parameters of the system can be calculated. Because water, instead of air, is used for the current experiments, one can see from Table 7.2 that the mass ratio μ is very large, even for a plate of moderate length.

Because the system is set up in a hanging configuration, when the elastomer plate is long, as discussed in Chapter 5, the gravitational force has a significant effect on the dynamics of the system. As shown in Fig. 7.1(a), it is found that visible flutter (i.e., oscillation of substantial amplitude) occurs only at the most leeward segment of the elastomer plate (refer to the work by Lemaitre et al. (2005)), while the upstream

TABLE 7.1. Physical parameters of the system

Length of the elastomer plate L	Variable
Length of upstream rigid segment L_0	$9.17 \times 10^{-2}\,\mathrm{m}$
Plate thickness h	$1 \times 10^{-3}\,\mathrm{m}$
Plate width B	$7.4 \times 10^{-2}\,\mathrm{m}$
Mass density of the plate material ρ_P	$1.137 \times 10^{3}\,\mathrm{kg/m^3}$
Young's modulus of the plate material E	$3.62 \times 10^{6}\,\mathrm{N/m^2}$
Poisson ratio of the plate material ν	0.49
Material damping coefficient (Kelvin-Voigt type) a	$4.64 \times 10^{-4}\,\mathrm{s}$
Mass density of the fluid (water) ρ_F	$1.0 \times 10^{3}\,\mathrm{kg/m^3}$

TABLE 7.2. Nondimensional parameters of the system with various lengths of the elastomer plate

Plate length L (mm)	240	150	120	90	60
Mass ratio μ	211	132	106	79.2	52.8
Rigid segment length l_0	0.382	0.611	0.764	1.02	1.53
Material damping coefficient α ($\times 10^4$)	1.49	3.82	5.97	10.6	23.9
Gravity parameter γ_G	46.7	11.4	5.84	2.46	0.73

region is stretched straight. Due to the limitation in the calibration/measurement range of the laser distance (displacement) sensor, as shown in Fig. 7.1(b) (see also Figs. E.13(a) and E.14(b) for the calibration), the dynamics of the system is only recorded with a video for the cases with $L \geqslant 150\,\mathrm{mm}$. On the other hand, the maximum flow velocity of the water tunnel is around 4.8 m/s (see the flow velocity calibration in Fig. E.10), and the flutter of the elastomer plate with the length $L = 60\,\mathrm{mm}$ can only be observed at flow velocities close to the capacity of the water tunnel. Therefore, shortening of the plate was stopped at $L = 60\,\mathrm{mm}$.

The experimental observations of the dynamics of the system, with various lengths of the elastomer plate, with increasing flow velocity are presented in Figs. 7.2 through 7.6, which are snapshots picked from the video footage recorded during the experiments. As one can see from these figures, flutter occurs at sufficiently high flow velocities for all lengths of the elastomer plate that have been tested. However, it is noticed that the flutter amplitudes are very small, and they can be better scaled in terms of plate thickness, unlike those observed in previous experiments in air flow

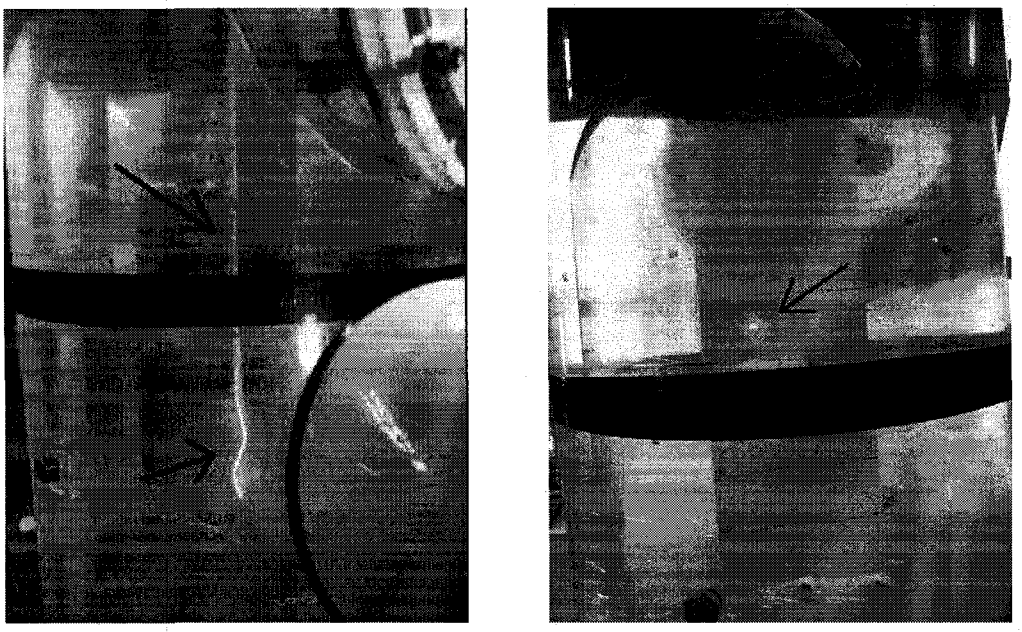

(a) Flutter observed at the most leeward region of the plate with upstream section stretched straight

(b) The lowest point that the laser system can reach for calibration and measuring

FIGURE 7.1. The difficulties in measuring the vibration of a long plate ($L = 240\,\text{mm}$).

where the flutter had a large amplitude (say 20% of the plate length). Another problem encountered in the experiments is the small but ubiquitous vibration of the whole water tunnel caused by the circulation pump, which could be significant when it runs at high rpm. Unsteadiness in the water flow is caused by the pump and the vibration of the water tunnel, which is confirmed by fluctuations in the reading of the flow velocity, and the trembling of the elastomer plate, observed even at low flow velocities. The small flutter amplitudes, combined with unsteady effects in the water flow, result in difficulties in the observation and subsequent measurement of the motions of the elastomer plate. Nevertheless, the onset of flutter can still be determined within a reasonably small range of flow velocities for any given experiment. For example, as shown in Fig. 7.2(a) for $L = 240\,\text{mm}$, the plate trembles, with high frequency and not in any discernible vibration mode, at $U = 2.35\,\text{m/s}$; while, as seen in Fig. 7.2(b), when the flow velocity is increased to $U = 2.61\,\text{m/s}$, flutter with a relatively low frequency and readable instantaneous modal shape (visible with the aid of a stroboscope) emerges. The "critical points" so identified through experimental observations are listed in Table 7.3 and then plotted in Fig. 7.8.

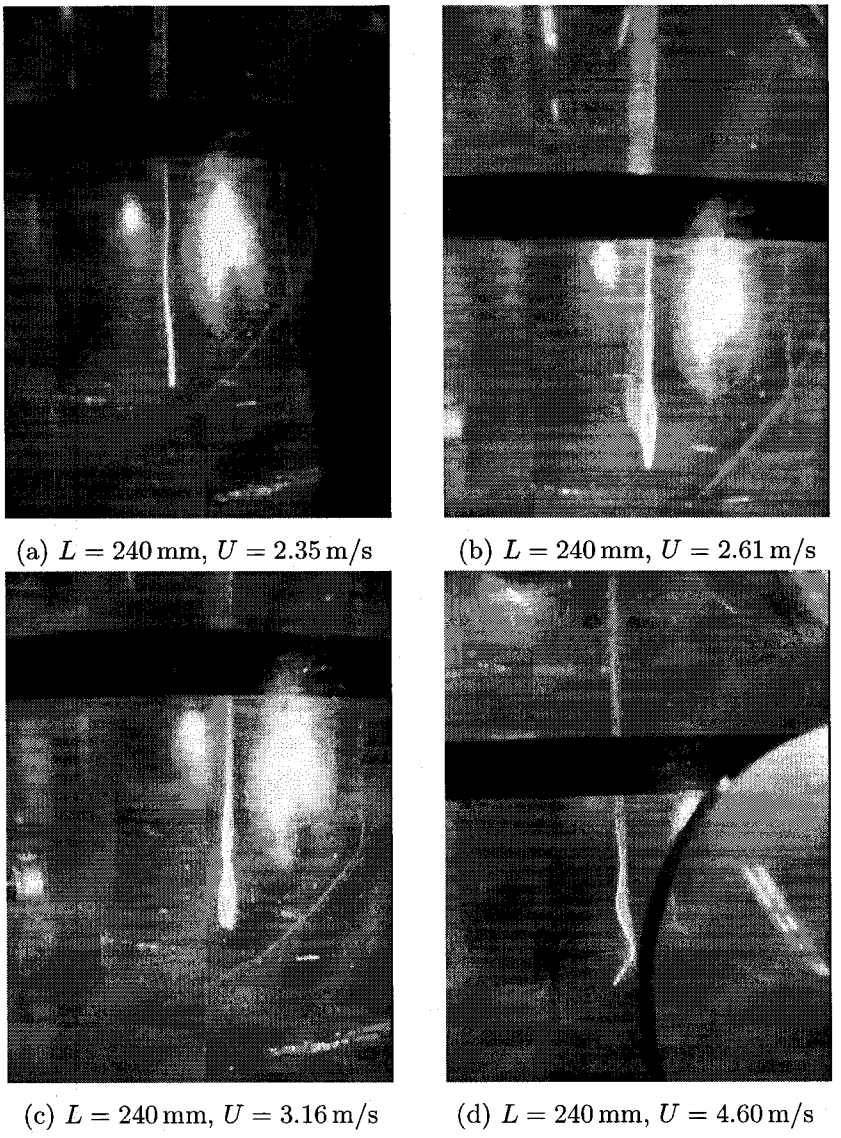

(a) $L = 240\,\text{mm}$, $U = 2.35\,\text{m/s}$ (b) $L = 240\,\text{mm}$, $U = 2.61\,\text{m/s}$

(c) $L = 240\,\text{mm}$, $U = 3.16\,\text{m/s}$ (d) $L = 240\,\text{mm}$, $U = 4.60\,\text{m/s}$

FIGURE 7.2. The dynamics of the elastomer plate $L = 240\,\text{mm}$ at various flow velocities.

As shown in Fig. 7.7, the onset of flutter for the plates used in the experiments can be predicted by the theory developed in this thesis (refer to Section 5.1 of Chapter 5, neglecting viscous drag); the results are listed in Table 7.3. However, because the simulation with a large μ is indeed very time-consuming (measured in days, rather than hours, for a single run), only the two cases of $L = 90\,\text{mm}$ and $L = 60\,\text{mm}$ are investigated theoretically. The results of the numerical simulations are listed in Table 7.4 and then presented in Fig. 7.8.

It can be seen in Fig. 7.8(a) that, for the cases $L \leqslant 150\,\text{mm}$, the experimental values of the critical flow velocity U_c decrease as L is increased; however, a higher

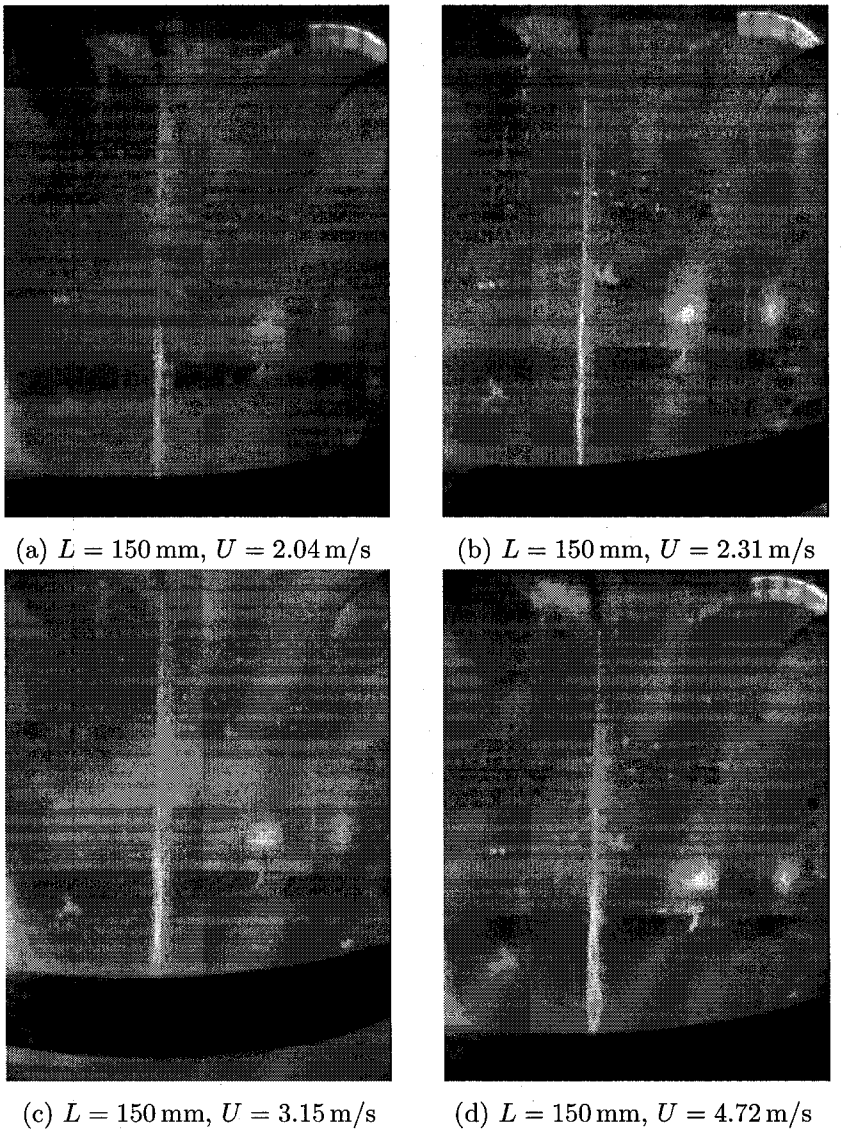

(a) $L = 150\,\text{mm}$, $U = 2.04\,\text{m/s}$ (b) $L = 150\,\text{mm}$, $U = 2.31\,\text{m/s}$

(c) $L = 150\,\text{mm}$, $U = 3.15\,\text{m/s}$ (d) $L = 150\,\text{mm}$, $U = 4.72\,\text{m/s}$

FIGURE 7.3. The dynamics of the elastomer plate $L = 150\,\text{mm}$ at various flow velocities.

value of U_c has been obtained for the case $L = 240\,\text{mm}$ than $L = 150\,\text{mm}$. It is observed in the experiments that spanwise bending, as shown in Fig. 7.9, occurs at the leeward region of long elastomer plates, say for $L = 240\,\text{mm}$. This phenomenon would increase the bending stiffness of the structure and result in a higher critical flow velocity. However, as the length of the elastomer plate decreases, the spanwise bending subsides gradually; it is still visible for $L = 150\,\text{mm}$ and $L = 120\,\text{mm}$, and it becomes negligible for the cases $L = 90\,\text{mm}$ and $L = 60\,\text{mm}$. This observed spanwise bending and its variation with respect to the length of the elastomer plate may account for the increase in the critical flow velocity for the case $L = 240\,\text{mm}$.

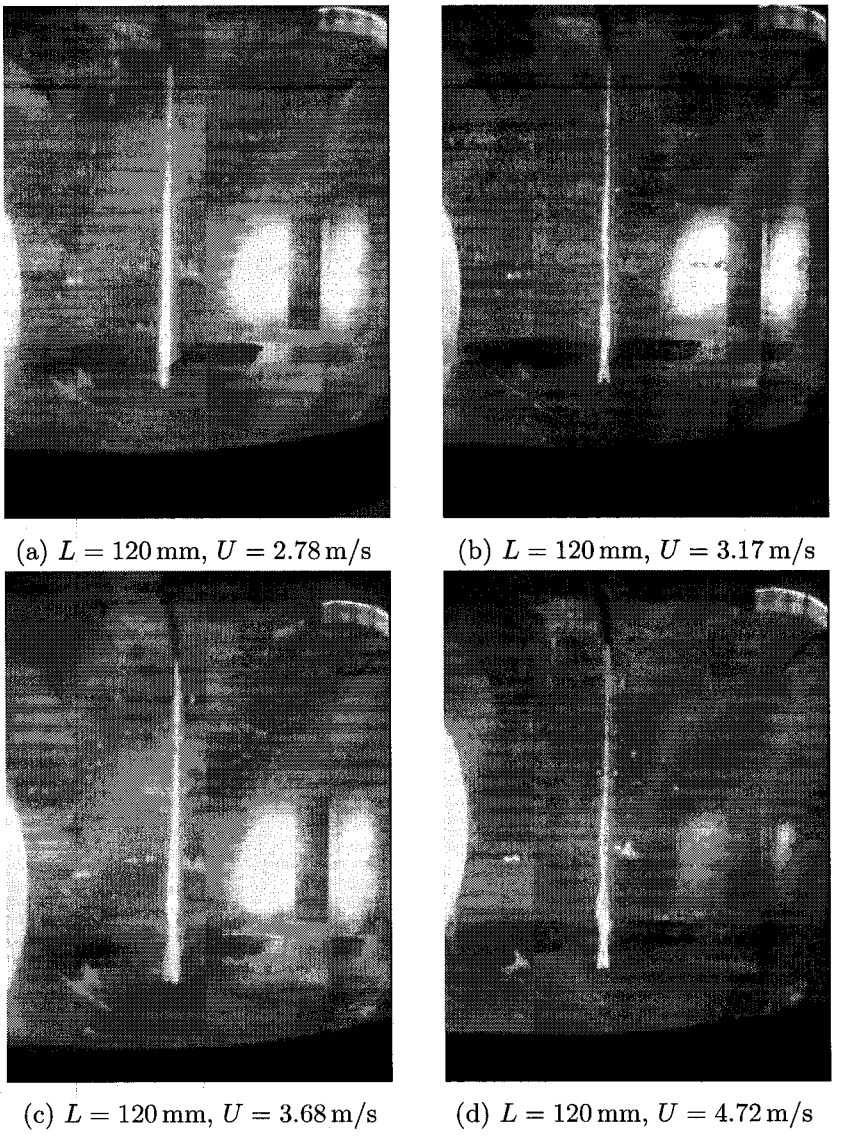

(a) $L = 120\,\text{mm}$, $U = 2.78\,\text{m/s}$ (b) $L = 120\,\text{mm}$, $U = 3.17\,\text{m/s}$

(c) $L = 120\,\text{mm}$, $U = 3.68\,\text{m/s}$ (d) $L = 120\,\text{mm}$, $U = 4.72\,\text{m/s}$

FIGURE 7.4. The dynamics of the elastomer plate $L = 120\,\text{mm}$ at various flow velocities.

The theoretical flutter boundaries predicted by the present theory using the experimental parameters (for the two cases of $L = 90\,\text{mm}$ and $L = 60\,\text{mm}$) and for the systems in the vertical configuration with smaller mass ratios than those investigated in the current experiments are also presented in Fig. 7.8. First, as expected, it can be seen in Figs. 7.8(a) and (b) that the theoretical prediction underestimates the flutter threshold for a specific length of the elastomer plate (note that μ is solely determined by L when the other parameters ρ_{P}, h and ρ_{F} are fixed), most likely due to the absence of viscous drag in the numerical simulations ($C_{\text{D}} = 0$, see Table 7.4). Second, it is of interest to find in Fig. 7.8(c) that both the theoretical predictions and experimental

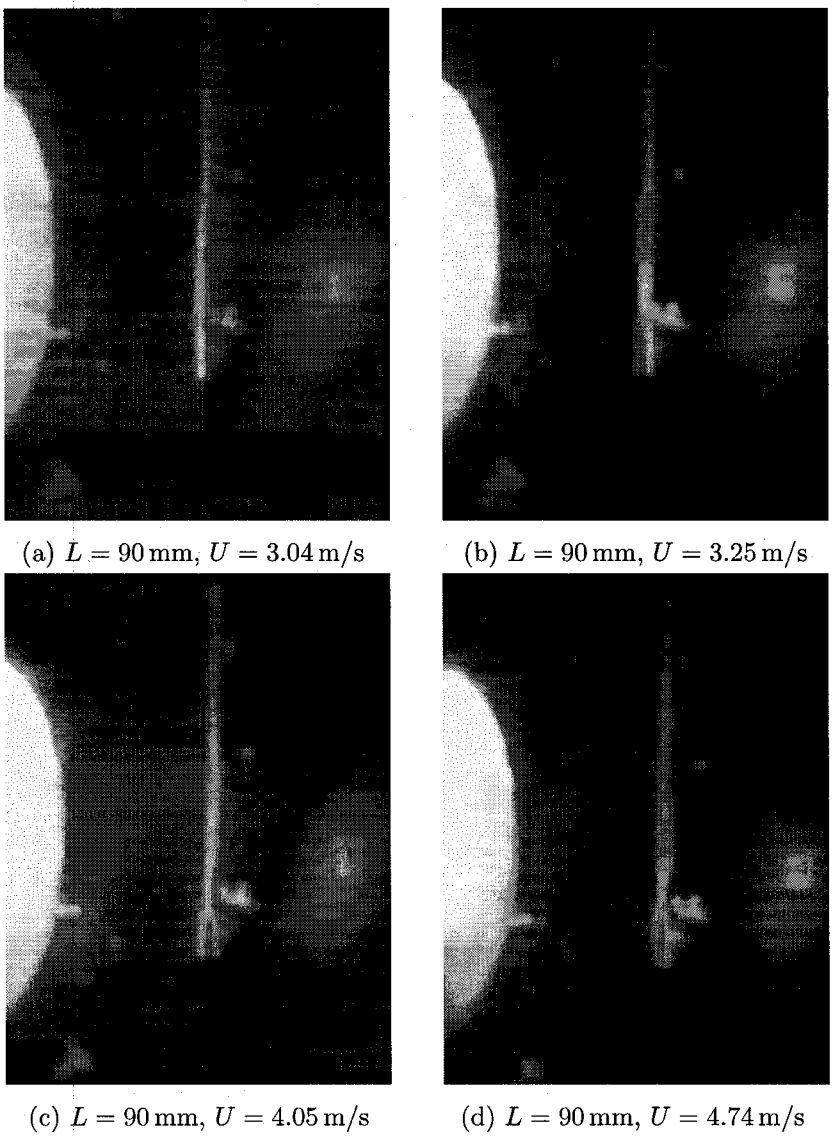

(a) $L = 90\,\text{mm}$, $U = 3.04\,\text{m/s}$ (b) $L = 90\,\text{mm}$, $U = 3.25\,\text{m/s}$

(c) $L = 90\,\text{mm}$, $U = 4.05\,\text{m/s}$ (d) $L = 90\,\text{mm}$, $U = 4.74\,\text{m/s}$

FIGURE 7.5. The dynamics of the elastomer plate $L = 90\,\text{mm}$ at various flow velocities.

observations for the system with large values of μ, even though they are obtained for the system in the *hanging configuration*, can approximately be viewed as a continuation of the flutter boundary obtained in Chapter 4 for the system in the *vertical configuration*. The importance of this observation lies in that the extension of the flutter boundary to a mass ratio as large as $\mu = 200$ is, for the first time, confirmed by the current experiments. It should be mentioned that, although the theoretical flutter boundary of the system in either the vertical or hanging configuration can be extended to an arbitrarily large value of μ, it is impossible in practice to check the theory with experiments in *air flow* when μ is very large, say $\mu > 40$. In particular, as shown in Table 7.5, if a plate made from the same material as the one used in

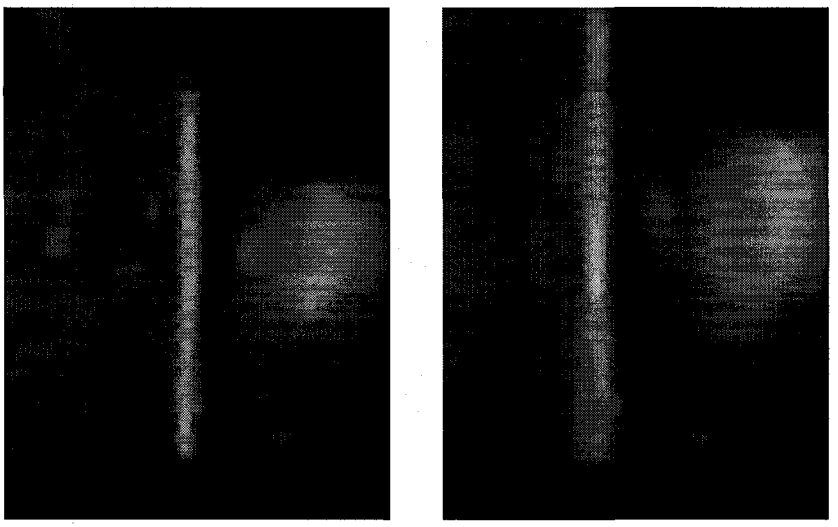

(a) $L = 60\,\text{mm}$, $U = 4.53\,\text{m/s}$ (b) $L = 60\,\text{mm}$, $U = 4.75\,\text{m/s}$

FIGURE 7.6. The dynamics of the elastomer plate $L = 60\,\text{mm}$ at various flow velocities.

TABLE 7.3. The flutter boundaries of the system with various lengths of the elastomer plate obtained through experimental observations

Plate length L (mm)	240	150	120	90	60
Mass ratio μ	211	132	106	79.2	52.8
Lower boundary of U_c (m/s)	2.35	2.04	2.78	3.04	4.53
Upper boundary of U_c (m/s)	2.61	2.31	3.17	3.25	4.75
Corresponding values of U_{Rc} and U_{Rc}/μ					
Lower boundary of U_{Rc}	1.49	3.82	5.97	10.6	23.9
(U_{Rc}/μ)	(0.143)	(0.124)	(0.168)	(0.186)	(0.275)
Upper boundary of U_{Rc}	46.7	11.4	5.84	2.46	7.30
(U_{Rc}/μ)	(0.159)	(0.140)	(0.192)	(0.198)	(0.288)

the current experiments is considered for experiments in air flow, in order to obtain a mass ratio $\mu = 79.2$ (as the case $L = 90\,\text{mm}$ in the current experiments), one has to use a plate as long as 90 m with a thickness of $h = 1\,\text{mm}$, or a "plate" as thin as $1.0 \times 10^{-3}\,\text{mm}$ for a fixed length of $L = 90\,\text{mm}$!

Moreover, in previous work, the dynamics of the system with a mass ratio $\mu > 40$ (i.e., beyond the limit of Fig. 4.16) was studied theoretically by Yamaguchi et al. (2000b) and Souilliez et al. (2006), and only a single case of $\mu = 85.2$ can be found in the experiments conducted by Watanabe et al. (2002b); the results of these theoretical predictions and experimental observations are presented in Fig. 7.8(c). It can be seen that the trend of the current experimental flutter boundary is again confirmed by the

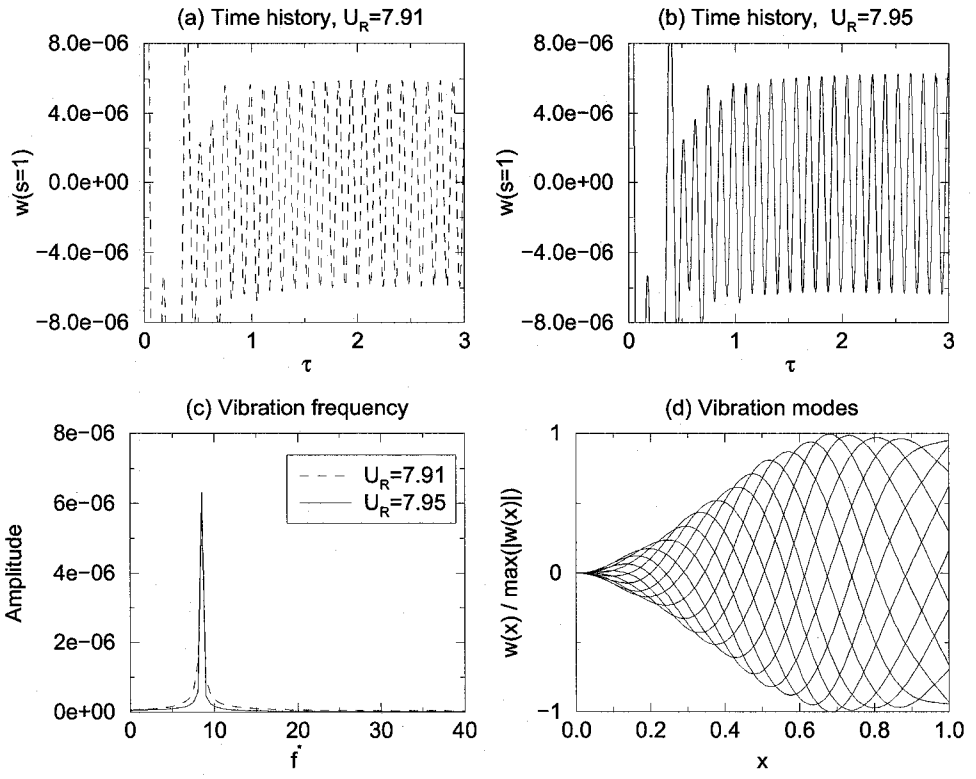

FIGURE 7.7. The dynamics of the system theoretically predicted at the critical point for the case $L = 90\,\text{mm}$.

TABLE 7.4. Critical points predicted by the present theory using the experimental data for the cases $L = 90\,\text{mm}$ and $L = 60\,\text{mm}$

Plate length L (mm)	90	60
Parameters for simulation		
Mass ratio μ	79.2	52.8
Rigid segment length l_0	1.02	1.53
Material damping coefficient α ($\times 10^4$)	10.6	23.9
Gravity parameter γ_G	2.46	0.73
Viscous drag coefficient C_D	0	0
Simulation results		
Critical reduced flow velocity U_{Rc}	7.93	6.88
Critical flutter frequency $f_c^\star$	8.5	6.5
Corresponding dimensional data		
Critical flow velocity U_c (m/s)	1.65	2.14
Critical flutter frequency f_c (Hz)	19.6	33.7

theories of Yamaguchi et al. (2000b) and Souilliez et al. (2006), and they agree with theoretical predictions much better than the singe data point provided by Watanabe et al. (2002b).

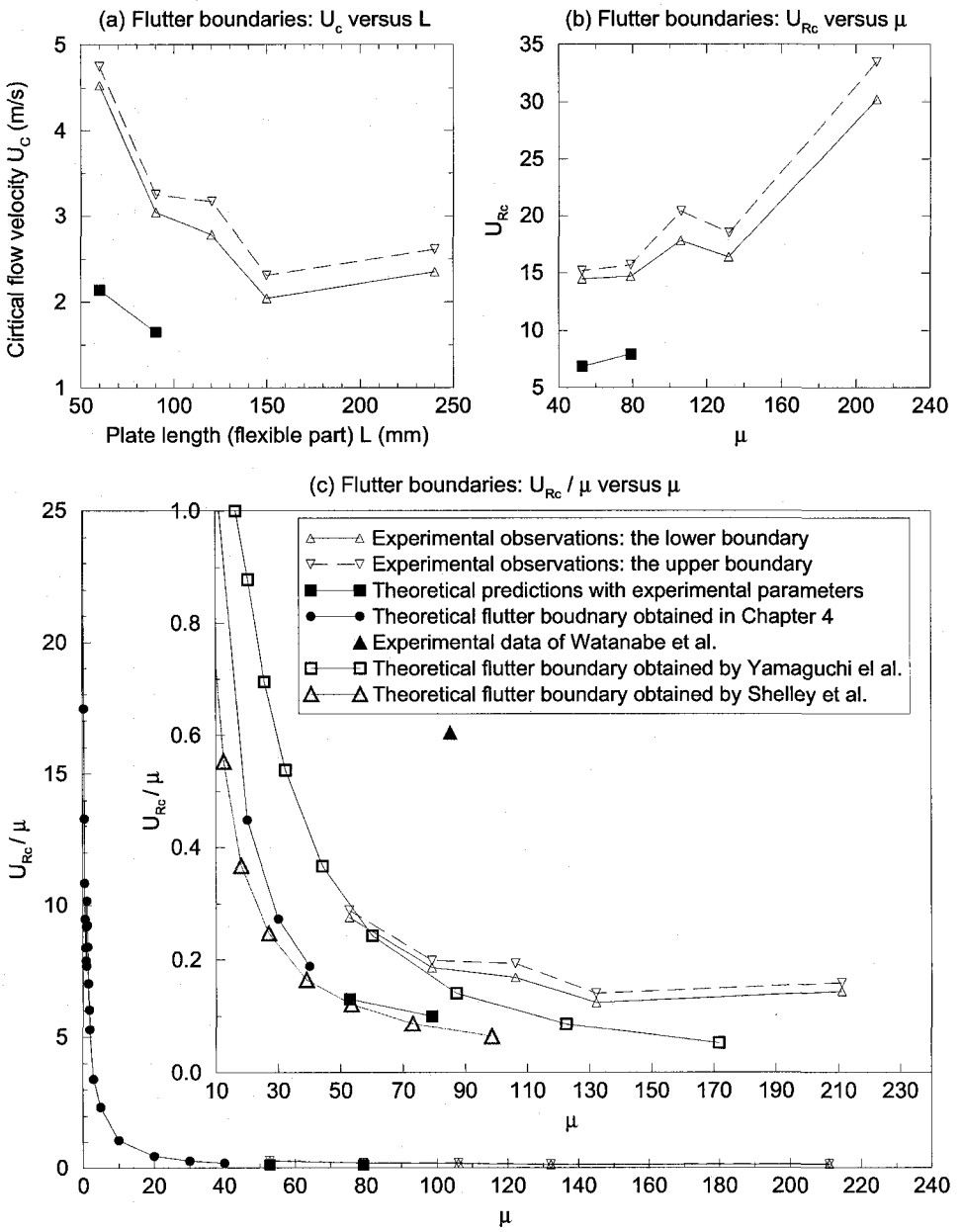

FIGURE 7.8. The flutter boundaries of the system with various lengths of the elastomer plate. Note that the upstream rigid segment has a fixed length of $L = 91.7\,\text{mm}$ in all experiments. Moreover, as for the theoretical flutter boundary obtained in Chapter 4, the other nondimensional parameters of the system are: $l_0 = 0.01$, $\alpha = 0.004$ and $C_D = 0$ (refer to Fig. 4.16).

In the current experiments, for the elastomer plate with a given length, larger flutter amplitudes are observed, in general, as the flow velocity is increased. However, it is also found that the flutter amplitude could become smaller with increasing flow velocity. Moreover, non-instrument-aided observations suggested spontaneous flutter

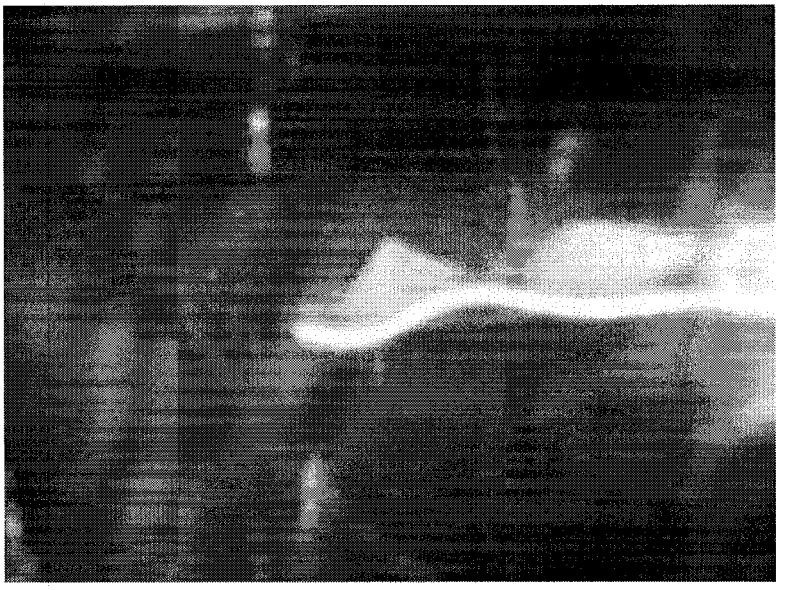

FIGURE 7.9. The spanwise bending observed for a long elastomer plate $L = 240\,\text{mm}$.

TABLE 7.5. Assumed physical data of the system with a large mass ratio for putative experiments in air flow

Mass ratio μ	79.2	79.2
Mass density of the plate ρ_P (kg/m^3)	1.137×10^3	1.137×10^3
Mass density of the fluid (air) ρ_F (kg/m^3)	1.226	1.226
Plate thickness h (mm)	1	1.0×10^{-3}
Plate length L (m)	90	0.09

at some flow velocities below the "critical point". In the current experiments, instantaneous displacements of the elastomer plate at a point close to the trailing edge are measured by the laser distance sensor with a sampling frequency rated at 10 kHz; from the recorded time history of displacement data at a specific flow velocity, one can obtain the vibration amplitude and spectrum. In particular, the vibration amplitudes of the elastomer plate at various flow velocities for the case $L = 90\,\text{mm}$ are shown in Fig. 7.10, and the corresponding vibration spectra are shown in Figs. 7.11 through 7.13. It should be mentioned that, due to the unsteadiness in the water flow, the readings of flow velocity fluctuate during measurement; therefore, the data in Fig. 7.10 are locally averaged values for both the flow velocities and vibration amplitudes. It can be seen in Fig. 7.10 that the largest vibration amplitude occurs at $U = 4.06\,\text{m/s}$, while two other peaks can be seen at $U = 2.28\,\text{m/s}$ and $U = 3.02\,\text{m/s}$. Two data-fitting curves, a linear one for the points $U < 4.06\,\text{m/s}$, and the other

one with cubic spline for the points $U \leqslant 4.06\,\mathrm{m/s}$ are also plotted in Fig. 7.10; the intersection point is found to be located at $U = 3.22\,\mathrm{m/s}$. This point is regarded as the "critical point", which agrees well with the one found in experimental observations at $U = 3.25\,\mathrm{m/s}$ shown in Figs. 7.5(a) and (b). Moreover, when $U = 3.25\,\mathrm{m/s}$ the first three peaks of the corresponding vibration spectrum in Fig. 7.12(c) are at $f = 16.8\,\mathrm{Hz}$, $15.0\,\mathrm{Hz}$ and $20.3\,\mathrm{Hz}$; the highest peak ($f = 16.8\,\mathrm{Hz}$) is not too far from the theoretical critical flutter frequency $f_c = 19.6\,\mathrm{Hz}$ shown in Fig. 7.7(c) and Table 7.4.

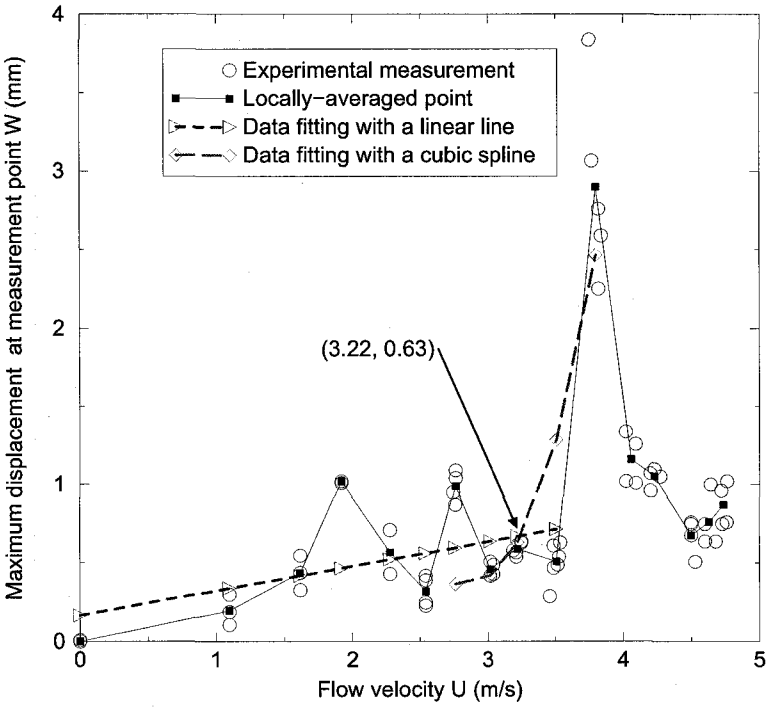

FIGURE 7.10. Vibration amplitudes of the elastomer plate at the measurement point and the determination of the critical point for the case $L = 90\,\mathrm{mm}$.

The underlying mechanism of the multiple peaks in Fig. 7.10 is still an open question. A possible reason may be the unsteadiness in the water flow. That is, the motion of the plate may be a combination of the self-induced flutter and the externally-excited vibration. As has already been shown in Chapter 5 for the system with a small oscillating component in the oncoming undisturbed flow, a plate may vibrate with significant amplitudes when the frequency of external excitation approaches the critical frequency f_c of the system. It should nevertheless be mentioned

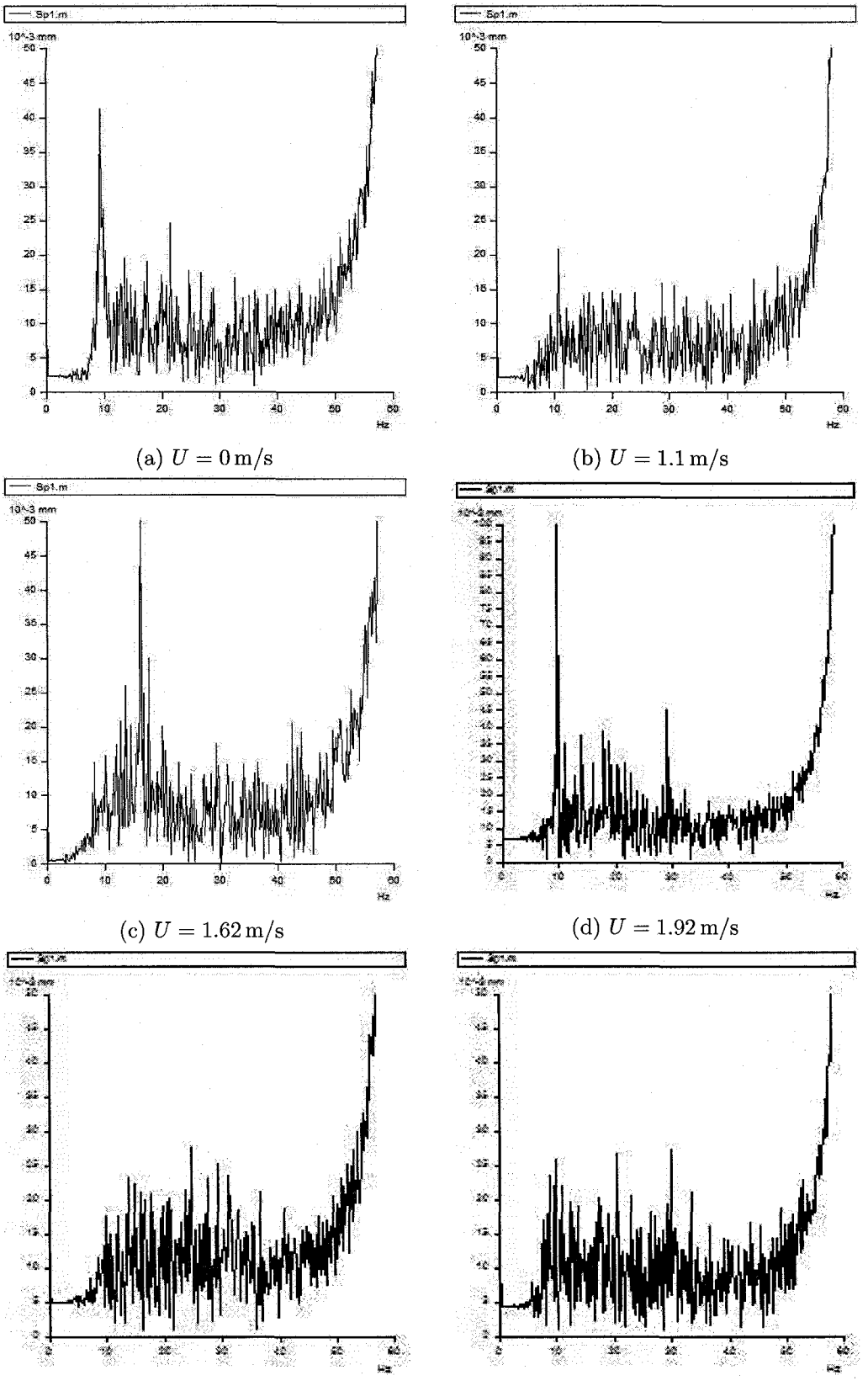

(a) $U = 0\,\mathrm{m/s}$ (b) $U = 1.1\,\mathrm{m/s}$

(c) $U = 1.62\,\mathrm{m/s}$ (d) $U = 1.92\,\mathrm{m/s}$

(e) $U = 2.28\,\mathrm{m/s}$ (f) $U = 2.54\,\mathrm{m/s}$

FIGURE 7.11. Vibration frequency of the elastomer plate $L = 90\mathrm{mm}$ at various flow velocities (part 1).

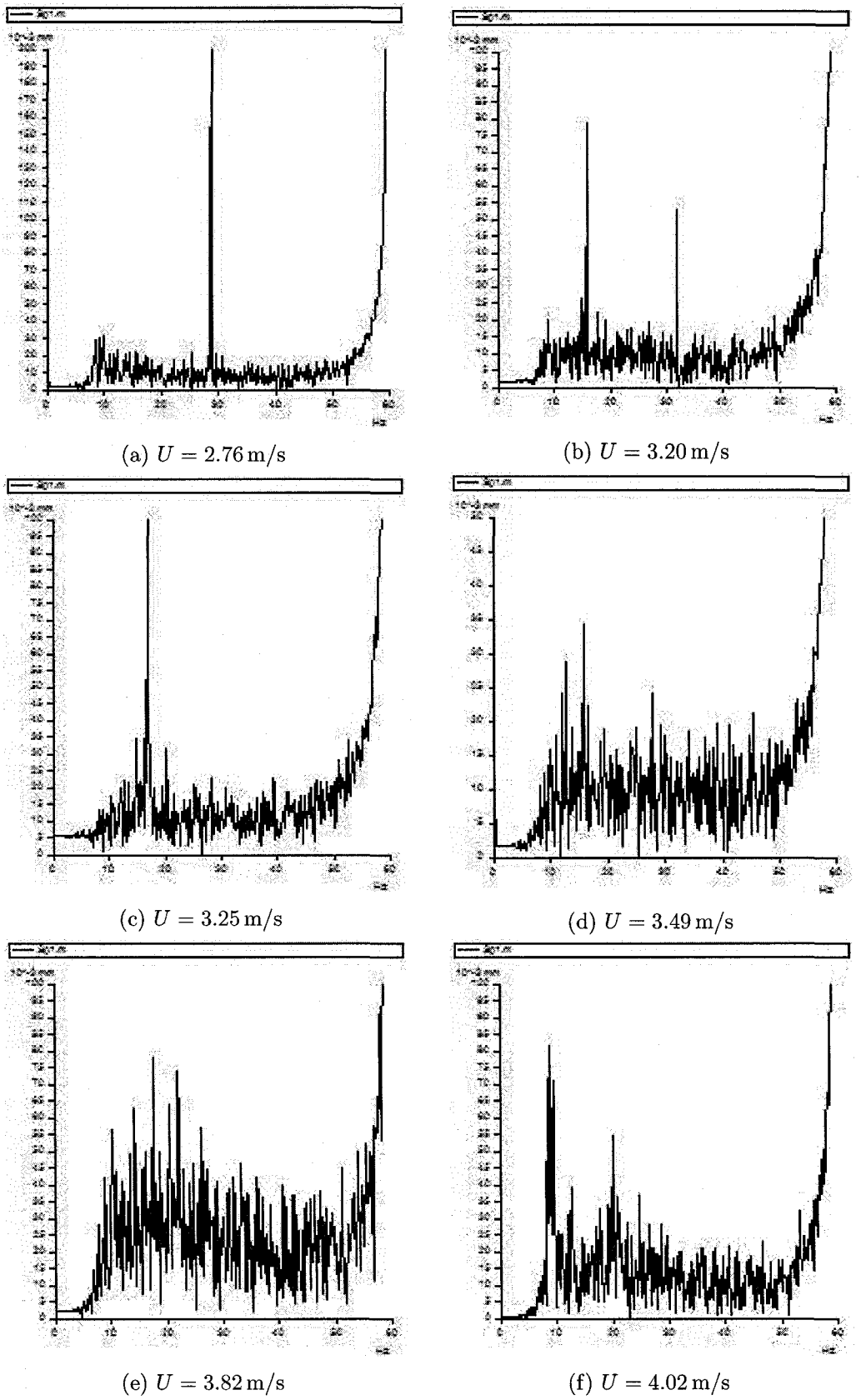

(a) $U = 2.76\,\mathrm{m/s}$

(b) $U = 3.20\,\mathrm{m/s}$

(c) $U = 3.25\,\mathrm{m/s}$

(d) $U = 3.49\,\mathrm{m/s}$

(e) $U = 3.82\,\mathrm{m/s}$

(f) $U = 4.02\,\mathrm{m/s}$

FIGURE 7.12. Vibration frequency of the elastomer plate $L = 90\mathrm{mm}$ at various flow velocities (part 2).

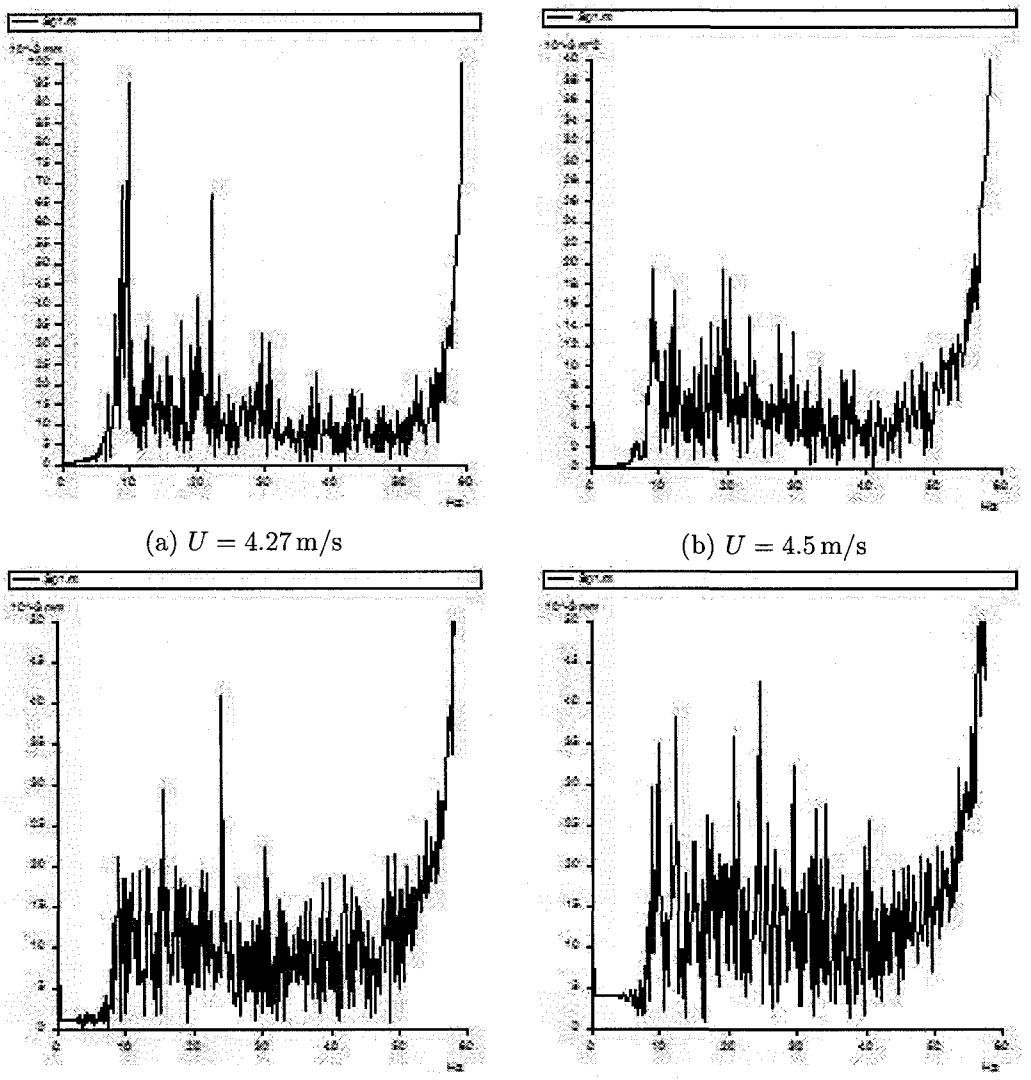

(a) $U = 4.27\,\mathrm{m/s}$ (b) $U = 4.5\,\mathrm{m/s}$

(c) $U = 4.6\,\mathrm{m/s}$ (d) $U = 4.76\,\mathrm{m/s}$

FIGURE 7.13. Vibration frequency of the elastomer plate $L = 90\mathrm{mm}$ at various flow velocities (part 3).

that the case studied in Chapter 5 is for a system with a small value of μ, in which the first two beam modes dominate the dynamics; while in the current case with a large mass ratio, as one can see in Fig. 7.7(d), beam modes up to the fourth one are important.

It should also be mentioned that we can use another criterion for the onset of flutter, namely the transition from turbulence/unsteadiness-induced random vibration to coherent periodic oscillation. From Figs. 7.11 and 7.12, we see that this occurs at $U = 1.92\,\mathrm{m/s}$ with a frequency of $f = 9.7\,\mathrm{Hz}$ and again at $U = 2.76\,\mathrm{m/s}$ with a frequency of $f = 28.9\,\mathrm{Hz}$ and also at $U = 3.25\,\mathrm{m/s}$ with a frequency of $f = 16.8\,\mathrm{Hz}$. The

intriguing possibility arises that the onset of flutter, albeit with small amplitude, occurs at the first of these ranges of coherent oscillation, which means at $U_c = 1.92\,\mathrm{m/s}$. The other coherent peaks would then be interpreted to correspond to other modes of flutter, with larger amplitude, including the one found by the traditional method of Fig. 7.10. What is interesting is that the critical flow velocity would then be lower by a factor of two approximately, and thus be quite close to the current theoretical prediction shown in Fig. 7.8. Clearly more work is needed: more experiments and more sophisticated measurements, perhaps with multiple sensors, before this matter and the conjecture made in this paragraph can be fully resolved.

7.3. Summary

In this chapter, some experiments with cantilevered flexible plates in axial flow, in the hanging configuration, have been presented. Because water flow is used, we are able to investigate experimentally the dynamics of the system with very large values of mass ratio. The vibration (flutter) amplitudes of the elastomer plates in water flow are very small and can be scaled in terms of the plate thickness, instead of the plate length as adopted in all previous experiments conducted in air flow. The small vibration amplitude of the plate and the unsteadiness in the flow cause a lot difficulties in the experiments and subsequent interpretation of the results. Nevertheless, the onset of flutter can be identified as a small range of flow velocities rather than a single value for the cases studied, both qualitatively and quantitatively. However, no solid information can be obtained from the current experiments as to the nature of flutter (supercritical or subcritical) and the post-critical dynamics of the system, partly because the amplitudes are so small. The flutter thresholds of the system for two chosen cases investigated experimentally are predicted by the present theory; the theoretical predictions agree with experimental observations reasonably well. Moreover, a segment of the flutter boundary is defined *via* the current experiments, which agrees with the overall trend of the flutter boundary obtained in Chapter 4 and can thus be regarded as an extension of the latter one to the range of large mass ratios.

Chapter 8

Conclusion and Future Work

8.1. General comments

In this chapter, we summarize the work done in this thesis on the dynamics of two-dimensional cantilevered flexible plates in axial flow and outline possible future work. One can see in the organizing diagram of Fig. 1.6 that, in Chapters 2 and 3 of this thesis, we have developed the analytical model for the fluid-structure interaction system and the corresponding solution method. The dynamics of the system in its basic configuration was extensively studied in the multiparameter space in Chapter 4; the influence of various parameters on the dynamics of the system were discussed therein. Then, in Chapter 5, the investigation on the dynamics of cantilevered flexible plates in axial flow was extended to cover systems in a variety of modified configurations; the influence of the parameters arising from these new features were discussed. The motivation for the work in this thesis was two-fold: one was to improve understanding in general; and the other, discussed in Chapter 6, was to propose a new concept for an energy-harvesting device (the "flutter-mill"), utilizing the flutter motions of cantilevered flexible plates in axial flow and based on the analysis of energy transfer between the plate and the surrounding fluid flow. Moreover, design considerations for this energy-harvesting device in the light of the dynamics of the system, in either the basic configuration or the modified configurations, were discussed. Finally,

in Chapter 7, experiments conducted in this thesis were discussed and the results were compared to predictions obtained using the present theory.

This thesis aimed to give a comprehensive, but by no means complete, picture of the global dynamics of cantilevered flexible plates in axial flow. Therefore, a relatively simple but efficient model has been adopted in the study of the dynamics of the system. Refined models should be considered in future work, on the one hand to verify the results obtained in this thesis, and on the other hand to overcome the limitations of the present theory. Moreover, in the future, an optimization process should be considered in order to achieve the best possible performance of the proposed flutter-mill; also, a prototype of this device should be built to verify the new energy-harvesting concept.

8.2. Summary and conclusion

In this thesis, a model for studying the dynamics of the cantilevered plate was developed using the inextensibility assumption, i.e., assuming that the centreline of the plate remains unstretched during deformation. The panel method, in particular, the unsteady lumped vortex model associated with a dynamic vortical wake was used for calculating the aero/hydro-dynamic loads acting on the plate. The aero/hydro-dynamics model of the system is discrete *per se*, while the Galerkin method has been used to discretize the governing partial differential equation of the plate. Although the equation of motion only accounts for the transverse deformations of the plate, the longitudinal deformations can conveniently be recovered utilizing the inextensibility assumption. The deformations and vibration velocities in both the transverse and longitudinal directions were taken into account in the aero/hydro-dynamics model of the system. The simulation results obtained using the fluid-structure interaction model developed in this thesis were first compared with experimental observations/measurements published by other researchers; it was found that the present theory can well capture the inherent characteristics of the dynamics of the system, in

terms of the flow velocity and vibration frequency at the critical point and the modes of post-critical vibrations.

Through nondimensionalization of the analytical model, nondimensional parameters of the system have been identified; the dynamics of the system was studied in the multiparameter space consisting of the mass ratio μ, the reduced flow velocity U_{R}, the length of the upstream rigid segment l_0, the material damping coefficient α and the viscous drag coefficient C_{D}.

For a specific system, a critical reduced flow velocity (i.e., the critical point) U_{Rc} exists: flutter takes place when $U_{\mathrm{R}} > U_{\mathrm{Rc}}$; while the plate remains its static flat state and any disturbance to the system is attenuated when $U_{\mathrm{R}} < U_{\mathrm{Rc}}$. The present theory predicts the onset of the dynamic instability (flutter) in a supercritical manner, although subcritical onset of flutter is more commonly observed in experiments. The discrepancy between theories (the present theory and all the other theories to date) and experiments has been discussed regarding the type of instability predicted/observed; in this thesis, an explanation is proposed in regards of the correlation between the stability of the system and the evolution of a von Kármán vortical wake street to a flutter wake street. As for the post-critical behaviour of the system, the flutter amplitude of the plate increases with increasing U_{R}, but the vibration modes of the system are qualitatively the same for a fixed value of μ.

The influence of the parameters l_0, α and C_{D} on the dynamics has been investigated. It was found that U_{Rc} increases with increasing α; while the variation of U_{Rc} with respect to l_0 depends on the value of μ. With a larger value of C_{D}, U_{Rc} grows and the flutter frequency at a fixed U_{R} beyond the critical point increases significantly. For a system with a fixed value of μ, the variations of l_0, α and C_{D} do not change *qualitatively* the vibration modes of the system.

Flutter boundaries in terms of μ were predicted using the present theory. In order to give a clearer and more physically meaningful representation, the flutter boundaries are plotted using U_{Rc}/μ as the ordinate. The flutter boundaries obtained using the present theory are compared to some of the previous theoretical predictions

and experimental observations; the present theory achieves a better agreement with experimental observations than previous theories. With the U_{Rc}/μ versus μ plots of the the flutter boundaries obtained using different theories and experiments, a global trend of the flutter boundary could be clearly identified in terms of the dimensional critical flow velocity U_{c} and the dimensional length of the (flexible) plate L when the other physical parameters, ρ_{P}, ρ_{F}, h and D, of the system are fixed. In particular, when the plate is short (say $\mu < 1$), U_{c} is very sensitive to L; while, when the plate is sufficiently long (say $\mu > 4$), U_{c} is almost a constant, varying very gradually with changing L. In general, U_{c} decreases with increasing L; however, as L increases, local rise-and-then-subsidence phenomena may be observed due to transitions in the flutter mode shapes. Another important conclusion made from the comparison of the flutter boundaries obtained using various theories and experiments is that: for a specific system with only varying length of the (flexible) plate L, when the plate is long the various available theories are in good agreement with each other as well as with measurements from different experiments; in contrast, for short plates agreement between the various theories and with experiments is relatively poor. Although the dynamics of the system has been studied in a multiparameter space and the influences of various factors affecting the dynamics of the system are interwoven, it is demonstrated in Appendix D that the wake has much less influence on the stability of the fluid-structure system for long plates than it does for short ones.

Modified configurations of the system have also been considered, taking into account gravitational forces, parallel solid walls, an additional spring support, an additional concentrated mass, an oscillating incidence angle of the undisturbed flow and two identical cantilevered flexible plates parallel to each other. Rich dynamics has been observed for systems in the modified configurations; the influence of the new parameters, arising from the various new features, to the dynamics of the system were investigated. In particular, these new parameters, in their nondimensional forms, include: the gravity parameter γ_{G} when the system is set up in the horizontal or hanging configuration, the distances between the neutral plane of the flexible plate $h_{1,2}$ and the upper/lower parallel solid walls present, the stiffness k_{L} (in the case

of a linear spring) or k_{C} (in the case of a nonlinear spring of the cubic type) and the location s_{S} when an additional spring support is considered, the magnitude σ_{M} and the location s_{M} when an additional concentrated mass is taken into account, the magnitude α_U and the frequency f_{α_U} when the undisturbed flow has an oscillating incidence angle with respect to the neutral plane of the plate, and the separation distance d_{P} when the system has two identical plates aligned in parallel. It should be emphasized that, if not otherwise specified, the investigations carried out in this thesis for modified configurations of the basic system are based on a fixed set of parameters, i.e., $\mu = 0.2$, $l_0 = 0.01$, $\alpha = 0.004$ and $C_{\mathrm{D}} = 0$.

If the system is in the horizontal configuration, the plate was found to statically deform under the action of the gravitational force when U_{R} is small. At a critical point U_{Rc}, which is higher than its counterpart of the basic configuration, flutter takes place. Moreover, when $U_{\mathrm{R}} > U_{\mathrm{Rc}}$, the vibration modes are no longer symmetric with respect to the neutral plane of the plate. With increasing γ_{G}, the increase in U_{Rc} and the asymmetry in the vibration modes become more significant. On the other hand, when the plate is set up in the hanging configuration, the gravitational forces contribute to the tension in the plate; moreover, higher values of U_{Rc} and higher flutter frequencies can be observed, as compared to the corresponding cases of the basic configuration.

When parallel solid walls confine the flow laterally, only the cases of $h_1 = h_2$ were considered in this thesis. In the presence of the parallel solid walls, the critical point U_{Rc} of the system was found to be below its counterpart in the basic configuration. It was found that U_{Rc} increases as the value of $h_1 = h_2$ is increased: U_{Rc} is sensitive to the size of the channel when $h_1 = h_2 < 2$; while, it changes slowly as the value of $h_1 = h_2$ is varied when $h_1 = h_2 > 2$ and finally converges to the critical point for the unconfined system when $h_1 = h_2 = 10$. However, the presence of the parallel solid walls does not *qualitatively* change the vibration modes of the system.

With the installation of an additional linear spring support, the primary instability of the system was found to still be of the dynamic type when k_{L} is small; while the system loses stability through static divergence (buckling) when k_{L} is sufficiently

large. The system dynamics depends on the location of the linear spring support: flutter of a plate with a linear spring support at the trailing edge may disappear, the plate becoming subject to buckling instead, at a larger value of U_{R}; if the linear spring support is located at $s_{\mathrm{S}} = 0.8$, the plate may develop flutter after buckling, at larger U_{R}. Only symmetric limit cycle oscillations have been observed in the flutter region of the system with an additional linear spring support; the flutter amplitude increases with increasing U_{R} at a fixed value of k_{L}. A stronger-constraint/less-stable phenomenon is found for the plate with an additional linear spring support located in the interval $0.5 \leq s_{\mathrm{S}} \leq 0.8$, where the system with $\mu = 0.2$ loses stability through flutter.

A rich spectrum of nonlinear dynamics has been observed for cantilevered plates with an additional cubic spring support in axial flow. Beyond the primary instability of the dynamic type, the system develops symmetric limit cycle oscillations; the symmetry is broken at a larger U_{R}. With further increases in U_{R}, a series of period-doubling bifurcations lead to chaotic oscillations. Finally, when U_{R} is sufficiently large, the plate becomes statically buckled. The system dynamics with an additional cubic spring support also depends on the spring location. With the cubic spring support at $s_{\mathrm{S}} = 1$, a neat period-doubling route to chaos can be identified. The dynamics becomes more complicated when the cubic spring support is mounted at $s_{\mathrm{S}} = 0.8$: the flutter amplitude may decrease with increasing U_{R}; beyond the primary region of chaotic motions, regular limit cycle oscillations re-emerge and another period-doubling route leads to the main region of chaos. The critical point U_{Rc} of the system with an additional concentrated mass depends on the parameters σ_{M} and s_{M}. When $s_{\mathrm{M}} = 0.75$, U_{Rc} increases with increasing σ_{M}. On the other hand, when $s_{\mathrm{M}} = 1$, U_{Rc} first decreases as σ_{M} increases; a plateau is reached in the range $0.1 < \sigma_{\mathrm{M}} < 0.2$. With further increase in σ_{M}, U_{Rc} grows. This observed trend of U_{Rc} versus σ_{M}, for the case of $s_{\mathrm{M}} = 1$, is correlated with the variation in flutter modes of the plate at the different values of σ_{M}. Moreover, when $s_{\mathrm{M}} = 1$, it was found that even a small value of σ_{M} can significantly alter the dynamics of the system in that the flutter takes

place in a more abrupt manner and the rear part of the plate may become wrapped forward at relatively high values of U_{R}.

When the undisturbed flow has an small incidence angle with respect to the neutral plane of the plate, in particular, $\alpha_U = 5^{\circ}$ and $f^{\star}_{\alpha_U} = 0$, the plate first becomes statically deformed under the action of the fluid loads; then, at a smaller value of U_{Rc} than its counterpart in the basic configuration, flutter takes place. The post-critical dynamics of the system is the same as that of the basic configuration, except that a buckling component can be observed; moreover the vibration modes of the system are no longer symmetric with respect to the neutral plane of the plate. When the undistributed flow has a small oscillating incidence angle, i.e., $f^{\star}_{\alpha_U} \neq 0$, resonance phenomena in the frequency-response of the system can be observed. However, since the plate is flexible and the vibration modes of the system vary at different values of $f^{\star}_{\alpha_U}$, the locations of the frequency-response peaks depend on the location chosen to observe the response amplitude. The pattern of the frequency-response shows that an external excitation, i.e., the small oscillating incidence angle of the undisturbed flow, has been applied to the system. However, because the undisturbed flow and the plate are two inseparable parts of an integrated system and the aero/hydro-dynamic forces (with a small oscillating incidence angle) depend on the motions of the plate, one cannot be sure to observe subharmonic/superharmonic phenomena in the frequency response of the system.

When the system consists of two identical plates aligned in parallel in axial flow, it has been found the the in-phase modes are more stable than the out-of-phase modes. As compared to the system in the basic configuration, with decreasing values of d_{P}, the two-plate system becomes increasingly less stable in the out-of-phase modes; while, on the contrary, it becomes increasingly more stable in the in-phase modes. When d_{P} is sufficiently large, the coupling between the two plates diminishes, and they vibrate independently. When the value of d_{P} is relatively small, at a fixed U_{R}, the oscillations of the plates in the out-of-phase modes can naturally be predicted through numerical simulations; while those in the in-phase modes have to be obtained using artificial constraints applied to the system. That is, the two-plate system may

have two coexisting states: one is stable in the out-of-phase modes and has a larger vibration amplitude; and the other one is unstable in the in-phase modes and has a smaller vibration amplitude. No matter whether the two plates vibrate out-of-phase or in-phase, the vibration modes of either plate are *qualitatively* the same as their counterparts in the basic configuration. However, the plates undergo symmetrical vibrations with respect to the flow axis when they vibrate in-phase. While, when the two plates vibrate out-of-phase, the dynamics of either plate is the mirror image of the other one; a small buckling in the direction away from the other plate can be observed in association with the oscillations.

The instability and the post-critical dynamics of cantilevered flexible plates in axial flow have also been examined by the energy transfer between the plate and the surrounding fluid flow, in which the longitudinal fluid load f_{D} is treated as a tension term in the plate and only the transverse fluid load f_{L} does work on the plate. When flutter takes place, a balance in the energy transfer process is attained between the work done by f_{L} and the internal dissipation of the plate. With further increase in U_{R}, both the power of the work done by f_{L} and the internal dissipation grows, and a balance in energy transfer is attained at higher levels of exchange rates. Cantilevered flexible plates in axial flow vibrate in various modes; the points at different locations along the length of the plate do not oscillate in phase. Moreover, for various systems with different values of μ, the vibration modes are qualitatively different. Therefore, the work done by f_{L} at different locations along the length of the plate is not uniform. It was found that that f_{L} does positive work at some sections of the plate but negative work at others. The distribution of positive/negative work of f_{L} depend on the value of U_{R} and the vibration modes of the system (and hence the value of μ). However, it has been found that f_{L} always does negative work at the most leeward section of the plate. The energy transfer has also been investigated in terms of individual vibration modes of the system; it was confirmed that most of the energy transfer occurs in the dominant mode of the dynamics of the system.

A new concept of energy-harvesting, the flutter-mill, has been proposed in this thesis to utilize the flutter motions of cantilevered flexible plates in axial flow, so as

to generate electrical power. The conceptual design of the device is closely correlated to the dynamics of the system studied in this thesis, both in its basic configuration and in various modified configurations. Although a comprehensive optimization has not been undertaken, the preliminary evaluation of the performance of the flutter-mill shows that, at the very least, it is comparable to that of other wind-energy converters.

Finally, experiments with cantilevered flexible plates in axial water flow, in the hanging configuration, have been conducted and reported in this thesis. This work extends our investigation of the dynamics of the system to values of μ as large as 200. The experimental observations were compared with the simulation results obtained by using the present theory; reasonably good agreement is achieved for the flutter boundary and flutter frequency of the system.

8.3. Future work

The work conducted in this thesis can be continued and extended in several directions.

First of all, the dynamics of two-dimensional cantilevered flexible plates in axial flow has been extensively studied in a multiparameter space. But the current work cannot claim to provide a complete picture of the global dynamics of the system. Thus, although the influence of a variety of parameters of the system, in both the basic configuration and various modified configurations, on the dynamics has been investigated, it would be worth extending this investigation to ranges of the parameters not covered in this thesis so as to further explore the dynamics of the system.

A relatively simple model has been developed in this thesis to enable a comprehensive investigation of the dynamics in the multiparameter space. This model can be refined to take into account viscous effects of the fluid flow in a way closer to physical reality. To this end, a computational fluid dynamics (CFD) model based on the Navier-Stokes equations may be considered in the future. Taking advantage of the CFD approach, (i) the characteristics of the fluid flow in the vicinity of the plate, (ii) the evolution of the wake, (iii) the influence of parallel solid flow-confining

walls, (iv) the coupling of two or more flexible plates in parallel, with or without the presence of confining walls, and additionally (v) a new configuration of the system with the fluid flow passes only one-side of the plate, can be studied.

Both the plate and the fluid flow are considered to be two-dimensional in this thesis; three-dimensional cases can be studied in the future. This can be conducted in two steps. First, one may consider the three-dimensional effects of the fluid flow with a plate of finite spanwise dimension, which is still modelled as a two-dimensional structure; the variation in the aero/hydro-dynamic loads across the spanwise dimension of the plate can be investigated in terms of the aspect ratio of the plate. Then, real three-dimensional plates can be considered to examine the three-dimensional deformations of the plate subjected to a three-dimensional axial flow.

A particular feature of the dynamics which remained unresolved in this thesis is the qualitative discrepancy between theoretical predictions and experimental observations regarding the nature of the flutter instability of the system. Although flutter has been observed in experiments to occur in a subcritical way, all theories to date predict supercritical bifurcations. This point can be re-examined with an improved analytical model of the system, considering viscous as well as three-dimensional effects of the fluid flow and three-dimensional deformations of the plate. Moreover, the possible correlation between the instability of the system and the evolution of the wake behind the plate has been discussed in a preliminary way; this should be verified with a refined model.

One piece of future work which is already taking place is the continuation of the experiments described in Chapter 7. More experiments will be conducted, with several new cantilevered plates, some with smaller mass ratio μ (heavier plates) to merge with some of the available air-flow experimental data. More sophisticated measurement techniques need to be implemented, so as to define better the critical flow velocity for flutter, even when the amplitude is small and the flutter perhaps supercritical.

A new concept of energy-harvesting utilizing the flutter motions of a cantilevered flexible plate in axial flow, the flutter-mill, is proposed in this thesis. The performance of this energy-harvesting device has been evaluated preliminarily and compared to other designs of energy converters. In the future, a comprehensive optimization of the design regarding the performance/efficiency should be conducted. A prototype should be constructed and tested to verify the feasibility of the new design. Moreover, the performance of the device, off-load and on-load (i.e., without/with consideration of the induced electromagnetic forces), should be re-evaluated for the detailed design of the prototype.

Finally, due to time constraints, a block of work is omitted in this thesis, i.e., the propulsion of actively oscillatory cantilevered flexible plates in axial flow. It would be of great interest to investigate the propulsion efficiency of the actively oscillating motions of a cantilevered flexible plate and ultimately the active propulsion mechanism. The experience gained in this thesis and the tools developed make such a study feasible and potentially fruitful.

Bibliography

Abbott, I. H., and A. E. von Doenhoff. 1959. *Theory of Wing Sections: Including a Summary of Airfoil Data.* 1st ed. New York: Dover Publications.

Adamko, D. A., and J. D. DeLaurier. 1978. An experimental study of an oscillating-wing windmill. In *Proceedings of the Second Canadian Workshop on Wind Engineering*, pp. 64–66.

ADINA. 2006. ADINA-FSI. http://www.adina.com/adinafsi.html.

Alban, L., and V. Michel. 2004. Interaction between fluid and self-propelled fish-like body motion. In *Flow Induced Vibration*, ed. E. de Langre and F. Axisa, pp. 1–6. Ecole Polytechnique, Paris.

Allen, J. J., and A. J. Smits. 2001. Energy harvesting eel. *Journal of Fluids and Structures* 15:629–640.

Anderson, A., U. Pesavento, and Z. J. Wang. 2005. Unsteady aerodynamics of fluttering and tumbling plates. *Journal of Fluid Mechanics* 541:65–90.

Anderson, J. D. 2001. *Fundamentals of Aerodynamics.* 3rd ed. Boston: McGraw Hill.

Anderson, T. J., A. H. Nayfeh, and B. Balachandran. 1996. Experimental verification of the importance of the nonlinear curvature in the response of a cantilevered beam. *Journal of Vibration and Acoustics* 118:21–27.

ANSYS. 2006. ANSYS-FSI. http://www.ansys.com/solutions/fsi.asp.

Arafat, H. N. 1999. Nonlinear Response of Cantilever Beams. PhD Thesis, Virginia Ploytechnic Institute and State University, Blacksburg, Virginia.

Argentina, M., and L. Mahadevan. 2005. Fluid-flow-induced flutter of a flag. *Proceedings of the National Academy of Science of the United States of America* 102: 1829–1834.

Attar, P. J., E. H. Dowell, and D. M. Tang. 2003. Modeling aerodynamic nonlinearity for two aeroelastic configurations: Delta wing and flapping flag. In *Proceedings of the 44th AIAA/ASME/ASCE/AHS Structures, Structural Dynamics, and Materials Conference*, pp. 12–22.

Auman, L., and C. W. Dahlke. 2001. Drag characteristics of ribbons. *AIAA Paper No. 2001-2011* .

Aurégan, Y., and C. Depollier. 1995. Snoring: linear stability analysis and in-vitro experiments. *Journal of Sound and Vibration* 188:39–53.

Balint, T. S., and A. D. Lucey. 2005. Instability of a cantilevered flexible plate in viscous channel flow. *Journal of Fluids and Structures* 20:893–912.

Bathe, K. J., and S. Bolourchi. 1979. Large displacement analysis of three-dimensional beam structure. *International Journal for Numerical Methods in Engineerng* 14:961–986.

Beards, C. F. 1996. *Structural Vibration: Analysis and Damping.* 1st ed. New York: John Wiley & Sons.

Bejan, A. 1982. The meandering fall of paper ribbons. *Physics of Fluids* 25(5): 741–742.

Bélanger, F., M. P. Païdoussis, and E. de Langre. 1995. Time-marching analysis of fluid-coupled system with large added mass. *AIAA Journal* 33:752–755.

Benjamin, B. T. 1961. Dynamics of a system of articulated pipes conveying fluid. I. Theory. *Proceedings of the Royal Society (London) A* 261:457–486.

Bishop, R. E. D., and D. C. Johnson. 1979. *The Mechanics of Vibration.* Cambridge: Cambridge University Press.

Bisplinghoff, R. L., and H. Ashley. 1962. *Principles of Aeroelasticity.* New York: John Wiley.

Bisplinghoff, R. L., H. Ashley, and R. L. Halfman. 1955. *Aeroelasticity.* Cambridge, MA: Addison-Wesley.

Burton, T., D. Sharpe, N. Jenkins, and E. Bossanyi. 2001. *Wind Energy: Handbook.* New York: John Wiley & Sons, Inc.

Carpenter, P. W., and A. D. Garrad. 1985. The hydrodynamic stability of flow over karmer-type compliant surfaces. Part 1. Tollmien-Schlichting instability. *Journal of*

Fluid Mechanics 155:465–510.

———. 1986. The hydrodynamic stability of flow over karmer-type compliant surfaces. Part 2. Fluid-induced surface instability. *Journal of Fluid Mechanics* 170: 199–232.

Carroll, C. B. 2002. Energy harvesting eel. *United State Patnet 6424079* .

Carruthers, A. C., and A. Filippone. 2005. Aerodynamic drag of streamers and flags. *Journal of Aircraft* 42(4):976–982.

Chandrasekhar, S. 1961. *Hydrodynamic and Hydromagnetic Stability.* Oxford: Clarendon Press.

Chang, Y. B., and P. M. Moretti. 2002. Flow-induced vibration of free edges of thin films. *Journal of Fluids and Structures* 16:989–1008.

Chen, S. S. 1971. Flow-induced instability of an elastic tube. *ASME Paper No. 71-Vibr.-39* .

Crighton, D. G. 1985. The Kutta condition in unsteady flow. *Annual Review of Fluid Mechanics* 17:441–445.

Crighton, D. G., and J. E. Oswell. 1991. Fluid loading with mean flow. I. response of an elastic plate to localized excitation. *Philosophical Transactions of Royal Society of London* 335:557–592.

Cveticanin, L. J., T. M. Atanackovic, and D. S. Djukic. 1995. Beck's rod with shear, compressibility and pulsating force. *Continuum Mechanics and Themodynamics* 8: 103–113.

Datta, S. K., and W. G. Gottenberg. 1975. Instability of an elastic strip hanging in an airstream. *Journal of Applied Mechanics* 42:195–198.

Davidson, K. 2002. Scientific head-scratchers survive meteorites, flapping flags remain mystery. *San Francisco Chronicle* A–8, January 21.

De Breuker, R., M. M. Abdallay, and Z. Gürdal. 2006. Flutter of partially rigid cantilevered plates in axial flow. *AIAA Paper No. 2006-1730* .

de Langre, E. 2002. *Fluides et Solides.* Paris: Les Éditions de L'école Polytechnique.

Doaré, O., T. Paes, and M. Ferré. 2006. Feedback control of the flutter of a cantilevered plate in an axial flow. *Proceedings of PVP2006-ICPVT-11 (No. 93840)* .

Dowell, E. H. 1975. *Aeroelasticity of Plates and Shells.* Leyden: Noordhoff International Publishing.

Dowell, E. H., and K. C. Hall. 2001. Modeling of fluid-structure interaction. *Annual Review of Fluid Mechanics* 33:445–490.

Dowell, E. H., H. C. Curtiss Jr., R. H. Scanlan, and F. Sisto. 1989. *A Modern Course in Aeroelasticity.* Dordrecht: Kluwer Academic Publishers.

Elishakoff, I. 2005. Controversy associated with the so-called "folower forces": Critical overview. *ASME Applied Mechanics Reviews* 58:117–142.

Eloy, C., C. Souilliez, and L. Schouveiler. 2007. Flutter of a rectangular cantilevered plate. *Journal of Fluids and Structures* 23:904–919.

Epureanu, B. I., L. Tang, and M. P. Païdoussis. 2004a. Coherent structures and their influence on the dynamics of aeroelastic panels. *International Journal of Non-Linear Mechanics* 39:977–991.

———. 2004b. Exploiting chaotic dynamics for detecting parametric variations in aeroelastic systems. *AIAA Journal* 42(4):728–735.

Fairthrone, R. A. 1930. Drag of Flags. Rept. 1345, Aeronautical Research Council ARC Reports and Memoranda, U.K.

Farnell, D. J. J., T. David, and D. C. Barton. 2004. Coupled states of flapping flags. *Journal of Fluids and Structures* 19:29–36.

Frederiks, W., H. C. J. Hilberink, and J. A. Sparenberg. 1986. On the Kutta condition for the flow along a semi-infinite elastic plate. *Journal of Engineering Mathematics* 20:27–50.

Fung, Y. C. 1993. *An Introduction to the Theory of Aeroelasticity.* New York: Dover Publishions, Inc.

Gear, C. W. 1971. *Numerical initial value problems in ordinary differential equations.* 1st ed. Englewood Cliffs: Prentice-Hall.

Greenhalgh, S., H. C. Curtiss Jr., and B. Smith. 1984. Aerodynamic properties of a two-domensional inextensible flexible airfoil. *AIAA Journal* 22(7):865–870.

Gregory, R. W., and M. P. Païdoussis. 1966. Unstable oscillation of tubular cantilevers conveying fluid. II. Experiments. *Proceedings of the Royal Society (London) A* 293:528–542.

Guo, C. Q., and M. P. Païdoussis. 2000. Stability of rectangular plates with free side-edges in two-dimensional inviscid flow. *Journal of Applied Mechanics* 67:171–176.

Hempels Aviation. 2007. Advertising. http://www.hempelsaviation.com/au.

Hoerner, S. F. 1958. *Fluid-Dynamic Drag; Practical Information on Aerodynamic Drag and Hydrodynamic Resistance.* 2nd ed. Midland Park, N.J.: Author.

Houbolt, J. C. 1950. A recurrence matrix solution for the dynamic response of elastic aircraft. *Journal of the Aeronautic Sciences* 17:540–550.

Howell, R. M., A. D. Lucey, and P. W. Carpenter. 2006. Instability of a cantilevered flexible plate in inviscid channel flow. *Proceedings of PVP2006-ICPVT-11 (No. 93941)* .

Hsieh, S. R., S. W. Shaw, and C. Pierre. 1993. Normal modes for large amplitude vibration of a cantilevered beam. *International Journal of Solids and Structures* 31: 1981–2014.

Huang, L. X. 1995. Flutter of cantilevered plates in axial flow. *Journal of Fluids and Structures* 9:127–147.

Hydrodynamics Laboratory. 1998. Water Tunnel. Mannual 1, McGill University, Montreal, Quebec.

Isogai, K., M. Yamazaki, M. Matsubara, and T. Asaoka. 2003. Design study of elastically supported falpping wing power generator. *Proceedings of International Forum on Aeroelasticity and Structural Dynamics* .

Johnson, D. E. 1966. A proof of the stability of the houbolt method. *AIAA Journal* 4(8):1450–1451.

Jones, K. D., and K. B. Center. 1996. Numerical wake visualization for airfoils undergoing forced and aeroelastic motions. *AIAA Paper No. 96-0055* .

Jones, K. D., C. M. Dohringz, and M. F. Platzer. 1996. Wake structures behind plunging airfoils: A comparison of numerical and experimental results. *AIAA Paper No. 96-0078* .

Jones, K. D., K. Lindsey, and M. F. Platzer. 2003. An investigation of the fluid-structure interaction in an oscillating-wing micro-hydropower generator. In *Fluid Structure Interaction II*, ed. S. K. Chakrabarti, C. A. Brebbia, D. Almorza, and

R. A. Gonzalez-Palma, 73–82. Southampton, UK: WIT Press.

Jones, K. D., and M. F. Platzer. 1995. Time-domain aeroelastic analysis of a two airfoil system with application to unsteady rotary wing flowfields. *AIAA Paper No. 95-0337* .

———. 1997. Numerical computation of flapping-wing propulsion and power extraction. *AIAA Paper No. 96-0826* .

———. 1999. Oscillating-wing power generator. *Proceedings of ASME/JSME-FEDSM99 (No. FEDSM-7050)* .

Katz, J., and A. Plotkin. 2001. *Low-Speed Aerodynamics.* 2nd ed. New York: Cambridge University Press.

Katz, J., and D. Weihs. 1978. Hydrodynamic propulsion by large amplitude oscillation of an airfoil with chordwise flexibility. *Journal of Fluid Mechanics* 202: 485–497.

Kornecki, A. 1978. Aeroelastic and hydroelastic instabilities of infinitely long plates. I. *SM Archives* 3:381–440.

Kornecki, A., E. H. Dowell, and J. O'Brien. 1976. On the aeroelastic instability of two-dimensional panels in uniform incompressible flow. *Journal of Sound and Vibration* 47:163–178.

Lee, A. 2004. Extraction of energy from flowing fluids. *Canadian Patents CA 2266632* .

Lemaitre, C., P. Hémon, and E. de Langre. 2005. Instability of a long ribbon hanging in axial air flow. *Journal of Fluids and Structures* 20:913–925.

Levin, D., G. Daser, and Z. Shpund. 1997. On the aerodynamic drag of ribbons. *AIAA Paper No. 1997-1525* .

Libai, L. J. 1992. Equations for nonlinear planar deformation of beams. *Transactions of the ASME, Journal of Applied Mechanics* 59:1028–1030.

Lighthill, M. J. 1969. Hydromechanics of aquatic animal propulsion. *Annual Review of Fluid Mechanics* 302(1):413–446.

Lock, R. C., and B. R. Williams. 1987. Viscous-inviscid interactions in external aerodynamics. *Progress in Aerospace Sciences* 24:51–171.

Lopes, J. L., C. Semler, and M. P. Païdoussis. 2002. Linear and nonlinear dynamics of cantilevered cylinders in axial flow. Part 2: The equations of motion. *Journal of Fluids and Structures* 16:715–737.

Ly, K. H., and V. A. L. Chasteau. 1981. Experiments on an oscillating-wing aerofoil and application to wing-energy converters. *Journal of Energy* 5(2):116–121.

Malatkar, P. 2003. Nonlinear Vibrations of Cantilever Beams and Plates. PhD Thesis, Virginia Ploytechnic Institute and State University, Blacksburg, Virginia.

Manwell, J. F., J. G. McGowan, and A. L. Rogers. 2002. *Wind Energy Explained: Theory, Design and Application.* New York: John Wiley & Sons, Inc.

Mateescu, D. 1995. *Subsonic Aerodynamics.* Montreal: McGill University Course Notes.

Matsumoto, M., Y. Honmachi, K. Okubo, and Y. Ito. 2006. Fundamental study on the efficiency of power generation system by use of the flutter instability. *Proceedings of PVP2006-ICPVT-11 (No. 93773)* .

McCroskey, W. J. 1982. Unsteady airfoils. *Annual Reviews of Fluid Mechanics* 14: 285–311.

McKinney, W., and J. D. DeLaurier. 1981. The wingmill: An oscillating-wing windmill. *Journal of Energy* 5(2):109–115.

Miles, J. W. 1956. On the aerodynamic instability of thin panels. *Journal of Aeronautical Sciences* August:771–780.

Modarres-Sadeghi, Y. 2006. Nonlinear Dynamics of Slender Flexible Cylinder Subjected to Axial Flow. PhD Thesis, McGill University, Montréal, Québec.

Modarres-Sadeghi, Y., M. P. Païdoussis, and C. Semler. 2005. A nonlinear model for an extensible slender flexible cylinder subjected to axial flow. *Journal of Fluids and Structures* 21:609–627.

Modarres-Sadeghi, Y., C. Semler, M. Wadham-Gagnon, and M. P. Païdoussis. 2007. Dynamics of cantilevered pipes conveying fluid. Part 3: Three-dimensional dynamics in the presence of an end-mass. *Journal of Fluids and Structures* 23:589–603.

Moon, F. C. 1987. *Chaotic Vibrations.* 1st ed. New York: John Wiley & Sons.

———. 1992. *Chaotic and Fractal Dynamics.* 1st ed. New York: John Wiley & Sons.

Moretti, P. M. 2003. Tension in fluttering flags. *International Journal of Acoustics and Vibration* 8:227–230.

———. 2004. Flag flutter amplitudes. In *Flow Induced Vibration*, ed. E. de Langre and F. Axisa, pp. 1–6. Ecole Polytechnique, Paris.

Müller, U. K. 2003. Fish 'n flag. *Science* 302:1511–1512.

Nanakorn, P., and L. N. Vu. 2006. A 2D field-consistent element for large displacement analysis using the total lagrangian formulation. *Finite Elements in Analysis and Design* 42:1240–1247.

Nayfeh, A. H., C. Chin, and S. A. Nayfeh. 1995. Nonlinear normal modes of a cantilever beam. *Journal of Vibration and Acoustics* 117:477–481.

Newman, B. G. 1987. Aerodynamic theory for membranes and sails. *Progress in Aerospace Science* 24:1–27.

Newman, B. G., and H. T. Low. 1991. The stability of two-dimensional membranes in streaming flow. *Journal of Fluids and Structures* 5:443–454.

Pai, P. F., T. J. Anderson, and E. A. Wheater. 2000. Large-deformation tests and total-lagrangian finite-element analysis of flexible beams. *International Journal of Solids and Structures* 37:2951–2980.

Pai, P. F., and S. Y. Lee. 2003. Non-linear structural dynamics characterization using a scanning laser vibrometer. *Journal of Sound and Vibration* 264:657–687.

Païdoussis, M. P. 1998. *Fluid-Structure Interactions. Slender Structures and Axial Flow*, vol. 1. London: Academic Press.

———. 2004. *Fluid-Structure Interactions. Slender Structures and Axial Flow*, vol. 2. London: Elsevier Academic Press.

Païdoussis, M. P., and P. E. des Trois Maisons. 1969. Free vibrations of a heavy, damped cantilever in a plane inclined to the vertical. Technical report M.E.R.L. No. 69-6, McGill Univeristy, Montreal, Québec.

———. 1971. Free vibrations of a heavy, damped, vertical cantilever. *Journal of Applied Mechanics* 38:524–527.

Païdoussis, M. P., E. Grinevich, D. Adamovic, and C. Semler. 2002. Linear and nonlinear dynamics of cantilevered cylinders in axial flow. Part 1: Physical dynamics. *Journal of Fluids and Structures* 16:691–713.

Païdoussis, M. P., and C. Semler. 1994. Non-linear dynamics of a fluid-conveying cantilevered pipe with a small mass attached at the free end. *Journal of Sound and Vibration* 165:577–599.

Païdoussis, M. P., C. Semler, M. Wadham-Gagnon, and S. Saaid. 2007. Dynamics of cantilevered pipes conveying fluid. Part 2: Dynamics of the system with intermediate spring support. *Journal of Fluids and Structures* 23:569–587.

Pedley, T. J., and S. J. Hill. 1999. Large-amplitude undulatory fish swimming: Fluid mechanics coupled to internal mechanics. *The Journal of Experimental Biology* 202: 3431–3438.

Prasanth, T. K., S. Behara, S. P. Singh, R. Kumar, and S. Mittal. 2006. Effect of blockage on vortex-induced vibrations at low reynolds number. *Journal of Fluids and Structures* 22:865–876.

Rayleigh. 1879. On the stability of jets. *Proceedings of the London Matematical Society* 10:4–12.

Reddy, J. N. 1984. *Energy and Variational Methods in Applied Mechanics.* 1st ed. New York: John Wiley & Sons.

Rinaldi, S. 2007. A vertical cantilevered cylinder: the determination of flexural regidity and material damping coefficients. Technical report, McGill Univeristy, Montreal, Québec.

Saje, M. 1990. A variation principle for finite planar deformation of straight slender elastic beam. *International Journal of Solids and Structures* 26:887–900.

Segala, J. 2006. Experimental study on nonlinear dynamics of a fluid-conveying cantilevered pipe with an intermediate spring support. Technical report, McGill Univeristy, Montreal, Québec.

Semler, C. 1991. Nonlinear dynamics and chaos of a pipe conveying fluid. Master's Thesis, McGill University, Montréal, Québec.

———. 1996. Pipe conveying fluid: a paradigm of nonlinear dynamics. PhD Thesis, McGill University, Montréal, Québec.

Semler, C., W. C. Gentleman, and M. P. Païdoussis. 1996. Numerical solutions of second order implicit non-linear ordinary differential equations. *Journal of Sound and Vibration* 195:553–574.

Semler, C., G. X. Li, and M. P. Païdoussis. 1994. The non-linear equations of motion of pipes conveying fluid. *Journal of Sound and Vibration* 165:577–599.

Semler, C., J. L. Lopes, N. Augu, and M. P. Païdoussis. 2002. Linear and nonlinear dynamics of cantilevered cylinders in axial flow. Part 3: Nonlinear dynamics. *Journal of Fluids and Structures* 16:739–759.

Shayo, L. K. 1980. The stability of cantilever panels in uniform incompressible flow. *Journal of Sound and Vibration* 68:341–350.

Shelley, M., N. Vandenberghe, and J. Zhang. 2005. Heavy flags undergo spontaneous oscillations in flowing water. *Physical Review Letters* (094302):1–4.

Snowdon, J. C. 1968. *Vibration and Shock in Damped Mechanical Systems.* 1st ed. New York: John Wiley & Sons.

Souilliez, C., C. Eloy, and L. Schouveiler. 2006. An experimental study of flag flutter. *Proceedings of PVP2006-ICPVT-11 (No. 93864)* .

Sparenberg, J. A. 1962. On the waving motion of a flag. *Proceedings of the Koninklijke Nederlandse Akademie Van Wetenschappen, Series B: Physical Sciences* 65: 378–392.

Stoker, J. J. 1968. *Nonlinear Elasticity.* New York: Gordon and Breach.

Sugiyama, Y., and M. A. Langthjem. 2007. Physical mechanism of the destabilizing effect of damping in continuous non-conservative dissipative systems. *International Journal of Non-Linear Mechanics* 42:132–145.

Taneda, S. 1958. Oscillation of the wake behind a flat plate parallel to the flow. *Journal of the Physical Society of Japan* 13(4):418–425.

———. 1968. Waving motions of flags. *Journal of the Physical Society of Japan* 24: 392–401.

Tang, D. M., E. H. Dowell, and K. C. Hall. 1999a. Limit cycle oscillations of a cantilevered wing in low subsonic flow. *AIAA Journal* 37(3):364–371.

Tang, D. M., J. K. Henry, and E. H. Dowell. 1999b. Limit cycle oscillations of delta wing models in low subsonic flow. *AIAA Journal* 37(11):1355–1362.

Tang, D. M., H. Yamamoto, and E. H. Dowell. 2003. Flutter and limit cycle oscillations of two-dimensional panels in three-dimensional axial flow. *Journal of Fluids and Structures* 17:225–242.

Tang, Y. 2003. Numerical evaluation of uniform beam modes. *ASCE Journal of Engineering Mechanics* 129(12):1475–1477.

Taylor, G. W., J. R. Burns, S. A. Kammann, W. B. Powers, and T. R. Welsh. 2001. The energy harvesting eel: A small subsurface ocean/river power generator. *IEEE Journal of Osceanic Engineering* 26(4):539–547.

Tetlow, G. A., A. D. Lucey, and T. S. Balint. 2006. Instability of a cantilevered flexible plate in viscous channel flow driven by constant pressure drop. *Proceedings of PVP2006-ICPVT-11 (No. 93943)* .

Theodorsen, T. 1935. General theory of aerodynamic instability and the mechanism of flutter. *NACA Report No. 496* .

Thomsen, J. J. 1997. *Vibrations and Stability, Order and Chaos.* 1st ed. London: McGraw-Hill.

Triantafyllou, M. S., G. S. Triantafyllou, and D. K. P. Yue. 2000. Hydrodynamics of fishlike swimming. *Annual Review of Fluid Mechanics* 202:3431–3438.

Visbal, M. R., and R. E. Gordnier. 2004. Numerical simulation of the interaction of a transitional boundary layer with a 2-D flexible panel in the subsonic regime. *Journal of Fluids and Structures* 19:881903.

Visual Numerics Inc. 1998. *IMSL Fortran 90 Routines and Functions.* Houston: Visual Numerics.

Wadham-Gagnon, M., M. P. Païdoussis, and C. Semler. 2007. Dynamics of cantilevered pipes conveying fluid. Part 1: Nonlinear equations of three-dimensional motion. *Journal of Fluids and Structures* 23:545–567.

Wagner, H. 1965. Large-amplitude free vibrations of a beam. *Journal of Applied Mechanics* 32:887–892.

Watanabe, M., and Y. Koyama. 2006. Active feedback control of leakage-flow-induced sheet flutter by injection and suction of fluid at inlet or outlet of passage. *Proceedings of PVP2006-ICPVT-11 (No. 93616)* .

Watanabe, Y., K. Isogai, S. Suzuki, and M. Sugihara. 2002a. A theoretical study of paper flutter. *Journal of Fluids and Structures* 16:543–560.

Watanabe, Y., S. Suzuki, M. Sugihara, and Y. Sueoka. 2002b. An experimental study of paper flutter. *Journal of Fluids and Structures* 16:529–542.

White, F. M. 1991. *Viscous Fluid Flow.* New York: McGraw-Hill.

———. 2003. *Fluid Mechanics.* Boston: McGraw-Hill.

WIKIPEDIA. 2007. Cluster bomblet. http://en.wikipedia.org/Clusterbomb.

Wolfgang, M. J., J. M. Anderson, M. A. Grosenbaugh, D. K. Yue, and M. S. Triantafyllou. 1999. Near-body flow dynamics in swimming fish. *The Journal of Experimental Biology* 202:2303–2327.

Wu, X., and S. Kaneko. 2005. Linear and nonlinear analyses of sheet flutter induced by leakage flow. *Journal of Fluids and Structures* 20:927–948.

Yadykin, Y., V. Tenetov, and D. Levin. 2000. The drag of flexible strip hanging vertically in a parallel flow. *AIAA Paper No. 2000-4228* .

———. 2001. The flow-induced vibration of a flexible strip hanging vertically in a parallel flow, Part 1: Temporal aeroelastic instability. *Journal of Fluids and Structures* 15:1167–1185.

Yamaguchi, N., T. Sekiguchi, K. Yokota, and Y. Tsujimoto. 2000a. Flutter limits and behaviors of a flexible thin sheet in high-speed flow – II: Experimental results and predicted behaviors for low mass ratios. *ASME Journal of Fluids Engineering* 122:74–83.

Yamaguchi, N., K. Yokota, and Y. Tsujimoto. 2000b. Flutter limits and behaviors of a flexible thin sheet in high-speed flow – I: Analytical method for prediction of the sheet behavior. *ASME Journal of Fluids Engineering* 122:65–73.

Yao, Z. X., and D. D. Liu. 1998. Vortex dynamics of blade-blade interaction. *AIAA Journal* 36(4):497–504.

Ye, W. L., and E. H. Dowell. 1991. Limit cycle oscillation of a fluttering cantilever plate. *AIAA Journal* 21(11):225–242.

Zhang, J., S. Childress, A. Libchaber, and M. Shelley. 2000. Flexible filaments in a flowing soap film as a model for one-dimensional flags in a two-dimensional wind. *Nature* 408:835–839.

Ziegler, H. 1977. *Principles of Structural Stability.* 2nd ed. Basel: Birkhäuser.

Appendix A

The Inextensibility Assumption and the Equation of Motion for an Inextensible Plate

In this appendix, a two-dimensional cantilevered, originally straight, flexible plate is treated as a beam, and its equation of motion is developed using the inextensibility assumption. Although similar work can be found in previous work by Semler (1991, 1996), Semler et al. (1994) and Tang et al. (2003), the inextensibility assumption itself and the derivation of the equation of motion are summarized herein to facilitate further work. Moreover, some details of the equation of motion that were not given sufficient attention before, for example the longitudinal displacement and the formulation of the boundary conditions, are discussed.

A.1. The inextensibility assumption

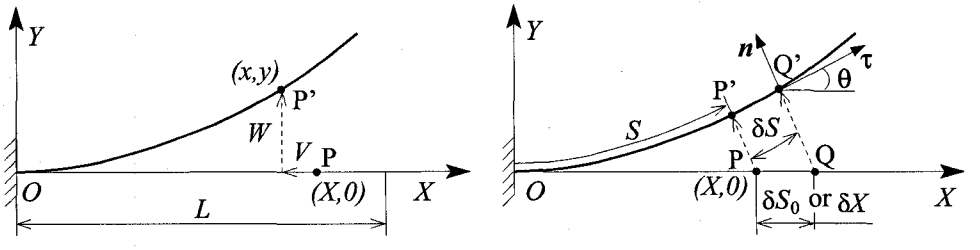

FIGURE A.1. A cantilevered flexible plates in axial flow.

To illustrate the inextensibility assumption, let P and Q be two distinct material points on the beam centreline, as shown in Fig. A.1, and P' and Q' be the same material points after deformation. Let (X, Y) define the position of P in the original state of the beam (lying along the X axis and $Y \equiv 0$), and (x, y) the position of the same material point in the deformed state. Then, the longitudinal and transverse displacements of the point P are, respectively, defined as $V = x - X$ and $W = y - Y = y$. Denoting by δS_0 the distance between P and Q, and by δS that between P' and Q', then by definition,

$$(\delta S_0)^2 = (\delta X)^2 + (\delta Y)^2 = (\delta X)^2, \quad (\delta S)^2 = (\delta x)^2 + (\delta y)^2. \tag{A.1}$$

Note that $\delta Y = 0$, since $Y \equiv 0$ for all material points on the beam. Hence, the change of this distance is obtained from

$$(\delta S)^2 - (\delta S_0)^2 = (\delta x)^2 + (\delta y)^2 - (\delta X)^2 = \left[\left(\frac{dx}{dX}\right)^2 + \left(\frac{dy}{dX}\right)^2 - 1\right](\delta X)^2. \tag{A.2}$$

For an inextensible beam, $\delta S = \delta S_0 = \delta X$, so that

$$(dx/dX)^2 + (dy/dX)^2 = 1, \quad (dx/dS)^2 + (dy/dS)^2 = 1, \tag{A.3}$$

or in terms of displacement variables V and W,

$$\left(1 + \frac{\partial V}{\partial X}\right)^2 + \left(\frac{\partial W}{\partial X}\right)^2 = 1, \quad \left(1 + \frac{\partial V}{\partial S}\right)^2 + \left(\frac{\partial W}{\partial S}\right)^2 = 1. \tag{A.4}$$

A.2. The curvature of the beam

As shown in Fig. A.1, θ is the angle between the tangent of the beam centreline and the X axis, and the curvature is defined by

$$\kappa = \frac{\partial \theta}{\partial S}. \tag{A.5}$$

By the definition of the angle θ, one has

$$\cos\theta = \frac{\delta x}{\delta S} = \frac{\delta V + \delta X}{\delta S} = 1 + \frac{\partial V}{\partial s}, \quad \sin\theta = \frac{\delta y}{\delta S} = \frac{\delta W}{\delta S}. \tag{A.6}$$

It follows that

$$\frac{\partial}{\partial S}\left(\frac{\sin\theta}{\cos\theta}\right) = \frac{1}{\cos^2\theta}\frac{\partial\theta}{\partial S} = \frac{1}{(1+\partial V/\partial S)^2}\frac{\partial\theta}{\partial S} = \frac{\partial}{\partial S}\left(\frac{\partial W/\partial S}{1+\partial V/\partial S}\right), \tag{A.7}$$

and the curvature $\kappa = \partial\theta/\partial S$ can be expressed as

$$\kappa = \frac{\partial\theta}{\partial S} = \frac{\partial^2 W}{\partial S^2}\left(1+\frac{\partial V}{\partial S}\right) - \frac{\partial W}{\partial S}\frac{\partial^2 V}{\partial S^2} = \frac{\partial^2 y}{\partial X^2}\frac{\partial x}{\partial X} - \frac{\partial y}{\partial X}\frac{\partial^2 x}{\partial X^2}. \tag{A.8}$$

Taking the first derivative with respect to S on both sides of Eq. (A.4), one obtains

$$-\frac{\partial W}{\partial S}\frac{\partial^2 V}{\partial S^2} = \frac{(\partial W/\partial S)^2\,(\partial^2 W/\partial S^2)}{1+\partial V/\partial S}. \tag{A.9}$$

Substituting Eq. (A.9) into Eq. (A.8), one obtains

$$\kappa = \frac{\partial^2 W/\partial S^2}{\sqrt{1-(\partial W/\partial S)^2}}, \tag{A.10}$$

where the inextensibility assumption, i.e., Eq. (A.4) has been used for replacing $(1+\partial V/\partial S)$.

A.3. The energy method and some preliminaries

The equation of motion is developed using the energy method (Reddy, 1984), of which the variational expression is normally written as

$$\delta\int_{t_1}^{t_2}\mathcal{L}\,dt + \int_{t_1}^{t_2}\delta\mathcal{W}\,dt = 0, \tag{A.11}$$

where $\mathcal{L} = \mathcal{T} - \mathcal{V}$ is the *Lagrangian* of the system; $\mathcal{T}$ and $\mathcal{V}$ denote, respectively, the kinetic and potential energies of the system, and $\delta\mathcal{W}$ is the virtual work done by the forces not included in the *Lagrangian*.

The kinetic energy $\mathcal{T}$ is given by

$$\mathcal{T} = \frac{1}{2}\rho_{\mathrm{P}}h\int_0^L\left(\dot{V}^2+\dot{W}^2\right)dS, \tag{A.12}$$

and, in the case of an inextensible beam, the potential energy by (Stoker, 1968)

$$\mathcal{V} = \frac{1}{2} D \int_0^L \kappa^2 \, dS. \tag{A.13}$$

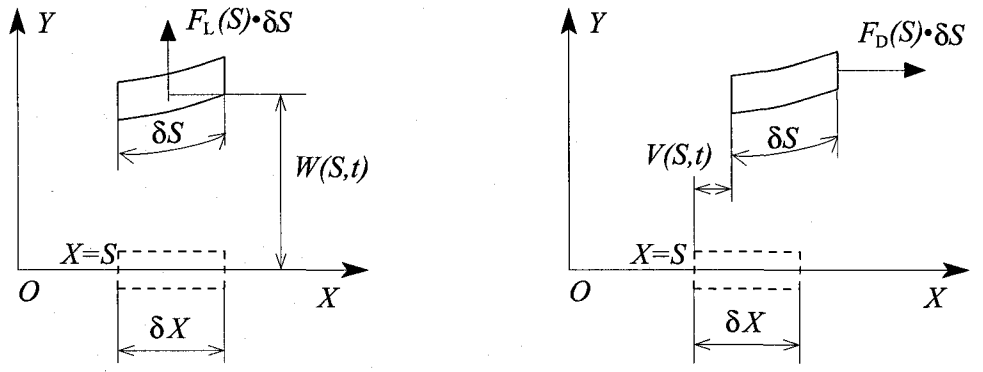

FIGURE A.2. The virtual work done by the transverse and longitudinal force distributions.

The virtual work due to the transverse/longitudinal force distributions, i.e., F_{L} and F_{D} as shown in Fig. A.2, is

$$\mathcal{W} = \int_0^L (W F_{\mathrm{L}} + V F_{\mathrm{D}}) \, dS. \tag{A.14}$$

Note that the measurement of the distance along the centreline between a material point on the beam to the origin, S, is used for developing the equation of motion. One can imagine that the inextensible beam is straightened along the X axis; S and X are always identical for a fixed material point on the beam, so do the values of δS and δX. It should be emphasized that an inextensible cantilevered flexible beam undergoing deformations does have longitudinal displacement, especially when the vibration amplitude is large; one must carefully map the forces, i.e., $F_{\mathrm{L}}(X)$ and $F_{\mathrm{D}}(X)$, obtained in the fixed X-Y coordinate system to $F_{\mathrm{L}}(S)$ and $F_{\mathrm{D}}(S)$ in the coordinate system embedded in the beam.

On the other hand, in some cases, the evaluation of the loads F_{L} and F_{D} needs both values of the transverse/longitudinal displacements W and V. It can be found from Eq. (A.4) that V is related to W as

$$V'^2 + 2V' = -W'^2, \tag{A.15}$$

where the prime denotes $\partial(\,)/\partial S$. If assuming that the quantity $W' \sim \mathcal{O}(\epsilon)$ is small, i.e., $W' \ll L$, one finds that $V' \sim W'^2 \sim \mathcal{O}(\epsilon^2)$ and hence $V'^2 \sim W'^4 \sim \mathcal{O}(\epsilon^4)$. Neglecting higher order terms, one has

$$V' = -\frac{1}{2}W'^2 + \mathcal{O}(\epsilon^4) \approx -\frac{1}{2}W'^2. \tag{A.16}$$

It follows that

$$V = -\frac{1}{2}\int_0^S W'^2\, dS. \tag{A.17}$$

It can be seen in Eq. (A.17) that the longitudinal displacement V is always negative, i.e., $V(S,t) < 0$. Differentiating both sides of Eq. (A.17) twice with respect to time, one obtains

$$\ddot{V} = -\int_0^S \left(\dot{W}'^2 + W'\ddot{W}'\right) dS, \tag{A.18}$$

where the overdot denotes $\partial(\,)/\partial t$.

One can also take the variation of Eq. (A.4) to obtain

$$\delta V' = -W'\left(1 + \frac{1}{2}W'^2 + \mathcal{O}(\epsilon^4)\right)\delta W' \approx -W'\left(1 + \frac{1}{2}W'^2\right)\delta W'. \tag{A.19}$$

It follows that

$$\delta V = -\int_0^S W'\left(1 + \frac{1}{2}W'^2\right)\delta W'\, dS = -W'\delta W + \int_0^S W''\delta W\, dS, \tag{A.20}$$

where $\left[W'\left(1 + W'^2/2\right)\delta W\right]_{S=0} = 0$ has been used.

According to Eq. (A.10), the term κ^2 in Eq. (A.13) can be rewritten as

$$\kappa^2 = \frac{W''^2}{\sqrt{1 - W'^2}} = W''^2\left(1 + W'^2 + \mathcal{O}(\epsilon^4)\right) \approx W''^2\left(1 + W'^2\right). \tag{A.21}$$

Finally, it should be mentioned that the important equality

$$\int_0^L g(s)\left(\int_0^s f(r)\delta y\, dr\right) ds = \int_0^L \left(\int_s^L g(r)\, dr\right) f(s)\delta y\, ds \tag{A.22}$$

is frequently used in the application of the energy and variational method, of which the proof has been given by Semler (1991).

A.4. The boundary conditions

In the fixed X-Y coordinate system, as shown in Fig. A.1, the boundary conditions of the cantilevered beam are

$$W(x=0,t) = \partial W(x=0,t)/\partial x = 0 \tag{A.23}$$

at the clamped end, and

$$\partial^2 W(x(S=L),t)/\partial x^2 = \partial^3 W(x(S=L),t)/\partial x^3 = 0 \tag{A.24}$$

at the free end. Note that $x \neq L$ at the free end due to the longitudinal displacement $V(S=L)$. Therefore, when the equation of motion is developed in terms of S in a coordinate system attached to the beam undergoing deformation, the boundary conditions at both ends should be checked (Wagner, 1965).

At the clamped end,

$$W(S=0,t) \equiv 0 \tag{A.25}$$

is naturally guaranteed since $S=0$ is identical to $x=0$ and $W(x=0) \equiv 0$. Moreover, because $\partial W(x=0,t)/\partial x = 0$ (note $\theta(X=0) \equiv 0$) and

$$\partial W/\partial x = \frac{\partial W}{\partial S}\frac{\partial S}{\partial x}, \tag{A.26}$$

one can also find that

$$\partial W(S=0,t)/\partial S \equiv 0, \tag{A.27}$$

which has already been used in Eq. (A.20). Note that it has been assumed that the term $\partial S/\partial x$ in Eq. (A.26) has a finite value, i.e., its inverse

$$\partial x/\partial S \neq 0. \tag{A.28}$$

This additionally imposed condition means that the beam cannot wrap forward or have a tangent being vertical to the X axis. Thus, substituting Eq. (A.28) into

Eq. (A.3), one gets the inequality

$$|\partial W/\partial S| < 1. \tag{A.29}$$

The boundary conditions at the free end indicates vanishing of the moment $(D\kappa)$ and the shear force $(d(D\kappa)/dS)$, i.e.,

$$\kappa(S = L) = 0, \qquad d\kappa(S = L)/dS = 0. \tag{A.30}$$

According to Eq. (A.10), when $\kappa(S = L) = 0$, one has

$$\kappa(S = L) = \left[\frac{\partial^2 W/\partial S^2}{\sqrt{1 - (\partial W/\partial S)^2}}\right]_{S=L} = 0. \tag{A.31}$$

It follows that

$$\partial^2 W(S = L, t)/\partial S^2 \equiv 0, \tag{A.32}$$

since $\sqrt{1 - (\partial W/\partial S)^2} \neq 0$ according to Eq. (A.29).

Using another form of the curvature κ given in Eq. (A.8), one also has

$$\kappa(S = L) = \left[\frac{\partial^2 W}{\partial S^2}\frac{\partial x}{\partial S} - \frac{\partial W}{\partial S}\frac{\partial^2 x}{\partial S^2}\right]_{S=L} = 0. \tag{A.33}$$

Hence,

$$\left[\frac{\partial W}{\partial S}\frac{\partial^2 x}{\partial S^2}\right]_{S=L} = 0, \tag{A.34}$$

of which the first derivative with respect to S, is given by

$$\left[\frac{\partial^2 W}{\partial S^2}\frac{\partial^2 x}{\partial S^2} + \frac{\partial W}{\partial S}\frac{\partial^3 x}{\partial S^3}\right]_{S=L} = \left[\frac{\partial W}{\partial S}\frac{\partial^3 x}{\partial S^3}\right]_{S=L} = 0, \tag{A.35}$$

where Eq. (A.32) has been applied. On the other hand, directly taking the first derivative of Eq. (A.33) with respective to S gives

$$\left[\frac{\partial^3 W}{\partial S^3}\frac{\partial x}{\partial S} - \frac{\partial W}{\partial S}\frac{\partial^3 x}{\partial S^3}\right]_{S=L} = 0. \tag{A.36}$$

When considering Eqs. (A.35), (A.36) and (A.28) together, one finally arrives at

$$\partial^3 W(S = L, t)/\partial S^3 \equiv 0. \tag{A.37}$$

Therefore, all the boundary conditions of an inextensible cantilevered flexible beam in terms of S, as defined by Eqs. (A.25), (A.27), (A.32) and (A.37), have exactly the same forms as they are in the fixed X-Y coordinate system defined by Eqs. (A.23) and (A.24).

A.5. The equation of motion

It follows from Eq. (A.12) that

$$\delta\int_{t_1}^{t_2}\mathcal{T}\,dt = -\rho_{\mathrm{P}}h\int_{t_1}^{t_2}\int_0^L\left\{\left[-\int_0^S\left(\dot{W}'^2+W'\ddot{W}'\right)dS\right]\times\left[-W'\delta W+\int_0^S W''\delta W\,dS\right]+\ddot{W}\delta W\right\}dS\,dt, \tag{A.38}$$

where $\left[\dot{V}\delta V+\dot{W}\delta W\right]_{t_1}^{t_2}=0$ has been assumed, and Eqs. (A.18) and (A.20), respectively, for $\ddot{V}$ and δV have been utilized. It is convenient to split Eq. (A.38) into three parts:

$$\delta\int_{t_1}^{t_2}\mathcal{T}_1\,dt=-\rho_{\mathrm{P}}h\int_{t_1}^{t_2}\int_0^L\left(\ddot{W}\delta W\right)dS\,dt, \tag{A.39a}$$

$$\delta\int_{t_1}^{t_2}\mathcal{T}_2\,dt=-\rho_{\mathrm{P}}h\int_{t_1}^{t_2}\int_0^L\left[W'\int_0^S\left(\dot{W}'^2+W'\ddot{W}'\right)dS\right]\delta W\,dS\,dt, \tag{A.39b}$$

$$\begin{aligned}\delta\int_{t_1}^{t_2}\mathcal{T}_3\,dt &= \rho_{\mathrm{P}}h\int_{t_1}^{t_2}\int_0^L\left\{\left[\int_0^S\left(\dot{W}'^2+W'\ddot{W}'\right)dX\right]\left[\int_0^S W''\delta W\,dS\right]\right\}dS\,dt\\ &= \rho_{\mathrm{P}}h\int_{t_1}^{t_2}\int_0^L W''\left\{\int_S^L\left[\int_0^S\left(\dot{W}'^2+W'\ddot{W}'\right)dS\right]dS\right\}\delta W\,dS\,dt.\end{aligned} \tag{A.39c}$$

Note that Eq. (A.22) has been used in Eq. (A.39c).

It follows from Eqs. (A.13) and (A.21) that

$$\begin{aligned}\delta\int_{t_1}^{t_2}\mathcal{V}\,dt &= \frac{1}{2}D\delta\left\{\int_{t_1}^{t_2}\int_0^L\left[W''^2\left(1+W'^2\right)\right]\,dS\,dt\right\}\\ &= D\int_{t_1}^{t_2}\int_0^L\left[W''''\left(1+W'^2\right)+4W'W''W'''+W''^3\right]\delta W\,dS\,dt,\end{aligned} \tag{A.40}$$

where the boundary conditions, i.e., Eqs. (A.25), (A.27), (A.32) and (A.37), have been used to eliminate the terms

$$\left[W''\left(1+W'^2\right)\delta W'\right]_0^L,\quad \left[W''^2W'\delta W\right]_0^L,\quad \left[\left[W''\left(1+W'^2\right)\right]'\delta W\right]_0^L \tag{A.41}$$

arising from integration by parts.

It follows from Eq. (A.14) that

$$\int_{t_1}^{t_2}\delta\mathcal{W}\,dt=\int_{t_1}^{t_2}\int_0^L\left[F_{\mathrm{L}}-W'F_{\mathrm{D}}+W''\int_S^L F_{\mathrm{D}}\,dS\right]\delta W\,dS\,dt, \tag{A.42}$$

where Eq. (A.20) for δV and Eq. (A.22) have been used.

Substituting Eqs. (A.39a) through (A.40) and Eq. (A.42) into Eq. (A.11), one obtains the equation of motion for the transverse displacement W:

$$\begin{aligned}&\rho_{\mathrm{P}}h\ddot{W}+D\left[W''''\left(1+W'^2\right)+4W'W''W'''+W''^3\right]\\ &+\ \rho_{\mathrm{P}}hW'\int_0^S\left(\dot{W}'^2+W'\ddot{W}'\right)dS-\rho_{\mathrm{P}}hW''\int_S^L\left[\int_0^S\left(\dot{W}'^2+W'\ddot{W}'\right)dS\right]dS\\ &=\ F_{\mathrm{L}}-W'F_{\mathrm{D}}+W''\int_S^L F_{\mathrm{D}}\,dS,\end{aligned} \tag{A.43}$$

which is a nonlinear equation correct to order $\mathcal{O}\left(\epsilon^3\right)$.

When a material damping of the Kelvin-Voigt type (Snowdon, 1968) is considered, the bending stiffness of the beam, D, is actually replaced by $D(1+a\partial/\partial t)$ (Stoker, 1968; Semler et al., 1994), where a is the material (viscoelastic) damping coefficient.

Therefore, Eq. (A.43) becomes

$$\begin{aligned} & \rho_{\mathrm{P}} h \ddot{W} + D\left(1 + a\frac{\partial}{\partial t}\right)\left[W''''\left(1 + W'^2\right) + 4W'W''W''' + W''^3\right] \\ + \; & \rho_{\mathrm{P}} h W' \int_0^S \left(\dot{W}'^2 + W'\ddot{W}'\right) dS - \rho_{\mathrm{P}} h W'' \int_S^L \left[\int_0^S \left(\dot{W}'^2 + W'\ddot{W}'\right) dS\right] dS \\ = \; & F_{\mathrm{L}} - W' F_{\mathrm{D}} + W'' \int_S^L F_{\mathrm{D}}\, dS. \end{aligned} \tag{A.44}$$

Appendix B

The Equations of Motion for an Axially Extensible Plate, Solution Method and Preliminary Results

In this Appendix, we first develop the equations of motion of the cantilevered flexible plate without using the inextensibility assumption; that is, the plate is supposed to be *axially extensible*, as it should be. However, in the derivation of the equations of motion, it is found that the boundary conditions of the longitudinal and transverse displacements are coupled together; an additional assumption about the modes of the longitudinal and transverse displacements has to be imposed. Under this circumstance, two nonlinear partial differential equations, respectively for the longitudinal and transverse displacements, are obtained. Subsequently, the traditional Galerkin method based on the assumed modes of the system is utilized, and we thus get a set of nonlinear ordinary differential equations, which is then coupled to the aero/hydrodynamics model of the system. However, considerable difficulties are encountered in the solution of the resulting numerical model; no stable limit cycle oscillations (flutter) can be obtained. For flow velocities beyond the critical point, the solution is found to be divergent when the vibration amplitudes exceed a certain, still very small, value. Nevertheless, convergent solutions can be obtained when the flow velocity is

below the critical point, and thus we are still able to identify the critical point of the system.

B.1. The equations of motion

If the plate is considered to be extensible, the nonlinear equations of motion of a two-dimensional cantilevered flexible plate, which is still regarded as an Euler-Bernoulli beam, can be developed either in the curvilinear coordinate system as has been done for inextensible beams in Appendix A (see also the work by Bathe and Bolourchi (1979), Libai (1992) and Pai et al. (2000)) or in the fixed X-Y coordinate system (Saje, 1990; Nanakorn and Vu, 2006). In order to remain generally consistent with the equation of motion developed utilizing the inextensibility assumption (see Appendix A) and to keep the solution of the full model of the aero/hydro-elastic system amenable (i.e., to avoid coordinate-mapping processes in the solution), the equations of motion without using the inextensibility assumption are derived in this Appendix, following the the work by Modarres-Sadeghi (2006), in the fixed X-Y coordinate system.

B.1.1. Consideration of extensibility and the curvature. When it is considered to be extensible, as shown in Fig. A.1, the distances between two material points on the beam are, δS and δX respectively before and after a deformation; note that $\delta S \neq \delta X$. Therefore, the axial strain along the centreline of the beam can be defined by

$$\varepsilon(X) = \frac{\delta S - \delta X}{\delta X} = \frac{dS}{dX} - 1 = \sqrt{\left(1 + \frac{dV}{dX}\right)^2 + \left(\frac{dW}{dX}\right)^2} - 1. \tag{B.1}$$

It follows that

$$\frac{dX}{dS} = \frac{1}{1 + \varepsilon(X)} = \frac{1}{\sqrt{(1 + dV/dX)^2 + (dW/dX)^2}}, \tag{B.2}$$

and

$$\cos\theta = \frac{dx}{dS} = \frac{dx}{dX}\frac{dX}{dS} = \frac{1 + dV/dX}{\sqrt{(1 + dV/dX)^2 + (dW/dX)^2}}, \tag{B.3}$$

$$\sin\theta = \frac{dy}{dS} = \frac{dy}{dX}\frac{dX}{dS} = \frac{dW/dX}{\sqrt{(1 + dV/dX)^2 + (dW/dX)^2}}. \tag{B.4}$$

The curvature of the beam is defined by

$$\kappa = \frac{d\theta}{dS} = \frac{d\theta}{dX}\frac{dX}{dS} = \frac{1}{1 + \varepsilon(X)}\frac{d\theta}{dX}. \tag{B.5}$$

Conducting similar manipulations as in Appendix A in terms of the curvilinear coordinate S, one obtains

$$\frac{d\theta}{dS} = \frac{1}{(1 + \varepsilon(X))^2}\left(\frac{dx}{dX}\frac{d^2y}{dX^2} - \frac{d^2x}{dX^2}\frac{dy}{dX}\right). \tag{B.6}$$

Hence, the curvature κ can be calculated by

$$\begin{aligned} \kappa &= \frac{1}{(1 + \varepsilon(X))^3}\left(\frac{dx}{dX}\frac{d^2y}{dX^2} - \frac{d^2x}{dX^2}\frac{dy}{dX}\right) \\ &= \frac{1}{(1 + \varepsilon(X))^3}\left[\left(1 + \frac{dV}{dX}\right)\frac{d^2W}{dX^2} - \frac{d^2V}{dX^2}\frac{dW}{dX}\right]. \end{aligned} \tag{B.7}$$

If one uses the inextensibility assumption (i.e., $\varepsilon \equiv 0$) and regards dX and dS to be interchangeable, κ becomes

$$\kappa = \left(1 + \frac{dV}{dS}\right)\frac{d^2W}{dS^2} - \frac{d^2V}{dS^2}\frac{dW}{dS} = \frac{d^2W/dS^2}{\sqrt{1 - (dW/dS)^2}}, \tag{B.8}$$

which is exactly the same as Eq. (A.10). Note that the following two relationships

$$\left(1 + \frac{dv}{dS}\right) = \sqrt{1 - \left(\frac{dW}{dS}\right)^2}, \qquad \frac{d^2V}{dS^2} = \frac{(dW/dS)\,(d^2W/dS^2)}{\sqrt{1 - (dW/dS)^2}}, \tag{B.9}$$

which can be obtained directly from Eq. (A.4), have been used in the derivation, to go from Eq. (B.7) to Eq. (B.8).

B.1.2. The energy method. Again, as given by Eqs. (A.11) through (A.14) in Appendix A, the energy method is utilized to derive the equations of motion of

the beam; it should be noted that, when the beam is extensible (i.e., $\varepsilon \neq 0$), the independent variable is X instead of S, and the potential energy should be calculated by (Stoker, 1968)

$$\mathcal{V} = \int_0^L \left[\frac{1}{2}Eh\varepsilon^2 + \frac{1}{2}D(1+\varepsilon)^2\kappa^2\right] dX. \tag{B.10}$$

B.1.3. The boundary conditions. As shown in Fig. A.1, the boundary conditions for the transverse and longitudinal displacement fields $W(X)$ and $V(X)$ at the clamped end $X = 0$ can be obtained from geometry, i.e.,

$$W(X=0) = 0, \quad V(X=0) = 0, \tag{B.11}$$

$$\theta(X=0) = 0. \tag{B.12}$$

Substituting Eq. (B.12) into Eq. (B.4), one finds that

$$dW(X=0)/dX = 0. \tag{B.13}$$

Substituting Eq. (B.13) into Eq. (B.1), one further obtains

$$dV(X=0)/dX = \varepsilon(0). \tag{B.14}$$

It should be noted that $dV(X=0)/dX \neq 0$ because $\varepsilon(X=0) \neq 0$. Actually, if there is a distribution of longitudinal force F_{D} acting on the beam, as shown in Fig. A.2, the stain ε at the clamped end may be calculated by

$$\varepsilon(X=0) = \frac{\int_0^L F_{\mathrm{D}}\, dX}{Eh}. \tag{B.15}$$

At the free end of the beam, the beam is supposed to be free of any moment and shear force, i.e.,

$$d\theta(X=L)/dS = 0, \quad d^2\theta(X=L)/dS^2 = 0. \tag{B.16}$$

Because it is generally assumed that $dX/dS \neq 0$ (i.e., $\theta(X) < \pi/2$), Eq. (B.16) can conveniently be rewritten as

$$d\theta(X=L)/dX = 0, \quad d^2\theta(X=L)/dX^2 = 0. \tag{B.17}$$

Moreover, from Eqs. (B.3) and (B.4), one has

$$\tan\theta(X) = \frac{dW/dX}{1 + dV/dX}. \tag{B.18}$$

Taking the derivative of Eq. (B.18) with respect to X once and substituting therein Eq. (B.3) for $\cos\theta$, one gets

$$\frac{d\theta}{dX} = \frac{(1 + dV/dX)\,(d^2W/dX^2) - (d^2V/dX^2)\,(dW/dX)}{(1 + dV/dX)^2 + (dW/dX)^2}. \tag{B.19}$$

It follows from Eq. (B.17) that

$$\left[\left(1 + \frac{dV}{dX}\right)\frac{d^2W}{dX^2} - \frac{d^2V}{dX^2}\frac{dW}{dX}\right]_{X=L} = 0. \tag{B.20}$$

Note that Eq. (B.20) signifies that the curvature of the beam $\kappa(X = L) = 0$ according to Eq. (B.5). Taking the derivative of Eq. (B.19) with respect to X one more time and substituting Eq. (B.20), one further obtains

$$\left[\left(1 + \frac{dV}{dX}\right)\frac{d^3W}{dX^3} - \frac{d^3V}{dX^3}\frac{dW}{dX}\right]_{X=L} = 0. \tag{B.21}$$

It is now clear that, one cannot determine the boundary conditions for either the transverse or the longitudinal displacement from Eqs. (B.20) and (B.21); further approximations have to be made. To this end, we *assume* that the transverse displacement $W(X)$, at the free end $X = L$, has the usual boundary conditions of a linear cantilevered beam, which is defined by

$$\frac{d^2W(X = L)}{dX^2} = \frac{d^3W(X = L)}{dX^3} \equiv 0. \tag{B.22}$$

Consequently, it can be determined from Eqs. (B.20) and (B.21) that

$$\frac{d^2V(X = L)}{dX^2} = \frac{d^3V(X = L)}{dX^3} \equiv 0, \tag{B.23}$$

providing that $[1 + dV/dX]_L$ is finite and

$$dW(X = L)/dX \neq 0; \tag{B.24}$$

according to Eq. (B.18) for $\tan\theta$, these two additionally imposed conditions mean additionally that

$$\theta(X = L) \neq 0, \tag{B.25}$$

which is generally satisfied if no pure first-mode motion is observed in the vibrations of the cantilevered beam.

Finally, if no lumped longitudinal force acts at the free end of the beam, one has

$$\varepsilon(X = L) = 0; \tag{B.26}$$

and it follows from Eq. (B.1) that

$$\left[\sqrt{\left(1+\frac{dV}{dX}\right)^2+\left(\frac{dW}{dX}\right)^2}-1\right]_{X=L} = 0. \tag{B.27}$$

Substituting Eq. (B.24) into Eq. (B.27), one gets

$$dV(X = L)/dX \neq 0. \tag{B.28}$$

Moreover, by neglecting the higher-order quantity $(dV(X = L)/dX)^2$, one may get an additional boundary condition at the free end of the beam from Eq. (B.27) as

$$\left[\frac{dV}{dX}+\frac{1}{2}\left(\frac{dW}{dX}\right)^2\right]_{X=L} = 0. \tag{B.29}$$

B.1.4. The nonlinear equations of motion. Although the beam is extensible, it is assumed that the level of the strain ε is very small; one therefore still has $W' \sim \mathcal{O}(\epsilon)$ and $V' \sim \mathcal{O}(\epsilon^2)$ (see Appendix A) according to Eq. (B.1), where the prime denotes a derivative with respect to X.

It follows from Eqs. (B.5) and (B.19) that

$$\begin{aligned}\frac{d\theta}{dX} &= (1+\varepsilon)\kappa = \frac{(1+V')W'' - V''W'}{(1+V')^2+W'^2} \\ &= W'' - 2V'W'' - W'^2W'' + V'W'' - V''W' + \mathcal{O}\left(\epsilon^5\right),\end{aligned} \tag{B.30}$$

and hence

$$(1+\varepsilon)^2\kappa^2 = W''^2 - 2V'W''^2 - 2W'^2W''^2 - 2V''W'W'' + \mathcal{O}\left(\epsilon^5\right). \tag{B.31}$$

Further, it follows from Eq. (B.1) that

$$\varepsilon = \sqrt{(1+V'^2)+W'^2} - 1 = V' + \frac{1}{2}W'^2 - \frac{1}{2}V'W'^2 - \frac{1}{8}W'^4 + \mathcal{O}\left(\epsilon^5\right), \tag{B.32}$$

and hence

$$\varepsilon^2 = V'^2 + V'W'^2 + \frac{1}{4}W'^4 + \mathcal{O}\left(\epsilon^5\right). \tag{B.33}$$

Splitting Eq. (B.10) into two parts, one gets

$$\mathcal{V}_1 = \int_0^L \left[\frac{1}{2}Eh\varepsilon^2\right] dX, \qquad \mathcal{V}_2 = \int_0^L \left[\frac{1}{2}D(1+\varepsilon)^2\kappa^2\right] dX. \tag{B.34}$$

Substituting Eq. (B.33) into Eq. (B.34) for $\mathcal{V}_1$, one has

$$\begin{aligned}
\delta\int_{t_1}^{t_2}\mathcal{V}_1\,dt &= \frac{1}{2}Eh\delta\left\{\int_{t_1}^{t_2}\int_0^L\left[V'^2 + V'W'^2 + \frac{1}{4}W'^4\right] dX\,dt\right\} \\
&= -Eh\int_{t_1}^{t_2}\int_0^L\left[\left(V'' + W'W''\right)\delta V\right. \\
&+ \left.\left(V'W'' + V''W' + \frac{3}{2}W'^2W''\right)\delta W\right] dX\,dt,
\end{aligned} \tag{B.35}$$

where the boundary conditions given in Eqs. (B.11) and (B.13) have been used to eliminate the terms

$$[V'\delta V]_{X=0}, \quad \left[\frac{1}{2}W'^2\delta V\right]_{X=0}, \quad [V'W'\delta W]_{X=0}, \quad \left[\frac{1}{2}W'^3\delta W\right]_{X=0} \tag{B.36a}$$

arising from integration by parts, which are evaluated at $X = 0$. At the same time, the boundary condition Eq. (B.29) has been invoked to eliminate the terms

$$[V'\delta V]_{X=L}, \quad \left[\frac{1}{2}W'^2\delta V\right]_{X=L}, \quad [V'W'\delta W]_{X=L}, \quad \left[\frac{1}{2}W'^3\delta W\right]_{X=L}, \tag{B.36b}$$

arising from integration by parts, which are evaluated at $X = L$ and which can actually be reorganized during the derivation as

$$\left[\left(V' + \frac{1}{2}W'^2\right)\delta V\right]_{X=L}, \qquad \left[W'\left(V' + \frac{1}{2}W'^2\right)\delta W\right]_{X=L}. \tag{B.36c}$$

On the other hand, substituting Eq. (B.31) into Eq. (B.34) for $\mathcal{V}_2$, one obtains

$$\begin{aligned}
\delta\int_{t_1}^{t_2}\mathcal{V}_2\,dt &= \frac{1}{2}D\delta\left\{\int_{t_1}^{t_2}\int_0^L\left[W''^2 - 2V'W''^2 - 2W'^2W''^2 - 2V''W'W''\right]dX\,dt\right\} \\
&= -D\int_{t_1}^{t_2}\int_0^L\left[\left(W''W''' + W'W''''\right)\delta V\right. \\
&- \left(W'''' - 3V'''W'' - 4V''W''' - 2V'W'''' - 2W''^3 - 8W'W''W'''\right. \\
&- \left.\left.2W'^2W'''' - V''''W'\right)\delta W\right]dX\,dt,
\end{aligned} \tag{B.37}$$

where the boundary conditions given in Eqs . (B.11), (B.13), (B.22) and (B.23) have been used to eliminate the terms

$$\begin{aligned}
&[W''\delta W']_{X=0}^{X=L}, \quad [W'''\delta W]_{X=0}^{X=L}, \quad \left[W''^2\delta V\right]_{X=0}^{X=L}, \quad [V'W''\delta W']_{X=0}^{X=L}, \\
&\left[(V'W'')'\delta W\right]_{X=0}^{X=L}, \quad \left[W'W''^2\delta W\right]_{X=0}^{X=L}, \quad \left[W'^2W''\delta W'\right]_{X=0}^{X=L}, \\
&\left[\left(W'^2W''\right)'\delta W\right]_{X=0}^{X=L}, \quad [W'W''\delta V']_{X=0}^{X=L}, \quad \left[(W'W'')'\delta V\right]_{X=0}^{X=L}, \\
&[V''W''\delta W]_{X=0}^{X=L}, \quad [V''W'\delta W']_{X=0}^{X=L}, \quad \left[(V''W')'\delta W\right]_{X=0}^{X=L},
\end{aligned} \tag{B.38}$$

arising from integration by parts.

Moreover, it follows from Eqs. (A.12) and (A.14), respectively, that

$$\delta\int_{t_1}^{t_2}\mathcal{T}\,dt = -\rho_{\mathrm{P}}h\int_{t_1}^{t_2}\int_0^L\left(\ddot{V}\delta V + \ddot{W}\delta W\right)dX\,dt, \tag{B.39}$$

$$\int_{t_1}^{t_2}\delta\mathcal{W}\,dt = \int_{t_1}^{t_2}\int_0^L\left(F_{\mathrm{D}}\delta V + F_{\mathrm{L}}\delta W\right)dX\,dt, \tag{B.40}$$

where in Eq. (B.39), $\left[\dot{V}\delta V + \dot{W}\delta W\right]_{t_1}^{t_2} = 0$ has been assumed.

Substituting Eqs. (B.35), (B.37), (B.39) and (B.40) into Eq. (A.11), one obtains the equations of motion for longitudinal and transverse displacements V and W as

$$\rho_{\mathrm{P}} h\ddot{V} - Eh\left(V'' + W'W''\right) - D\left(W''W''' + W'W''''\right) = F_{\mathrm{D}}, \tag{B.41a}$$

$$\begin{aligned}&\rho_{\mathrm{P}} h\ddot{W} - Eh\left(V'W'' + V''W' + \frac{3}{2}W'^2W''\right) + D\left(W'''' - 3V'''W'' - 4V''W'''\right.\\ -\ &\left. 2V'W'''' - 2W''^3 - 8W'W''W''' - 2W'^2W'''' - V''''W'\right) = F_{\mathrm{L}},\end{aligned} \tag{B.41b}$$

both of which are nonlinear with the accuracy up to $\mathcal{O}(\epsilon^3)$. Additionally, when considering the material damping to be of the Kelvin-Voigt type (see Appendix A), Eqs. (B.41a) and (B.41b) become

$$\begin{aligned}&\rho_{\mathrm{P}} h\ddot{V} - Eh\left(1 + a\frac{\partial}{\partial t}\right)\left(V'' + W'W''\right)\\ -\ &D\left(1 + a\frac{\partial}{\partial t}\right)\left(W''W''' + W'W''''\right) = F_{\mathrm{D}},\end{aligned} \tag{B.42a}$$

$$\begin{aligned}&\rho_{\mathrm{P}} h\ddot{W} - Eh\left(1 + a\frac{\partial}{\partial t}\right)\left(V'W'' + V''W' + \frac{3}{2}W'^2W''\right)\\ +\ &D\left(1 + a\frac{\partial}{\partial t}\right)\left(W'''' - 3V'''W'' - 4V''W''' - 2V'W'''' - 2W''^3 - 8W'W''W'''\right.\\ -\ &\left. 2W'^2W'''' - V''''W'\right) = F_{\mathrm{L}}.\end{aligned} \tag{B.42b}$$

Note that, as compared to the single equation of motion (i.e., Eq. (2.1)) for the transverse displacement W developed using the inextensibility assumption, Eqs. (B.42a) and (B.42b) account for both the longitudinal displacement V and the transverse displacement W simultaneously, and eliminate the involvement of nonlinear inertia terms. Moreover, it should be emphasized that $V'(X = 0, t) = 0$ is not a valid boundary condition for the longitudinal displacement V; on the contrary, one can find that $V'(X = 0, t) = \left(\int_0^L F_{\mathrm{D}}\, dX\right) / (Eh)$ (see Eqs. (B.14) and (B.15)). Note also that, when the beam is assumed to be inextensible, according to Eq. (2.2) for the relationship between V and W and Eq. (2.3) for the boundary conditions of W, one finds that $V'(X = 0, t) \equiv 0$; this is actually an important weak point of the equation of motion developed using the inextensibility assumption.

B.1.5. Recovery of the equation of motion for inextensible beam. We have already shown in Eqs. (B.8) that the expression for the curvature κ of an inextensible beam can be recovered from an extensible one if the inextensibility assumption is invoked. Moreover, one can prove that the equations of motion for an extensible beam given by Eqs. (B.41a) and (B.41b) are consistent with that for an inextensible one given by Eq. (A.43).

If one uses the inextensibility assumption (i.e., $\varepsilon(X) \equiv 0$) and regards dX and dS to be interchangeable, it is straightforward to insert Eq. (A.16) into Eqs. (B.41a) and (B.41b) and arrive at

$$\rho_{\mathrm{P}} h \ddot{V} - D\left(W' W'''\right)' = F_{\mathrm{D}}, \tag{B.43a}$$

$$\rho_{\mathrm{P}} h \ddot{W} + D\left(W'''' + 2W' W'' W''' + W''^3\right) = F_{\mathrm{L}}. \tag{B.43b}$$

Substituting Eq. (A.17) for V, Eq. (B.43a) becomes

$$\rho_{\mathrm{P}} h \int_0^S \left(\dot{W}'^2 + W' \ddot{W}'\right) dS = -D\left(W' W'''\right)' - F_{\mathrm{D}}. \tag{B.44}$$

It follows that

$$\rho_{\mathrm{P}} h W' \int_0^S \left(\dot{W}'^2 + W' \ddot{W}'\right) dS = -D W' \left(W' W'''\right)' - W' F_{\mathrm{D}}, \tag{B.45}$$

and also

$$\rho_{\mathrm{P}} h W'' \int_S^L \left[\int_0^S \left(\dot{W}'^2 + W' \ddot{W}'\right) dS\right] dS = D W' W'' W''' - W'' \int_S^L F_{\mathrm{D}}\, dS. \tag{B.46}$$

Substituting Eqs. (B.45) and (B.46) into Eq. (B.43b), one finally obtains

$$\begin{aligned} & \rho_{\mathrm{P}} h \ddot{W} + D\left[W''''\left(1 + W'^2\right) + 4W' W'' W''' + W''^3\right] \\ + \;& \rho_{\mathrm{P}} h W' \int_0^S \left(\dot{W}'^2 + W' \ddot{W}'\right) dS - \rho_{\mathrm{P}} h W'' \int_S^L \left[\int_0^S \left(\dot{W}'^2 + W' \ddot{W}'\right) dS\right] dS \\ = \;& F_{\mathrm{L}} - W' F_{\mathrm{D}} + W'' \int_S^L F_{\mathrm{D}}\, dS. \end{aligned} \tag{B.47}$$

That is, the equation of motion Eq. (A.43) for an inextensible beam is recovered.

It should be mentioned that the strain $\varepsilon(X)$ is normally very small for cantilevered flexible thin plates in axial flow, i.e., $\varepsilon(X) \approx 0$. It follows that the terms $(V'' + W'W'')$ and $\left(V'W'' + V''W' + 3W'^2W''/2\right)$ in Eqs. (B.42a) and (B.42b), respectively, are very small quantities and they vanish when $\varepsilon(X) = 0$.

B.1.6. Nondimensionalization. Using the scheme defined in Eq. (2.6) for nondimensionalization, the equations of motion (Eqs. (B.42a) and (B.42b)) and the associated boundary conditions (Eqs. (B.11), (B.13), (B.14), (B.22) and (B.23)) become

$$\ddot{v} - \chi\left(1 + \alpha\frac{\partial}{\partial\tau}\right)(v'' + w'w'') - \left(1 + \alpha\frac{\partial}{\partial\tau}\right)(w''w''' + w'w'''') = (f_{\mathrm{D}})_{\mathrm{eff}}, \tag{B.48a}$$

$$\begin{aligned} &\ddot{w} - \chi\left(1 + \alpha\frac{\partial}{\partial\tau}\right)\left(v'w'' + v''w' + \frac{3}{2}w'^2w''\right) \\ + &\left(1 + \alpha\frac{\partial}{\partial\tau}\right)\left(w'''' - 3v'''w'' - 4v''w''' - 2v'w'''' - 2w''^3 - 8w'w''w'''\right. \\ - &\left.2w'^2w'''' - v''''w'\right) = (f_{\mathrm{L}})_{\mathrm{eff}}, \end{aligned} \tag{B.48b}$$

with associated boundary conditions

$$w(x=0,\tau) = w'(x=0,\tau) = w''(x=1,\tau) = w''(x=1,\tau) \equiv 0, \tag{B.49a}$$

$$v(x=0,\tau) = v''(x=1,\tau) = v'''(x=1,\tau) \equiv 0, \tag{B.49b}$$

where the effective longitudinal and transverse forces $(f_{\mathrm{D}})_{\mathrm{eff}}$ and $(f_{\mathrm{L}})_{\mathrm{eff}}$ are, respectively, defined by

$$(f_{\mathrm{D}})_{\mathrm{eff}} = \mu U_{\mathrm{R}} f_{\mathrm{D}}, \quad (f_{\mathrm{L}})_{\mathrm{eff}} = \mu U_{\mathrm{R}} f_{\mathrm{L}}. \tag{B.50}$$

In Eqs. (B.48a) through (B.49b), the overdot and the prime, respectively, represent $\partial(\ )/\partial\tau$ and $\partial(\ )/\partial x$. Moreover, a new nondimensional parameter, the length parameter χ, is introduced, defined by

$$\chi = \frac{EhL^2}{D} = 12(1-\nu^2)\left(\frac{L}{h}\right)^2; \tag{B.51}$$

similar to the length-to-thickness ratio ζ defined in Chapter 2, χ accounts for the ratio of the length of the flexible plate to the plate thickness. It should be noted that the value of the nondimensional parameter χ is normally very large for thin cantilevered flexible plates. For example, in the experiments by Tang et al. (2003), one has $\chi = 5.11 \times 10^6$ (see Appendix C for details).

B.2. Solution method

B.2.1. The Galerkin expansion. When applying the Galerkin expansion to the equations of motion, Eqs. (B.48a) and (B.48b) for extensible beams, the eigenmodes of the longitudinal and transverse displacement fields $v(x)$ and $w(x)$ should be considered separately. Considering the boundary conditions given in Eq. (B.49a), the eigenmodes of a linear *in vacuo* cantilevered beam defined in Eq. (3.2) are used for the $w(x)$ displacement field as comparison functions, where the independent spatial variable s should be replaced by x for extensible beams, i.e.,

$$\phi_m(x) = [\cosh(\beta_m x) - \cos(\beta_m x)] - \varsigma_m [\sinh(\beta_m x) - \sin(\beta_m x)], \tag{B.52}$$

On the other hand, it is very difficult to find a set of comparison functions for the displacement field $v(x)$, satisfying the boundary conditions given in Eq. (B.49b). It should be emphasized that one cannot use the eigenmodes of the linearized homogenous version of Eq. (B.48b) (i.e., the differential equation $\ddot{v} - \chi v'' = 0$ for the longitudinal vibrations of a *bar* being clamped at $x = 0$ and free at $x = 1$) because they do not satisfy the boundary conditions defined in Eq. (B.49b). However, through extensive observations and tests, the following set of modes may be regarded as candidate comparison functions:

$$\begin{aligned} \psi_m(x) &= [\cosh(\beta_m x) - \cos(\beta_m x)] - \varsigma_m [\sinh(\beta_m x) - \sin(\beta_m x)] + \beta_m x \\ &= \phi_m(x) + \beta_m x. \end{aligned} \tag{B.53}$$

That is, the modes for $v(x)$ are a modified form of those for $w(x)$. It can be seen in Table B.1 that $\psi_m(x)$, as defined in Eq. (B.53), satisfies all the boundary conditions given in Eq. (B.49b).

TABLE B.1. The modes $\psi_m(x)$ for the $v(x)$ displacement field and the corresponding derivatives evaluated at the clamped end and the free end

$\psi_m(x)$ and its derivatives	clamped end, $x=0$	free end, $x=1$
$\psi_m(x)=\phi_m(x)+\beta_m x$	$\equiv 0$	$\neq 0$
$\psi'_m(x)=\phi'_m(x)+\beta_m$	$\neq 0$	$\neq 0$
$\psi''_m(x)=\phi''_m(x)$	$\neq 0$	$\equiv 0$
$\psi'''_m(x)=\phi'''_m(x)$	$\neq 0$	$\equiv 0$

It follows from Eqs. (B.52) and (B.53) that the $v(x,\tau)$ and $w(x,\tau)$ displacements may be expanded as

$$v(x,\tau)=\sum_{m=1}^{M} p_m(\tau)\phi_m(x), \quad w(x,\tau)=\sum_{m=1}^{M} q_m(\tau)\phi_m(x), \tag{B.54}$$

where M is the number of modes utilized in the analysis; the same M is used for both $v(x)$ and $w(x)$ displacements for simplicity. Moreover, $p_m(\tau)$ and $q_m(\tau)$ are, respectively, the generalized coordinates of the $v(x)$ and $w(x)$ displacements. Substituting Eq. (B.54) into Eqs. (B.48a) and (B.48b), multiplying both sides of these two equations by $\psi_i(x)$ and $\phi_i(x)$, respectively, and then integrating from $x=0$ to $x=1$, one gets a set of nonlinear ordinary differential equations in terms of $p_i(\tau)$ and $q_j(\tau)$ as follows:

$$\widehat{M}_{im}\ddot{p}_m+\chi\left(1+\alpha\frac{\partial}{\partial\tau}\right)\left(\widehat{A}_{im}p_m+\widehat{B}_{imn}q_mq_n\right)+\left(1+\alpha\frac{\partial}{\partial\tau}\right)\widehat{C}_{imn}q_mq_n=f_{\mathrm{D}i}, \tag{B.55a}$$

$$\begin{aligned}&\ddot{q}_i+\chi\left(1+\alpha\frac{\partial}{\partial\tau}\right)\left(\widehat{D}_{imn}p_mq_n+\widehat{E}_{imnl}q_mq_nq_l\right)\\ &+\left(1+\alpha\frac{\partial}{\partial\tau}\right)\left(\widehat{F}_iq_i+\widehat{G}_{imn}p_mq_n+\widehat{H}_{imnl}q_mq_nq_l\right)=f_{\mathrm{L}i},\end{aligned} \tag{B.55b}$$

where, the numerical constants $\widehat{A}_{im}$, $\widehat{B}_{imn}$, $\widehat{C}_{imn}$, $\widehat{D}_{imn}$, $\widehat{E}_{imnl}$, $\widehat{F}_i$, $\widehat{G}_{imn}$, $\widehat{H}_{imnl}$ and $\widehat{M}_{im}$ are defined by

$$\widehat{A}_{im} = -\int_0^1 \psi_i \psi_m'' \, dx, \tag{B.56}$$

$$\widehat{B}_{imn} = -\int_0^1 \psi_i \phi_m' \phi_n'' \, dx, \tag{B.57}$$

$$\widehat{C}_{imn} = -\int_0^1 \psi_i \left(\phi_m'' \phi_n''' + \phi_m' \phi_n''''\right) \, dx, \tag{B.58}$$

$$\widehat{D}_{imn} = -\int_0^1 \phi_i \left(\psi_m' \phi_n'' + \psi_m'' \phi_n'\right) \, dx, \tag{B.59}$$

$$\widehat{E}_{imnl} = -\int_0^1 \frac{3}{2} \phi_i \phi_m' \phi_n' \phi_l' \, dx, \tag{B.60}$$

$$\widehat{F}_i = \beta_i^4, \tag{B.61}$$

$$\widehat{G}_{imn} = -\int_0^1 \phi_i \left(3\psi_m''' \phi_n'' + 4\psi_m'' \phi_n''' + 2\psi_m' \phi_n'''' + \psi_m'''' \phi_n'\right) \, dx, \tag{B.62}$$

$$\widehat{H}_{imnl} = -\int_0^1 \phi_i \left(2\phi_m'' \phi_n'' \phi_l'' + 8\phi_m' \phi_n'' \phi_l''' + 2\phi_m' \phi_n' \phi_l''''\right) \, dx, \tag{B.63}$$

$$\widehat{M}_{im} = \int_0^1 \psi_i \psi_m \, dx. \tag{B.64}$$

Moreover, $f_{\mathrm{D}i}$ and $f_{\mathrm{L}i}$ are given by

$$f_{\mathrm{D}i} = \int_0^1 \phi_i (f_{\mathrm{D}})_{\mathrm{eff}} \, dx, \quad f_{\mathrm{L}i} = \int_0^1 \phi_i (f_{\mathrm{L}})_{\mathrm{eff}} \, dx. \tag{B.65}$$

It should be mentioned that χ is normally very large for thin plates and the values of the quantities $\left(\widehat{A}_{im} p_m + \widehat{B}_{imn} q_m q_n\right)$ and $\left(\widehat{D}_{imn} p_m q_n + \widehat{E}_{imnl} q_m q_n q_l\right)$ are very small. Therefore, in order to avoid roundoff errors in the solution, it is not suggested to do coefficient combinations for the term $q_m q_n$ in Eq. (B.55a), and the terms $p_m q_n$ and $q_m q_n q_l$ in Eq. (B.55b).

B.2.2. The first-order formulation. Eqs. (B.55a) and (B.55b) can be rewritten as

$$\begin{aligned} &\widehat{M}_{im} \ddot{p}_m + \chi \left(\widehat{A}_{im} p_m + \widehat{B}_{imn} q_m q_n\right) + \chi\alpha \left[\widehat{A}_{im} \dot{p}_m + \left(\widehat{B}_{imn} + \widehat{B}_{inm}\right) q_m \dot{q}_n\right] \\ + \;& \widehat{C}_{imn} q_m q_n + \alpha \left(\widehat{C}_{imn} + \widehat{C}_{inm}\right) q_m \dot{q}_n = f_{\mathrm{D}i}, \end{aligned} \tag{B.66a}$$

$$\ddot{q}_i + \chi\left(\widehat{D}_{imn}p_m q_n + \widehat{E}_{imnl}q_m q_n q_l\right) + \chi\alpha\left[\widehat{D}_{imn}\left(\dot{p}_m q_n + p_m\dot{q}_n\right)\right.$$
$$+ \left.\left(\widehat{E}_{imnl} + \widehat{E}_{ilnm} + \widehat{E}_{imln}\right)q_m q_n\dot{q}_l\right] + \left(\widehat{F}_i q_i + \widehat{G}_{imn}p_m q_n + \widehat{H}_{imnl}q_m q_n q_l\right)$$
$$+ \alpha\left[\widehat{F}_i\dot{q}_i + \widehat{G}_{imn}\left(\dot{p}_m q_n + p_m\dot{q}_n\right) + \left(\widehat{H}_{imnl} + \widehat{H}_{ilnm} + \widehat{H}_{imln}\right)q_m q_n\dot{q}_l\right] = f_{\mathrm{L}i}. \tag{B.66b}$$

Because no nonlinear inertia terms are involved (in contrast to Eq. (3.12)), it is convenient to simultaneously solve Eqs. (B.66a) and (B.66b) using the following first-order formulation:

$$\mathbb{M}\dot{\mathbf{Y}} = \mathbb{F}\mathbf{Y} + \mathbf{F}, \tag{B.67}$$

where the state and force vectors $\mathbf{Y}$ and $\mathbf{F}$ are, respectively, defined by

$$Y = \left[r_1, r_2, \cdots, r_M; s_1, s_2, \cdots, s_M; q_1, q_2, \cdots, q_M; p_1, p_2, \cdots, p_M\right]^{\mathrm{T}}, \tag{B.68}$$

$$F = \left[f_{\mathrm{L}1}, f_{\mathrm{L}2}, \cdots, f_{\mathrm{L}M}; f_{\mathrm{D}1}, f_{\mathrm{D}2}, \cdots, f_{\mathrm{D}M}; 0, 0, \cdots, 0; 0, 0, \cdots, 0\right]^{\mathrm{T}}, \tag{B.69}$$

where $r_{i,i=1,2,\cdots,M}$ and $s_{i,i=1,2,\cdots,M}$ are, respectively, defined by

$$r_i = \dot{q}_i, \quad s_i = \dot{p}_i. \tag{B.70}$$

The state matrix $\mathbb{M}$ is defined by

$$\mathbb{M}_{i,j} = \begin{cases} \delta_{i,j} & \text{when} \quad 1 \le i \le M, \\ \widehat{M}_{i-M,j-M} & \text{when} \quad (M+1) \le i \le 2M, \\ \delta_{i-2M,j-2M} & \text{when} \quad (2M+1) \le i \le 3M, \\ \delta_{i-3M,j-3M} & \text{when} \quad (3M+1) \le i \le 4M, \\ 0 & \text{otherwise.} \end{cases} \tag{B.71}$$

Moreover, the matrix $\mathbb{F}$ accounts for the nonlinearities involved in Eqs. (B.66a) and (B.66b), that is

$$\mathbb{F}_{ij}\mathbf{Y}_j = \begin{cases} -\Big\{\chi\left(\widehat{D}_{imn}p_m q_n + \widehat{E}_{imnl}q_m q_n q_l\right) + \chi\alpha\left[\widehat{D}_{imn}\left(s_m q_n + p_m r_n\right)\right. \\ \left. + \left(\widehat{E}_{imnl} + \widehat{E}_{ilnm} + \widehat{E}_{imln}\right) q_m q_n r_l\right] + \left(\widehat{F}_i q_i + \widehat{G}_{imn}p_m q_n + \widehat{H}_{imnl}q_m q_n q_l\right) \\ + \alpha\left[\widehat{F}_i r_i + \widehat{G}_{imn}\left(s_m q_n + p_m r_n\right) + \left(\widehat{H}_{imnl} + \widehat{H}_{ilnm} + \widehat{H}_{imln}\right) q_m q_n r_l\right]\Big\} \\ \qquad\qquad \text{when} \quad 1 \le i \le M, \\ -\Big\{\chi\left(\widehat{A}_{im}p_m + \widehat{B}_{imn}q_m q_n\right) + \chi\alpha\left[\widehat{A}_{im}s_m + \left(\widehat{B}_{imn} + \widehat{B}_{inm}\right) q_m r_n\right] \\ + \widehat{C}_{imn}q_m q_n + \alpha\left(\widehat{C}_{imn} + \widehat{C}_{inm}\right) q_m r_n\Big\} \\ \qquad\qquad \text{when} \quad (M+1) \le i \le 2M, \\ r_i \qquad\qquad \text{when} \quad (2M+1) \le i \le 3M, \\ s_i \qquad\qquad \text{when} \quad (3M+1) \le i \le 4M. \end{cases} \tag{B.72}$$

Finally, Gear's backward scheme (Gear, 1971), in particular the subroutine DIVPAG provided by ISML (Visual Numerics Inc, 1998), is used to solve Eq. (B.67).

B.3. Preliminary results

Using the numerical model developed in this Appendix for extensible cantilevered flexible plates in axial flow, some preliminary calculations were performed. As shown in Fig. B.1(a), it has been found that the time history diverges when the oscillation amplitude of the plate becomes relatively large, say $w(x = 1) > 0.003$. Therefore, stable limited cycle oscillations cannot be obtained. The exact reason to the phenomenon is still unknown; however, it is believed that the assumptions made for the boundary conditions, i.e., Eqs. (B.22) and (B.23), may be responsible for the problem. However, as shown in Figs. B.1(b) and (c), when the reduced flow velocity U_{R} and the oscillation amplitude $w(x = 1)$ are relatively small, one can still obtain the cortical point of the system through examination of the convergence/divergence of the time histories. In particular, for the case $\chi = 1 \times 10^6$ shown in Figs. B.1(b) and (c), the cortical point can be identified to be laying in the range $8.43 < U_{\mathrm{Rc}} < 8.45$.

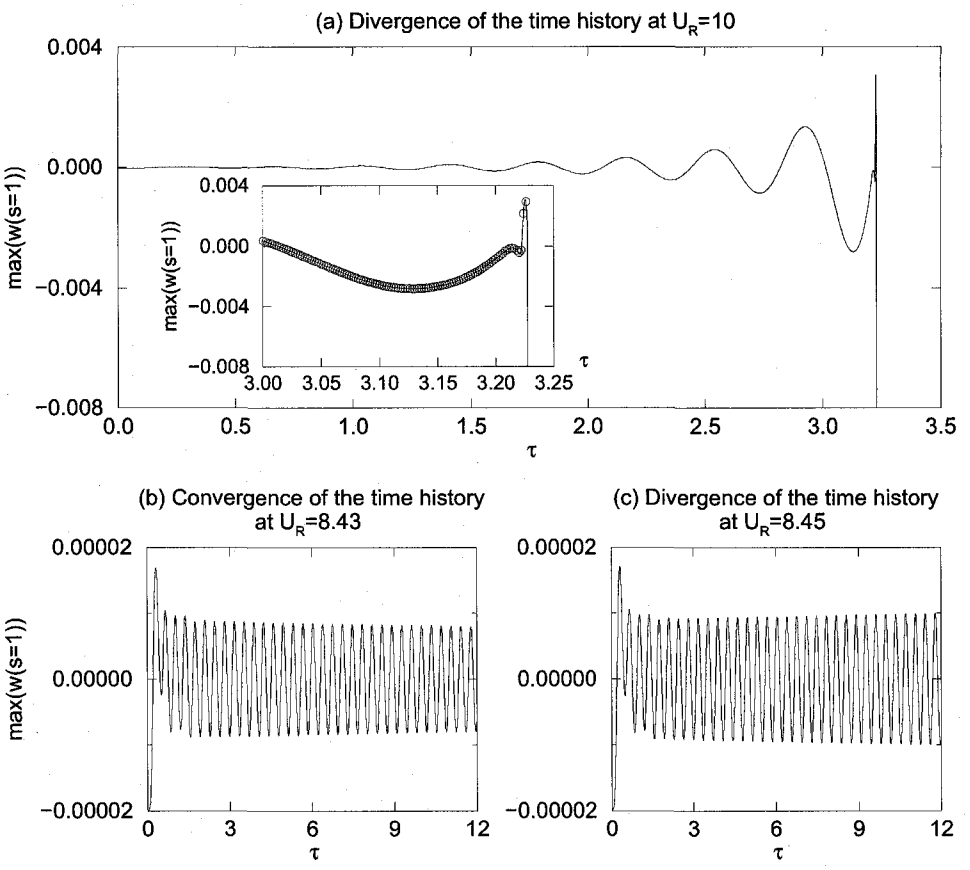

FIGURE B.1. The dynamics of the system obtained using the extensible model. The other parameters of the system are $\chi = 1 \times 10^6$, $\mu = 0.3$, $l_0 = 0.01$, $\alpha = 0.004$ and $C_D = 0$.

Because no limited cycle oscillation can be obtained, a complete convergence test can only be conducted in the early transient of the dynamics of the system. Convergence tests in terms of the number of modes M and time step $\Delta\tau$ for the case $\chi = 1 \times 10^6$ are presented in Fig. B.2. It is found that a relatively good convergent simulation can be obtained using $M = 10$ and $\Delta\tau = 5 \times 10^{-5}$.

The flutter boundary in terms of the value of the length parameter χ is presented in Fig. B.3. It is of interest that over a large range of χ, say $10^2 \leqslant \chi \leqslant 10^8$, the flutter boundary is $8.43 < U_{Rc} < 8.45$, which is higher than that obtained using the inextensible model of the plate, i.e., $U_{Rc} = 8.276$. While for $\chi > 1 \times 10^8$, U_{Rc} decreases as χ increases. It can be seen in Fig. B.3 that, the value of U_{Rc} for the case $\chi = 5 \times 10^{10}$ is well below that obtained using the inextensible model of the plate.

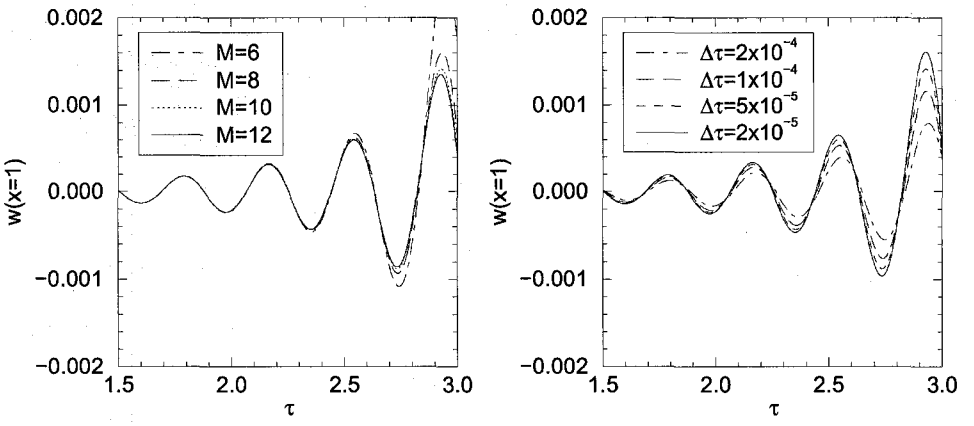

FIGURE B.2. The convergence tests of the extensible model with respect to the number of modes M and time step $\Delta\tau$. The other parameters of the system are $\mu = 0.3$, $U_{\mathrm{R}} = 10$, $l_0 = 0.01$, $\alpha = 0.004$ and $C_{\mathrm{D}} = 0$.

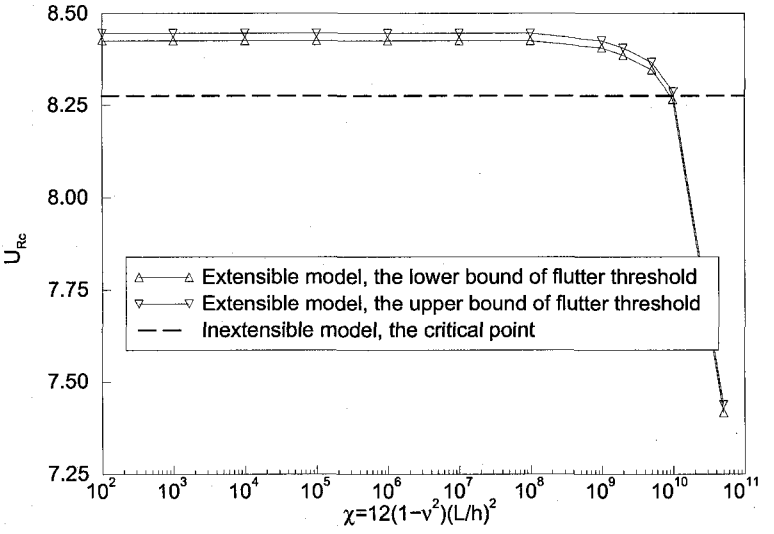

FIGURE B.3. The flutter boundary in terms of the length parameter χ. The other parameters of the system are $\mu = 0.3$, $l_0 = 0.01$, $\alpha = 0.004$ and $C_{\mathrm{D}} = 0$.

Appendix C

The Nondimensional Parameters: a Sample Case

The dynamics of cantilevered flexible plates in axial flow is examined in this thesis with the aid of nondimensional control parameters. Therefore, it is necessary to determine the values of these parameters when one compares the simulation results obtained using the present theory with experimental observations. To this end, the nondimensional parameters calculated according to the system studied by Tang et al. (2003) are summarized here. It should be noted that not all information about the experiments conducted by Tang et al. (2003) is made available in their publications; additional data have to be assumed from other sources.

In the experiments of Tang et al. (2003), the geometric parameters of the system are: length of the flexible plate $L = 0.2667\,\mathrm{m}$, length of the leading-edge rigid segment $L_0 = 0.1016\,\mathrm{m}$, plate thickness $h = 3.9 \times 10^{-4}\,\mathrm{m}$ and width $B = 0.127\,\mathrm{m}$. The plate is made of aluminium-7075, with mass density is $\rho_P = 2.84 \times 10^3\,\mathrm{kg/m^3}$; Young's modulus is $E = 7.056 \times 10^{10}\,\mathrm{Pa}$; and, the Poisson ratio is supposed to be $\nu = 0.3$. The mass density of the air was not given by Tang et al. (2003); it is supposed to be $\rho_F = 1.226\,\mathrm{kg/m^3}$. The experiments were conducted in a wind tunnel which has a test-section of dimensions $0.7\,\mathrm{m} \times 0.53\,\mathrm{m}$ (Attar et al., 2003); it is supposed that the height of the tunnel, i.e., the dimension in the y-axis direction of Fig. 5.5, is $0.7\,\mathrm{m}$. Therefore, when the plate is aligned along the centreline of the tunnel, we

have $H_1 = H_2 = 0.35\,\mathrm{m}$. No information about the material damping was provided by Tang et al. (2003). However, we find that the range of the coefficient of the material damping (Kelvin-Voigt type) is $0.0004 \rightarrow 0.001\,\mathrm{s}$ (Beards, 1996) for aluminium alloy material, and thus carefully choose a value close to the lower bound, i.e., $a = 0.0005\,\mathrm{s}$, for the theoretical analysis in this thesis to avoid unreasonably high flutter thresholds. Finally, flutter motions with a frequency around $f = 23.5\,\mathrm{Hz}$ were observed when the flow velocity was $27.5\,\mathrm{m/s} < U < 29.8\,\mathrm{m/s}$; we use $U = 28.5\,\mathrm{m/s}$ as a typical flow velocity for calculating the relevant parameters.

Some important quantities that may not be directly used in the investigation of the system dynamics are first calculated as follows:

- the bending stiffness of the two-dimensional plate

$$D = \frac{Eh^3}{12(1-\nu^2)} = 0.383\,\mathrm{N}\cdot\mathrm{m}, \tag{C.1}$$

- the solid time

$$T_\mathrm{S} = \sqrt{\frac{\rho_P h L^4}{D}} = 0.121\,\mathrm{s}, \tag{C.2}$$

- the fluid time

$$T_\mathrm{F} = \frac{L}{U} = 0.00936\,\mathrm{s}, \tag{C.3}$$

- the power coefficient

$$\zeta_\mathrm{P} = \rho_\mathrm{F} U^2 \sqrt{\frac{D}{\rho_\mathrm{P} h}} = 585.6\,\mathrm{watt/m}, \tag{C.4}$$

- the work coefficient

$$\zeta_\mathrm{W} = \rho_\mathrm{F} U^2 L^2 = 70.83\,\mathrm{J/m}. \tag{C.5}$$

The nondimensional parameters can be calculated as

- the mass ratio

$$\mu = \frac{\rho_F L}{\rho_P h} = 0.295, \tag{C.6}$$

- the reduced flow velocity (when $U = 28.5\,\mathrm{m/s}$)

$$U_{\mathrm{R}} = \frac{T_{\mathrm{S}}}{T_{\mathrm{F}}} = UL\sqrt{\frac{\rho_{\mathrm{P}} h}{D}} = 12.9, \tag{C.7}$$

- the reduced frequency (when $f = 23.5\,\mathrm{Hz}$)

$$f_{\mathrm{R}} = \frac{2\pi f^{\star}}{U_{\mathrm{R}}} = 1.38, \tag{C.8}$$

- the material damping coefficient (when $a = 0.0005\,\mathrm{s}$)

$$\alpha = \frac{a}{T_{\mathrm{S}}} = \frac{a}{\sqrt{\rho_{\mathrm{P}} h L^4 / D}} = 0.0041, \tag{C.9}$$

- the length of the leading rigid segment

$$l_0 = \frac{L_0}{L} = 0.381, \tag{C.10}$$

- the aspect ratio

$$\mathcal{AR} = \frac{B}{L} = 0.476, \tag{C.11}$$

- the length-to-thickness ratio

$$\zeta = \frac{L}{h} = 683.8, \tag{C.12}$$

- the length parameter

$$\chi = \frac{EhL^2}{D} = 12(1-\nu^2)\left(\frac{L}{h}\right)^2 = 5.11 \times 10^6, \tag{C.13}$$

- the Reynold number (when the kinematic viscosity of the air $\nu_{\mathrm{F}} = 15.11 \times 10^{-6}\,\mathrm{m/s^2}$)

$$\mathrm{Re} = \frac{UL}{\nu_{\mathrm{F}}} = 5.03 \times 10^5, \tag{C.14}$$

- the distances between the plate and the upper/lower parallel solid walls

$$h_{1,2} = \frac{H_{1,2}}{L} = 1.31, \tag{C.15}$$

- the gravity parameter (when the gravitational acceleration $g = 9.8\,\mathrm{m/s^2}$)

$$\gamma_G = \frac{(\rho_P - \rho_F)hgL^3}{D} = \frac{12(1-\nu^2)(\rho_P - \rho_F)gL^3}{Eh^2} = 0.537. \tag{C.16}$$

Appendix D

The Influence of the Wake on the Stability of Cantilevered Flexible Plates in Axial Flow

It has been shown in Chapter 4 (see Fig. 4.16) that, for a specific system with varying length of the flexible plate L but fixed values for the other physical parameters (ρ_{P}, ρ_{F}, h and D), when the plate is long, the various available theories are in very good agreement with each other as well as with measurements from different experiments. In contrast, agreement between the various theories and with experiments is rather poor for short plates. In this Appendix, we aim to correlate these observations to the influence of the wake beyond the trailing edge of the plate. It is proposed that the wake has much less influence on the stability of the fluid-structure system for long plates than it does for short ones.

It should be mentioned that in this Appendix, the analysis is carried out on the flutter boundary; for each case of μ the dynamics of system is examined at the corresponding critical point U_{Rc}, after a small initial disturbance has been imposed on the system. Under these circumstances, the vibration amplitude of the plate is always very small. Therefore, the longitudinal deformations of the plate are not substantial, and the measured S can be regarded as being identical to the coordinate X in the fixed X-Y system.

D.1. On the flutter boundary

The characteristics of the system along the flutter boundary are studied first. Four cases, $\mu = 0.2$ and 0.6 for short plates and $\mu = 4$ and 20 for long plates, are selected, and the computed time history, frequency and vibration modes at the critical point U_{Rc} for each μ are obtained using the present theory; they are shown in Figs. D.1 and D.2.

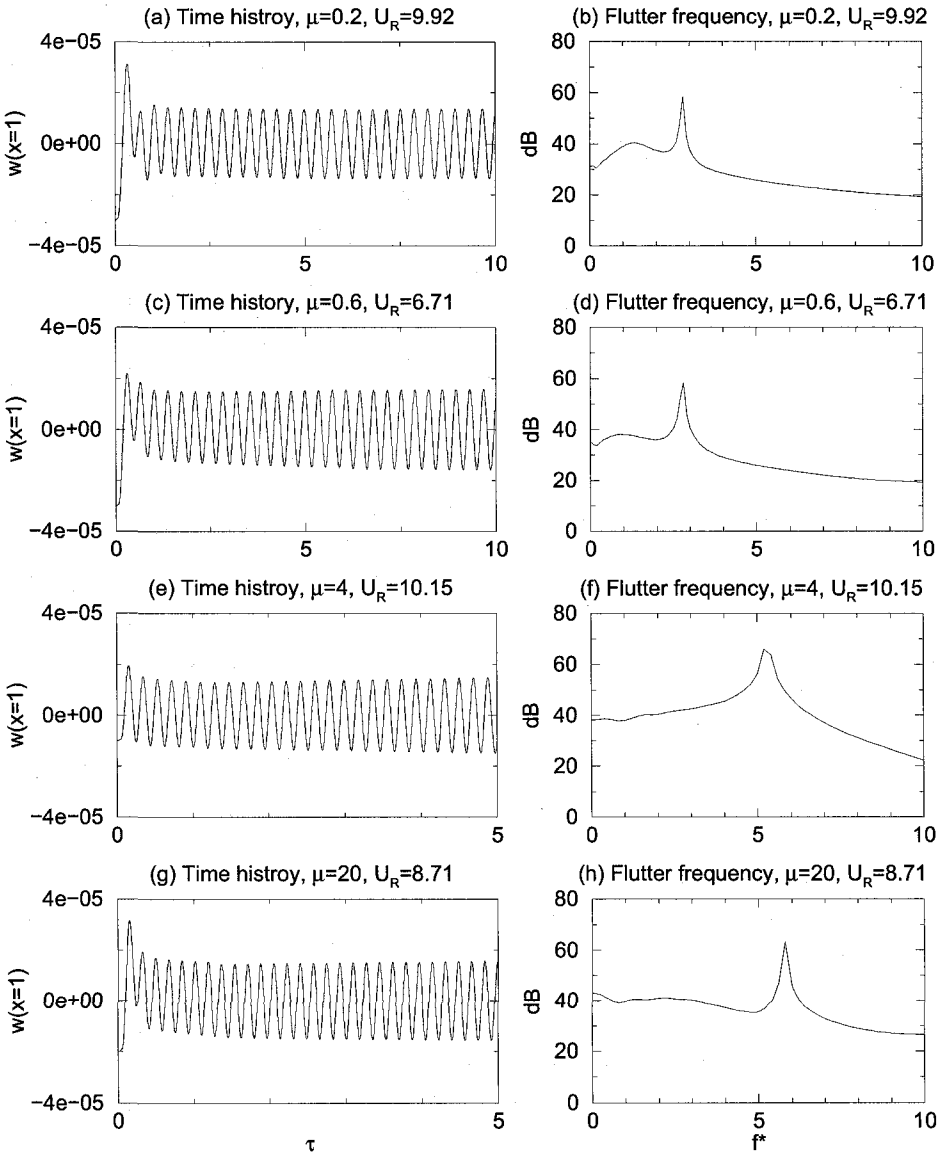

FIGURE D.1. The system dynamics (time history and flutter frequency) for the chosen values of mass ratio μ. The other system parameters are: $l_0 = 0.01$, $\alpha = 0.004$ and $C_{\mathrm{D}} = 0$.

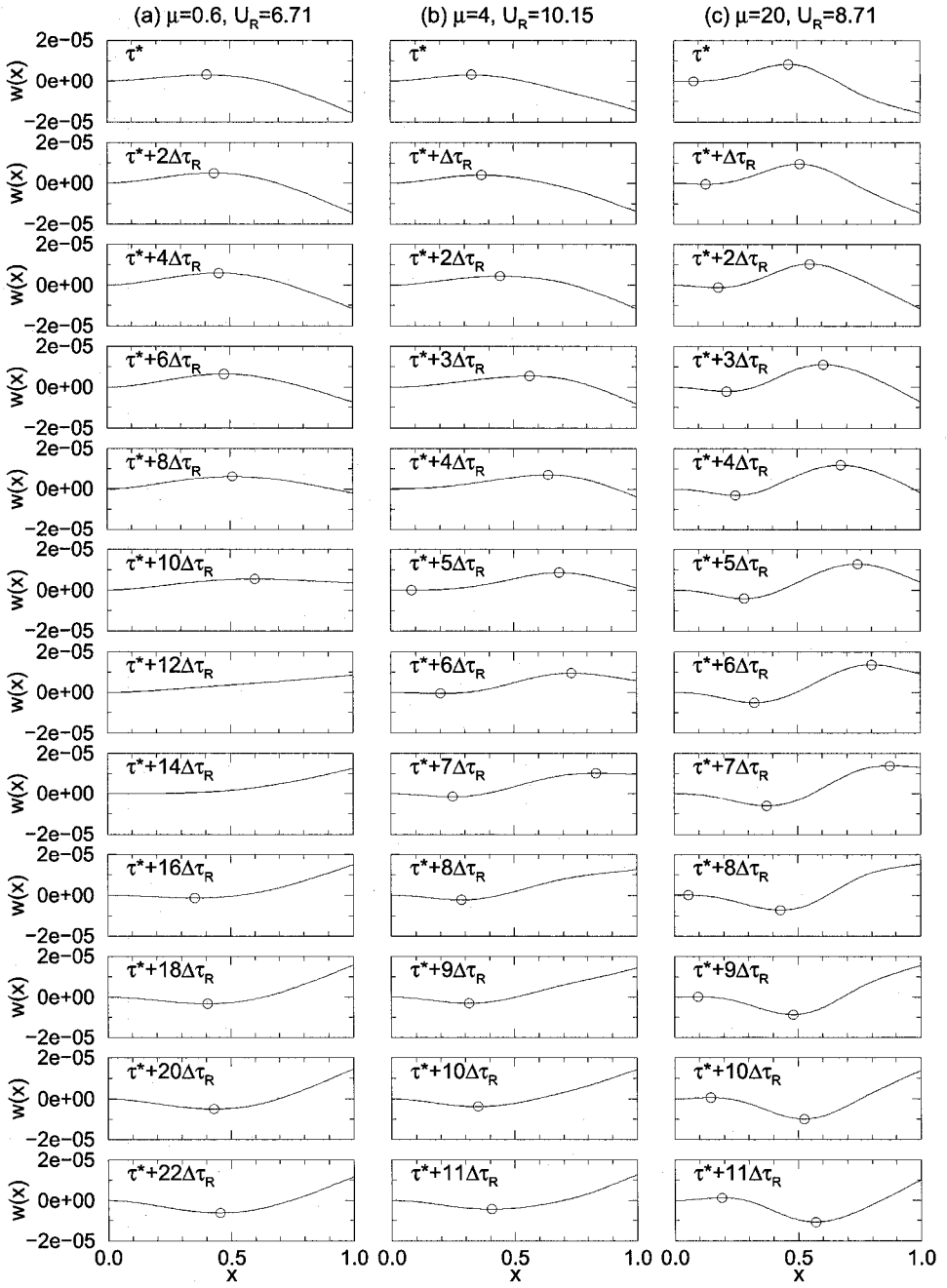

FIGURE D.2. The flutter modes of the system for the chosen values of mass ratio μ. The other system parameters are: $l_0 = 0.01$, $\alpha = 0.004$ and $C_{\mathrm{D}} = 0$.

It should be mentioned that the parameters involved in these simulations, including U_{R}, initial conditions q_1^0 (the other parts of the initial conditions are $q_{i,i\neq 1}^0 = 0$ and $\dot{q}_i^0 = 0$), time step $\Delta\tau$ and stop-time τ_E (listed in Table D.1) are not the same for all values of μ. First, as U_{Rc} varies with μ, the value of U_{Rc} in each case is different. One may notice in Table D.1 that the relation between U_{Rc} and μ exhibits an irregular

TABLE D.1. Simulation conditions and results for various cases of μ

	Short plates		Long plates	
μ	0.2	0.6	4	20
Simulation conditions				
U_{Rc}	9.92	6.71	10.15	8.71
Initial condition q_1^0 ($\times 10^5$)	-1.5	-1.5	-5.0	-1.0
$\Delta\tau$	0.001	0.001	0.0001	0.0001
τ_{E}	10	10	5	5
Simulation results				
$\max(\lvert w(x=1)\rvert)$ ($\times 10^5$)	1.4	1.6	1.5	1.6
$f^\star$	2.8	2.8	5.2	5.8
Dominant mode	2nd	2nd	2nd & 3rd	3rd

pattern (see also Fig. 4.10). In particular, $U_{\mathrm{Rc}} = 9.92$, 6.71, 10.15 and 8.71, respectively, for $\mu = 0.2$, 0.6, 4 and 20; there is not a global trend such as that observed in the U_{Rc}/μ versus μ plot of Fig. 4.16. Secondly, the time step $\Delta\tau$ in each simulation is determined by the requirement of convergence (see Chapter 3); it is not necessarily the same for different μ. Note that the number of discrete point vortices N_{W} in a fixed length of truncated wake l_{W} ($l_{\mathrm{W}} = 9$ is used in the current study) is related to $\Delta\tau$ by $N_{\mathrm{W}} = L_{\mathrm{W}}/(U\Delta t) = l_{\mathrm{W}}/(U_{\mathrm{R}}\Delta\tau)$ (taking the closest integer). Finally, as seen in Table D.1, different initial conditions and stop times τ_{E} are used for different cases of μ. The purpose of this is to obtain comparable flutter amplitudes $\max(|w(x=1)|)$ for all the values of μ tested, at a time instant close to τ_{E}, and consequently to ensure that the corresponding wakes have roughly the same strength. Since each simulation is carried out with the corresponding U_{Rc}, the time histories (still transient, not quite steady-state) in Fig. D.1 have a very small growth rate. Values of $\max(|w(x=1)|)$ at a time instant close to τ_{E} are listed in Table D.1; it can be seen that they are approximately the same.

It can be seen in Fig. D.1 that the nondimensional flutter frequency $f_{\mathrm{c}}^\star$ at the critical point U_{Rc} increases with μ. In particular, as listed in Table D.1, $f_{\mathrm{c}}^\star = 2.8$, 2.8, 5.2 and 5.8, respectively, for $\mu = 0.2$, 0.6, 4 and 20.

The plate instantaneous shapes at a series of successive time steps for $\mu = 0.6$, 4 and 20 are shown in Fig. D.2; each series roughly constitutes a half cycle of the oscillation.

In Fig. D.2, $\tau^\star$ is a selected time instant close to τ_{E}, such that at this moment the plate tip reaches its maximum negative displacement, which is not necessarily the same for all values of μ; $\Delta\tau_{\mathrm{R}} = 0.001$ is the nondimensional time step used for recording the plate shapes. It can be seen in Figs. D.2(a) hrough (c) that the plate basically oscillates in a second beam-mode shape for $\mu = 0.6$ (and also for $\mu = 0.2$, not shown); the third and higher beam-modes contribute a negligible part to the vibration. However, the third beam-mode component becomes comparable to that of the second beam-mode when $\mu = 4$, and it becomes the dominant one for $\mu = 20$. The local extrema of each deformed plate shape are marked with small circles in Fig. D.2; it can be seen that a wave travels downstream for each case of μ. Although it is clear in Fig. D.2 that the wave travels with a higher speed for long plates (for $\mu = 4$ and 20) than it does for the short one ($\mu = 0.6$), the wave travelling speed is not significantly different for $\mu = 4$ and 20.

D.2. The influence of the wake

Why do theoretical predictions and experimental measurements generally display better agreement for long plates than they do for short ones? Although, of course, a wake always exists in each individual experiment, there are important differences among various theories as to the treatment accorded to the wake behind the plate. In particular, Huang (1995), Watanabe et al. (2002b) and Argentina and Mahadevan (2005) used Theodorsen's theory Bisplinghoff et al. (1955) or one of its modified versions, and considered a wake behind the plate along the neutral plane ($Y = 0$, see Fig. 2.1). Yamaguchi et al. (2000b) adopted the linearly-varying vortex sheet model and Tang et al. (2003) used a vortex lattice model for calculating fluid loads; both included a wake behind the plate along the neutral plane. Guo and Païdoussis (2000) and Eloy et al. (2007) tried direct solutions of the potential flow problem for the

fluid part of the system and completely neglected the wake. Shelley et al. (2005) applied localized excitation theory (Crighton and Oswell, 1991) without taking the wake into account. Finally, the present theory works with the lumped-vortex model and considers a wavy wake street. An important conclusion can be reached from this compact literature review: that the wake must have but a small influence on system stability when the plate is sufficiently long.

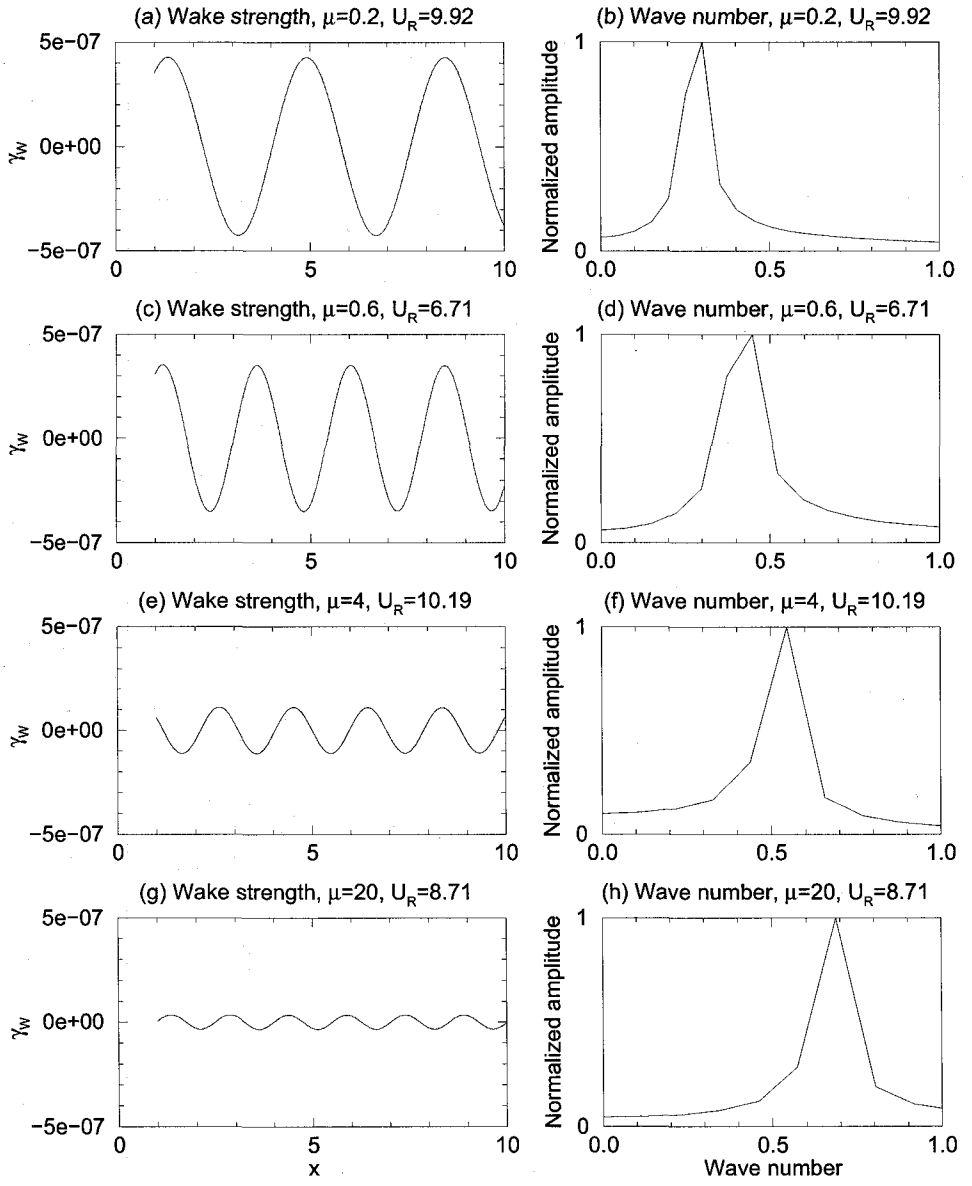

FIGURE D.3. The instantaneous wake for the chosen values of mass ratio μ, which is obtained using the corresponding U_{Rc}. The other system parameters are: $l_0 = 0.01$, $\alpha = 0.004$ and $C_{\mathrm{D}} = 0$.

In Fig. D.3, for $\mu = 0.2$, 0.6, 4 and 20, the strength of the discrete point vortices γ_W in the wake is plotted against their longitudinal coordinate x_W. The time instants for these plots are selected using the same rule as that for determining $\tau^\star$ in Fig. D.2: i.e., a time instant close to τ_E is chosen, such that at that moment the plate tip reaches its maximum negative displacement. It can be seen in Fig. D.3 that the γ_W versus x_W plot also has a wavy form. Note that both the x_W-γ_W wave and the x_W-y_W wave (as illustrated in Fig. 2.2, see also Figs. 4.8(e) through (h)) have the same wavelength and phase. In the current study of the flutter boundary, the vibration amplitude of the plate is always very small (of the order of 10^{-5}, see Figs. D.1 and D.2), i.e., $\max(|y_W|) = \max(|w(x = 1)|) \ll 1$. Therefore, all wake vortices can be regarded as lying along the neutral plane ($y = 0$) when one calculates the influence of the wake on the plate.

Two factors affecting the influence of the wake on the plate are its vortical strength and distribution in space. The strength for a wake consisting of discrete point vortices (as obtained using the present theory) should be determined by the number of wake vortices N_W in a fixed truncated wake length l_W ($l_W = 9$ in the current study) and the strength of each individual vortex γ_W. Without considering the distribution and the strength variation of wake vortices in space, one may use $N_W \times \max(|\gamma_W|)$ as a rough indicator of the equivalent strength for a wake having a regular wavy form. The equivalent strengths $N_W \times \max(|\gamma_W|)$ calculated for individual cases of μ are listed in Table D.2.

TABLE D.2. Equivalent strength of wake vorticity and wake-induced flow velocity at $x_0 = 0.5$

	Short plates		Long plates	
μ	0.2	0.6	4	20
N_W ($l_W = 9$)	907	1341	8867	10333
$1/\lambda_W$	0.28	0.42	0.5	0.7
$\max(\lvert\gamma_W\rvert) \times 10^7$	6.51	5.26	0.559	0.351
$N_W \times \max(\lvert\gamma_W\rvert) \times 10^4$	5.90 (100%)	7.05 (119%)	4.96 (84%)	3.63 (62%)
$w_W(x_0 = 0.5) \times 10^5$	3.22 (100%)	2.97 (92.9%)	0.65 (20%)	0.53 (16%)

Also, the wake-induced flow velocity (the *downwash*) w_{W} at a point $(x = x_0, y = 0)$ on the plate can be calculated by

$$w_{\mathrm{W}}(x_0) = \frac{1}{2\pi} \sum_{j=1}^{N_{\mathrm{W}}} \frac{\gamma_{\mathrm{W}j}}{x_{\mathrm{W}j} - x_0}, \tag{D.1}$$

where the distribution of wake vortices in space has been taken into account. The calculated $w_{\mathrm{W}}(x_0 = 0.5)$, also listed in Table D.2, can be regarded as an evaluation of the influence of the wake on the plate when comparing various cases of μ.

In Table D.2, the calculated values of $N_{\mathrm{W}} \times \max(|\gamma_{\mathrm{W}}|)$ and $w_{\mathrm{W}}(x_0 = 0.5)$ are expressed as a percentage of those for the reference case of $\mu = 0.2$. It can be seen that the equivalent strengths of the wake, $N_{\mathrm{W}} \times \max(|\gamma_{\mathrm{W}}|)$, for various cases of μ are similar. In contrast, the wake-induced flow velocity, $w_{\mathrm{W}}(x_0 = 0.5)$, decreases significantly as μ increases. It is easy to prove that the decrease of w_{W} with increasing μ is due to the variation of wavelength of the wake λ_{W} as shown in Fig. D.3 and also listed in Table D.2 in terms of the wavenumber $1/\lambda_{\mathrm{W}}$. For a shorter wavelength λ_{W} (i.e., a larger wavenumber $1/\lambda_{\mathrm{W}}$), successive effective wake vortices with alternating positive and negative signs (refer to Fig. 2.3(c), see also Figs. 4.8(e) through (h)) come closer to each other; and thus the wake has a smaller overall influence (in terms of w_{W}) on the plate. Note that λ_{W} is related to $f^\star$ through

$$\lambda_{\mathrm{W}} = \frac{U_{\mathrm{R}}}{f^\star}. \tag{D.2}$$

Therefore, as μ increases, the decrease in λ_{W} is actually caused by the increase of the flutter frequency $f^\star$ of the plate.

When evaluating the influence of the wake on the plate, one has to consider the plate motion as well. In Fig. D.4, the plate displacement $w(x)$ and the vibration velocity $dw(x)/d\tau$ along the plate, the wake-induced flow velocity $w_{\mathrm{W}}(x)$, as well as the ratio $(dw(x)/d\tau)/(w_{\mathrm{W}}(x)U_{\mathrm{R}})$ are presented for $\mu = 0.2$, 0.6, 4 and 20. Note that the presence of U_{R} in the ratio arises from nondimensionalization, i.e.,

$$\frac{dW(X)/dt}{W_{\mathrm{W}}(X)} = \frac{Ldw(x)/(\sqrt{\rho_{\mathrm{P}} h L^4/D}\, d\tau)}{U w_{\mathrm{W}}(x)} = \frac{1}{UL}\sqrt{\frac{D}{\rho_{\mathrm{P}} h}}\frac{dw(x)/d\tau}{w_{\mathrm{W}}(x)} = \frac{dw(x)/d\tau}{w_{\mathrm{W}}(x)U_{\mathrm{R}}}, \tag{D.3}$$

where $W_{\mathrm{W}}(X)$ is the dimensional wake-induced flow velocity, which is normalized using the undisturbed flow velocity U. For each μ, the time instant for the data presented is again selected from a point close to τ_{E}, and at this moment the plate tip should reach its negative maximum displacement, as shown in Fig. D.4(a).

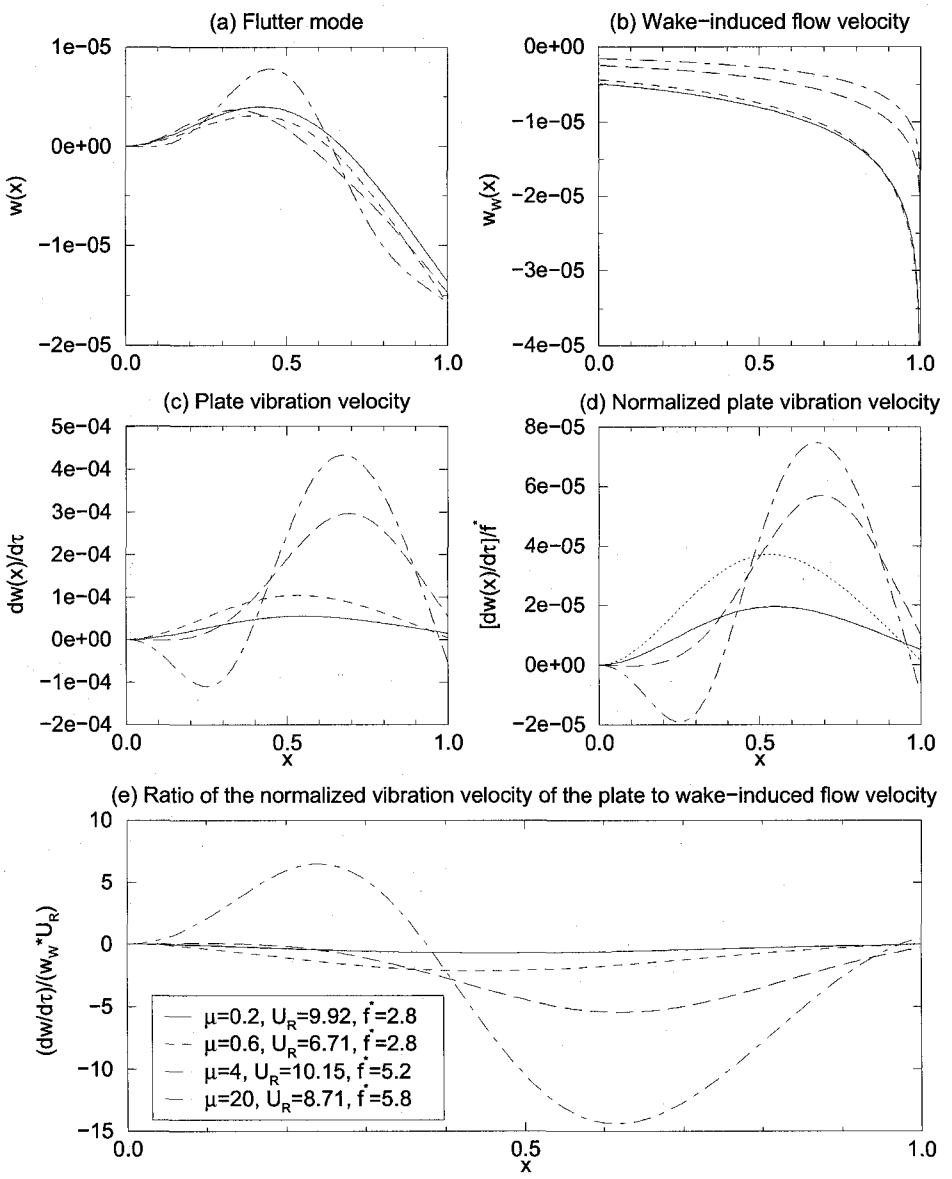

FIGURE D.4. The evaluation of the influence of the wake for the chosen values of mass ratio μ in terms of the ratio of the vibration velocity of the plate to the normalized wake-induced flow velocity. The other system parameters are: $l_0 = 0.01$, $\alpha = 0.004$ and $C_{\mathrm{D}} = 0$.

It can be seen in Fig. D.4(b) that the $w_{\mathrm{W}}(x)$ versus x curves are quantitatively similar to each other, and at a fixed point on the plate the magnitude of $w_{\mathrm{W}}(x)$ decreases monotonically as μ is increased due to the increase in flutter frequency $f^{\star}$.

The plate vibration velocity $dw(x)/d\tau$, for all values of μ under consideration, is plotted in Fig. D.4(c). Note that $dw(x)/d\tau$ is the instantaneous velocity distribution along the plate, which is a function not only of the flutter frequency $f^\star$ but also of the vibration mode. In order to examine the influence of the vibration mode, the normalized plate vibration velocities, defined by $(dw(x)/d\tau)/f^\star$, are plotted in Fig. D.4(d). It can be seen that, because higher-order modes present in the flutter become more important for the systems with larger μ, the overall magnitude of $(dw(x)/d\tau)/f^\star$ increases with increasing μ, although the instantaneous plate shapes $w(x)$ for all cases of μ are roughly the same (see Fig. D.4(a)).

Finally, in Fig. D.4(e), the plots of $(dw(x)/d\tau)/(w_{\rm W}U_{\rm R})$ are used for a comparison of the influence of the wake on the plate for the cases of μ under consideration. It can be observed that, with increasing μ, the overall magnitude of $(dw(x)/d\tau)/(w_{\rm W}U_{\rm R})$ grows significantly.

TABLE D.3. An evaluation of influence of the wake on system stability and the underlying mechanism

	Short plates		Long plates	
μ	0.2	0.6	4	20
$\int_0^1 \lvert w_{\rm W}(x)\rvert dx \times 10^6$	9.97 (100%)	9.60 (96%)	5.30 (53%)	3.62 (36%)
$\int_0^1 \lvert \frac{dw(x)}{d\tau}\rvert dx \times 10^5$	3.37 (100%)	5.98 (177%)	13.5 (399%)	18.4 (545%)
$\int_0^1 \lvert \frac{dw(x)/d\tau}{w_{\rm W}(x)U_{\rm R}}\rvert dx$	0.39 (100%)	1.13 (292%)	2.41 (624%)	6.31 (1637%)

In summary, quantitative evaluations of the wake-induced flow velocity $w_{\rm W}(x)$, the plate vibration velocity $dw(x)/d\tau$ and the ratio $(dw(x)/d\tau)/(w_{\rm W}(x)U_{\rm R})$, for individual cases of μ, in terms of the area enclosed by the curves shown in Figs. D.4(b), (c) and (e) and the x axis are listed in Table D.3. It can be seen from the last row of Table D.3 that $\int_0^1 \lvert(dw(x)/d\tau)/(w_{\rm W}(x)U_{\rm R})\rvert dx = 0.386$, 1.13, 2.41 and 6.31 for $\mu = 0.2$, 0.6, 4 and 20, respectively. That is, $w_{\rm W}$ becomes increasingly less important than $dw(x)/d\tau$ with increasing μ. Note that this trend is caused not only by the decrease in $\int_0^1 \lvert w_{\rm W}(x)\rvert dx$ but also by the increase in $\int_0^1 \lvert dw(x)/d\tau\rvert dx$ as μ increases, as respectively indicated by the first and second rows of Table D.3.

Furthermore, although it does not reveal the underlying mechanism, the most direct way for assessing the influence of the wake on system stability is to find the

TABLE D.4. The influence of wake on the stability of the system with various values of μ: the critical points obtained with or without taking into account the wake

	Short plates		Long plates	
μ	0.2	0.6	4	20
U_{Rc}	9.92	6.71	10.15	8.71
$U_{\mathrm{Rc}}^{\star}$	5.71	7.04	10.33	8.21
$\lvert U_{\mathrm{Rc}} - U_{\mathrm{Rc}}^{\star}\rvert$	4.21	0.35	0.18	0.50
$\lvert(U_{\mathrm{Rc}}/\mu) - (U_{\mathrm{Rc}}^{\star}/\mu)\rvert$	21.05	0.58	0.045	0.025

new critical point $U_{\mathrm{Rc}}^{\star}$ with a modified model *excluding* the wake and to then compare it with U_{Rc} obtained with the full model. For each case of μ, the critical points U_{Rc} and $U_{\mathrm{Rc}}^{\star}$ are listed in Table D.4. When μ grows from 0.2 to 0.6 and then to 4, it can be seen that the difference between U_{Rc} and $U_{\mathrm{Rc}}^{\star}$ decreases. However, $|U_{\mathrm{Rc}} - U_{\mathrm{Rc}}^{\star}| = 0.5$ for $\mu = 20$ does not follow this decreasing trend. Nevertheless, when the value of $|(U_{\mathrm{Rc}}/\mu) - (U_{\mathrm{Rc}}^{\star}/\mu)|$ is evaluated, a sharp decreasing trend with respect to μ can be observed for all values of μ under consideration. Therefore, when the physical parameters ρ_{P}, h, D and ρ_{F} of the fluid-structure system are fixed, one can draw the conclusion that the wake has a diminishing influence on system stability as the length of the plate is increased. That is, the *dimensional* critical flow velocity U_{c} for long plates is little affected by the wake, whereas this is not true for short plates.

Regarding the large values of $|(U_{\mathrm{Rc}}/\mu) - (U_{\mathrm{Rc}}^{\star}/\mu)|$ for $\mu = 0.2$ and 0.6, as listed in Table D.4, one can also conclude that the wake has an important influence on system stability for short plates, the underlying mechanism of which may be illustrated using the diagram in Fig. D.5. Note that, for a case of small μ, the plate vibrates in the second beam-mode (see the curve $w(x)$ for $\mu = 0.2$ in Fig. D.4(a)), and one can approximately consider the flexible plate, at a given time instant, as a rigid thin cambered airfoil moving upward with a velocity dW/dt, as shown in Fig. D.5, and also be subjected to a wake-induced flow velocity W_{W}. The directions of dW/dt and W_{W} are determined, respectively, in accordance with the signs of $dw(x)/d\tau$ and $w_{\mathrm{W}}(x)$ shown in Fig. D.4 for $\mu = 0.2$. It can be seen in Fig. D.5 that, when W_{W} is equal to or larger than dW/dt (refer to the value of $\int_0^1 |(dw(x)/d\tau)/(w_{\mathrm{W}}(x)U_{\mathrm{R}})|dx$ listed in Table D.3 for $\mu = 0.2$), the neglect of W_{W} will decrease the angle θ and

then increase the effective angle of incidence α_{eff}. It follows that the lift, which would destabilize the plate, grows. Therefore, a smaller value of the critical flow velocity U_{c} can be expected, i.e., U_{c} would be underestimated. It should be emphasized that this simple theory can only be used for a very short plate ($\mu = 0.2$). With increasing values of μ, the vibration of the plate becomes complicated, and it is not a good idea to present the vibrating flexible plate with distributed $dW(X)/dt$ (which may not be in phase at different X) and $W_{\text{W}}(X)$ as a rigid airfoil with only one dW/dt and one W_{W}.

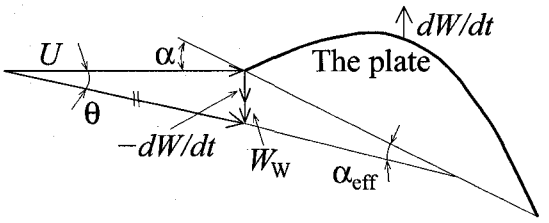

FIGURE D.5. A short plate and the flow conditions.

TABLE D.5. A short plate studied by Kornecki et al. (1976)

μ	U_{Rc}	$U_{\text{Rc}}^{\star\star}$	$\lvert U_{\text{Rc}} - U_{\text{Rc}}^{\star\star}\rvert$	$\lvert (U_{\text{Rc}}/\mu) - (U_{\text{Rc}}^{\star\star}/\mu)\rvert$
0.232	5.93	0.582	5.32	22.93

As a supplement to Table D.4, a well-deserved mention should be made the work by Kornecki et al. (1976) who studied a system with $\mu = 0.232$. In this work, a full model based on Theodorsen's theory was used for predicting the critical point (U_{Rc} as listed in Table D.5), as well as a quasi-static model neglecting the motion of the plate for another critical point (denoted by $U_{\text{Rc}}^{\star\star}$ in Table D.5). Note that neglecting the motion of the plate, instead of neglecting the wake (refer to Fig. D.5 and the discussions in the foregoing) also significantly *changes* the value of the critical point for a short plate.

D.3. Concluding remarks

It is well known that a challenging difficulty in the problem of stability of a cantilevered flexible plate in axial flow arises from the finite length of the plate; a wake exists and affects the system dynamics. However, from a physical point of view,

when the length of the plate increases sufficiently so as to approach an infinitely long plate, the influence of the wake on the system dynamics should diminish and then disappear (recall the much improved agreement for long plates shown in Fig. 4.16, between the theoretical predictions of Huang (1995), Guo and Païdoussis (2000), Yamaguchi et al. (2000b), Watanabe et al. (2002a), Shelley et al. (2005), Argentina and Mahadevan (2005) and Eloy et al. (2007) as well as the present theory). In this Appendix, we have studied the influence of the wake on the stability of cantilevered plates in axial flow and the underlying mechanisms.

In order to compare the flutter boundaries predicted/measured by various theories/experiments, the nondimensional mass ratio μ and reduced flow velocity U_{R} are used as parameters. However, as the parameters μ and U_{R} share some physical elements, a monotonic trend cannot be observed in the U_{Rc} versus μ plot. To resolve this problem, all flutter boundaries are presented in a U_{Rc}/μ versus μ plot, in which a clear monotonic trend in the relation between the *dimensional* parameters U_{c} and L is discovered, supposing that the parameters ρ_{P}, h, D and ρ_{F} remain fixed. To this end, using U_{Rc}/μ as the ordinate in Fig. 4.16 does not just simply represent the theoretical/experimental data in a different way (refer to Fig. 9 in Ref. Watanabe et al. (2002a), which has been extensively used in other publications); it does reveal an intrinsic property of the system, with direct physical meaning.

Taking advantage of the clear trend in the U_{Rc}/μ versus μ plot, a global assessment of the flutter boundaries by various theories and experiments can be made: the various theories (no matter whether they consider a wake or not) and experiments (where a wake always exists) agree with one another very well for long plates. However, for short plates, various theoretical predictions and experimental measurements exhibit quite large discrepancies. These observations immediately lead to the conclusion that the wake has less influence on system stability for long plates than it does for short ones. As we have mentioned in Chapter 4, all influencing factors including the length of leading rigid segment, the level of material damping, the aspect ratio (for three-dimensional considerations) and so on, have less effect on system stability for

long plates than they do for short ones. However, in this appendix, we have focused on the influence of the wake and its effect on flutter.

It should be emphasized that the only conclusion that we have been able to reach with confidence is deliberately limited to the different levels of influence of the wake on stability, respectively for long and short plates; whether a wake would stabilize or destabilize the system is not discussed. Moreover, although quantitative analysis has frequently been used, the assessment of the importance of the wake, regarding the level of its influence on system stability, is still qualitative.

To evaluate the influence of a dynamic wake is not an easy task. First, an accurate model of the wake and the unsteady flow conditions surrounding an oscillating deformable solid body requires sophisticated and refined knowledge, to a level not yet attainable. Second, the influence of various parameters in such a complicated system as a cantilevered plate in axial flow are normally interwoven, and they do not necessarily have a monotonic/uniform pattern in terms of a specific parameter; this fact would make an assessment of the influence of the wake even more complicated. However, the observed overall trend of the flutter boundary in Fig. 4.16 is so starkly clear that a relatively simple wake model and the associated analytical approach used in this Appendix can and do reveal the underlying mechanism of the influence of the wake, with a fairly high degree of confidence.

Through a carefully arranged study on the dynamics of the system along the flutter boundary, it is found that longer plates have higher critical frequencies, which lead to shorter wavelengths in the wake and consequently to smaller wake-induced flow velocities (*downwash*) on the plate. On the other hand, more higher-order mode components are found in the plate vibration at the critical point for longer plates, which, in conjunction with the higher critical frequencies, result in higher overall plate vibration velocities. Under the combined action of these two factors, the ratio of plate vibration velocity and to wake-induced flow velocity becomes higher for longer plates; therefore, it can be concluded that for longer plates the wake has a smaller influence.

Appendix E

Preparation of the Experiment

In this Appendix, we summarize the preparatory work conducted for the experiment; this is supposed to be a documentation of the work carried out on refurbishing of the water tunnel, calibration of new measurement instruments, making of flexible plates and determination of the material properties of the plates.

E.1. The water tunnel and refurbishment work

A schematic diagram of the water tunnel used for the experiment is shown in Fig. E.1. This water tunnel is of a closed-circulation vertical type. The water inside the tunnel circulates by means of pump 1, driven by an SCR(Silicon-Controlled-Rectifier) variable-speed motor, allowing bulk flow velocities up to 6 m/s. The test-section of the water tunnel consists of a 740 mm long vertical acrylic cylinder channel of 205 mm internal diameter. At the top and bottom ends, there are two circular plexiglas windows, allowing access to the test-section without removing it.

Two Venturi flow meters (see valves #17-18 and #19-20 in Fig. E.1 for their location) were mounted in parallel on the water tunnel. The old measurement section included two manometers (see section IV in Fig. E.1), which were, respectively, connected to the two Venturi meters. Before the experiment, these two manometers were dismounted and replaced by two differential-pressure transducers (Huba-692), of which the readings are, respectively, displayed on two controllers (ATR141, used

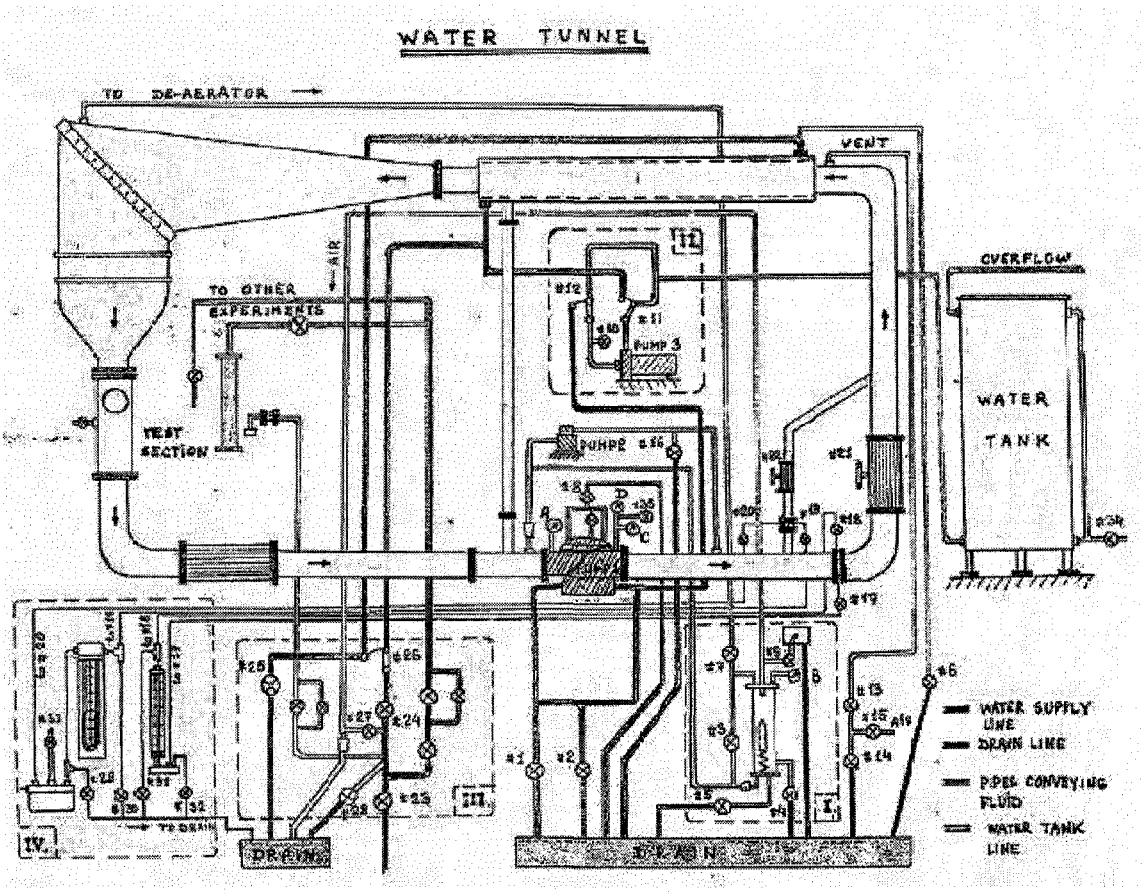

FIGURE E.1. A schematic diagram of the water tunnel in the Fluid-Structure Interactions Laboratory, Department of Mechanical Engineering, McGill University (Hydrodynamics Laboratory, 1998).

as read-out units). Another pressure transducer (ADZ-SML 10.0) is installed at the test-section. This latter transducer monitors the pressure in the water tunnel and is connected to a controller (ATR400), which is operated with a prescribed set-point and sends a signal to control the opening of the control valve (TR24-SR-T US) installed on a bypass pipe at the manual water supply valve #24 (see Fig. E.1 for its location). The components newly installed and the corresponding electrical connection diagram are, respectively, shown in Figs. E.2 and E.3. Moreover, the controllers (two ATR141 and one ATR400) are mounted on a control box, where electrical power for the transducers, controllers and control valve is supplied.

It should be noted that a special fixture, as shown in Figs. E.4 and E.5, is designed for mounting the pressure transducer at the test-section, which has a concave surface at one end and a pair of differential threads to ensure that the end-surface be flush

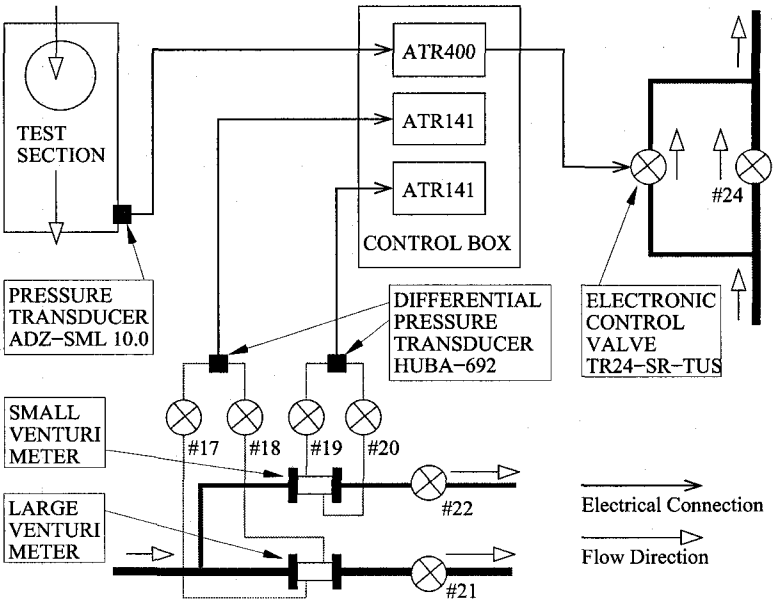

FIGURE E.2. A schematic diagram of new installations on the water tunnel.

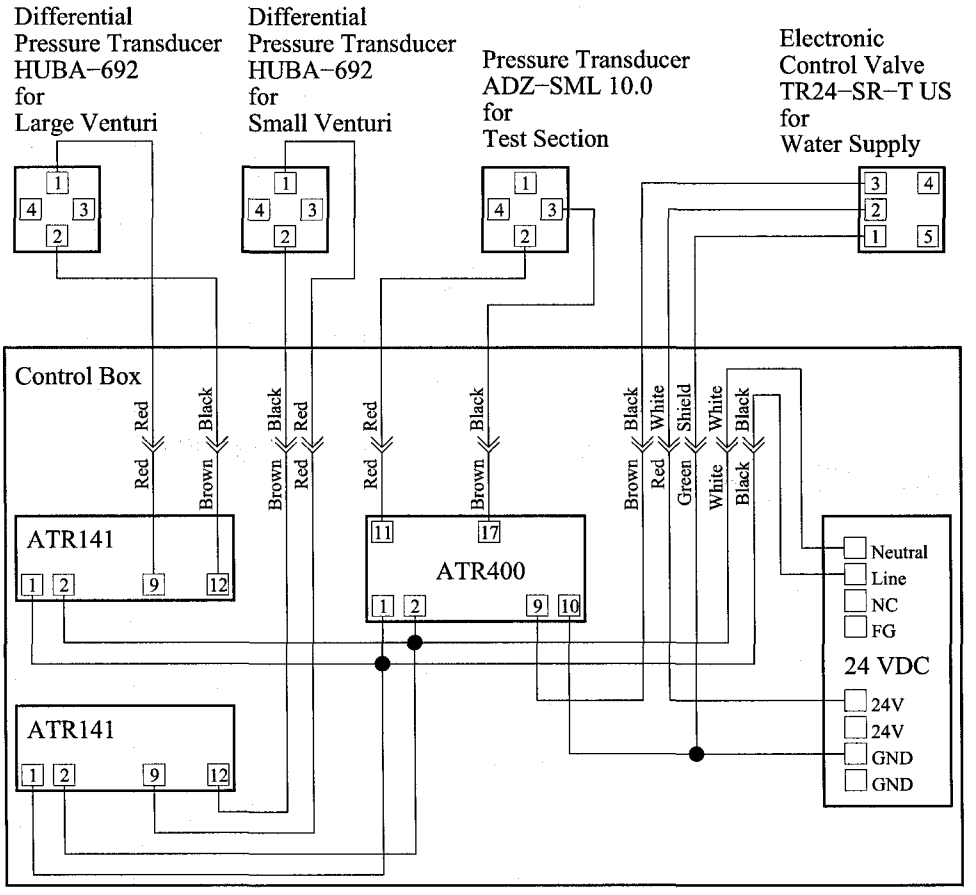

FIGURE E.3. A schematic diagram of the electrical connections.

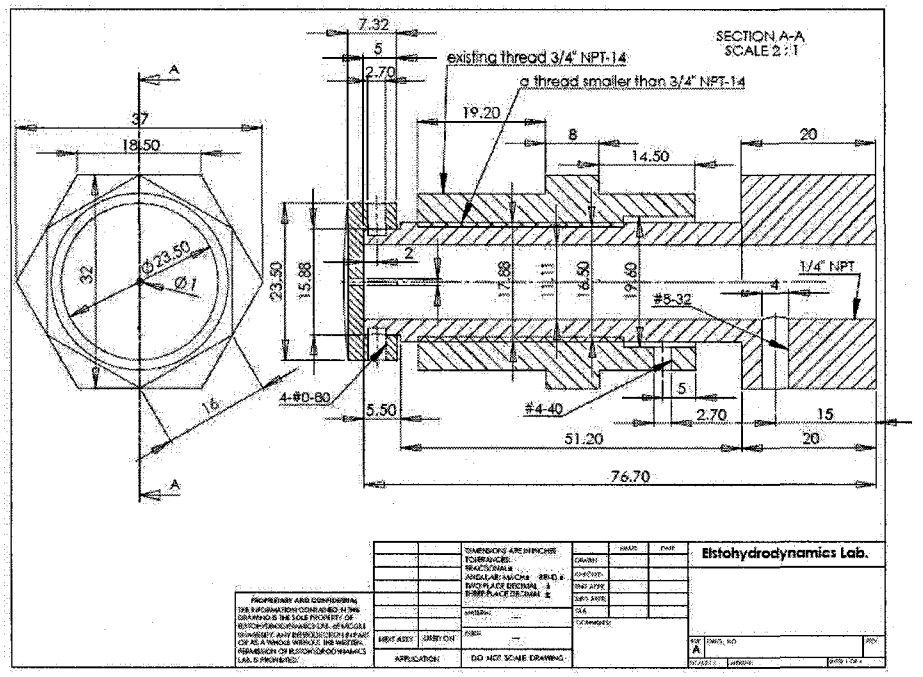

FIGURE E.4. The assembly drawing of the fixture for mounting the transducer ADZ-SML 10.0 at the test-section.

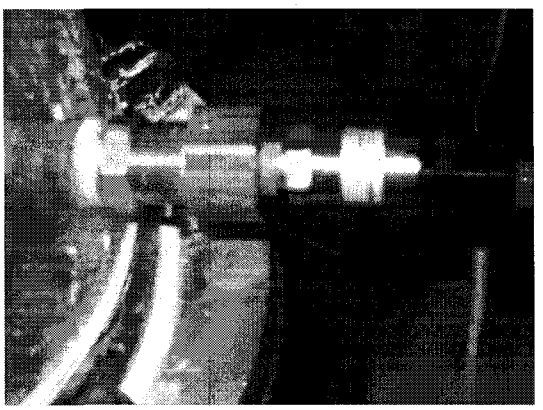

(a) The installation of the pressure transducer and the fixture for holding it

(b) The concave end-surface of the fixture

FIGURE E.5. The fixture for holding the pressure transducer ADZ-SML 10.0.

with the circular cross-section internal surface of the test-section upon installation. A small hole, in 1 mm diameter, at the centre of the concave end serves as the pressure tap, thus avoiding the influence of the flow velocity on the reading of the (static) pressure in the water tunnel.

E.2. The design and installation of the support fixture

A support fixture has been designed for clamping the upstream end of a flexible plate and holding it in place in the test-section, as shown in Figs. E.6 and E.7. Because it is very difficult to remove the test-section from the water tunnel and reinstall it repeatedly, the support fixture has a two-part design: a fixed part and a removable part. The fixed part is installed in the test-section before the experiment, across a diameter, and sits securely in two grooves on the wall of the test-section. Alignment is carefully adjusted to ensure that the support fixture (the fixed part) is vertically set up in the test-section. On the other hand, the removable part, together with the flexible plate attached to it, can enter the test-section through the top access window. Therefore, one can change the flexible plate for different experiments without removing/re-installing the test-section.

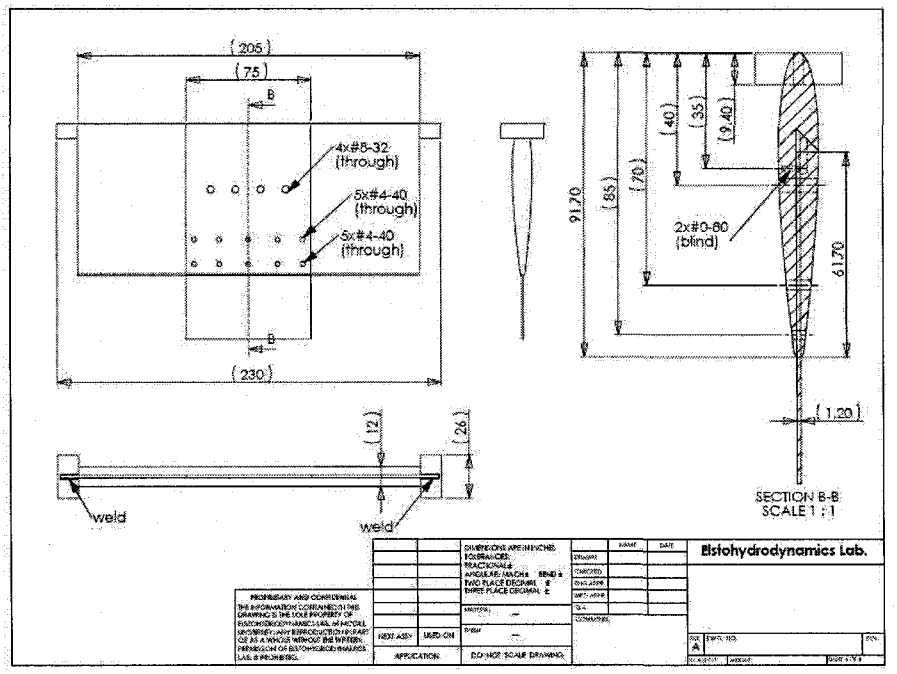

FIGURE E.6. The assembly drawing of the support fixture for clamping a flexible plate.

When the removable and fixed parts fit together, they form a straight NACA0012 wing (Abbott and von Doenhoff, 1959). Note that the nominal chord length of the wing is 95 mm, while its trailing edge is chamfered with a relatively large radius,

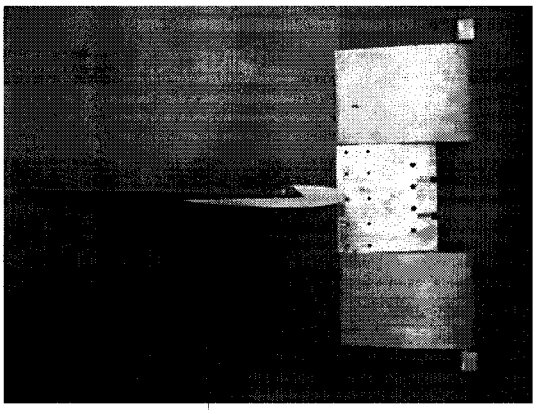

(a) The fixed part and the removable part

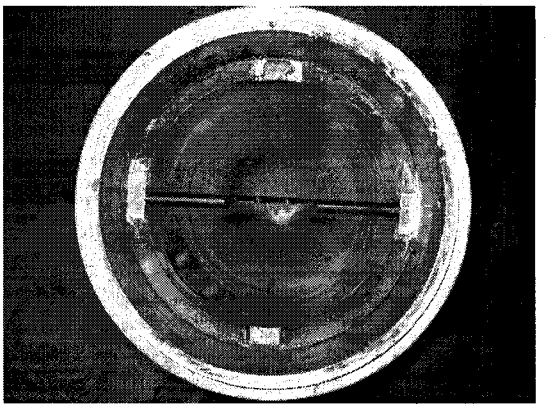

(b) The installation of the fixed part in the test-section, viewed from above

FIGURE E.7. The support fixture for clamping the plate.

avoiding a sharp edge. The actual chord length of the wing-shaped supporter is 91.7 mm, as one can see in Fig. E.6. The gap between the removable and fixed parts of the support fixture (wherein the flexible plate would be fitted) is 1.2 mm; when the thickness of a flexible plate is less than 1.2 mm, gaskets made from brass sheet can be used to fill the gap fully. A flexible plate is first fixed to the removable part with two screws. Then the removable part as well as the flexible plate, together, are moved through the access-window and matched to the fixed part. Finally, the removable part and the fixed part, with a part of the flexible plate sandwiched in the middle, are fixed together with three rows of set-screws, as shown in Fig. E.6.

E.3. Flow velocity measurement calibration

The reading on the controller ATR141 for the differential pressure transducer (Huba-692) connected to the large Venturi meter is calibrated using a Pitot-tube and a mercury manometer, as shown in Fig. E.8. Note that only the large flow-path (where the large Venturi meter is installed) is used in the experiment; the choke valve #22 is always closed in the calibration and future experiments. The Pitot-tube is inserted into the test-section through the lower access-window; and its tip is carefully aligned with the centreline of the test-section. A mercury manometer is connected to the Pitot-tube; from the height of the Hg-column, one can calculate the flow velocity

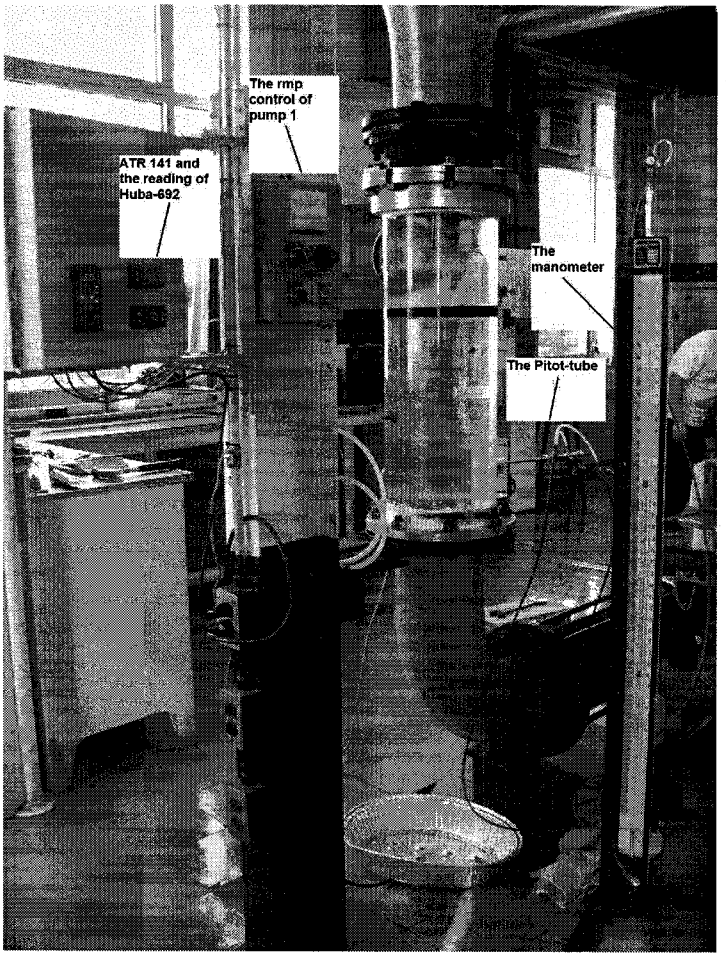

FIGURE E.8. The set-up of the calibration of flow velocity.

in the test-section according to

$$U = \sqrt{2\left(\frac{\rho_{\mathrm{Hg}}}{\rho_{\mathrm{Water}}} - 1\right) g H_{\mathrm{Hg}}} = 15.69\sqrt{H_{\mathrm{Hg}}}, \tag{E.1}$$

where $\rho_{\mathrm{Hg}} = 13.546 \times 10^3\,\mathrm{kg/m^3}$ and H_{Hg} are, respectively, the density of mercury and the height of the Hg-column (m), $\rho_{\mathrm{Water}} = 1 \times 10^3\,\mathrm{kg/m^3}$ is the density of water, and g is the gravitational acceleration.

Measurements made in the calibrations are presented in Fig. E.9. The water circulates by means of Pump 1 (see Fig. E.1), of which the capacity is regulated at the rmp control box shown in Fig. E.8. At a fixed level of rmp for Pump 1, eight pairs of readings at the ATR141 and the manometer are recorded. A linear line is obtained through a curve fit in Fig. E.9. It should be mentioned that the signal range of the Huba-692 is from 4.040 mA to 20.0 mA. In the calibration, the range of the

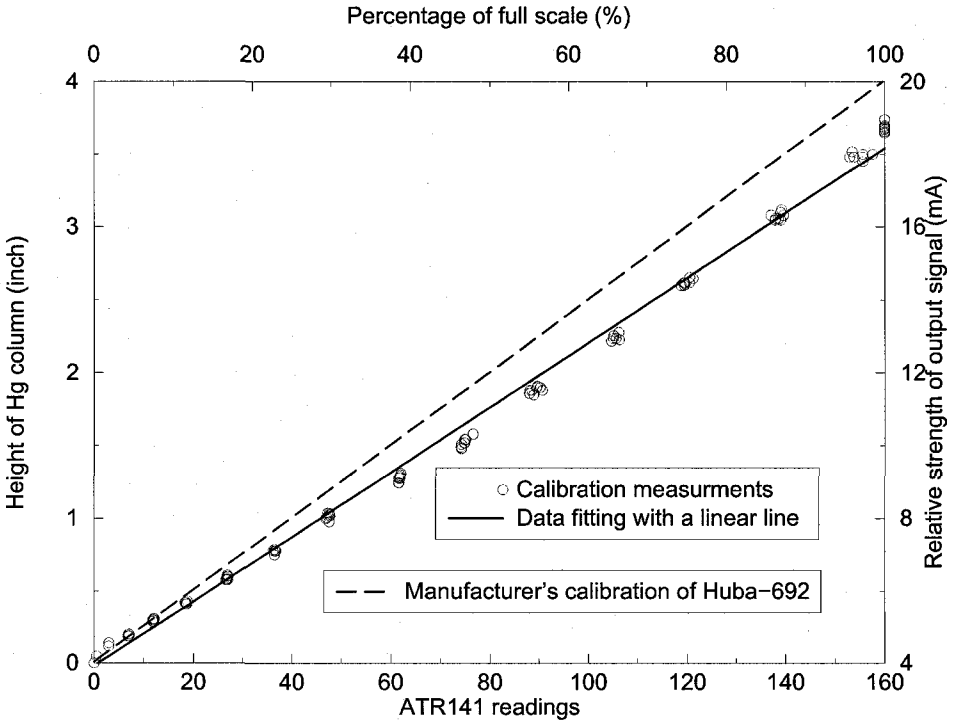

FIGURE E.9. The measurements made in the calibration of the reading on the ATR141.

display on the ATR141 is set as from 0 to 160 with the resolution of 0.1; the zero point of the reading corresponds to $U = 0\,\mathrm{m/s}$, i.e., the pump being in idle state. In Fig. E.9, the manufacturer's calibration line for the transducer Huba-692, in terms of the output signal versus the percentage of the capacity range, is also presented; the variation in the slope of the current calibration line with respect to the one provided by the manufacturer is found to be 11.5%.

With the data in Fig. E.9, the relationship between the flow velocity and the reading of the ATR141 is attained according to Eq. (E.1); the results are presented in Fig. E.10. Moreover, a curve fit is obtained in Fig. E.10 using a 6th degree polynomial, based on which one can convert the readings of the ATR141 to flow velocities in experiments (for $U > 0.7\,\mathrm{m/s}$).

E.4. The making of a plate

As shown in Fig. E.11, a special casting module has been designed for making highly flexible plates from silicone rubber (Silastic RTV), which consists a aluminium

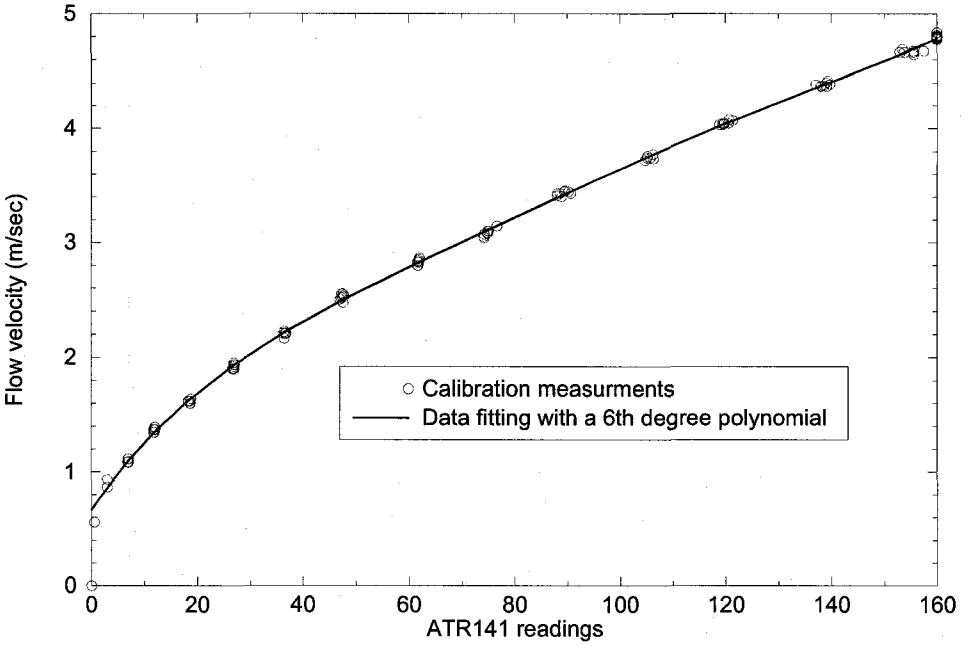

FIGURE E.10. The calibration of the flow velocity.

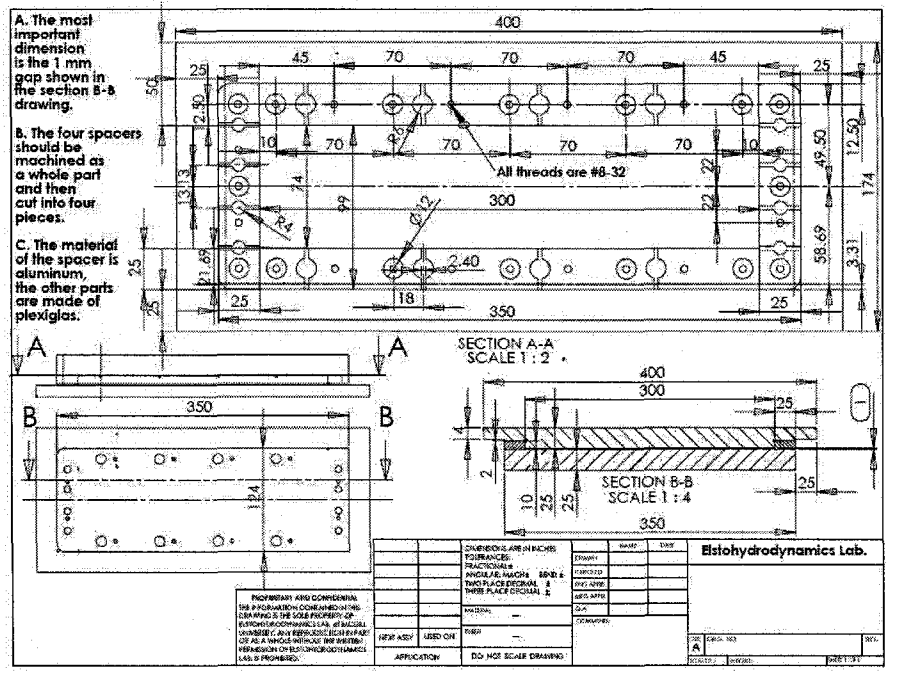

FIGURE E.11. The assembly drawing of the casting module for making flexible plates from silicone rubber (Silastic RTV).

base, four aluminium spacers and a plexiglas cover. The dimensions of the plate that can be made with this module are 300 mm × 74 mm × 1 mm. The width of the plate is limited by the diameter of the top access-window. A part of of the plate of the

length 60 mm at one end is used for clamping it in the support fixture; therefore the maximum effective length of the plate is 240 mm.

(a) The liquid silicone rubber, curing agent and tools used for mixing

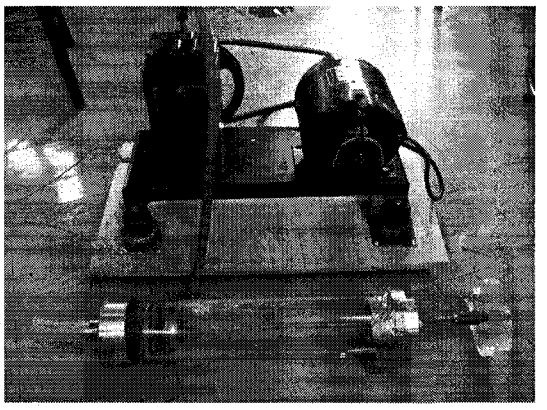

(b) The plexiglas piston and vacuum pump

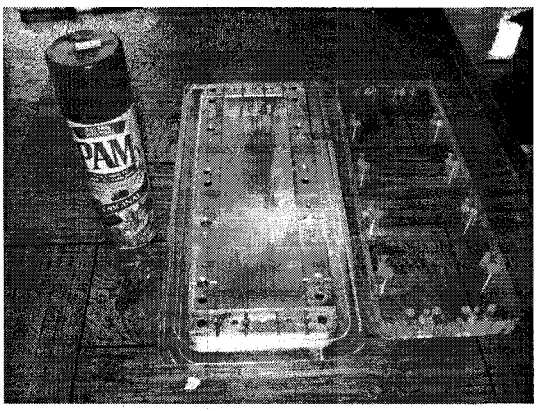

(c) The casting module

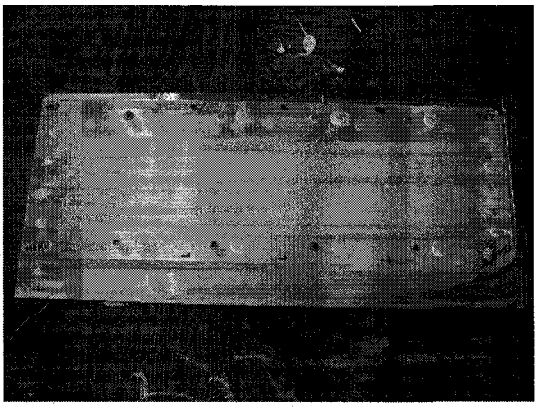

(d) The closed casting module with silicone mixture inside

FIGURE E.12. The casting processes.

The process of casting a plate is shown in Fig. E.11. First, the liquid silicone rubber (Sylgard® 184 Silicone Elastomer Base) and curing agent are mixed with the weight ratio 10 : 1 in a container and sufficiently mixed with the aid of a special tool. The mixture is then introduced into a plexiglas piston which is later connected to a vacuum pump for deaeration. The deaerated mixture in the plexiglas piston is slowly poured into the reservoir formed by the base and the four spacers of the casting module, avoiding trapping of air pockets in the process. Subsequently, the cover of the casting module is placed on the top of the silicone mixture, pressed tightly and fixed with the screws to the base. It should be mentioned that a thin oil film should

be applied to the contacting surface of the base, the spacers as well as the cover of the casting module before pouring in the silicone mixture in order to facilitate the removal of the plate from the module. Moreover, the setting time of the silicone mixture is 30 minutes; the mixing, deaeration and pouring processes should be complected in this duration. The module containing the silicone mixture is left alone for 48 hours (curing time) before opening the module.

E.5. The material properties of the plate

A cylinder made of the same silicone material, the same batch of the silicone liquid used for the plate, was recently tested. The cylinder was clamped at one end and free at the other one, and it was set up in a hanging configuration. The damped natural frequencies of the first three modes of the cylinder were tested (Segala, 2006), and the flexural rigidity and the damping coefficients can be determined according to the work by Païdoussis and des Trois Maisons (1969, 1971).

TABLE E.1. Data of the free lateral vibration of a vertically cantilevered cylinder (Rinaldi, 2007)

	1st mode	2nd mode	3rd mode
Damped natural frequency (Hz)	1.123	4.279	10.938
Circular frequency of oscillation Ω (rad/s)	7.056	27.0	68.73
Logarithmic decrement δ_D	0.0492	0.112	0.184

In particular, as provided by Rinaldi (2007), the data of the free lateral vibration (in air) of a cylinder is listed in Table E.1. Moreover, the parameters of the cylinder are: length 0.458 m, mass per unit length 0.189 kg/m, outer diameter 15.875 mm and inner diameter 6.35 mm. Therefore, the flexural rigidity can be found to be $EI = 0.011\,\mathrm{N}\cdot\mathrm{m}$, where $I = 3.038 \times 10^{-9}\,\mathrm{m}^4$ is the second moment of area of the cylinder. It follows that Young's modulus of the material can be calculated as $E = 3.621\,\mathrm{N/m}^2$.

From the parameters of the cylinder above mentioned, one can calculate the mass density of the silicone material to be $1.137 \times 10^3\,\mathrm{kg/m}^3$. No direct information concerning the Poisson ratio of the silicone material is available. However, from the

experience obtained from previous work conducted at the Fluid-Structure Interactions Laboratory, it is believed that $\nu = 0.49$. Note that the Poisson ratio of natural rubber is within the range $0.28 \sim 0.49$.

TABLE E.2. The determination of the value of material damping coefficient

	1st mode	2nd mode	3rd mode
The value of $\delta_D/(a^\star + a\Omega)$	1.04	2.44	2.84
With $a^\star = 0.041$ and $a = 0.000449$ s			
Calculated value of $\delta_D/(a^\star + a\Omega)$	1.134	2.233	2.718
Error	9.02%	−8.48%	−4.28%
With $a^\star = 0.041$ and $a = 0.000472$ s			
Calculated value of $\delta_D/(a^\star + a\Omega)$	1.131	2.212	2.669
Error	8.71%	−9.33%	−6.03%
With $a^\star = 0.039$ and $a = 0.00046$ s			
Calculated value of $\delta_D/(a^\star + a\Omega)$	1.187	2.315	2.779
Error	14.12%	−5.14%	−2.15%
With $a^\star = 0.040$ and $a = 0.00046$ s			
Calculated value of $\delta_D/(a^\star + a\Omega)$	1.159	2.268	2.735
Error	11.43%	−7.06%	−3.68%
With $a^\star = 0.041$ and $a = 0.00046$ s			
Calculated value of $\delta_D/(a^\star + a\Omega)$	1.132	2.222	2.693
Error	8.87%	−8.91%	−5.17%

In the work by Païdoussis and des Trois Maisons (1969, 1971), two types of material damping were taken into account, and Young's modulus of the material E was replaced by $E[1 + (a^\star/\Omega + a)\partial/\partial t]$, where $a^\star$ is the material damping coefficient when the dissipation is considered to be a hysteretic effect, and a is the coefficient of the material damping of the Kelvin-Voigt type. For a specific cylinder, the values of the expression $\delta_D/(a^\star + a\Omega)$ can be found in the work by by Païdoussis and des Trois Maisons (1971) for the first three modes of the cylinder; one can thus determine the values of $a^\star$ and a, through a trial and error process, to obtain the closest approximations to values of the expression for individual modes. The values of $a^\star$ and a so determined, i.e., $a^\star = 0.041$ and $a = 0.00046$ s, are listed in Table E.2. It should be noted that only the material damping of the Kelvin-Voigt type, i.e., $a = 0.00046$ s, is considered in this thesis for the model of the plate.

E.6. Displacement measurement calibration

As shown in Fig. E.13, a laser distance sensor MEL-M27 is used for measuring the displacement of a chosen point on the the plate. The laser distance sensor is connected, *via* an electronic unit, to the signal conditioner IMC CRONOS-PL CS-7008; and the latter is connected to a computer with a ethernet cable. The output signal of laser distance sensor is directly displayed, in terms of distance, on the computer with the software provided by the supplier of the signal conditioner.

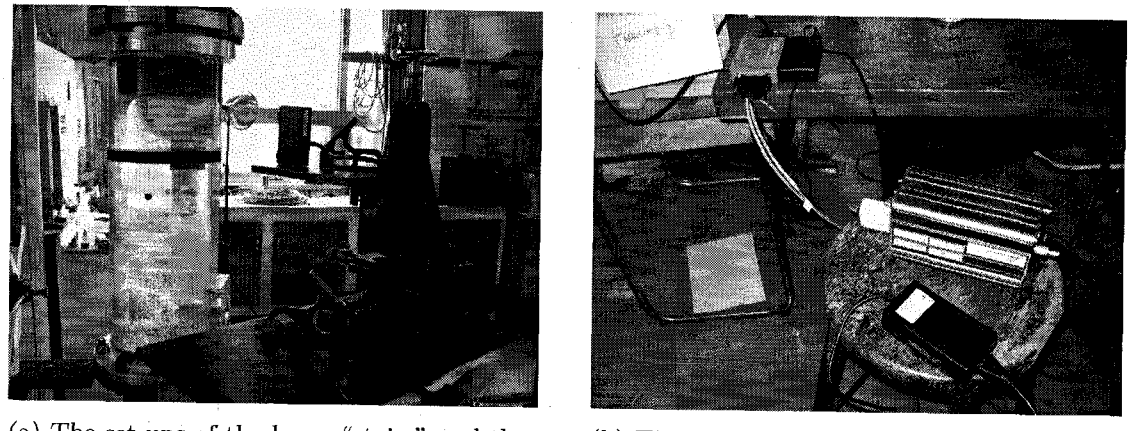

(a) The set-ups of the brass "stairs" and the laser distance sensor MEL-M27

(b) The electronic unit M27 and the signal conditioner Imc CRONOS-PL CS-7008

FIGURE E.13. The laser system for displacement measurement.

The reading of the laser distance sensor is calibrated with the aid of a special reference object, i.e., the brass "stairs" shown in Figs. E.13(a) and E.14, of which the two dimensions of the two steps are respectively, 27 mm and 62 mm. The output signal of the laser distance sensor is affected by the wall of the test-section, the water inside the test-section, and the material surface characteristics. Therefore, in the calibration, the brass "stairs" device is placed in the test-section and elastomer (silicone rubber) strips are glued on the surface of the "stairs" to mimic the plate used in the experiment.

Because the test-section has a circular wall, the first step of calibration is to align the sensor and to find the correct calibration position. As illustrated in Fig. E.13(a), the sensor is horizontally moved from left to right and then vice versa, and the readings of the sensor, at 12 points on each elastomer strip are recorded. As shown in Fig. E.15,

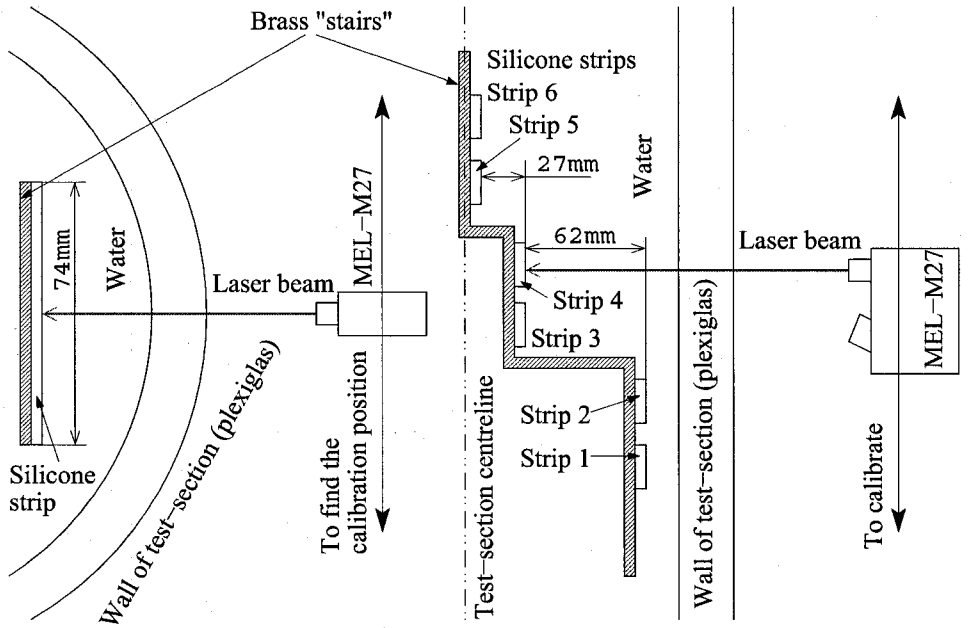

(a) Top–view: the calibration position (b) Side–view: the calibration direction

FIGURE E.14. The calibration of the displacement measurement.

a minimum reading can be seen at the position 6 or 7 for each strip; we choose the position 7 for calibration and future measurements. The data presented in Fig. E.15 are obtained after the movement of the laser distance sensor in the calibration process has been aligned in parallel to the silicone strips (thus the laser beam is vertical to the strips); this alignment is achieved and also confirmed by attaining a probability-distribution-like for the plot of the readings versus the locations along a strip. It should be noted that both the inner and outer surfaces of the plexiglas wall of the test-section are somewhat stained/scrached here and there and the plexiglas contains micro-fissures, which may account for the abnormal points in Fig. E.15.

After the correct calibration position has been found, the laser distance sensor is vertically moved along the reference object as illustrated in Figs. E.13(a) and E.14(b). The readings corresponding to three points on each strip are recorded, and the results are listed in Table E.3. The calibration results are also plotted in Figs. E.13 in conjunction with the data line-fit; the conversion ratio of the reading of the laser distance sensor to the actual displacement of the plate is found to be 2.524.

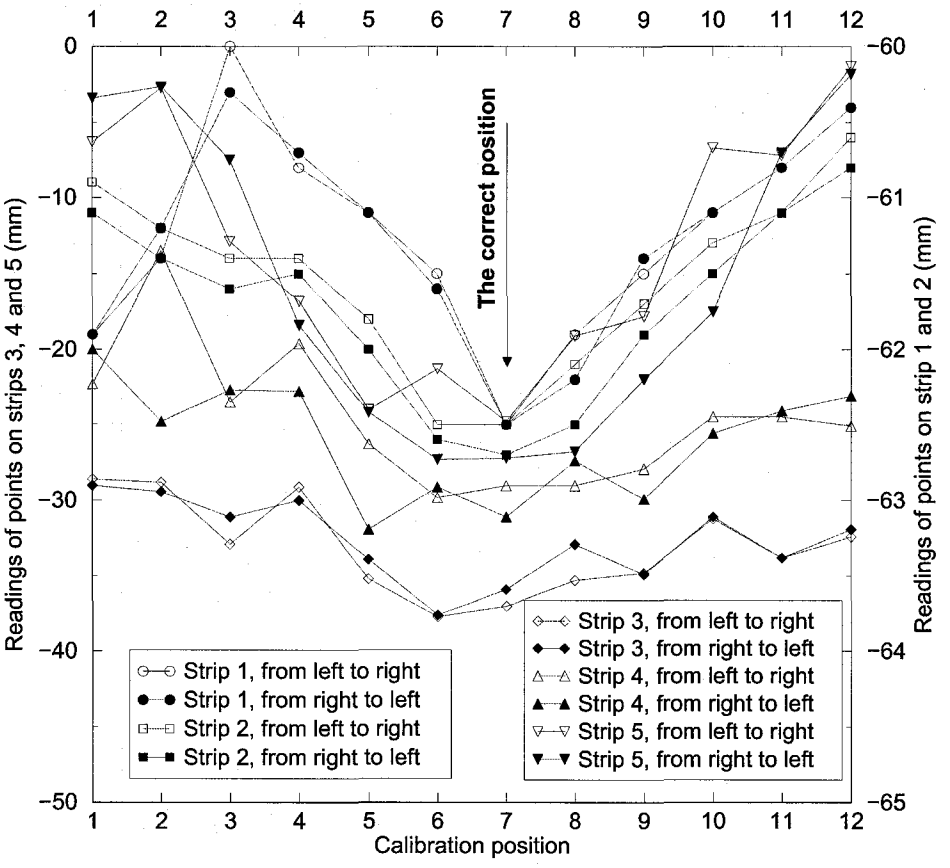

FIGURE E.15. The determination of the correct position for calibration.

TABLE E.3. The results of the calibration of the laser distance sensor

	Strips 1 & 2	Strips 3 & 4	Strips 5 & 6
Averaged sensor reading (mm)	62.5	37.4	26.2
Difference of the reading (mm)	N/A	25.1	11.2
Actual distance (mm)	N/A	62	27

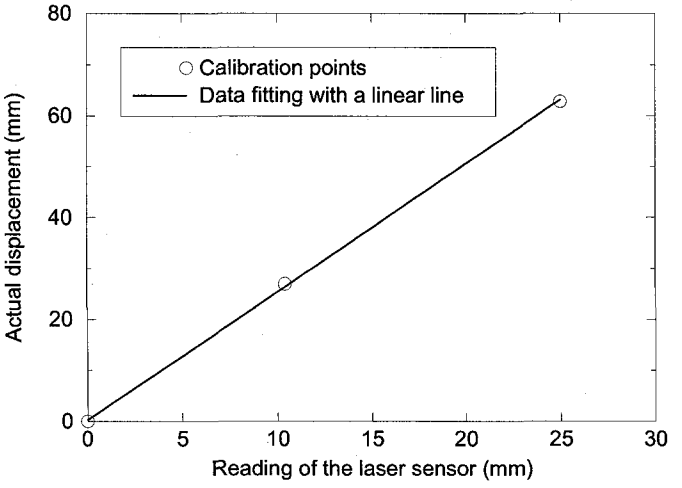

FIGURE E.16. The calibration of the displacement measurement.

Document Log:

Manuscript Version 1 — November, 2007

Typeset by $\mathcal{A}\mathcal{M}\mathcal{S}$-LaTeX — 29 November 2007

LIAOSHA TANG

Department of Mechanical Engineering, McGill University, 817 Sherbrooke St. W., Montréal (Québec) H3A 2K6, Canada, *Tel.* : (514) 398-6290

E-mail address: liaosha.tang@mail.mcgill.ca

Typeset by $\mathcal{A}\mathcal{M}\mathcal{S}$-LaTeX